

Tribology and Rotordynamics of Small High-Speed Cryogenic Turboexpander

*Dissertation submitted in partial fulfillment
of the requirements of the degree of*

Doctor of Philosophy

in

Mechanical Engineering

by

Suraj Kumar Behera

(Roll Number: 511ME437)

based on the research carried out

under the supervision of

Prof. Sunil Kumar Sarangi

and

Mr. Trilok Singh



April, 2017

Department of Mechanical Engineering
National Institute of Technology Rourkela



Department of Mechanical Engineering
National Institute of Technology Rourkela

Feb 26th, 2018

Certificate of Examination

Roll Number: *511ME437*

Name: *Suraj Kumar Behera*

Title of Dissertation: *Tribology and Rotordynamics of Small High-Speed Cryogenic Turboexpander.*

We the below signed, after checking the dissertation mentioned above and the official record book (s) of the student, hereby state our approval of the dissertation submitted in partial fulfillment of the requirements of the degree of *Doctor of Philosophy in Mechanical Engineering at National Institute of Technology, Rourkela.* We are satisfied with the volume, quality, correctness, and originality of the work.

Trilok Singh
Co-Supervisor

Sunil Kumar Sarangi
Principal Supervisor

Ranjit Kumar Sahoo
Caretaker Supervisor and
Member (DSC)

Sukesh Chandra Mohanty
Member (DSC)

Shishir Kumar Sahu
Member (DSC)

Somashekhar S. Hiremath
Examiner

Kalipada Maity
Chairman (DSC)



Department of Mechanical Engineering
National Institute of Technology Rourkela

Prof. Sunil Kumar Sarangi
Ex-Director, NIT Rourkela

Mr. Trilok Singh
Retd. Outstanding Scientist, BARC

Prof. Ranjit Kumar Sahoo
Professor

April 15, 2017

Supervisors' Certificate

This is to certify that the work presented in this dissertation entitled *Tribology and Rotordynamics of Small High-Speed Cryogenic Turboexpander* by *Suraj Kumar Behera*", Roll Number 511ME437, is a record of original research carried out by him under our supervision and guidance in partial fulfillment of the requirements of the degree of *Doctor of Philosophy in Mechanical Engineering*. Neither this dissertation nor any part of it has been submitted for any degree or diploma to any institute or university in India or abroad.

Trilok Singh
Co-Supervisor

Sunil Kumar Sarangi
Principal Supervisor

Ranjit Kumar Sahoo
Caretaker Supervisor

Dedicated

To

My Wife

Suraj Kumar Behera

Declaration of Originality

I, *Suraj Kumar Behera*, Roll Number 511ME437 hereby declare that this dissertation entitled *Tribology and Rotordynamics of Small High-Speed Cryogenic Turboexpander* presents my original work carried out as a doctoral student of NIT Rourkela and, to the best of my knowledge, contains no material previously published or written by another person, nor any material presented by me for the award of any degree or diploma of NIT Rourkela or any other institution. Any contribution made to this research by others, with whom I have worked at NIT Rourkela or elsewhere, is explicitly acknowledged in the dissertation. Works of other authors cited in this dissertation have been duly acknowledged under the sections “Reference” or “Bibliography”. I have also submitted my original research records to the scrutiny committee for evaluation of my dissertation.

I am fully aware that in case of any non-compliance detected in future, the Senate of NIT Rourkela may withdraw the degree awarded to me on the basis of the present dissertation.

April 15, 2017
NIT Rourkela

Suraj Kumar Behera

Acknowledgment

I am extremely privileged to be involved in an exciting and challenging research project on turboexpander. This project has given me an opportunity to work for the true prosperity of technology and work with the people endowed with many countless qualities.

At First, I would like to express my deep sense of gratitude and respect to my supervisors Prof. S. K. Sarangi and Mr. Trilok Singh for their excellent supervision, suggestions throughout the project. I will always remember their helping hands and moral support in my good and evil day during this period. The pleasant behavior of Prof. S. K. Sarangi and Mr. Trilok Singh has been unified perfectly with knowledge that creates an endless impression in my mind. I am very much inspired by the endurance and confidence of Prof. R. K. Sahoo, which will be fruitful throughout my life and career. Without him, I could not get confidence handle such cutting-edge project.

I take this opportunity to express my sincere gratitude to all my DSC members, Prof. K. P. Maity (Chairman), Prof. S. C. Mohanty of Mechanical Engineering Department and Prof. S. K. Sahu of Civil Engineering Department for thoughtful advice and useful discussions. I am thankful to Prof. D.R.K Parhi (HOD), Prof. S. S. Mohapatra, Prof. S. K. Sahu, Prof. S. K. Acharya, Prof. Saurav Datta, Prof. A. K Satpathy, Prof. Alok Satpathy, Prof. R.K. Behera, Prof. J. Srinivasa, Prof. Manoj K. Moharana, Prof. Suman Ghosh, Prof. Manoj Masanta, Prof. Amitesh Kumar and other professors of my department for constant encouragement and backing in pursuing the Ph.D. parallel with my profession.

I take this opportunity to express my deepest gratitude to Mr. Kamal Charan Das, Mr. Arabinda Khuntia, Mr. G. Syamaghan Reddy, Mr. Jyana Ranjan Nayak, Mr. Naren Bisoi, Mr. Sudhananda Pani , Mr. Somnath Das, Mr. Kunal Nayak and other staffs of the department for their support throughout my Ph.D. work. Beside them, I am also grateful towards Mr. C. S. Mohanty for his assistance in official matters.

I record my appreciation and thanks for the helping hand extended by Dr. Balaji Kumar Choudhury, Dr. Sachindra Kumar Rout, Mr. Pankaj Kumar, Mr. Ajay Kumar Gupta and Mr. Manoj Kumar, Mr. Debashish Panda and Mr. Sai Manoj being my co-research fellow.

Thanks go to my parents, brothers, sister, sister-in-law, brother-in-law, nieces and nephews for their loving support and encouragement for my Ph.D. study. I am most grateful to my beloved wife Mrs. Sujata Behera for her loving support and co-operation all time during my Ph.D. work. I am happy with both of my sons, Shreyas and Vivash for their patience and understanding during my Ph.D. program.

April 15, 2017
NIT Rourkela

Suraj Kumar Behera
Roll Number: 511ME437

Abstract

Turboexpander is considered as the heart of present-day cryogenic process plants such as helium, hydrogen and nitrogen liquefiers, low-temperature refrigerators and air separation units, . The operational objective of a turboexpander is to refrigerate a gas stream, by removing work from the gas, and expanding the gas nearly isentropically. The turbine based cryogenic process plants in recent years are low-pressure system and have the advantage of high thermodynamic efficiency and high reliability. The high efficiency is possible at high-speed of the turboexpander, and these turboexpanders in a typical cryogenic refrigerator or liquefier run at high-speed greater than 50,000 rpm without contaminating the process gas. Such operating condition imposes rigorous constraints on tribo-pair design. Oil-free gas bearings have advanced as the most acceptable solution for supporting small and high-speed cryogenic turboexpander rotors. An inherent issue with classic gas bearing is its lower dynamic properties such as stiffness and damping because of its low viscosity. Low stiffness and damping are prone to instability at high rotational speed. So gas foil bearings (GFBs) have received much attention for research, development, and experiment over past three decades for its ability to tailor the stiffness and damping with the use of compliant foils. Bump type compliant foil gas bearing is quite popular among researchers for various turbomachines for its high load carrying capacity, simplified numerical analysis, and easy fabrication methodology compared to other types. In the present work, a modest attempt is made to understand, standardize and document the numerical analysis, design methodology and fabrication methodology. It evaluates the rotor bearing performance to determine the feasibility of bump type gas foil bearings for axial and radial support of cryogenic turboexpanders.

The work presented in current dissertation classified into five parts. The first part includes the status of research and development in the field of gas bearings in turboexpanders and a broad literature review of gas foil bearings. The outcome of the literature review directs that extensive research is essential for designing and development of gas bearing for a more advanced cryogenic system which is technically and economically better than present gas bearings.

The second part deals with the design and numerical analysis of gas foil journal and thrust bearings and its feasibility to apply in a small and high-speed cryogenic

turboexpander. The numerical analysis helps to fix the dimensions of foils such as its thickness, bump length, and pitch. for a previously designed rotor and its load carrying capacity. The dynamic properties of the bearings are determined to be used in the rotordynamics analysis. Finally, a step by step detailed design procedure itemized for both the gas foil bearings.

Transverse vibration being a major issue for high speed rotating machinery such as a cryogenic turboexpander, a detailed vibration analysis completed in part three. The vibration analysis includes determination of critical speeds, mode shapes and unbalanced response for the desired configuration of the rotor-bearing system with determined stiffness and damping from previous part.

A small clearance between the gas bearings and the rotor is maintained in order of 10 to 40 μm ; This makes a cryogenic turboexpander with gas foil bearing a precision equipment. All precision equipment demands micron scale manufacturing tolerance, so fourth part of the dissertation explains the details design methodology for gas foil bearings, the rotor and other associated parts of turboexpander. A broad analysis is done on bump forming methodology for fabrication of bump foil of the desired dimension. A Finite Element Method (FEM) simulation of forming process carried to simplifies the die design process. Special attention is given to the material selection of bearing components, balancing of the rotor, tolerance analysis, fabrication, coating of solid lubricant and assembly of the turboexpander.

The last part includes performance study of the fabricated turboexpander with gas foil journal and thrust bearing. Several issues are encountered during this phase, and most of them are rectified either by modification of design process or rectification in fabrication methodology. A vibration study is done using accelerometers on the bearing housing close to the journal bearings. The vibration analysis reveals gas foil bearings can be an alternative rotor bearing system for a high-speed small sized cryogenic turboexpander. A satisfactory operation is carried out for the duration of 30 hrs with an achievable speed of 81,000 rpm with multiple starts and stops.

Keywords: Turboexpander; Gas bearings; Gas foil bearings; Bump foil; Bump forming method; Transfer matrix method; Critical speed, Unbalanced response.

Contents

Certificate of Examination	ii
Supervisors' Certificate	iii
Dedication	iv
Declaration of Originality	v
Acknowledgements	vi
Abstract	vii
Contents	ix
List of Figures	xi
List of Tables	xvi
Nomenclature	xvii
1 Introduction	1
1.1 Anatomy of cryogenic turboexpander	2
1.2 Bearing for cryogenic turboexpander	4
1.3 Gas foil bearings	5
1.4 Objectives and organization of the thesis	6
2 Literature Review	8
2.1 Gas bearings for high-speed rotor.....	8
2.2 Gas bearings for cryogenic turboexpanders.....	10
2.3 Gas foil bearings state of the art	14
2.5 Development of gas foil bearings	22
2.6 Gaps in literature.....	27
3 Bump Type Gas Foil Journal Bearing	28
3.1 The working principle.....	29
3.2 Bearing geometry.....	29
3.3 Performance analysis of gas foil journal bearings	30
3.4 Numerical procedure.....	36
3.5 Results and discussion	43
3.6 Detail design procedure for gas foil journal bearing	48
4 Bump Type Gas Foil Thrust Bearing	49
4.1 Thrust load calculation.....	50
4.2 Working principle and bearings geometry of GFTB	54
4.3 Performance analysis of gas foil thrust bearing.....	56
4.4 Axial passive magnetic bearings.....	67
4.5 Detail design procedure of gas foil thrust bearings	71

5 Rotordynamics of the Prototype Rotor.....	73
5.1 Transfer matrix method with gyroscopic effect.....	74
5.2 The lumped inertia model of the prototype rotor.....	81
5.3 Computation of critical speeds.....	83
5.4 Computation of unbalance response	87
6 Fabrication of Turboexpander with Gas Foil Bearings.....	91
6.1 The rotor.....	91
6.2 Fabrication of gas foil journal bearings	95
6.3 Fabrication of gas foil thrust bearings	110
6.4 Fabrication of other parts of turboexpander.....	120
6.5 Assembly of turboexpander components.....	126
7 Performance of Turboexpander with Gas Foil Bearings.....	132
7.1 Turboexpander test set-up.....	132
7.2 Speed and vibration measuring equipment	134
7.3 The experiments.....	136
8 Conclusions.....	143
8.1 Overview.....	143
8.2 Contributions.....	143
8.3 Future research scope.....	145
References.....	146
Appendix.....	152
Curriculum Vitae.....	183

List of Figures

1.1	Schematic layout of a typical nitrogen liquefaction process plant based on Claude cycle.....	1
1.2	1/4 th solid cut model of a typical cryogenic turboexpander.....	2
1.3	a. Front section view b.1/4 th solid cut model of a bearing unit	4
1.4	Schematic diagram of bump type gas foil bearings: (a) Journal (b) Thrust..	6
2.1	Types of gas bearings: (a) Aerostatic thrust bearings (b) Spiral groove thrust bearings (c) Herringbone groove journal bearings and (d) Tilting pad journal bearings.....	10
2.2	Fabricated gas bearing for a cryogenic turboexpander at NIT Rourkela: (a) Tilting pad journal bearings (b) Aerostatic thrust bearings and (c) Spiral grooved thrust bearings	13
2.3	Compliant bump-shaped foils: (a) Generation I (b) Generation II and (c) Generation III	15
3.1	Schematic diagram of a bump type journal foil bearings for the vertically oriented rotor.....	28
3.2	Geometrical parameters of gas foil journal bearing.....	30
3.3	Configuration of bump foil.....	30
3.4	Sign convention of the journal forces.....	33
3.5	Bump geometric parameters for bump stiffness calculation.....	35
3.6	Discretization of journal bearing surface.....	36
3.7	Flow chart for computation of journal bearing performance.....	39
3.8	Variation of load carrying capacity with grid size.....	40
3.9	Validation of load carrying capacity with open literature	40
3.10	Non-Dimensional pressure profile of gas foil bearings.....	42
3.11	Non-Dimensional gas film thickness of journal foil bearings.....	42
3.12	Non-Dimensional load carrying capacity of journal foil bearings.....	42
3.13	Effect of bump foil materials on the load carrying capacity	43
3.14	Effect of bump foil thickness on the load carrying capacity	44
3.15	Effect of bump half-length on the load carrying capacity	45
3.16	Effect of bump foil pitch on the load carrying capacity.....	45
3.17	Pressure profile with designed data.....	46

3.18	Film thickness with designed data.....	47
3.19	Load carrying capacity with designed data.....	48
3.20	Frictional torque with designed data.....	49
4.1	Schematic of bump type gas foil thrust bearings.....	49
4.2	Schematic diagram of thrust bearing and the shaft collar.....	50
4.3	Axial forces on the vertical rotor.....	51
4.4	Bump and top foil configuration of thrust bearing.....	55
4.5	Gas foil thrust bearings parameters.....	55
4.6	Discretization of single sector of thrust bearing surface.....	59
4.7	Flow chart for computation of thrust bearing performance.....	60
4.8	Schematic of a double thrust bearings.....	62
4.9	Variation of load carrying capacity with grid size.....	63
4.10	Non-dimensional load at various angular extent of a pad.....	64
4.11	Non-dimensional load for different film thickness ratio.....	64
4.12	Load for different film thickness ratio.....	65
4.13	Non-dimensional pressure profile over a single sector of the lower thrust bearing surface.....	65
4.14	Non-dimensional pressure profile over the lower bearing surface.....	66
4.15	Non-dimensional film thickness over a single sector of the l thrust bearing surface.....	66
4.16	Non-dimensional pressure profile over a single sector of the upper thrust bearing surface.....	66
4.17	Non-dimensional pressure profile over the upper thrust bearing surface	67
4.18	Non-dimensional film thickness over a single sector of the upper thrust bearing surface	67
4.19	Arrangements of ring magnets as axial passive magnetic bearings.....	68
4.20	Configuration and arrangements of ring magnets.....	69
4.21	Variation of repulsive forces against distance between ring magnets.....	71
5.1	Model of a rotor-bearing system with discrete segments.....	74
5.2	Free-body diagrams of the elements in the n th rotor station	75
5.3	Elastic field of n th element in x-z plane.....	78
5.4	Elastic field of n th element in x-y plane.....	78

5.5	Inertial model of the prototype rotor.....	81
5.6	Flow chart for critical speed and mode shape computation.....	84
5.7	Mode shape at 1 st natural frequency for the prototype rotor.....	85
5.8	Mode shape at 2 nd natural frequency for the prototype rotor.....	86
5.9	Mode shape at 3 rd natural frequency for the prototype rotor.....	86
5.10	Mode shape at 4 th natural frequency for the prototype rotor.....	86
5.11	Flow chart for determination of unbalance response.....	87
5.12	Unbalance response near journal bearing on turbine side.....	88
5.13	Unbalance response near journal bearing on compressor side.....	88
5.14	Unbalance response near expansion turbine.....	89
5.15	Unbalance response near brake compressor.....	89
5.16	Unbalance response near shaft collar.....	89
6.1	FEM analysis of rotor at designed speed: (a) Stress and (b) Deformation...	93
6.2	The prototype rotor: (a) with dimension (b) assembled rotor.....	93
6.3	Schematic showing the planes and bearing support for balancing the prototype rotor.	94
6.4	Rotor with removed unbalance mass.	95
6.5	Parts of gas foil journal bearings.....	96
6.6	Fabrication methodologies of gas foil journal bearings.....	96
6.7	Prototype journal bearings base with single axial hole: (a) Isometric view (b) Actual photograph.....	97
6.8	Prototype journal bearings base with two axial holes: (a) Isometric view (b) Actual photograph.....	97
6.9	Top foil: (a) After wire EDM cut (b) Rolled and coated with MoS ₂	99
6.10	Preform foil before forming of journal bumps.....	100
6.11	Parameters of journal bump foil.....	100
6.12	Designed generation I bump foil for journal bearings	101
6.13	Schematic of tooling for fabrication of bump journal foil with top flexible rubber sheet.....	102
6.14	Lower rigid die for fabrication of bump journal foil	102
6.15	Actual photograph die set: (a) Bottom rigid die (b) Rubber sheet (c) Top metal plate.....	103

6.16	Photograph of journal bump forming operation	104
6.17	Load displacement curve during journal bump formation.....	104
6.18	Defective fabricated bump foil	104
6.19	Tooling for fabrication of journal bump foil with rigid top and bottom dies	106
6.20	Load prediction curves for the top die during bump forming simulation over phosphor bronze.....	107
6.21	Simulated displacement for phosphor bronze journal bump foil.....	107
6.22	Simulated stress distribution for phosphor bronze journal bump foil.....	107
6.23	Simulated damage for phosphor bronze journal bump foil.....	107
6.24	Fabricated rigid dies for the generation I and II bump foil: (a) Top die (b) Bottom die.....	108
6.25	Fabricated journal bump foil with 2 nd die set.....	108
6.26	Assembly of bump and smooth foil on a single axial hole.....	109
6.27	Load vs Extension graph to determine bump stiffness.....	110
6.28	Fabrication methodologies of gas foil thrust bearings.....	111
6.29	Prototype thrust bearings base: (a) Isometric view (b) Fabricated thrust bearing base with pins and screws.....	112
6.30	Prototype thrust top foil: (a) Dimension and (b) Fabricated.....	112
6.31	Pre-form of thrust bump foil: (a) 2D geometry (b) Fabricated.....	113
6.32	Designed bump foil for thrust bearing.....	113
6.33	Tooling for fabrication of generation II bump journal foil: (a) Isometrics view (b) Actual figures bottom die and plate	115
6.34	Load-displacement curve during journal bump formation.....	115
6.35	Fabricated thrust bump foils: (a) Moderate deformation (b) Deformation with a crack (c) Complete deformation	115
6.36	Tooling for fabrication of thrust bump foil with rigid top and bottom dies..	116
6.37	Load prediction curves for phosphor bronze bump forming.....	117
6.38	Simulated displacement for phosphor bronze bump foil.....	117
6.39	Simulated stress distribution for phosphor bronze thrust bump foil.....	118
6.40	Simulated damage for phosphor bronze thrust bump foil.....	118
6.41	Fabricated die for thrust bump forming.....	118
6.42	Fabricated thrust bump foils using 2 nd die set for upper and lower thrust bearing.....	119

6.43	Assembled bump foil with the bearing base.....	119
6.44	Assembled lower and upper gas foil thrust bearing with layer of MoS ₂ coating on top foil.....	120
6.45	Cut view model of the bearing housing.....	121
6.46	Fabricated bearing housing.....	122
6.47	Labyrinth seal: (a) The location of the seal (a) Actual photograph.....	122
6.48	Position of spacers in the turboexpander.....	123
6.49	Fabricated spacers: (a) Spacer I (a) Spacer II and (c) Spacer .I.....	123
6.50	Locknuts: (a) Upper (b) Lower.....	124
6.51	Configuration of magnetic ring bearings a. E1 and E2.....	125
6.52	Parts of auxiliary passive magnetic bearing.....	125
6.53	Dimensional linkage between bearing housing and other parts.....	128
6.54	Assembled turboexpander bearing housing.....	130
7.1	Schematic of turboexpander test set up.....	132
7.2	Assembled bearing housing with cold end and warm end housing.....	133
7.3	The test bed with the turboexpander assembly and instrumentation.....	134
7.4	Mounting of the accelerometer on the bearing base.....	135
7.5	Piezoelectric accelerometers: (a) B&K 4507 (b) B&K 4508	136
7.6	The rotor at stable operational speed without warm end unit.....	136
7.7	Thrust bearings without coating after the test a. Upper b. Lower.....	137
7.8	MoS ₂ coated thrust beating after test a. upper b. lower	139
7.9	Wear on the shaft after the test	139
7.10	Spectrum in time domain at a speed close to 1st critical speed (25,250 rpm) near lower journal bearing.....	140
7.11	Spectrum in time domain at a speed close to 2nd critical speed (29,850 rpm) near lower journal bearing.....	140
7.12	Spectrum in time domain at a speed 80,125 rpm speed near lower journal bearing.....	140
7.13	FFT Spectrum at a speed 80000 rpm speed near upper journal bearing....	141
7.14	FFT Spectrum at a speed 80000 rpm speed near lower journal bearing....	141

List of Tables

2.1	Summary of cryogenic turboexpander and their bearings from open literature.....	11
3.1	Compliant foil journal bearing data to study the feasibility of GFB.	41
3.2	Compliant foil journal bearing data with modified bump structure.....	46
4.1	Wheel data for thrust load calculation at 140,000 rpm of rotor.....	51
4.2	Thrust load calculation at 140,000 rpm of the rotor	53
4.3	Common thrust bearing data for numerical simulation.....	63
4.4	Film thickness data for upper and lower thrust bearings	65
4.5	Design data of the ring magnets.....	70
5.1	Formula for inertial properties of cylindrical element.....	82
5.2	The rotor data.....	83
5.3	Station data of the prototype rotor.....	83
5.4	Computed critical speed of the rotor.....	85
5.5	Location of shaft for calculation of unbalance response.....	88
5.6	Sensitivity analysis for critical speed of the rotor.....	90
5.6	Sensitivity analysis for unbalance response.....	90
6.1	Balancing report of the prototype rotor.....	95
6.2	Chemical composition and mechanical properties of phosphor bronze.....	98
6.3	Spring back ratio of various foil material.....	99
6.4	Dimensions of bumps for journal bearings.....	100
6.5	Effect of forming load on journal bump formation.....	104
6.6	Input parameters for forming simulation of journal bump.....	106
6.7	Designed bearings data for thrust bearing from Chapter 4.....	110
6.8	Input parameters for forming simulation of thrust bump.....	117
6.9	Instruments used in metrology of fabricated components.....	127
7.1	Specification of the accelerometer.....	135
7.2	Specification of the oscilloscope.....	135

Nomenclature

b	= Extent of the ramp as a function of β
C	= Radial clearance
D_{IC}	= Inlet mean diameter
D_{OC}	= Outlet diameter
D_{SC}	= Shaft Diameter
D_{IT}	= Inlet diameter
D_{OT}	= Outlet diameter
D_{ST}	= Shaft Diameter
e	= Eccentricity
E	= Young's modulus
E_n	= Modulus of elasticity of n^{th} element
R	= Shaft radius
F_1	= Pressure force acting on the tip surface
F_2	= Pressure force at the shroud surface
F_3	= Impulsive force
F_4	= Pressure force at the back faces
F_{CW}	= Resulting axial force acting on the compressor wheel
F_{TW}	= Resulting axial force acting on the turbine wheel
F_{Total}	= Resultant axial forces acting on the rotor
F_x	= Journal Force in x-direction
F_y	= Journal Force in y-direction
\bar{F}_x	= Normalised force in x-direction, $\frac{F_x}{p_a R^2}$
\bar{F}_y	= Normalised force in y-direction, $\frac{F_y}{p_a R^2}$
$[F]_n$	= Field matrix of the n^{th} station
h	= Film thickness
h_b	= Bump height
h_1	= Inlet film thickness
h_2	= Minimum film thickness
\bar{h}	= Normalized film thickness
	For journal bearing: h/C
	For thrust bearing: h/h_2
I_n	= Area moment of inertia of the n^{th} station

- L = Axial length of the bearing
 l_b = Half bump length
 l_n = Shaft element length
 \dot{m}_C = Mass flow rate of compressor
 \dot{m}_T = Mass flow rate of turbine
 $M_{y_n}^L$ = Bending moments on the left of the n^{th} disc
 $M_{y_n}^R$ = Bending moments on the right of n^{th} the disc

 P = Pressure
 \bar{P} = Normalised pressure, P/P_a
 P_a = Ambient pressure
 P_{IC} = Inlet pressure of compressor
 P_{OC} = Outlet pressure of compressor
 P_{IT} = Inlet pressure of turbine
 P_{OT} = Outlet pressure of turbine
 $P_{(r, \theta)}$ = Pressure at coordinate (r, θ)
 $\{Q\}_n$ = $\{w, \theta, M, V\}^T$, The state vectors at the n^{th} node

 R_1 = Inner radius of sector
 R_2 = Outer radius of sector
 R_b = Bump radius
 s = Bump pitch
 t_b = Bump thickness
 \bar{T} = Non-dimensional Torque

For journal bearing: $\frac{T}{P_a C R^2}$
For thrust bearing: $\frac{T}{p_a h_2 R_2^2}$

 V_n^L = Shear forces at the left faces of the n^{th} disc
 V_n^R = Shear forces at the right faces of the n^{th} disc
 W_t = Weight of the rotor
 \bar{W} = Non-dimensional Load

For journal bearing: $\frac{W}{p_a R^2}$
For Thrust bearing: $\frac{W}{P_a R_2^2}$

 w = Deflection

Greek Symbols

- ϵ = Eccentricity ratio (e/C)
 ν = Poisson ratio
 η = Viscosity of the gas
 ω = Speed of the rotor(rad/sec)
 ϕ = Attitude angle
 ρ = Density of the gas
 Λ = Bearing or Compressibility number,
 For journal bearing: $\frac{6\omega\eta_0}{p_a} \left(\frac{R}{C}\right)^2$
 For thrust bearing: $\frac{6\omega\mu_0}{p_a} \left(\frac{R_2}{h_2}\right)^2$
 α = Compliance number,
 For Journal bearing: $\frac{2p_a s}{CE} \left(\frac{l_b}{t_b}\right)^3 (1-\nu^2)$
 For thrust bearing: $\frac{2p_a s}{h_2 E} \left(\frac{l_b}{t_b}\right)^3 (1-\nu^2)$
 ρ_{IC} = Density of the gas at inlet
 ρ_{II} = Density of gas at the inlet
 β = Angular extent of a bearing pad

Abbreviation

- CW: Compressor Wheel
 CFD: Computational Fluid Dynamics
 EDM: Electro Discharge Machining
 FDM: Finite Difference Method
 FEM: Finite Element Method
 GFB: Gas Foil Bearing
 GFJB: Gas Foil Journal Bearing
 GFTB: Gas Foil Thrust bearing
 RPM: Rotation Per Minute
 TW: Turbine Wheel
 TMM: Transfer Matrix Method

Chapter 1

Introduction

A turboexpander is also referred as rotatory expansion device used in gas processing, energy recovery, geothermal power generation, and cryogenic liquefaction. The operational objective of a turboexpander is to refrigerate a gas stream, by expanding the process gas in an expansion turbine. From expansion turbine, the work is extracted through the rotor, which leads to a significant temperature drop from the process gas. Ideally, there is an isentropic expansion. Cryogenic turboexpanders are used in applications such as air separation, natural gas processing, petrochemical processing and liquefaction of gasses such as nitrogen, oxygen and helium. Liquefaction of gasses is necessary for large-scale storage and transportation. The low temperature of the liquefied gas is also found useful in the steel and semiconductor industries, cryogenic treatment of cutting tools, preservation of tissues and superconducting magnets.

Expansion of process gas can be done using the high, medium or low-pressure systems. The turboexpander based cryogenic process plants in recent years are low-pressure system and have the advantage of high thermodynamic efficiency and high reliability. A schematic layout of a typical turboexpander based nitrogen liquefaction Claude cycle is shown in Fig. 1.1[1].

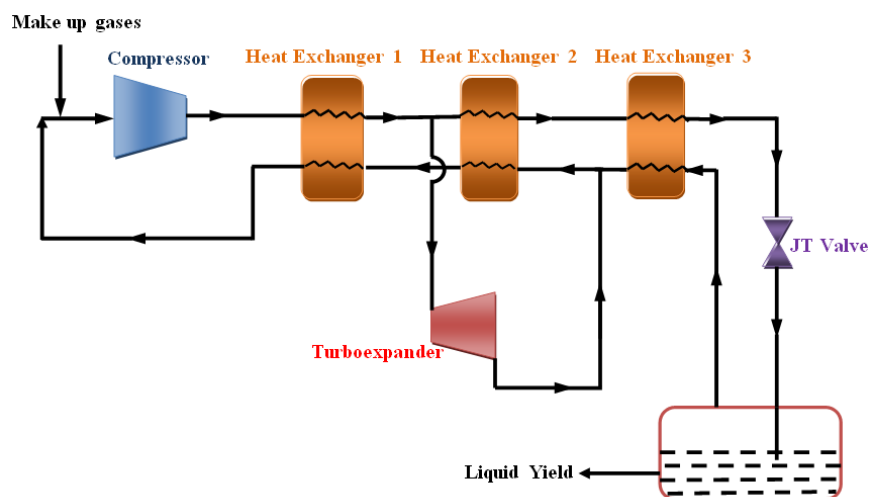


Figure 1.1: Schematic of a typical nitrogen liquefaction process plant based on Claude cycle.

For high expansion ratio, small flow-rate and high efficiency of cryogenic gas processing plant, the turboexpander can be of large diameter with low-speed or small diameter with high-speed. At cryogenic temperature, volume decreases so also the flowrate which needs small diameter. Small diameter and high-speed turboexpander is

preferable due to ease of design and fabrication of turbine, compressor, nozzle and diffuser [1]. High-speed brings constraints on the selection of axial and radial bearings. To meet high-speed requirements, gas bearings are found to be suitable for such application, where process gas is used as lubricants for the bearings. The gasses unlike liquid lubricants have an inherently low viscosity, which lead to lower stiffness and damping. Bearings with low stiffness and damping are prone to instability at high rotational speed. The gas foil bearings with compliant or spring-like structure have the ability to tailor stiffness and damping and they have been successfully used in turbomachines such as air cycle machine and turbo-compressor. In the current project, a modest attempt has been made to analyze, design, and document the axial and radial gas foil bearings and other associated parts of a cryogenic turboexpander. The work is further extended to test the developed turboexpander to study its rotor-bearing performance. The project is a part of the continuous cryogenic turboexpander development program at NIT Rourkela.

1.1 Anatomy of cryogenic turboexpander

A cryogenic turboexpander consists of three major units, and they are cold end unit, bearing unit and warm end unit (Fig.1.2).

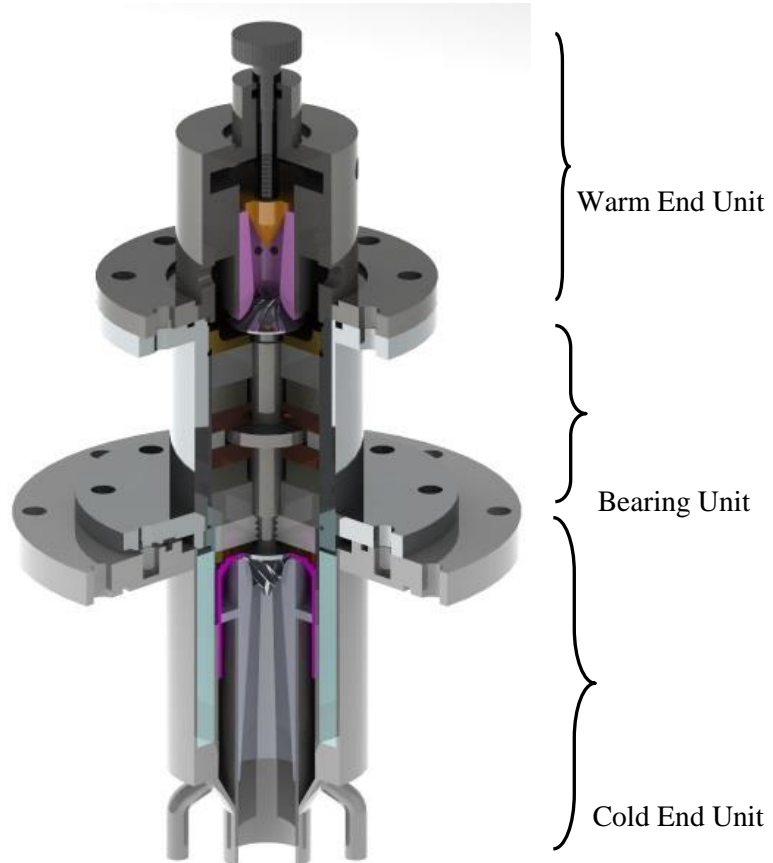
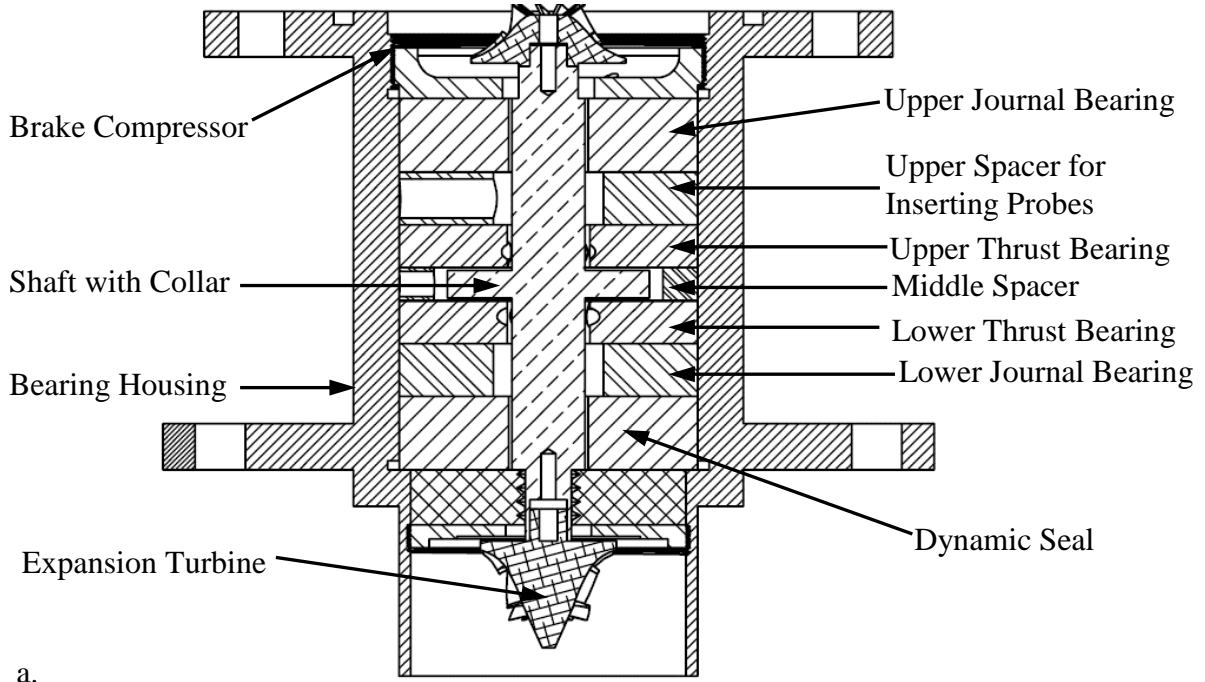


Figure 1.2: 1/4th solid cut model of a typical cryogenic turboexpander.

The cold end unit consists of nozzle, diffuser, and an arrangement for inlet and outlet of the process gas. The static pressure energy of gas stream is converted to kinetic energy by a nozzle. When this stream of the process gas with high kinetic energy hits the expansion turbine blade, one part is converted to rotational shaft energy and other part is expanded to refrigerate the gas stream and passes through the diffuser. The rotational energy of the expansion turbine can be used for compression of gasses or can be connected to an alternator for generation of electrical energy to take out work from the system. In small cryogenic turboexpander, the compressor is used as a brake to control the speed of the rotor. The rotor comprises of expansion turbine is at one end and a brake compressor is at another end of the shaft. The rotor is supported by a pair of journal (radial) bearings to support the radial load and a pair of thrust (axial) bearings to supports the axial load. The unit, which assembles the rotor and the bearings together, is termed as bearing unit (Figs. 1(a) and 1(b)). Current work concentrates on modification of the bearing unit with gas foil bearings, an alternate to previously developed tilting pad and aerostatic bearings at NIT Rourkela. The warm end unit of the turboexpander includes the nozzle and diffuser of the brake compressor. These turboexpanders in small and medium sized liquefaction plant are normally vertically oriented for easy installation and maintenance.



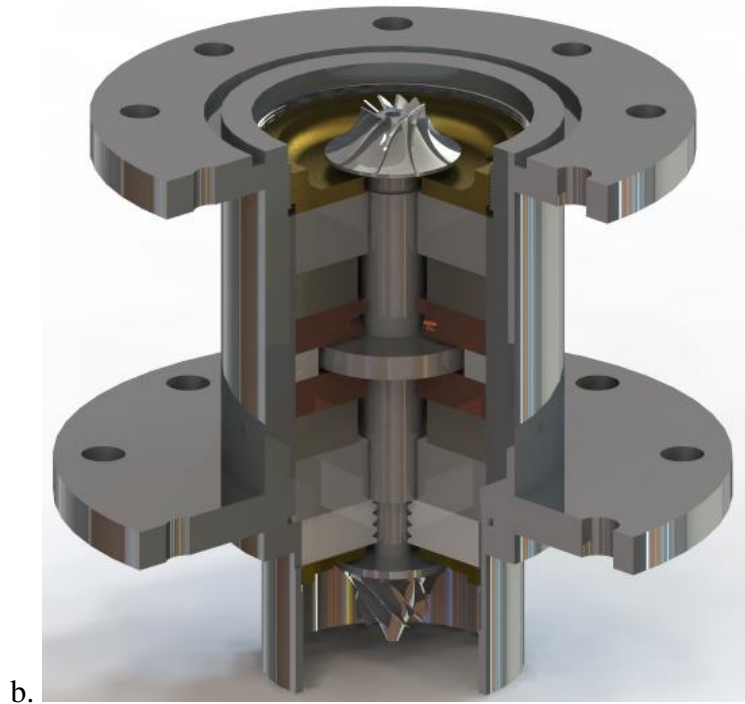


Figure 1.3: a. Front section view b. 1/4th solid cut model of the bearing unit.

A turboexpander designer concentrates on points mentioned below for the design and fabrication process of the turboexpander [2].

- i. Should have high reliability and efficiency.
- ii. Should be compact in size.
- iii. Should be environmentally safe.
- iv. Should have low maintenance and life cycle cost.

To satisfy above needs, three major issues faced by designers and they are:

- i. Selection and design of appropriate bearings.
- ii. Selection of materials for turbine, rotor, and compressor.
- iii. Precision manufacturing of major parts of turboexpander.

Current project concentrate on design and development of appropriate bearings for small high-speed cryogenic turboexpander.

1.2 Bearing for cryogenic turboexpander

Rolling element and oil lubricate bearings are reliable, commercially available, and inexpensive. Rolling element bearings seize to work efficiently at the high-speed of the rotor and oil lubricated bearings are prone to contaminate the process gas. So gas bearing is one of the choices for modern cryogenic turboexpander. Current advancements in

different turbomachines such as turbocharger and small size gas turbine have proved that gas bearings make the turbomachines more efficient and compact in addition to the oil-free system. In a gas bearing process gas is used as lubricants and unlike oil lubricants, the gas lubricants can operate in a higher range of temperature with smaller frictional losses and longer life [2]. These gas bearings can be aerodynamic, aerostatic or hybrid type. For aerodynamic or self-acting gas bearing, due to lower viscosity of gas lubricant, the aerodynamic pressure can only be developed if very small clearance is maintained. The small clearance leads to precision fabrication, which increases cost of the machine. Various aerodynamic gas bearings used in turboexpander are tilting pad, spiral grooved, herringbone grooved and cylindrical grooved. The self-acting bearings also suffer from the problem of half speed whirl instability. Aerostatic or externally pressurized gas bearing need an additional source of pressurized gas, and they are unstable at high speed. Hybrid gas bearings are a combination of aerodynamic and aerostatic principle. Thus design and development of appropriate gas bearings for the turboexpanders have always been a challenging task for engineers.

The bearings which can replace gas bearings are magnetic bearings; these bearings are used now-a-days. It is either active or passive magnetic bearings. Passive magnets or permanent magnet are found to be suitable as auxiliary bearings, which can support at the start and stop of the bearings else during higher rotation of the rotor, any increase or decrease in load will result in catastrophic failure of these bearings. The magnetic bearings which suit the need for small cryogenic turboexpander are active magnetic bearings and they work with position controlled servo mechanism. These bearings use electromagnet around the rotor and the magnetic field is varied by controlling the flow of current in coils around the electromagnet. The biggest issues with magnetic bearings are sensing rotor position correctly and precise control system and this makes the active magnetic bearings expensive [2].

1.3 Gas foil bearings

Gas foil bearings are aerodynamic bearings with the compliant structure. They are either constructed with several layers of sheet metal foils or with bump foils to behave as an elastic foundation for the gas bearings. Several researchers use various elastic foundations such as springs, structural shells, wire mesh and polymers, but the bump type gas foil

bearings are preferred for its simplified numerical analysis and easy fabrication methodology compared to other types. Figs 1.4(a) and 1.4(b) shows the schematic diagram of bump type gas foil journal and thrust bearings respectively. They are comprises of a smooth top foil, a bump foil beneath the top foil, a bearing base and an arrangement to attach both foils to the bearing base.

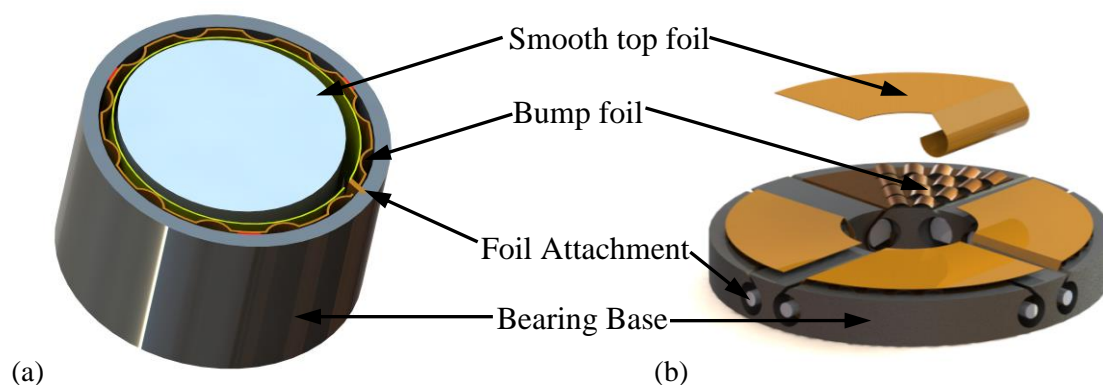


Figure 1.4: Schematic diagram of bump type gas foil bearings: (a) Journal (b) Thrust.

Similar to the liquid lubricated hydrodynamic bearings, the gas foil bearings works on the principle of hydrodynamic pressure generation. When two surface forms a converging wedge and one surface moves relative to the other surface, pressure is generated to carry the load and avoid contact between the two surfaces. The bottom bump foil in foil bearings creates an elastic structure and behaves as spring bed, which is responsible for increasing the bearing stiffness. Under the action of pressure, the top foil deforms and forces it away from shaft but towards the bump foil. So during rotation of rotor above liftoff speed, the journal does not touch the bearing. At the action of deformation there is friction between top foil – bump foil and bump foil- bearing base. This friction helps to generate Coulomb damping in the bearing. The variation of bump dimensions can also tailor the stiffness and damping of gas foil bearing.

1.4 Objectives and organization of the thesis

This dissertation focuses mainly on tribology and rotordynamics of bump type gas foil bearing. To achieve the objectives, the dissertation focuses on following points:

- Simulation and design of bump type gas foil journal and thrust bearings based on aerodynamic analysis and vibration analysis.
- Fabrication methodology for bump formation with dies under desired accuracy by using two different types of forming tools.
- Assembly of turboexpander components with designed tolerances.

- Testing of turboexpander in a test rig to study its rotor-bearing performance.

The central objective of above program is to suggest a structured design and fabrication methodology for bump type gas foil journal and thrust bearings through the theoretical and experimental studies.

The dissertation has been divided into eight chapters and one appendix. The *Chapter 1* presents a brief introduction to the turboexpander in cryogenic process plants. An extensive survey of gas foil bearings is documented in *Chapter 2*, which covers development history of gas foil bearings for various applications and available design methodology. This chapter also presents a brief outline of various technological issues related to design, fabrication, and testing of the gas foil bearing in the past. *Chapter 3* explains about working principle of gas foil journal bearing (GFJB) for a vertically oriented rotor. The aerodynamic analysis predicts the bump dimension for the desired radial load of the upper and lower journal bearings. This aerodynamic analysis is further explained for gas foil thrust bearings (GFTB) in *Chapter 4*. This chapter also focuses on the methodology to determine the axial load on rotor due to the pressure differential between turbine and compressor sides. An axial passive magnetic bearing design is elaborated in this chapter to resolve issues of start and stop in all aerodynamic bearings. The vibration analysis to determine the critical speed, unbalance response with flow chart is included in *Chapter 5*. All the above computational steps in preceding chapters lead to the production drawing. The production drawings of all parts of the bearing units of turboexpander and dies for forming bumps with geometrical tolerance are recorded in *Appendix A*. The fabrication and assembly methodology of the rotor, gas foil bearings and associated component of turboexpander such as spacers, dynamic seals, lock nuts and bearing housing is documented in *Chapter 6*. This chapter also highlights two different methods of bump forming methodology, one with a flexible top die and other with the rigid top die. *Chapter 7* explains the test rig and performance of the rotor-bearing system in operation of the prototype turboexpander. The vibration characteristics are measured and compared with the result obtained from previously developed aerostatic thrust and tilting pad journal bearings at NIT Rourkela as a part of continuous development program of turboexpanders. Finally, the dissertation is concluded in *Chapter 8* with a summary of the work done in this dissertation and a recommendation for the steps to be taken towards the development of cryogenic turboexpander with gas foil bearings and suggested future works for re-design re-fabrication and testing in the continuous program of turboexpander development.

Chapter 2

Literature Review

The increasing use of low-temperature refrigeration and liquefaction of gasses in the places such as industries, research institutes and medicals has created a significant demand for smaller, efficient and more durable turboexpanders. These high efficient turboexpanders rotate at very high speed, and high speed brings restraints on the selection of appropriate bearings. In recent years the interest for the use of gas bearings in the field of high-speed oil-free micro turbines like small turboexpander has significantly increased. The reason behind using gas bearings is the need of high speed by the advances in technology with new design methods. It leads to advanced fabrication methodology to fabricate bearings with tight clearance for high load carrying capacity and dynamic stabilization. The gas bearing application is also gaining its importance, where there is need of contamination free environment like manufacturing of medicine, processing of foods and liquefaction of gasses. In gas bearings, the process gas is used as a lubricating medium to prevent contamination instead of conventional lubricating oil. This chapter explains about the development history of gas bearings for cryogenic turboexpander. For applications characterized by very high speed or demanding operating conditions, it is necessary to use bearings not only with excellent dynamic properties but also with some possibilities of adaptation to changed dynamic conditions. Two types of bearings fulfill these requirements, namely Gas Foil Bearing (GFB) and tilting pad bearing. This chapter intends to explore the history of GFBs concerning small and high-speed turbomachines. A chronology of the development of GFB systems, its design and fabrication methodology is explained in detail.

2.1 Gas bearings for high-speed rotor

The type of bearings used in high-speed rotor defines its economic and technical parameters such as reliability, service life, mass and dimensions of the machine, labour and operating convenience[3]. In the past rolling element and oil bearings have been used for many high-speed applications but many concerns arise because of oil bearing, and they are as follows:

- i. Mass and dimensions increase to a greater extent.
- ii. Massive human labour requirement during operation of the machine.
- iii. Contamination of the process gas due to oil leakage into to gas cavities.

Rolling element and oil lubricated bearings are reliable, commercially available, and inexpensive; but as relative surface speed increases their Mean Time Between Maintenance (MTBM) decreases, and this is where gas bearings start to become more attractive. Over the last few decades, some research institutes and enterprises have actively designed, developed and tested gas lubricated bearings for various applications to address the above issues. Within these years of experience sufficient knowledge has been acquired for developing gas bearings for applications such as the turbo-liquefaction unit, aviation gas turbine units and precision manufacturing units. The ball bearings of aviation gas units are replaced with air-lubricated bearings to increase fire safety, reduction of engine weight, increased longevity and reduced operation and life cycle costs. Gas lubrication in turbo- liquefaction units additionally prevents the contamination of the process gasses by using same process gas as lubricating fluid.

Theory of gas lubrication was majorly developed in the late 19 centuries in the works the of Petrov, Reynolds, Sommerfeld and Chaplygin[4]. Gas lubricated bearings fall into two main classes: aerostatic and aerodynamic bearings. An additional process gas compressor is required to produce the pressure in an aerostatic bearing between the runner and the bearing, whereas an aerodynamic bearing generates the pressure by the action of simultaneous shearing and squeezing of the gas between the bearing surfaces in relative motion. Both these types of bearings can support either radial or axial loads or combination of two functions in a single member. A bearing can operate either entirely as aerostatic or aerodynamic, or start in one mode and change over to the other as speed changes. A bearing, which operate with a combination of both aerostatic and aerodynamic pressure generation is known as a hybrid bearing. Various gas bearings are shown in Figs. 2.1(a)-(d) such as aerostatic thrust bearings, grooved bearings includes spiral and herringbone and tilting pad journal bearings.

An inherent disadvantage of aerostatic bearings is that a pressure source and an exhaust sink are necessary, which makes the system bulky. The other disadvantages of aerostatic gas bearings are as follows[2]:

- i. A large percentage of working fluid is used, which considerably reduce the capacity of the machine.
- ii. The need of small feed holes makes the bearings highly sensitivity to the thermal deformation of the runner.

On the advantage side, aerostatic bearings can be made to relax manufacturing tolerances compared to aerodynamic bearings and former can provide support at zero speed i.e at the start and stop of the turbomachines. An externally pressurized bearing can work in a dust-laden atmosphere because the exhaust gas prevents the entry of solid particles from the environment. On the other hand, because of the low viscosity of the gaseous lubricant, an aerodynamic bearing can support only a small load per unit area depending upon the speed of the rotor. These bearings require careful manufacture and alignment and are only suitable for bearings whose surfaces are always in relative motion when loaded. However, auxiliary equipment for pressure generation is not needed, and there is no need of disposing of the exhaust gas.

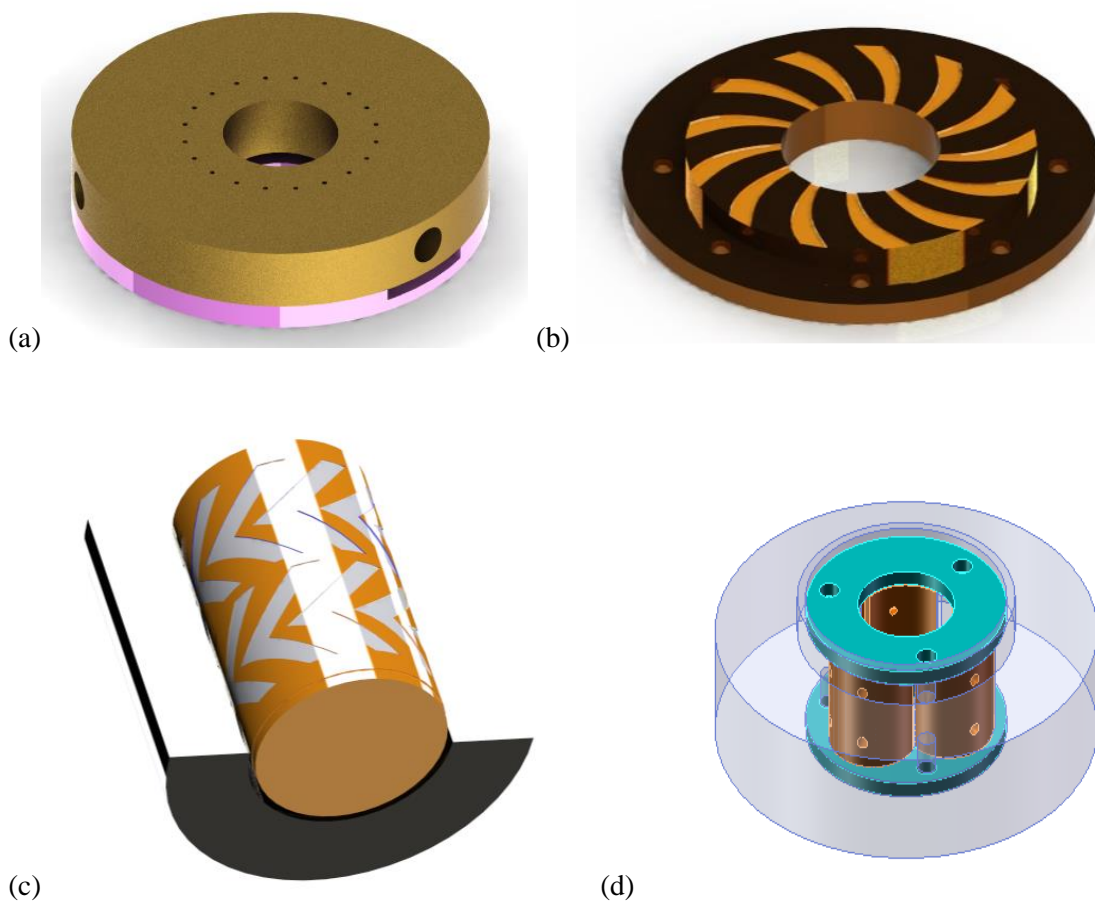


Figure 2.1: Types of gas bearings: (a) Aerostatic thrust bearings (b) Spiral groove thrust bearings (c) Herringbone groove journal bearings and (d) Tilting pad journal bearings.

2.2 Gas bearings for cryogenic turboexpanders

The turboexpander in cryogenic liquefier or refrigerator is considered to be the heart of modern plants. Various gasses liquefied in the cryogenic liquefier are nitrogen, helium, oxygen, hydrogen and methane. In 1950s, these turboexpanders are incorporated with

liquid lubricated bearings. The major issue with them is the possible contamination of the process gas due to leakage of oil from an oil-lubricated bearing unit, which subsequently solidifies and hinder smooth operation of the plant. An oil-free rotor bearing system is found to be suitable for a cryogenic turboexpander. Several decades of research on gas bearings for the cryogenic turboexpander has resulted in development of various aerostatic and aerodynamic gas bearings. In aerostatic bearings, a high percent of purified and compressed gas is used in the bearings, which increases the cost of the process plant with additional mountings. These are can be used for gas such as nitrogen and oxygen, where purification and re-compression is not very costly. When cost of the purified and compressed gasses are high for the gasses such as helium, the tribologists prefer to use suitable aerodynamic gas bearings to avoid additional gas inventory in aerostatic bearings. Various gas bearings for cryogenic turboexpander are tabulated in Table 2.1 based on the rotor dimension, speed and process gas [2, 5].

Table 2.1: Summary of cryogenic turboexpander and their bearings from open literature [2, 5].

Laboratory (Year of development)	Bearings	Shaft dia (mm)	RPM	Process gas
Univ. of Reading (1950)	Sixsmith type Externally pressurised	8	–	Helium
L'Air Liquide (1962)	Externally pressurised and Damping cavity stabilised	–	90,000	Helium
BOC (Rutherford Lab)(1964)	Sixsmith type Externally pressurised	–	456,000	First commercial helium turboexpander
NBS(1966)	Sixsmith type Externally pressurised	16	240,000	Helium
General Electric(1967)	Spiral grooved and Tilting pad	16	161,000	Helium
General Electric(1969)	Spiral grooved Tilting pad	6.2	245,000	Helium
Union Carbide, Linde Division (1969)	Elastically suspended damped bearings	42	48,000	Air
Atlas Copco, Rotoflow (1970)	Flexible pad	75	100,000	Hydrogen
Sulzer Bros. (1970)	Spiral grooved, auxiliary magnetic, Tilting pad	–	–	Helium

Sulzer Bros. (1974)	Spiral grooved and Tilting pad	22	222,000	Helium
Atlas Copco, Rotoflow(1980)	Flexible pad	40	60,000	Helium
Creare Inc. (1982)	Orifice compensated and Pneumatic	–	510,000	Helium
BOC(1984)	Magnetic bearing and ball bearings	–	–	Air / Nitrogen
Hitachi, Japan,(1986)	Tilting pad	6 and 4	816,000	Helium
Creare Inc. & NASA Goddard (1988)	Spiral grooved and Tilting pad	3.18	570,000	Neon
Academia Sinica(1990)	Spiral grooved and Herringbone	7	490,000	Helium
Academia Sinica,(1990)	Grooved, Oblique inlet slot	18	180,000	Air
Creare Inc. (1990)	Diaphragm type and Sixsmith type	4.8	384,000	Helium
JAERI / Kobe Steel,(1992)	Spiral grooved and Tilting pad	–	67,260	Helium
Mayeka Mfg. (1992)	Externally pressurised and tilting pad	14	230,000	Helium
JAERI(1994)	Foil, Auxiliary magnetic	12	136,000, 110,000	Helium
Geliymash, Russia(1994)	Foil	16	30,000 , 200,000	Helium
ACD Inc. (1995)	Foil bearing	–	–	Air / Nitrogen
CCI Cryogenics (1996)	Spiral grooved and Aerostatic	–	125000	Helium
Cryogenmash, Russia.(1996)	Tilting pad	–	–	Helium
Heliummash, Russia,(1996)	Hydrostatic and Aerostatic	–	–	Helium
Atlas Copco- Rotoflow(2000)	Magnetic (Auxiliary antifriction thrust bearing)	–	–	Air / Nitrogen
NIT Rourkela, India(2013)	Tilting pad journal, Aerostatic thrust bearing	16	140,000	Nitrogen
BARC, India(2014)	Spiral grooved thrust, Tilting pad journal and Auxiliary passive magnet bearings	16	270,000	Helium

Xi'an Jiaotong University(2015)	Foil journal and Aerostatic thrust bearings	25	93,300	Air
---------------------------------	---	----	--------	-----

Table 2.1 indicates that there is an evolution of gas bearings development for cryogenic turboexpander since 1950. The types of gas bearing developed are as follows:

- i. Aerostatic gas bearings to increase load carrying capacity of the bearings.
- ii. Sixsmith type aerostatic bearings to arrest dynamic instabilities at high speed of the rotor.
- iii. Grooved bearings such as spiral and herringbone are aerodynamic bearings.
- iv. Tilting pad gas bearings to improve load carrying capacity of aerodynamic bearings.
- v. Gas foil bearings to increase dynamic characteristics such as stiffness and damping coefficients of the bearings

Low stiffness of classical aerodynamic gas bearing has motivated researchers to develop gas foil bearings. Gas foil bearings are aerodynamic bearings with the additional compliant structure to improve the bearings stiffness. They are categorized based on the type of compliant structure such as tape type, leaf type, bump type, convex dot type and metal mesh type. Geliymash, Russia developed a leaf type gas foil bearings in 1994 for the turboexpander used in helium plant. Japan atomic energy research institute developed gas foil bearings for their centrifugal cryogenic pump in 1994, where the compliant structure contains spring foils. Industries such as ACD cryogenic equipment and R&D Dynamics have developed foil bearings for the cryogenic turboexpander. The fabrication methodology is mostly protected, so a modest attempt is made to design and develop a bump type gas foil bearings for a cryogenic turboexpander of nitrogen plant as a part of continuous development program at NIT Rourkela[1]. The gas bearings that are already developed at NIT Rourkela as part of turboexpander development program are shown in Figs. 2.2(a), (b) and (c).

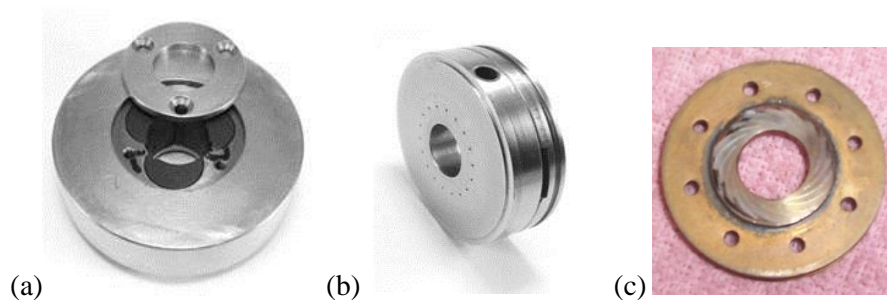


Figure 2.2: Fabricated gas bearing for a cryogenic turboexpander at NIT Rourkela: (a) Tilting pad journal bearings[1] (b) Aerostatic thrust bearings[1] and (c) Spiral grooved thrust bearings[6].

2.3 Gas foil bearings state of the art

The low viscosity of gas in gas bearings results in low load carrying capacity, low bearing stiffness and low damping coefficients compared with its counterpart liquid lubricated bearings. To address above issues researchers have developed various compliant gas bearings, where an additional compliant structure or spring bed is attached beneath the bearing surface to improve the stiffness and damping of the bearings. Several researchers use compliant structure or elastic foundations such as springs, structural shells, wire mesh, polymers, layers of foils. These compliant gas bearings have various other advantages such as higher reliability, lower operating cost, soft failure and higher durability at severe environmental conditions[7]. The working principles of gas foil journal and thrust bearings are explained in Chapter 3 and 4 respectively.

The first documented aerodynamic gas foil bearings are developed for tape industries in 1953[8]. In a tape recorder, the magnetic tape is passed over the recording head at very high speed, and gradually it loses contact with the recording surface and results in the poor quality of the recording. Baumeister of IBM research laboratory in the year 1958 patented a device to reduce tape float. At the same time, Gross of IBM research laboratory developed a mathematical model for the tape float. NASA was impressed with work of Gross and encouraged him to develop foil bearings for high-speed rotor operating at high temperature for the Brayton cycle in Turbo-Alternator Compressor (TAC). This program was to replace the pivoted-shoe gas bearings with gas foil bearing in TAC. This replacement solved the instability issue of rotor because of better damping of gas foil bearings compared to pivoted-shoe gas bearings. This GFB were tension-type (tape type) gas foil bearings. Henceforth all the Brayton cycle units of NASA works with gas foil bearings.

The next invention of foil bearings was with the air cycle machine (ACM) by Garrett AiResearch in 1969[7]. The ACM is a machine with high-speed rotor used in Environmental Control System (ECS) of aircraft to pressurize the aircraft cabins. The multi-pad gas foil bearing developed by Garrett AiResearch had replaced the ball bearing. The contamination free ACM with gas foil bearings one of the biggest achievement for Garrett AiResearch and this invention accelerated their ECS business. Hamilton Standard, a competitor of AiResearch in ECS business, worked with Mechanical Technologies Incorporated (MTI) and developed a bump type gas foil bearing for ACM in 1970[7].

The development of foil bearings did not stop with ACM and Brayton cycle unit but expanded its application for various high-speed rotor used in turbo-compressor, turbocharger, turboexpander and textile spindle. The growth in the development of gas foil bearings was committed to improving both load carrying capacity and dynamic properties such as stiffness and damping. Researchers around the world selected various types of compliant material beneath the top smooth foil. After tape and leaf type foils, tribologists established bump type gas foils which are easy to fabricate, assemble and less complicated to analyze its static and dynamic characteristics. Bump type gas foil bearings further advanced with Generation I, Generation II and Generation III type of bump foils (Fig. 2.3).

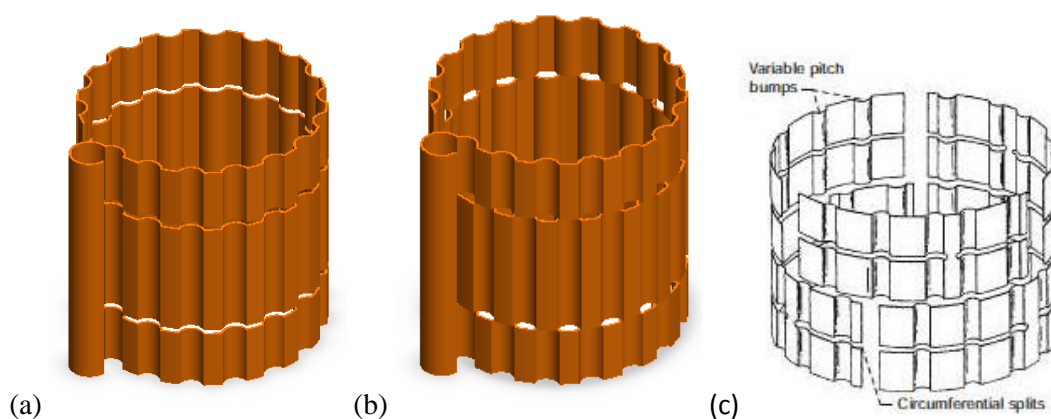


Figure 2.3: Compliant bump-shaped foils: (a) Generation I (b) Generation II and (c) Generation III[9].

Generation I bump foil have uniform stiffness in axial and radial direction (Fig. 2.3(a)). Generation II bump foils are modified to provide tailored stiffness in one of the direction (Fig. 2.3(b)) and Generation III with tailored stiffness in both the directions(Fig. 2.3(c)) [7]. The design of generation I is available in open literature, whereas Generation II and III is still protected.

The review articles on the development of foil bearing technology, technical challenges and opportunities indicates foil bearings have a strong potential to be used in various high-speed application[7, 10-12]. The growth path of foil bearings can be broadly classified into two major groups, and they are:

- a. Aerodynamic analysis to predict the static and dynamic characteristics.
- b. Development of gas foil bearings and its experimental studies.

This chapter discusses about development in the above two mentioned groups for bump type gas foil bearings.

2.4 Aerodynamic analysis of bump type gas foil bearings

The determinations of the static and dynamic coefficient of bearings are an essential portion of gas bearing design. The aerodynamic analysis is one of the verified approaches to determine static characteristics such as load carrying capacity, attitude angle, film thickness and torque. The same approach is extended to determine the dynamic coefficient such as stiffness and damping coefficients. The aerodynamic analysis of compliant gas bearing such as gas foil bearings needs to solve hydrodynamic and structural equation simultaneously. One of the pioneering works by Heshmat et al. [13, 14] in 1983, simplified the solution procedure by relating the gas film thickness of hydrodynamic equation with a compliant number. The compliant number is a function of bump parameters such as the thickness of bump foil, bump length, the pitch of bumps and elastic constants. The numerical method used by Heshmat et al. is Finite Difference Method (FDM) to solve the non-dimensional Reynold's equation. Heshmat et al. solved the Reynold's equation for both journals and thrust bump type gas foil bearings. Apart from FDM, several other methods are used are Finite Volume Method and Finite Element Method. Jamir et al. [15] in 2014 solved the coupled Reynolds equation by similar approach for studying the effect of bump foil thickness on the static characteristic of gas foil bearings. The finite difference approximation is used for discretization of the Reynolds equation and the pressure distribution is calculated by solving nonlinear matrix equation using Newton-Raphson technique.

Dellacorte and Valco [9] and Radil et al. [16] presented a different load calculation procedure in 2000 and 2001 respectively. The rule of thumb (ROT) is presented by them to avoid complex numerical simulation. The ROT is an empirical relation and based on first principles, and experimental data available in the open literature. The ROT relates bearing load capacity to the bearing size and speed through an empirically based load capacity coefficient. It is shown that load capacity is a function of bearing surface velocity and projected bearing area. This rule is found to be quite effective to study the feasibility of gas foil bearing for a specific application. A similar ROT is also developed by Dellacorte [17] to determine the bearing stiffness and damping coefficient. However, an

accurate aerodynamic analysis is always preferred by the researchers to study the behaviour of bearing parameters on its performance. The subsections 2.4.1 and 2.4.2 explain about growth phase on design methodology for gas foil journal and thrust bearing respectively.

2.4.1 Aerodynamic analysis of gas foil journal bearings

Heshmat et al. [13] have done the aerodynamic analysis for bump type gas foil journal bearing with the single and multi-pad configuration in 1983. The analysis was conducted to study the effects of numerous geometric, structural, and operating parameters on foil bearing performance. Above study is considered as the pioneering research in the field of aerodynamic analysis for gas foil bearings. The bearing performances analyzed are load carrying capacity, torque, attitude angle, film thickness and bearings stiffness.

The dynamic characteristic such as stiffness and damping of foil bearings are very much crucial to study the stability of the rotor-bearing system. So in 1987, Lund [18] elaborated the methods of computing above coefficients, which are used to study the unbalance response and stability of the rotor. In 1993, Peng and Carpino [19] developed a perturbation method to obtain the linearized dynamic coefficients (stiffness and damping). A major finding in their work is the effect of compliance of bumps on stiffness and damping. The stiffness and damping coefficients are found to be decreased as the compliance of bump structure is increased. Further Peng and Carpino [19] modelled the foil as a perfectly extensible surface on an elastic foundation. This model was developed to investigate the effect of Coulombs damping in the sub-foil structure of a gas foil journal bearing.

Many researchers around the world started their research on bump type gas foil journal bearings after 2000. The research was focused on developing more accurate models and determination of both static and dynamic coefficient of the foil bearings. In the year 2004, Peng and Khonsari [20] developed a model to predict the aerodynamic performance of a gas foil journal bearing accounting the compressibility of air and compliance of bearing surface. Prior to their research, the compressibility of the air is not considered. The model incorporates the modified eccentricity and the attitude angle to analyze the actual change in non-dimensional film thickness. The simulation results are compared with the existing experimental data of 1st generation bump foils, and a good

agreement has been achieved over a wide range of rotor speeds. Their work is further extended to determine limiting load carrying capacity of bump type journal bearings. A detailed comparison is made with analytical and numerical method [21]. Apart from load carrying capacity, Kim and Andrés [22] analysed to evaluate the limiting journal stiffness, eccentricity, and minimum film thickness for bearing at infinite rotor speed. The predictions determine that the ultimate load of a GFB cannot surpass that of its underlying compliant structure. Grau et al. [23] presented a numerical analysis of the static and dynamic performance of a compliant gas journal bearing, where the initial profile is considered a rigid surface. The above method also included the stability and unbalanced mass of the rotor. Finally, they estimated the amount of damping necessary to increase the stability of the rotor. However, no validation could be done due to the absence of experimental data. The effect of foil pivot positions on static characteristic is studied by Patil et al. [24] in the year 2013. Change in pivot position from vertical results in a reduction in load capacity. Nevertheless, for better load capacity, vertical pivot position is recommended by the authors.

The modelling of complaint structure of a gas foil bearing is complicated and researchers prefer to model the structure with simplified elements to avoid complexity. In 2005, Kim and Andrés [25] modelled the bumps as piecewise linear elastic supports for single and double active bumps. The study reveals that the double-layer active bumps improve the direct stiffness and damping coefficients. All the earlier conservative models included only the bumps as an equivalent stiffness uniformly distributed without considering the effect of top foil. Kai and Kaneko [26] investigated the bump type gas foil journal bearings for non-linear dynamic behaviour. The detailed parametric study of bearing shows the effect of bearing parameters on the static and dynamic performance of the bearings. The parameters included are number of bumps, bump foil thickness, bump height and foils of various materials. This study can be useful during the selection of bump configuration of a journal bearing. Feng Kai and Kaneko [27] extended their work by modifying their model with four factors and they are the elasticity of bump foil, the interaction forces between bumps, the friction forces at the contact surfaces, and the local deflection of top foil. The model used Castigliano's theorem to determine the stiffness of bumps. Swanson Erik [28] simplified the bump foil into two links and two springs to determine the damping coefficients of the bearings. The predicted data closely resembles the previous experimental data. The effect of Coulomb friction is studied by Dong-Hyun

et al. [29]. The modified model considered the hysteretic behaviour of the bump foils resulting from friction between bump-top foils and bump foil-bearing base. The foil structure was modelled using Finite Element Method (FEM). The results of the investigation show that numerous static equilibrium locations are presented for the one static load due to the friction and concluding its effects on the dynamic performance. But, the effect of friction on the minimum film thickness which governs the load capacity of the bearing is negligible. In 2016, Hoffmann et al. [30] developed a modified model as an extension of Lund's [18] work, where the pressure field is coupled with a 2D plate model, while a link-spring model simplifies the non-linear bump structure. The model includes Coulomb friction effects inside the bumps. The above dynamic stiffness model is validated with experimental data. Finally, the author suggests using infinitely small perturbation based on the non-linear structural models for most realistic values.

The selection of suitable numerical model analysis tool helps to determine the bearing characteristics accurately. In 2006, Andrés [31, 32] developed two finite element (FE) models for the top foil supported above the bump foils; one studies a 2D shell anisotropic construction and the other a 1D beam type construction. Between these two models, 1D top foil model is preferred because the model is compared best to the test data and with lower computational cost. The model is further tested with preload conditions; the prediction shows the improvement in load carrying capacity at low speed and low load. In the same year, the FE model developed by the Carpino and Talmage [33] predicted the rotordynamic coefficients. The model included the radial and circumferential deflection of the bump foil. The Coulomb friction between the top - bump foils and the bump foil - bearing base is modelled as viscous friction. The model demonstrated the effects of frequency, orbit size, and friction coefficient on the dynamic coefficients. They also used a dynamic model of the unbalanced rotor to predict periodic journal motion [34]. A perturbation analysis of the periodic motion determines the periodic changes in gas film thickness. Based on the change in film thickness, the pressure profile and foil deflection is also calculated. The above model also included the bending and membrane effect of smooth, thin top foil. A numerical model developed by Hou et al. [35], where the aerodynamic pressure of the gas is coupled with deformation of bump foil structure and the top smooth foil is modelled as a strip of rectangular thin plates supported at rigid points of bump foil. The solution method incorporated is FEM and the effects of bearing number,

eccentricity ratio, and a number of protuberances on the bearings performance were analyzed.

The aerodynamic analyses for the heavily loaded condition were limited. So in 2008, Kim and Andrés [36] developed a more accurate model to predict static and dynamic force characteristics such as stiffness and damping for gas foil journal bearings under heavily loaded conditions. The predicted data from the model is compared with the test data from gas foil bearings under heavy load and found to be comparable. The author suggests the advanced model is the suitable design of gas foil journal bearings under heavy loads.

The rotors with gas foil bearings rotate at very high speed, so a rotordynamic analysis is always part of the machine design. An investigation of nonlinear dynamics of a high-speed flexible rotor supported on the gas foil journal bearings is attempted by Bhore and Darpe [37] in the year 2013. A time domain orbit simulation is done, where the equations of rotor motion are added to already develop compliant Reynold's equation. Effect of various system parameters are studied and found to be quite useful in designing a rotor-bearing system with gas foil bearings. Schiffmann and Spakovszky [38] developed a model with time domain integration of the equations of motion of the rotor coupled with the Reynolds equation. The model is used to quantify the evolution of the rotor orbit, the underlying mechanism and the onset speed of instability. The author suggests various design guidelines to improve the rotor stability.

The different models are proposed by various authors to determine realistic static and dynamic characteristics of gas foil journal bearing. Many tribologists follow the model proposed by Heshmat et al. [13] to design and develop gas foil bearings because of simplicity in the design procedure.

2.4.2 Aerodynamic analysis of gas foil thrust bearings

An extensive research and test data are available for gas foil journal bearings compared to the gas foil thrust bearing. Hence, more work on gas foil thrust bearings is essential to improve the design database. This section documents some of the major findings in the aerodynamic analysis of bump type gas foil thrust bearing.

The pioneering work on bump type thrust bearing is done by Heshmat et al. [14] in 1983. They designed the basic model for foil thrust bearing, where the hydrodynamic equation is coupled with the structural equation. The parametric study shows effects of various operational and structural variables on bearing behaviour. The optimization study shows the optimised dimension are angular extend of 45° and the ratio of outer radius to inner radius of 2. In 1999, Iordanoff [39] simplified the elasto-aerodynamic model in order to reduce the computational time. The determined values of the new model are comparable with results obtained from the experimental work. The numerical method employed for above two models is FDM. In 2000, Heshmat et al. [40] used coupled Finite Difference (FD) and Finite Element (FE) methods. FD method is utilized for the aerodynamic analysis while FE is used to model the structural resiliency. This method is found to converge faster and within 2 or 3 iterations. This program could be proved to be an efficient method to deal with complex foil structures.

The dynamic characteristic of thrust bearing are essential to study stability of rotor-bearing system as in real system they strengthen the stiffness and damping of the journal bearing. In 2007, Park et al. [41] determined the static and dynamic characteristics of bump foil under the condition of various bump parameters. The method employed is coupled FE and FD method. The physical analysis and numerical model for prediction of the static and dynamic performance of gas thrust foil bearings for a turbocharger is done by Andres et al. [42]. For the specified load of the turbocharger, the static and dynamic characteristics are determined for gas foil thrust bearing. Gad and Kaneko [43] introduced a new structural stiffness model for the compliant structure in foil gas thrust bearings. The model considered the option that the flat section between bumps, which may deflect sideways and separate from the rigid bearing surface, the model also considered the interaction between the bump-top foil and bump foil -bearing surface. Kai et al. [44] modified the thrust bearing model with consideration of three effects, and they are the flexibility of the bump foil, frictional force at the contact surfaces and top foil deflection. Both static and dynamic characteristics of gas foil thrust bearing are predicted in the modified model.

The aerodynamic models for gas bearing are solved with the assumption that the process gas is a perfect gas. There is always the possibility that bearing performance can be different by incorporating real gas properties in the aerodynamic model. So In 2013, In Conboy [45] studied the real-gas effect in gas foil thrust bearings used in closed-cycle

supercritical CO₂ turbine. The simulation results showed higher load carrying capacity, frictional power loss and rotordynamic stiffness for CO₂ in comparison to air. Bruckner and DellaCorte [46] developed a model to analyze the aerodynamic, structural and thermal behavior of gas foil thrust bearing. Knudsen number effects are added to the model as the film thickness is very thin and affect the aerodynamic behavior of the bearing. Heat transfer between the gas lubricant and its surrounding is added to study its thermal behavior. The stiffness of the compliant structure is modeled as a distributed stiffness that supports the smooth top foil. Finally, the system of governing equation, is solved in a Mathematica computing environment.

The manufacturing of bumps being troublesome, various author replace the bump foil with various viscoelastic material such as silicon and fluorine rubber to determine the load capacity [47, 48].

2.5 Development of gas foil bearings

Development of gas foil bearings is always a bottleneck for the fabricators because of the tight tolerance in fabrication. However, recent advancement in fabrication technology and methodology has motivated the researchers to fabricate and test the foil bearing performance.

Davydenkov et al. [3] fabricated gas foil bearing with the leaf type compliant structure for a turboexpander used in helium liquefaction plant. The maximum operational speed of the rotor was 240,000 rpm with a shaft diameter of 16 mm. The maximum amplitude was under 2 μm . Xiong et al. [49, 50] developed a foil bearing (plate foil), where several copper wires of 0.2 mm are soldered over the 0.06 mm thick phosphor bronze to make it a compliant bearing structure. Similar plate foil is developed by Hou et al. [50] in 2000 for a cryogenic turboexpander. The maximum operational speed obtained was 230,000 rpm. The fabrication and assembly are found to be simpler for bending dominated foil such as bump and convex dot compared to leaf and tape type. Current research work is on development of bump type gas foil journal and thrust bearings. So the literature studies concentrate on the development of bump type journal and thrust foil bearing in next two subsequent sub-chapters.

2.5.1 Development of bump gas foil journal bearings

Heshmat [51] is one of the inventors in the development of bump type foil journal bearing test rig in open literature. He developed the test rig in the year 1994 to study the rotor-bearing performance. The developed rotor could reach a DN speed of 4.62×10^6 for a rotor diameter of 35 mm and radial clearance of 33 to 47 μm , which is beyond capability of any advanced oil lubricated system. In 2000, Heshmat [52] also developed a test rig to study the ability of a flexible rotor operating at its bending mode. The test rig supported the rotor with three foil bearings. The rotor could cross the 1st bending critical speed and operated at 2.5 times of its bending critical speed. The experimental concluded that the rotor could rotate above its bending critical speed with small amplitude of vibration, and foil bearing is quite a promising option for high-speed machinery in modern technology. After successful development of foil bearings, various author tailored the bump structures according to their application. DellaCorte et al. [53] explained the detailed fabrication methodology for the generation I and II bump foils. A low-cost tooling is designed and fabricated for forming of bumps. The documented steps have been quite useful for the researchers around the world as a starting point for the new development of bump type foil bearings for their application. In 2016, extensive work is done by Karim Shalash [54] for forming of bump foil for journal bearing with accurate dimension. He designed a prototype die for forming of bump foil after using various analysis tool such as the design of experiment(DOE) to quantify the effect forming parameters on forming process. He also included a Monte Carlo simulation to quantify uncertainty distributions for the bump geometrical errors, and finite element analysis (FEA) for stress analysis on foils. The designed die is fabricated and tested to prove significant enhancement in forming methodology. The designed die reduces the spring back and mean stress along the foil during the forming process by 69 % and 17.4 % respectively.

Few authors have developed bump type foil journal bearings for a high-speed turbomachine. In 2001, Chen et al. [55] replaced their old tape type foil bearings with the Generation-I bump type journal bearings for a helium turbo-compressor rotating between 40,000 to 90,000 rpm. Their work is documented with fabrication methodology and performance study of rotor- bearing system. Their work is found to be quite useful for the engineering community. Gas foil bearings are developed for high-speed turbocharger Sim et al. and Lee et al. [56-58]. Sim et al. [56] developed foil bearings for a high-speed turbocharger to study its rotor dynamic behaviours. They added a couple of shims in the

journal bearing to increase the pre-load of top foil on the journal; the application proved to be of higher load carrying capacity and reduction in the amplitude of subsynchronous motions. Kulkarni et al. [59] developed foil bearings for gas turbine application. The foil bearings developed are tested at a speed of 50,000 rpm under the simulated load conditions. In 2016, a pair of the generation I bump type journal foil bearings was developed by Hou et al. [60] in the year 2015, for a cryogenic turboexpander with 25 mm rotor diameter to study its behaviour with variable diametrical clearance. The experiment was done to study the behaviour of gas foil bearings by replacing the existing aerostatic journal bearings of commercially available turboexpander.

In 2010, Lee et al. [61] developed a test rig for supporting two types of foil bearings, one with viscoelastic foil bearing other with bump type foil bearings. The test is conducted to study unbalance response of the rotor rotating at its 1st bending critical speed. In 2007, Salehi et al. [62] developed a gas foil bearings of 216 mm diameter. The motive behind the work is to study structural stiffness and damping of a large bump type journal bearings. Lee et al. [63] developed a test rig with bump foil to simulate the operating characteristics of the micro power system. The power system with a rotor diameter of 7 mm operated stably at 300,000 rpm. The amplitude of synchronous vibration was within 20 μm . Rubio and Andres [64] developed a test rig for dynamic load experiments. The experiment assisted the author in determining structural stiffness, the coefficient of friction and a damping coefficient. The test was carried out for a range of temperature between 25 to 75 $^{\circ}\text{C}$ without any significant variation of bump foil parameters. To determine the stiffness and damping coefficient, a test rig was developed by Arora et al.[65]. The experiment was carried up to the speed of 60,000 rpm and sub-structuring approach is used to determine the dynamic characteristics of gas foil bearings. Kim and Park [66, 67] developed a test rig to address the issue of aerodynamic gas foil bearing during the start and stop of the machine. They incorporated externally pressurized gas facility to the gas foil bearing. The author suggests above combination reduce the starting torque, wear rate of top foil and cooling of the bearings. Structural stiffness is one of the parameters, which controls the bearing performance significantly. So Duan et al. [68] experimentally determined the structural stiffness of Inconel X-750 with various heat treatment by placing the bump foil between two metal pads.

In the year 1996, Laskowski and DellaCorte [69] studied the wear behaviour of high-temperature foil bearing materials using various tribo-tests. The chosen materials are Rene 41, Inconel X-750, Inconel 713C, MA956, Inconel 909 and Al_2O_3 . The experiment reveals that the formation oxides are responsible for reducing friction and wear at different temperatures. The author prescribes the suitability of various foil materials for various operation ranges of temperature. Foil bearings rely on the solid lubricant coating as they are aerodynamic bearing and susceptible to direct contact between the runner and bearing at their low speed during the start and stop of turbomachines. In 2004, DellaCorte et al. [70] experimented on the behaviour of various solid lubricant coating on bearing performance. A combination of self-lubricating shaft coatings combined with various wear resistant and lubricating foil coatings shows better performance of the bearings. The experiment shows the shaft coated with PS304 and a layer of MoS_2 running against Al-Cu coated foils give maximum load capacity. Jahanmir et al. [71] assessed the coating behaviour for tungsten disulfide, hydrogenated diamond-like carbon film and thin dense chrome plating deposited on the foil bearings.

2.5.2 Development of gas foil thrust bearings

Similar to aerodynamic analysis of gas foil thrust bearing; the development and experimental results are limited as very limited research work has been published till date. However, the progress on fabrication and testing of gas foil thrust bearings are presented in this section based on its availability in open literature.

Detailed design and fabrication methodology for a gas foil thrust bearing with low tooling cost is developed by Dykas et al. [72]. The bump foils are fabricated by forming operation. The detailed die design and forming methodology along with the design of fixture and tooling are explained. A prototype bearing is fabricated and tested to verify its performance. The basic method of fabrication of thrust bearings has been useful to foil bearing practitioner. The NASA Glenn research centre has developed two test rigs to test single sided gas foil thrust bearing [73]. One is vertical test rig, and other is horizontal. The drive unit for the vertical thrust bearing rig is a 5 kW electric motor, which can reach to speed up to 21,000 rpm. The vertical rig is also employed with temperature variation. The drive unit of the horizontal thrust bearing rig is an air turbine and has a practical speed limit of 60,000 rpm. The thrust bearings are fabricated based on the methodology as explained by Dykas et al. [72]. The objectives of the above test were to develop test

techniques of gas foil thrust bearings, to enumerate bearing-to-bearing changeability, and to produce an open source performance database. Balducchi et al. [74] also fabricated gas foil bearings based on the design methodology of Dykas et al. [72] to study the torque and lift-off velocity of the bearing. A dedicated test apparatus was developed to measure the speed of the rotor, the torque and the temperature of the bearing under the foil. The axial load on the bearing is varied from 5 N to 60 N. The value of start-up torque, and fluid film torque was confirmed by comparisons with results obtained with a rapid camera. This experiment has helped the researchers to validate their numerical models on gas foil bearings.

Bauman [75] developed a test rig, which is capable of testing thrust air foil bearing up to 100 mm in diameter. The rotor is driven by air impulse turbine and can reach up to 80,000 rpm. The test apparatus was used to determine the load capacity, friction, and its durability. The apparatus is also employed with high-temperature environment up to 650 °C with an expectation to use for future turbine application. The experimental data generated by the test rig are used to validate various numerical models. The detailed assembled drawings are quite useful for researchers and offer a direct guidance for future bearing development. Arora et al. [76] developed a test apparatus to study structural stiffness of a prototype thrust foil bearing. The setup was designed with single air foil bearing instead of double foil bearings to avoid initial high torque. The experiment was carried out at 60,000 rpm. Sub-structuring approach was used to identify the stiffness and damping characteristics. In the sub-structuring approach, each element was considered in isolation and the structural properties of the isolated structure were determined using experimental data. All the isolated elements were subsequently assembled to make complete rotor-bearing-support system. Lee et al. [77] developed an analytical model for thrust foil bearings with variable and irregular thrust load. The validations of the model were done by developing a thrust bearing setup with gas foil thrust bearing. Three different foil bearings were fabricated with an outer diameter of 45, 50 and 55 mm. The fabricated foil bearing was of Generation-I with eight pads. The rotational speed of the rotor was varied from 10,000 to 25,000 rpm. From the experimental results, the model using nonlinear stiffness was in better agreement compared to a model using linear stiffness.

Repeated start and stop of the turbomachines are always a matter of concern for aerodynamic bearings. Various coating are applied to avoid wear of the top foil or the runner. A type of coating suitable for a machine depends on loading condition and the operating environment. Fanning and Blanchet [78] tested the performance of gas foil thrust bearing with PS304 and KorolonTM 1350A for a high-temperature application with operating temperature of 540 °C. The tribological behaviour of both the coatings was studied and compared.

2.6 Gaps in literature

Turboexpander with gas bearing is a precision machine, where the bearing clearance is in the range of 10-40 µm [2]. Various gas bearings such as tilting pad, grooved bearings are fabricated and tested for turboexpander. However, there is always a demand for better bearings, which can improve the stability of the rotor bearing system. Foil bearings have been found to be suitable gas bearing for low load and high speed rotor. After extensive open literature review following gaps are found in the development of gas bearing for turboexpander and in the development of foil bearings.

- i. Developments of foil bearings for turboexpander are very few, and among them, many are protected due to their proprietary nature. So a structured design, fabrication, and testing procedure will help the engineering society to developed better gas foil bearing for turboexpander and also for other high-speed machines.
- ii. The design of tooling for fabrication of bump foil is complicated as very few researchers have worked on this field. So a FEM based process simulation system of the forming dies and bump forming will reduce fabrication cost of dies as well save the time.
- iii. Very few researchers have developed gas foil thrust bearing, so the available databases of experimental test results are minimal. The experimental work on gas foil thrust bearings will help to receive a complimentary level of research, and in future, these bearings can be an alternative solution for various high-speed oil-free turbomachinery.

Chapter 3

Bump Type Gas Foil Journal Bearing

Foil journal bearings have received much attention for research, development, and experiment over past three decades. The reason of above attention is to use foil bearings in the wide application areas, increased the load carrying capacity and understanding dynamic characteristics of bearings such as stiffness and damping.[13, 19]. The application of gas foil bearings (GFBs) to small and mid-range turbo machines can enable substantial savings in the design and operation [11]. These turbo machines have been designed, developed and experimented by various investigators with different types of foil journal bearings such as tape type, leaf type and bump type. Among them bump type journal foil bearing are more popular for higher load carrying capacity, with certain fabrication and assembly difficulties [55]. The gas foil journal bearings in current analysis consist of a smooth top foil, a bump foil, a bearings base and an attachment arrangement of foils with bearing base (Fig. 3.1). This type of gas bearing design is suitable for small size turboexpander to avoid contamination of process gas, accommodate misalignment, endurance to foreign matters, soft failure and tailored stiffness and damping [7]. This chapter provides a detailed design methodology of bump type GFB for small size and high-speed vertical oriented cryogenic turboexpander based on pioneering work of Heshmat et al. [13].

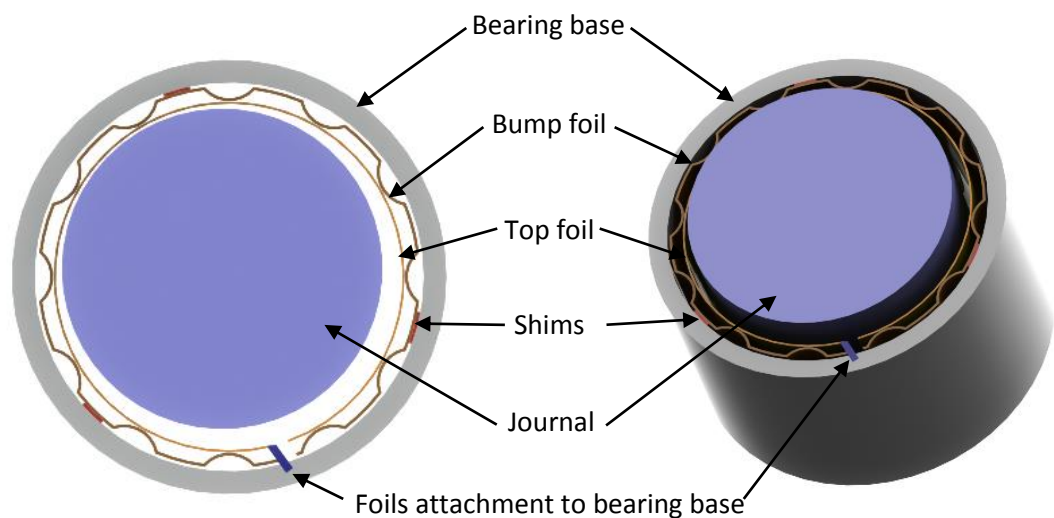


Figure 3.1: Schematic diagram of a bump type journal foil bearings for the vertically oriented rotor.

3.1 The working principle

Gas foil journal bearings operate on two main principles. One is aerodynamic lubrication, and other is structural dynamics. In the principle of aerodynamic lubrication, the lubricant or the gas is dragged into a converging geometry by the relative motion of two surfaces resulting in pressurized aerodynamic film generation. The aerodynamic pressure film developed between the smooth top foil and the journal is responsible for carrying the radial load of the journal. The bearing base houses a corrugated series of bumps made of a thin foil strip and a smooth top foil over it. The bottom bump foil creates an elastic structure and behaves as spring bed which is responsible for increasing bearing stiffness. One end of both these foils are welded or mechanically fixed with the bearing base and the other ends are free.

The converging wedge shape, which is responsible for the generation of aerodynamic pressure, depends on the orientation of rotor such as horizontal, vertical or inclined. For horizontal and inclined rotors the wedge is formed due to gravity, but for vertical rotors, an additional mechanism needs for developing converging wedge. In the current project, the bearing base is designed with shims (Figs. 3.1 and 3.2) to accommodate converging film thickness in the vertically oriented rotor. The presence of shims create contact between top foil and journal at predefined location. These contact points develop an initial preload of smooth top foil on the journal. This preload between the top foil and the journal remain in contact until lift-off speed is achieved. Under the action of pressure, the top foil deforms and forcing it away from shaft but towards the bump foil. So during rotation of rotor above liftoff speed, the journal does not touch the bearing. At the action of deformation there is friction between top foil – bump foil and bump foil- bearing base. This friction helps to generate Coulumbic damping in the bearing. Further, the bump materials and dimensions can be modified to tailor the stiffness and damping of the bearing.

3.2 Bearing geometry

The geometrical parameters of GFB and bump details are given in Figs. 3.2 and 3.3 respectively. These parameters are used in the governing equations to design gas foil bearings, and they also describe the bump configurations.

R: Shaft radius,

ω : Speed of the rotor(rad/sec),

C: Radial clearance,

e: Eccentricity,

ϵ : Eccentricity ratio (e/C),	ϕ : Attitude angle,
t_b : Bump thickness,	R_b : Bump radius,
l_b : Half bump length,	h_b : Bump height,
s : Bump pitch,	E : Young's modulus,
ν : Poisson ratio,	L : Axial length of the bearing,
η : Viscosity of the gas,	P : Pressure
P_a : Ambient pressure,	ρ : Density of the gas,
h : Film thickness.	

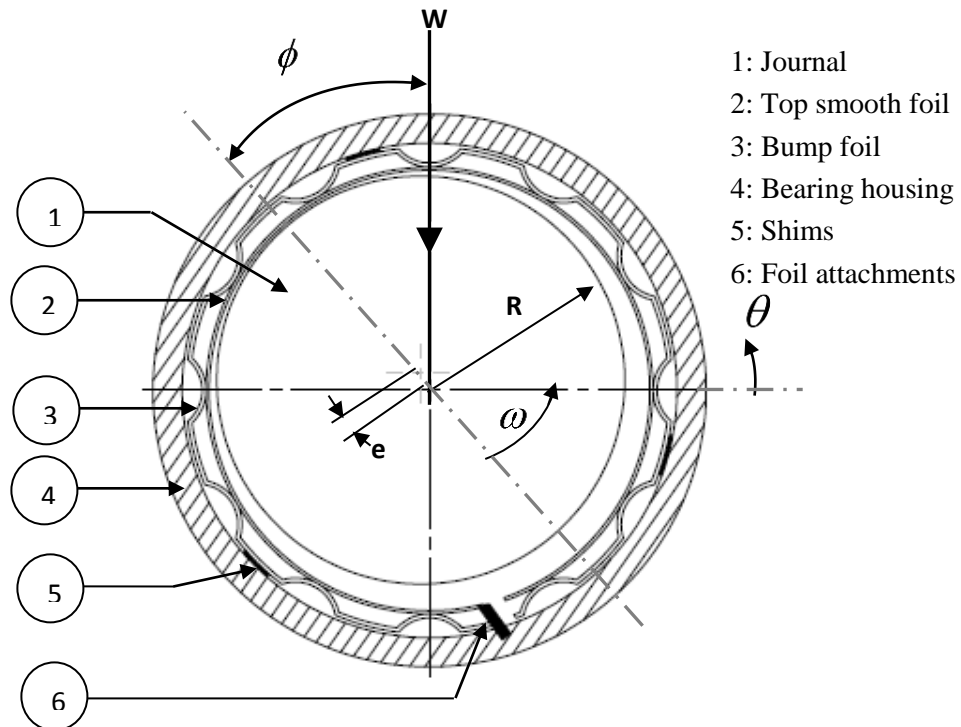


Figure 3.2: Geometrical parameters of gas foil journal bearings.

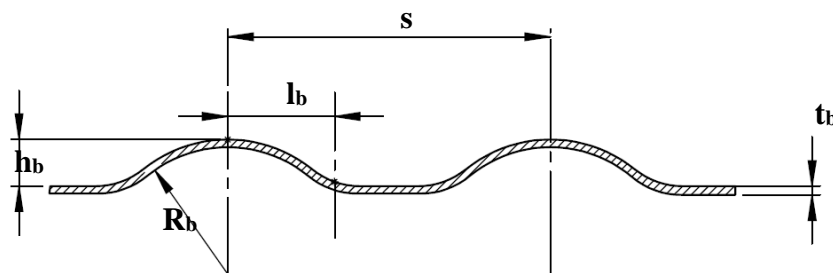


Figure 3.3: Configuration of bump foil.

3.3 Performance analysis of gas foil journal bearings

Several models have been developed by various authors to estimate steady state performances such as pressure profile over the bearing surface, gas film variation, load carrying capacity and frictional torque. Popular and easy methods to analyze gas foil

bearings are by solving aerodynamic and structural equation simultaneously, where the elastic equation of the bump foil deflection is interconnected with Reynold's equation. The resultant equation is a non-linear partial differential equation, and the computational cost for solving such equation is always very high. Hence instead of the exact solution, an approximate method such as Finite Difference Method (FDM) or Finite Element Method (FEM) is preferred. The solution of Reynolds equation facilitates to determine pressure profile and film thickness over the bearing surface[13, 20]. Further pressure profile is used to determine other bearing performance parameters such as load carrying capacity and frictional torque.

3.3.1 The governing equations

The generalized Reynold's equation (Eq. 3.1) in the form of Cartesian coordinates is used to evaluate the pressure profile over finite bearing surface[13, 20]. This equation accounts both physical wedge and squeeze action based on following assumptions:

- (i) The lubricant gas behaves as isothermal and perfect gas.
- (ii) The viscosity of the lubricant is constant.
- (iii) The force of gravity and fluid inertia are negligible in comparison to the viscous force.

$$\frac{\partial}{\partial x} \left(\frac{\rho h^3}{12\eta} \frac{\partial p}{\partial x} \right) + \frac{\partial}{\partial z} \left(\frac{\rho h^3}{12\eta} \frac{\partial p}{\partial z} \right) = \frac{1}{2} U \frac{\partial(\rho h)}{\partial x} + \frac{\partial(\rho h)}{\partial t} \quad (3.1)$$

The polar form of Reynolds Eq. (3.2) neglecting time variant helps to find a solution over R - θ coordinates, z being axial direction.

$$\frac{1}{R} \frac{\partial}{\partial \theta} \left(\frac{\rho h^3}{12\eta} \frac{1}{R} \frac{\partial p}{\partial \theta} \right) + \frac{\partial}{\partial z} \left(\frac{\rho h^3}{12\eta} \frac{\partial p}{\partial z} \right) = \frac{R\omega}{2} \frac{\partial(\rho h)}{R\partial \theta} \quad (3.2)$$

Assuming the gas behaves ideally and follows the relation, $\rho = \frac{p}{R_g T}$, the Eq. (3.2) is further modified to Eq. (3.3).

$$\frac{1}{R} \frac{\partial}{\partial \theta} \left(\frac{p h^3}{12\eta R_g T} \frac{1}{R} \frac{\partial p}{\partial \theta} \right) + \frac{\partial}{\partial z} \left(\frac{p h^3}{12\eta R_g T} \frac{\partial p}{\partial z} \right) = \frac{\omega}{2} \frac{\partial}{\partial \theta} \left(\frac{p h}{R_g T} \right) \quad (3.3)$$

Normalizing the above equation and assuming isothermal ($\bar{T} = 1$) and isoviscous ($\bar{\eta} = 1$) case Eq. (3.4) is obtained[13]:

$$\bar{z} = \frac{z}{L}, \bar{p} = \frac{p}{p_a}, \bar{h} = \frac{h}{C}, \bar{\eta} = \frac{\eta}{\eta_0} \text{ and } \bar{T} = \frac{T}{T_0}$$

$$\frac{\partial}{\partial \theta} \left(\bar{p} \bar{h}^3 \left(\frac{\partial \bar{p}}{\partial \theta} \right) \right) + \left(\frac{2R}{L} \right)^2 \frac{\partial}{\partial \bar{z}} \left(\bar{p} \bar{h}^3 \frac{\partial \bar{p}}{\partial \bar{z}} \right) = \Lambda \frac{\partial (\bar{p} \bar{h})}{\partial \theta} \quad (3.4)$$

Where $\Lambda = \frac{6\omega\eta_0}{P_a} \left(\frac{R}{C} \right)^2$, Λ is called bearing or compressibility number, which is a function of speed and geometrical parameters. Eq. (3.4) represents a standard non-dimensional compressible Reynolds equation. This equation is used to evaluate pressure profile of rigid and compliant gas bearings.

The difference between rigid bearings and compliant bearing is the normalized film thickness (\bar{h}). For rigid gas bearings, the functional form of film thickness is represented as in Eq.(3.5), where the film thickness is only a function of bearing geometry.

$$\bar{h} = 1 + \varepsilon \cos \theta \quad (3.5)$$

But, in the case of the foil bearing, where the bushing is compliant so the film thickness is a function of bearing geometry, pressure, foil materials and bump geometry [13, 79]. The film thickness is a function of pressure because the pressure deforms the top and bump foils and the film thickness changes. Similarly, the bump geometry and material determines the degree of deformation and represented by non-dimensional compliance number. This feature in a gas foil bearing helps the bearing to maintain positive pressure even above unity eccentricity ratio. The expression for non-dimensional film thickness is given in Eq. (3.6) based on following assumptions [20]:

- (i) The bumps are with uniform elastic foundation.
- (ii) Bump stiffness is constant and does not depend on bump deflection and adjacent bumps.
- (iii) The top foil does not sag between adjacent bumps. The top foil does not have either bending or membrane stiffness, and its deflection follows that of the bump

$$\bar{h} = 1 + \varepsilon \cos \theta + \alpha (\bar{p} - 1) \quad (3.6)$$

Where compliance number represented as $\alpha = \frac{2P_a S}{CE} \left(\frac{l_b}{t_b} \right)^3 (1-\nu^2)$

The Eq. (3.4) needs to be expanded before applying the numerical solution. The expanded equation is given in Eq. (3.7)

$$\begin{aligned}
& \bar{p}\bar{h}^{-3} \frac{\partial^2 \bar{p}}{\partial \theta^2} + \bar{p}3\bar{h}^{-2} \frac{\partial \bar{p}}{\partial \theta} \frac{\partial \bar{h}}{\partial \theta} + \bar{h}^{-3} \left(\frac{\partial \bar{p}}{\partial \theta} \right)^2 \\
& + \left(\frac{2R}{L} \right)^2 \left[\bar{p}\bar{h}^{-3} \frac{\partial^2 \bar{p}}{\partial \bar{z}^2} + \bar{p}3\bar{h}^{-2} \frac{\partial \bar{p}}{\partial \bar{z}} \frac{\partial \bar{h}}{\partial \bar{z}} + \bar{h}^{-3} \left(\frac{\partial \bar{p}}{\partial \bar{z}} \right)^2 \right] \\
& = \Lambda \left[\bar{p} \frac{\partial \bar{h}}{\partial \theta} + \bar{h} \frac{\partial \bar{p}}{\partial \theta} \right]
\end{aligned} \tag{3.7}$$

3.3.2 Boundary conditions

The necessary boundary conditions for solving the non-dimensional Reynolds equation are given in Eq. (3.8)

$$\left. \begin{aligned}
\bar{p} &= 1 \text{ at } \theta = 0 \text{ and } 2\pi \\
\bar{p} &= 1 \text{ at } \bar{z} = 0 \text{ and } 1 \\
\bar{p} &\geq 1
\end{aligned} \right\} \tag{3.8}$$

First boundary condition indicates the pressure at the leading edge and trailing edge of the foil is at ambient pressure. The second indicates ambient pressure at the start and end of the journal in the axial direction. Finally, the third condition indicates that the gas foil bearings do not permit generation of sub-ambient pressure.

3.3.3 Load carrying capacity

The forces of the gas film, acting on the journal are computed by integrating the pressure $\bar{p}(\theta, \bar{z})$ over the bearing surface[13].

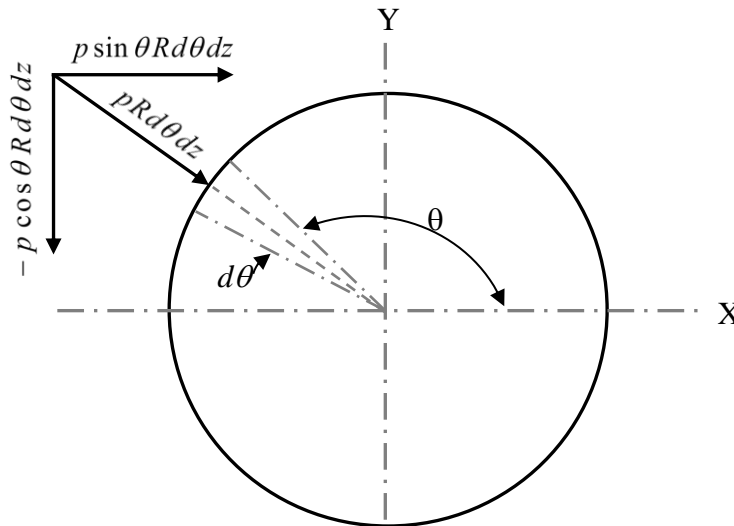


Figure 3.4: Sign convention of the journal forces.

The sign convention for the journal forces is shown in Fig. 3.4, Eqs. (3.9) and (3.10) shows forces in x and y-direction.

$$\begin{Bmatrix} F_x \\ F_y \end{Bmatrix} = \int_{-L/D}^{L/D} \int_0^{2\pi} (p - p_a) \begin{Bmatrix} \sin \theta \\ -\cos \theta \end{Bmatrix} R d\theta dz \quad (3.9)$$

The normalized form is:

$$\begin{Bmatrix} \bar{F}_x \\ \bar{F}_y \end{Bmatrix} = \frac{1}{p_a R^2} \begin{Bmatrix} F_x \\ F_y \end{Bmatrix} = \int_{-L/D}^{L/D} \int_0^{2\pi} (\bar{p} - 1) \begin{Bmatrix} \sin \theta \\ -\cos \theta \end{Bmatrix} d\theta d\bar{z} \quad (3.10)$$

The resultant non-dimensional load is calculated in Eq. (3.11)[13].

$$\bar{W} = \frac{W}{p_a R^2} = \sqrt{(\bar{F}_x)^2 + (\bar{F}_y)^2} \quad (3.11)$$

3.3.4 Frictional torque

Determination of frictional torque is important for the design of gas bearings and the normalized form of torque on journal is given in Eq. (3.12)[13].

$$\bar{T} = \frac{T}{P_a C R^2} = \int_{-L/D}^{L/D} \int_0^{2\pi} \left\{ \frac{\bar{h}}{2} \left(\frac{\partial \bar{p}}{\partial \theta} \right) + \frac{\Lambda}{6} \frac{1}{\bar{h}} \right\} d\theta d\bar{z} \quad (3.12)$$

3.3.5 Dynamic coefficients

Dynamic bearing performance parameters such as stiffness and damping are the most important factors for dynamic analysis of rotor-bearing system. Stiffness of three elements responsible for gas foil stiffness are bump foil, top foil and gas film. The top foil has negligible thickness and the loading is bending dominated hence structural stiffness of the top foil can be neglected.

Several researchers using Finite Element Method (FEM) and coupled FEM and FDM approach have predicted gas film stiffness. The method developed by Peng J. P. and Carpino M.,1993 [19] was found to be simple and effective. In this method, a small displacement perturbation applied to steady state operating condition and load in the perturbation state was calculated. Dividing the change in load by small perturbation will yield the stiffness and damping coefficient. For current application, the values of normalised gas film stiffness and damping coefficients are calculated from the results obtained by Peng and Carpino [19] for the designed bearing number of current application. The overall gas film stiffness coefficient at operating speed of 140,000 rpm is 7.22E+5 N/m.

The bump stiffness for current application is calculated using Jordanoff's formulae[39]. In Jordanoff's formulae, the structural stiffness is calculated considering influence of each bump, the radial position of the applied load and dry friction coefficient between the bump and bearing base. Following assumptions are made in the formulation of the formula.

- The bump material is isotropic.
- The pitch between bumps is constant.
- The interaction between bumps are neglected.

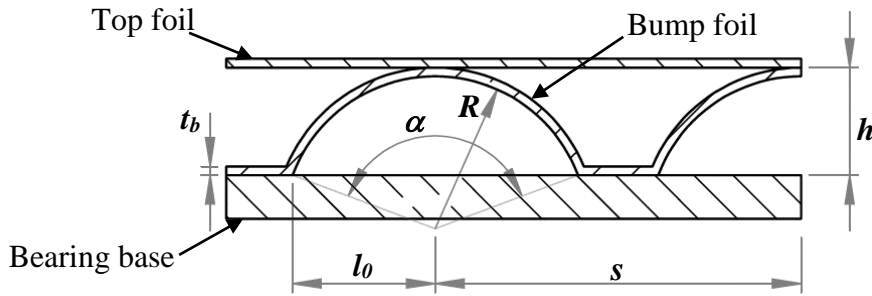


Fig 3.5: Bump geometric parameters for bump stiffness calculation

The stiffness, K_{bump} for a single bump with free ends condition, is given in Eq. (3.13)[80].

The total stiffness of bump foil is a number of bumps times K_{bump} .

$$K_{bump} = \frac{Et_b^3 \sin^3(\alpha/2)}{6l_0s^2(1-\nu^2)L} \left(\frac{1}{I(\alpha, \mu_f)} \right) \quad (3.13)$$

Where, $L = \frac{\text{Axial length of foil bearing}}{\text{No of bump strips}}$ and $\mu_f = \text{Dry friction coefficient}$

$$I(\alpha, \mu_f) = \left(A^2 + \frac{1+\mu_f^2}{2} \right) \frac{\alpha}{2} - \left(\frac{1-\mu_f^2}{4} \right) \sin \alpha - \frac{\mu_f}{2} (\cos \alpha - 1) - 2A \left(1 - \cos \left(\frac{\alpha}{2} \right) + \mu_f \sin \alpha \right)$$

$$A = \sin \left(\frac{\alpha}{2} \right) + \mu_f \cos \left(\frac{\alpha}{2} \right)$$

The value of the geometric parameters taken for prediction of bump stiffness is tabulated in Table 3.2. For current application, L is 16 mm. The material selected is phosphor bronze. The dry friction coefficient is between phosphor bronze and steel. The total number of bumps is 11. The bump stiffness with 11 bumps is 9.59E+5 N/m. The predicted value of bump stiffness is compared with the actual static stiffness of the fabricated gas

foil journal bearing in chapter 6. The overall stiffness neglecting top foil stiffness is calculated using Eq. (3.14) and its value is $4.12\text{E}+5$ N/m.

$$\frac{1}{K_{Total}} = \frac{1}{K_{Bump}} + \frac{1}{K_{gas}} \quad (3.14)$$

3.4 Numerical procedure

The elastohydrodynamic coupling Eq. (3.7) can be solved using several numerical methods such as finite difference method, finite element method, finite volume methods and spectral method. to find the pressure profile and film thickness. Among all the above-stated methods, finite difference method (FDM) is more popular because of simplicity of the approach[81]. Few investigators have used finite element method(FEM), and it was found that FDM is simple to use, saves computational time and well balances close to resultant accuracy [20]. So, the coupled Reynolds and the structural Eq. (3.7) are solved by the finite difference approach [13, 20, 79]. The derivatives of deflection and pressure are discretized using the central differencing method. A sparse version of the numerical grid is shown in Fig. 3.6.

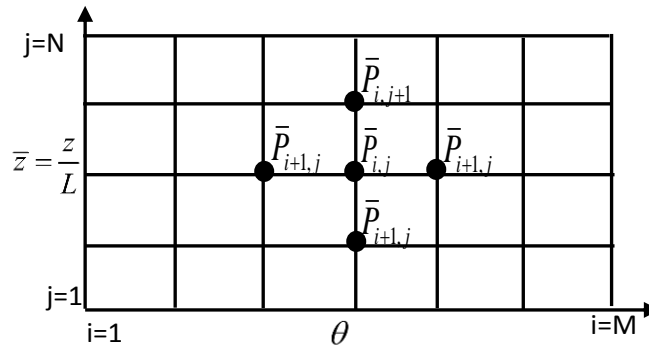


Figure 3.6: Discretization of journal bearing surface.

3.4.1 Discretization of equation

The solution region is divided into mesh with a uniform grid. Fig. 3.6 shows a uniform mesh, with a number of nodes M and N in θ and Z direction respectively, so a total number of nodes are $M_{\theta} \times N_z$. Grid refinement study determines the division of a mesh in both directions to predict the accurate result. So a detailed grid refinement study has been done in section 3.4.3.

Each node can express the distribution of normalized pressure in the whole region. According to the finite differential regularities, the partial derivatives at the node $O(i, j)$ can be represented by the surrounding node variables. The expression of the partial

derivatives of the intermediate difference at the node O(i, j) have the forms as shown in Eq. (3.15).

$$\left. \begin{aligned} \frac{\partial^2 \bar{p}}{\partial \theta^2} &= \frac{\bar{p}_{i+1,j} - 2\bar{p}_{i,j} + \bar{p}_{i-1,j}}{\Delta \theta^2}, & \frac{\partial^2 \bar{p}}{\partial \bar{z}^2} &= \frac{\bar{p}_{i,j+1} - 2\bar{p}_{i,j} + \bar{p}_{i,j-1}}{\Delta \bar{z}^2} \\ \frac{\partial \bar{p}}{\partial \theta} &= \frac{\bar{p}_{i+1,j} - \bar{p}_{i-1,j}}{2\Delta \theta}, & \frac{\partial \bar{h}}{\partial \theta} &= \frac{\bar{h}_{i+1,j} - \bar{h}_{i-1,j}}{2\Delta \theta} \\ \frac{\partial \bar{p}}{\partial \bar{z}} &= \frac{\bar{p}_{i,j+1} - \bar{p}_{i,j-1}}{2\Delta \bar{z}} \text{ and } \frac{\partial \bar{h}}{\partial \bar{z}} &= \frac{\bar{h}_{i,j+1} - \bar{h}_{i,j-1}}{2\Delta \bar{z}} \end{aligned} \right\} \quad (3.15)$$

The terms $\frac{\partial^2 \bar{p}}{\partial \theta^2}$ and $\frac{\partial^2 \bar{p}}{\partial \bar{z}^2}$ of Eq. (3.7) can be rearranged as shown in Eq. (3.16), so that the LHS of the equation contains $\bar{p}_{i,j}$ terms.

$$\begin{aligned} \frac{\partial^2 \bar{p}}{\partial \theta^2} + \left(\frac{2R}{L} \right)^2 \frac{\partial^2 \bar{p}}{\partial \bar{z}^2} = \\ - \frac{3}{\bar{h}} \left[\frac{\partial \bar{p}}{\partial \theta} \frac{\partial \bar{h}}{\partial \theta} \right] - \frac{1}{\bar{p}} \left[\left(\frac{\partial \bar{p}}{\partial \theta} \right)^2 + \left(\frac{2R}{L} \right)^2 \left(\frac{\partial \bar{p}}{\partial \bar{z}} \right)^2 \right] + \frac{\Lambda}{\bar{h}^3} \frac{\partial \bar{h}}{\partial \theta} + \frac{\Lambda}{\bar{p} \bar{h}^2} \frac{\partial \bar{p}}{\partial \theta} \end{aligned} \quad (3.16)$$

Substituting the partial derivatives terms from Eq. (3.15) into Eq. (3.16), The Reynolds equation in finite difference form will be:

$$\begin{aligned} \text{L.H.S.} &= \frac{\bar{p}_{i+1,j} - 2\bar{p}_{i,j} + \bar{p}_{i-1,j}}{\Delta \theta^2} + \left(\frac{2R}{L} \right)^2 \left[\frac{\bar{p}_{i,j+1} - 2\bar{p}_{i,j} + \bar{p}_{i,j-1}}{\Delta \bar{z}^2} \right] \\ \text{R.H.S.} &= - \frac{1}{\bar{p}_{i,j}} \left[\left(\frac{\bar{p}_{i+1,j} - \bar{p}_{i-1,j}}{2\Delta \theta} \right)^2 + \left(\frac{2R}{L} \right)^2 \left(\frac{\bar{p}_{i,j+1} - \bar{p}_{i,j-1}}{2\Delta \bar{z}} \right)^2 \right] - \frac{3}{\bar{h}_{i,j}} \left[\frac{\bar{h}_{i+1,j} - \bar{h}_{i-1,j}}{2\Delta \theta} \frac{\bar{p}_{i+1,j} - \bar{p}_{i-1,j}}{2\Delta \theta} \right] \\ &+ \frac{\Lambda}{\bar{h}_{i,j}^3} \frac{\bar{h}_{i+1,j} - \bar{h}_{i-1,j}}{2\Delta \theta} + \frac{\Lambda}{\bar{p}_{i,j} \bar{h}_{i,j}^2} \frac{\bar{p}_{i+1,j} - \bar{p}_{i-1,j}}{2\Delta \theta} \end{aligned}$$

Above equation can be written in quadratic form as:

$$A \bar{p}_{i,j}^2 + B \bar{p}_{i,j} + C = 0 \quad (3.17)$$

where,

$$A = \left[\frac{2}{(\Delta \theta)^2} + \left(\frac{2R}{L} \right)^2 \frac{2}{\Delta \bar{z}^2} \right]$$

$$\mathbf{B} = \left[\begin{array}{l} -\frac{\bar{p}_{i+1,j} + \bar{p}_{i-1,j}}{\Delta\theta^2} - \left(\frac{2R}{L}\right)^2 \left(\frac{\bar{p}_{i,j+1} + \bar{p}_{i,j-1}}{\Delta\bar{z}^2}\right) - \left(\frac{3}{\bar{h}_{i,j}}\right) \left(\frac{\bar{h}_{i+1,j} - \bar{h}_{i-1,j}}{2\Delta\theta}\right) \left(\frac{\bar{p}_{i+1,j} - \bar{p}_{i-1,j}}{2\Delta\theta}\right) \\ + \left(\frac{\Lambda}{\bar{h}_{i,j}^3}\right) \left(\frac{\bar{h}_{i+1,j} - \bar{h}_{i-1,j}}{2\Delta\theta}\right) \end{array} \right]$$

$$\mathbf{C} = -\left[\left(\frac{\bar{p}_{i+1,j} - \bar{p}_{i-1,j}}{2\Delta\theta}\right)^2 + \left(\frac{2R}{L}\right)^2 \left(\frac{\bar{p}_{i,j+1} - \bar{p}_{i,j-1}}{2\Delta\bar{z}}\right)^2 \right] + \left(\frac{\Lambda}{\bar{h}_{i,j}^2}\right) \left(\frac{\bar{p}_{i+1,j} - \bar{p}_{i-1,j}}{2\Delta\theta}\right)$$

and $\bar{h}_{i,j} = 1 + \varepsilon \cos \theta_{i,j} + \alpha(\bar{p}_{i,j} - 1)$

The solution begins by evaluating normalized pressure ($\bar{p}_{i,j}$) of Eq. (3.17) with an initial guess of ($\bar{p}_{i,j}$) and ($\bar{h}_{i,j}$) as unity. This is done iteratively until a convergence of the pressure is achieved. The numerical integration for calculating load carrying capacity and frictional torque is done using the Simpson's 1/3rd rule.

3.4.2 Convergence criteria

FDM has been used to solve the discretized Reynold's equation (Eq. 3.15) to find out pressure distribution over bearing surface. After pressure distribution over the bearings surface is determined, the non-dimensional top foil deflection is calculated. By substituting the new value of non-dimensional top foil deflection in the equation of film thickness, the resultant quadratic equation is solved for all the mesh points to estimate the pressure at all these points. This quadratic equation would not be satisfied for the pressures which are assumed to be constant in the beginning. Convergence is achieved when the relative error between two successive iterations fall below a specified value. Hence, Eq. (3.18) shows convergence criterion.

$$\frac{|\sum(\bar{p}^{k-1}) - \sum(\bar{p}^k)|}{|\sum(\bar{p}^k)|} \leq 10^{-6} \quad (3.18)$$

3.4.3 Flow chart and grid refinement study

A computer program using MATLAB is written to determine all essential bearing performance parameters. The algorithm for the computer program is given in Fig. 3.7 and validated with the open literature results. An elaborate grid refinement study is carried for the appropriate grid size to save computational time and to converge without much variation in overall results. For grid refinement study fixed value of length to diameter, compressibility number, and structural rigidity are considered as a unity. Based on the results shown in Fig. 3.8, the load carrying capacity has very small changes after grid size

of 80 X 80 along the circumferential and axial direction. Grid sizes higher than this would increase computational time without much variation in the overall results.

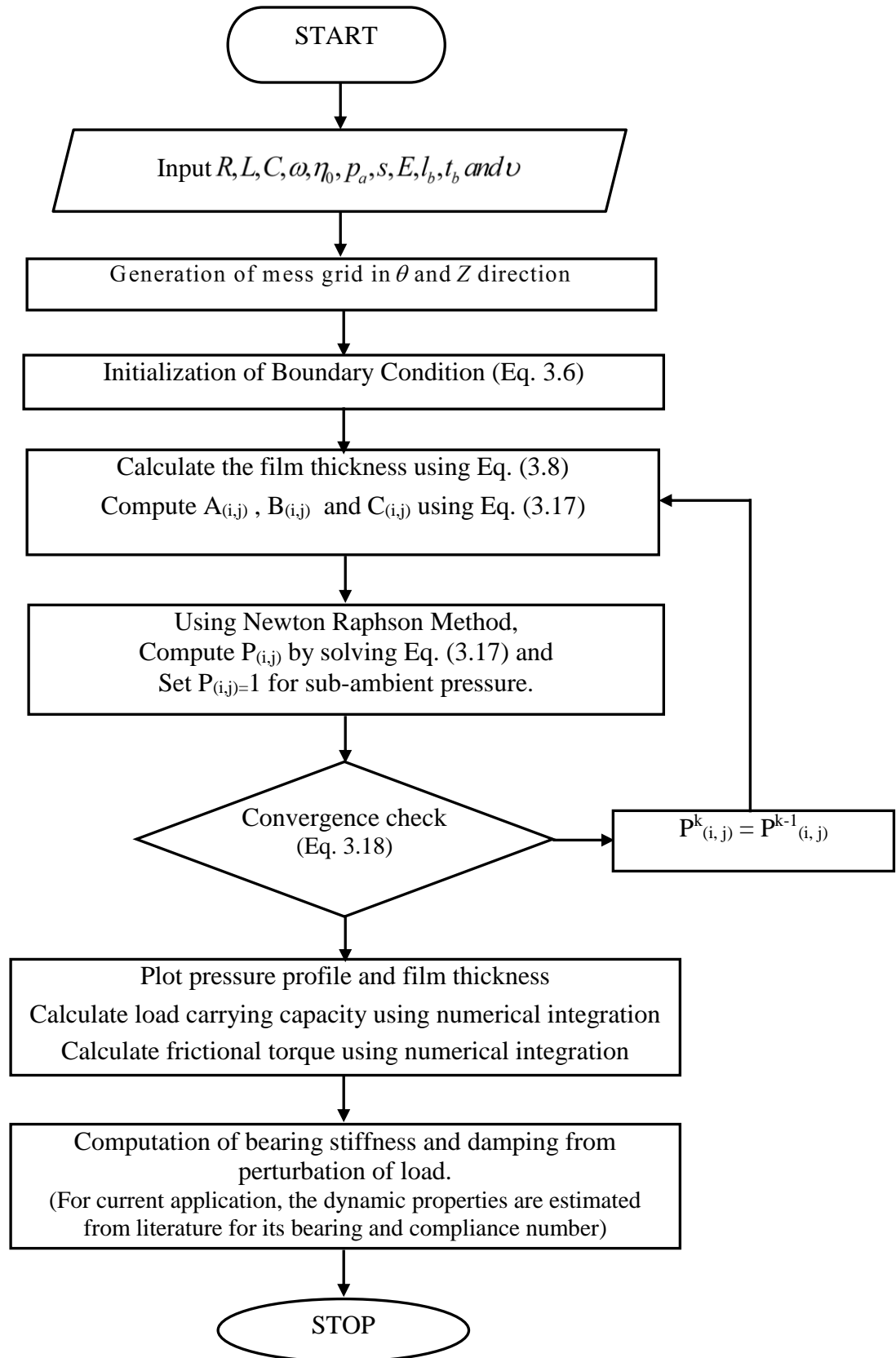


Figure 3.7: Flow chart for computation of journal bearing performance.

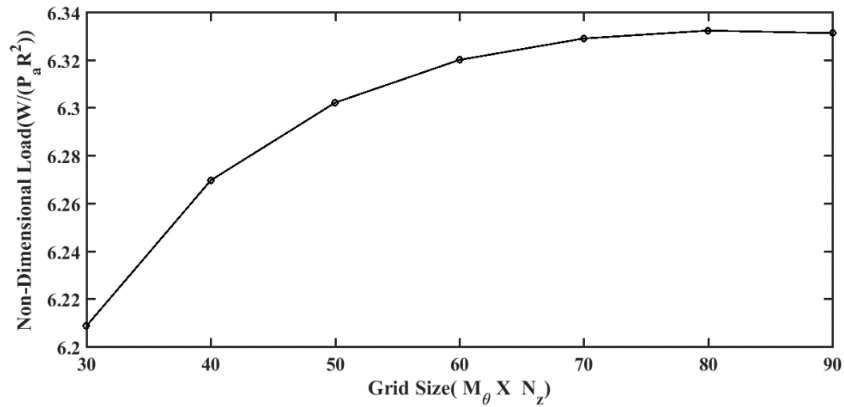


Figure 3.8: Variation of load carrying capacity with grid size.

3.4.4 Validation of computational program

The validity of the computational program is assessed by comparison of predictions with two published data available in the open literature with current analysis[13, 19]. The length to diameter, compliance number, and compressibility number are kept unity during the comparison. As shown in Fig. 3.9, it has been observed that the present results are in fairly good agreement with those from the references.

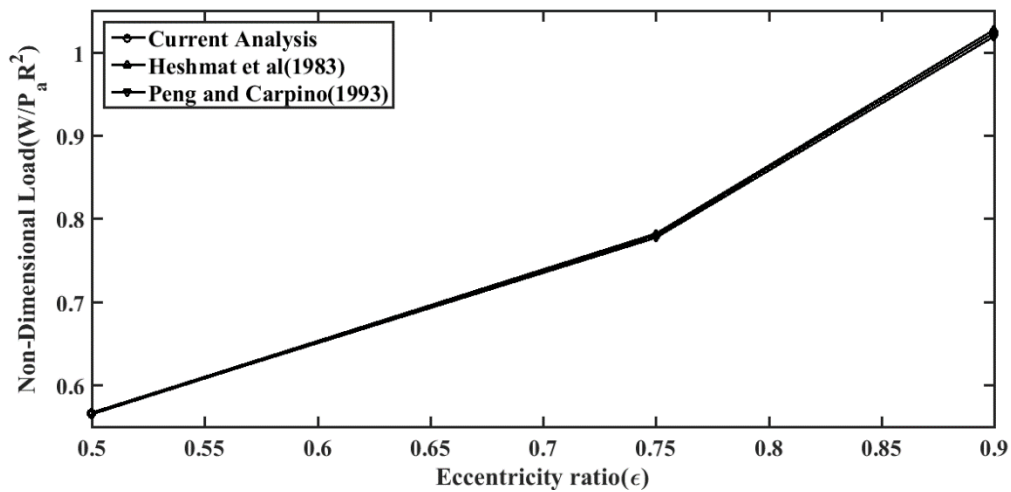


Figure 3.9: Validation of load carrying capacity with open literature.

3.4.5 Feasibility of GFB for current application from literature data

The bump structure for initial study was taken from literature to find feasibility of bump foil bearings for the current application. The bearings data and lubricant properties are given in Table 3.1. Static property analysis decides the feasibility foil bearing, and they are pressure profile, film thickness and load carrying capacity. This study is further extended in section 3.5 to optimize the bearing structure and bump geometry based on

load carrying capacity, availability of materials and difficulties on the forming of bump foil.

A three-dimensional bearing pressure distribution, gas film thickness, and load carrying capacity for the GFB is shown in Figs. 3.10, 3.11 and 3.12 respectively. The input data for the program is given in Table 3.1. From static analysis, the pressure reaches its maximum value just before the minimum clearance occurs, about 154° past the leading edge. The foil loses contact with the elastic foundation about 185° past the inlet. The calculated load from load curve (Fig. 3.13) for eccentricity ratio of 0.75 is 42.88 N, which is higher than to the possible unbalance radial load of 20 N for balanced rotor. The detail of balanced rotor is described in Chapter 6. (Unbalance mass of less than 10 mg at a distance of 7.5 mm, and rotating at 140,000 rpm). The radial unbalance force being low for current application, there is flexibility to select different bump foil materials and bump dimension for easy and cost effective bump formation.

Table 3.1: Compliant foil journal bearing data to study the feasibility of GFB.

	Bearing parameters	Dimensions
Fixed Data based on current application	Diameter of Shaft (R)	16 mm
	Bearing Length (L)	16 mm
	Rotational Speed (N)	140,000 rpm
	Viscosity (μ)	$178.4 \cdot 10^{-7}$ N.s/m ²
	Density (ρ_0)	1.1614 kg/m ³
Assumed Data from Literature[55]	Nominal Radial Clearance (C)	25 μ m
	Top Foil Thickness (t_t)	0.1 mm
	Bump Foil Thickness (t_b)	0.05 mm
	Bump Pitch (s)	3.17 mm
	Bump Length ($2l_b$)	2.36 mm
	Eccentricity ratio(ϵ)	0.95
	Bump Foil Young's Modulus (E)	214 GPa(Inconel X-750)
	Bump Foil Poisson's Ratio (ν)	0.29

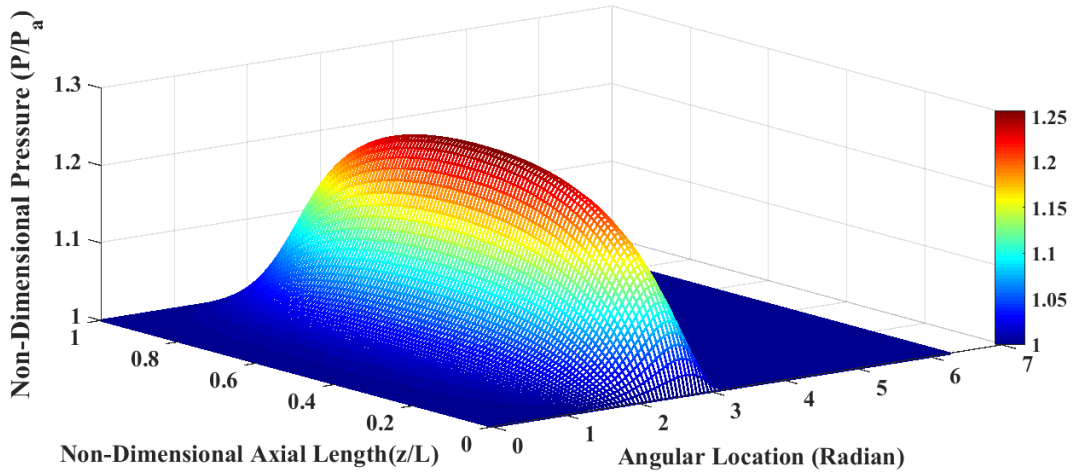


Figure 3.10: Non-Dimensional pressure profile of gas foil journal bearing.

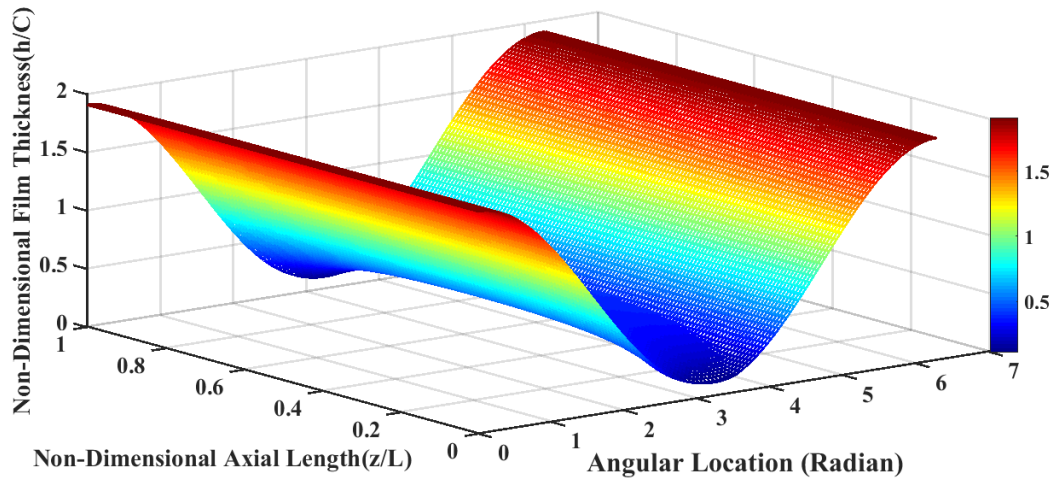


Figure 3.11: Non-Dimensional gas film thickness of journal foil bearing.

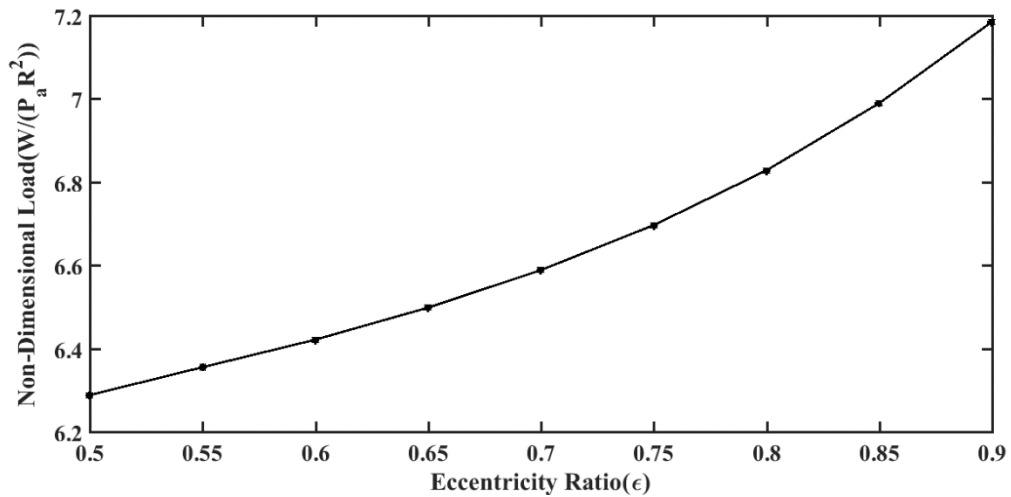


Figure 3.12: Non-Dimensional load carrying capacity of journal foil bearing.

3.5 Results and discussion

The radial load for vertically operated turboexpander is because of an unbalanced load. The unbalanced load is in the order of 20 N for a rotor with magnitude of unbalance less than 100 mg-mm rotating at a speed of 140,000 rpm [2]. The load carrying capacity of the journal bearing needs to be designed above 20 N to avoid any unknown forces during the operation, so a factor 2 is added to the journal bearing making its capacity as 40 N.

In order to find the suitable bump foil material and its dimension, the analysis is extended to study effect of bump parameters on load carrying capacity of the bearing. The bump material, foil thickness, bump pitch and bump length are selected based on higher load carrying capacity, availability of material, literature data and ease of forming bumps as discussed in the section 3.5.1 to 3.5.3.

3.5.1 Effect of bump foil materials on the static performances

Fig. 3.13 shows the load carrying capacity for a different material for various eccentricity ratios. The four different materials chosen are phosphor bronze, beryllium copper, SS 302 and Inconel X-750 based on their use as a bump material in past from open literature.

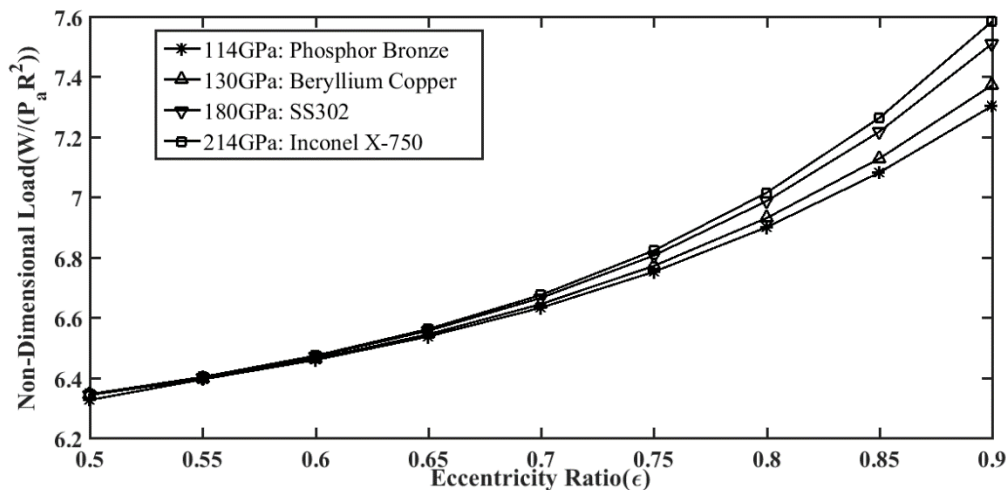


Figure 3.13: Effect of bump foil materials on the load carrying capacity.

The load carrying capacity shows similar behavior for all above four materials up to eccentricity ratio 0.7. So all chosen material is found suitable for the journal foil bearings foils, but phosphor bronze is chosen for current application for following reasons:

- a. SS 302 is not preferable because of its poor friction properties.

- b. Work with Inconel X-750 has been avoided because thin foils are not available in local market. The available foil thickness is 0.25 mm and forming of bumps with thick Inconel X-750 is difficult.
- c. The cost of Beryllium copper foil and Inconel X-750 is found to be very costly compared to Phosphor bronze.
- d. Phosphor bronze is preferred because it has better friction properties, self-lubricating properties and quite suitable for the low-temperature application.

3.5.2 Effect of bump foil thickness on the static performances

The thickness of bump foil is an important parameter for foil structure as it plays a vital role in structural rigidity, load carrying capacity and forming of bumps with equal dimension. To study the effect of bump foil thickness, the bump foil is selected as Phosphor bronze and other parameters are same as described in Table 3.1. Fig. 3.14 shows thin foil of thickness 0.05 has significantly low load carrying capacity and foils of thickness 0.1, 0.15 and 0.2 mm show increase in load carrying capacity with an increase of eccentricity ratio. Thick foils have better load carrying capacity, but they are difficult to form the bumps due to larger spring back and possibility of uneven bumps formation. So 0.1 mm thickness is selected for further analysis.

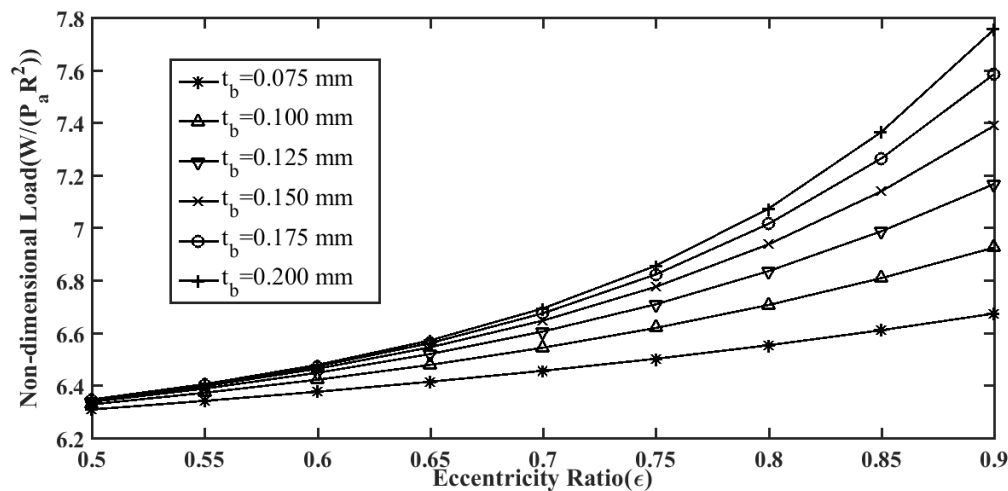


Figure 3.14: Effect of bump foil thickness on the load carrying capacity.

3.5.3 Effect of bump length and pitch on the static performances

The thickness of bump foil along with bump length and pitch completes the foil structure. So an analysis was done to find the effect of bump length and pitch on load carrying capacity. Fig. 3.15 shows the effect of half bump length on load carrying capacity. Smaller bump half-length gives better load carrying capacity, but the fabrication of bumps will be

difficult as dimensions of the groove on dies and punch will be smaller than 1.3 mm. So half-length of 1.32 mm is chosen for ease of fabrication of bump foil. The pitch should be greater than the length of the bump (i.e. 2.64 mm).

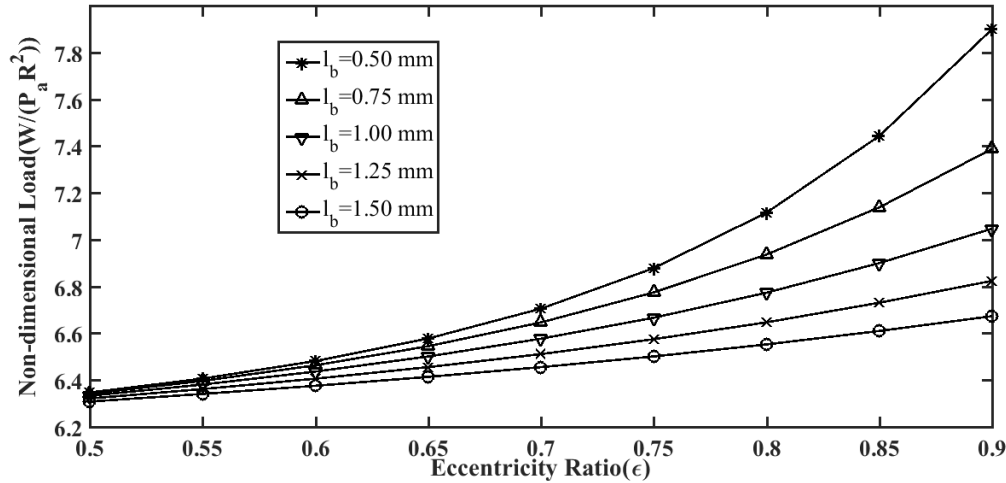


Figure 3.15: Effect of bump half-length on the load carrying capacity.

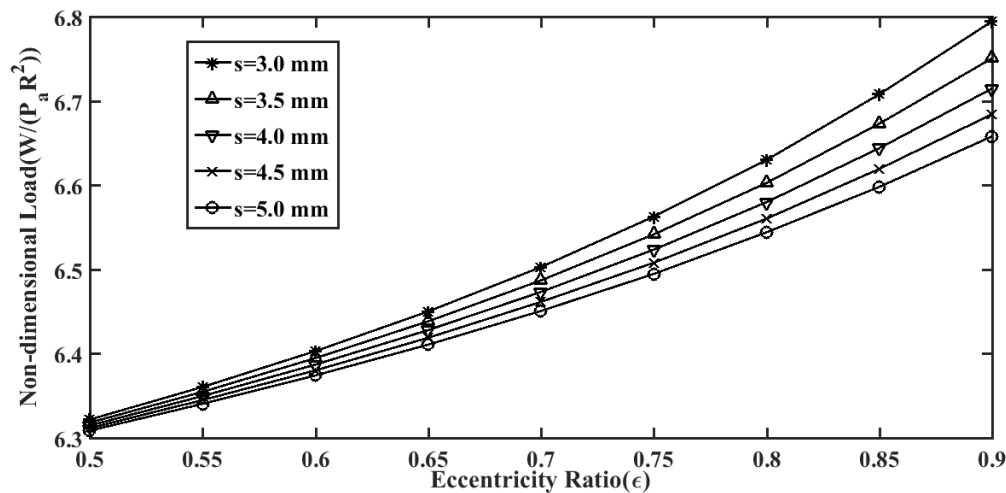


Figure 3.16: Effect of bump foil pitch on the load carrying capacity.

Figure 3.16 shows pitch of 3 mm gives better performance. However, there is a need of larger pitch during fabrication of a die and punch as fillets need to be provided on the sharp edges of the die to avoid damage of bumps during the forming operation. So the pitch is decided to be 4.2 mm based on a 3D model of the die.

3.5.4 Analysis with final dimensions of bump foil

The dimensions of the bump structure are finalized based on the static performance curve from Figs. 3.13 to 3.16. The final bearings parameters are shown in Table 3.2. The GFB

with these data are suitable to generate necessary pressure profile, film thickness, load carrying capacity, minimum frictional torque and stiffness.

Table 3.2: Compliant foil journal bearing data with modified bump structure.

Journal bearing parameters	Dimensions
Diameter of Shaft ($2R$)	16 mm
Bearing Length (L)	16 mm
Rotational Speed (N)	140,000 rpm
Nominal Radial Clearance (C)	25 μm
Eccentricity ratio(ϵ)	0.8
Top Foil Thickness (t_t)	0.1 mm
Bump Foil Thickness (t_b)	0.1 mm
Bump Pitch (s)	4.2 mm
Bump Length ($2l_b$)	2.64 mm
Bump Foil Young's Modulus (E)	114 GPa
Bump Foil Poisson's Ratio (ν)	0.35
Grid Size	80 \times 80
Viscosity	178.4×10^{-7} N.s/m ²

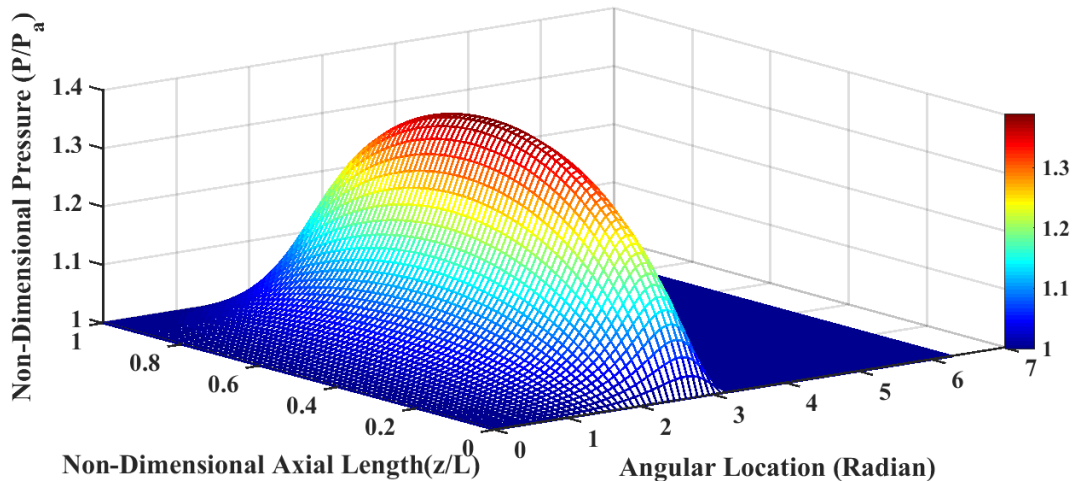


Figure 3.17: Pressure profile with designed data.

The pressure profile and film thickness over the bearing surface are shown in Figs. 3.17 and 3.18 respectively after selecting modified bump structures. The load capacity and frictional torque are found by numerical integration by the formulae listed earlier. Figs. 3.19 and 3.20 portrays load carrying capacity and frictional torque for various eccentricity ratios. The eccentricity ratio above 0.72 shows load carrying capacity above 40 N so that the GFB will work for eccentricity above 18 μm for radial clearance of 25 μm . The load carrying capacity can be improved with lesser radial clearance, but it increases the cost of the bearing. In the current application, a radial clearance of 25 μm is chosen in accordance

with available infrastructure to facilitate the fabrication of the journal bearing base. The production drawings of the bearing base with shims are document in Appendix (TEX-03).

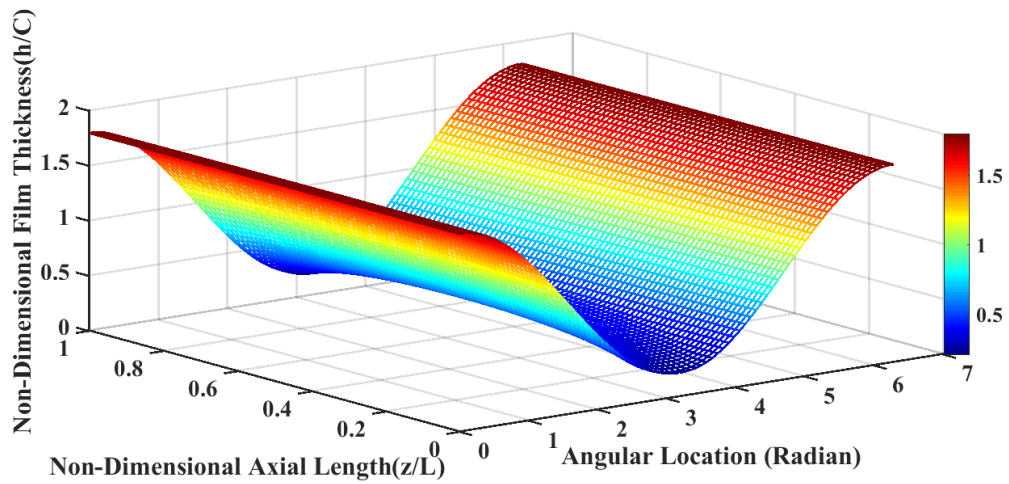


Figure 3.18: Film thickness with designed data.

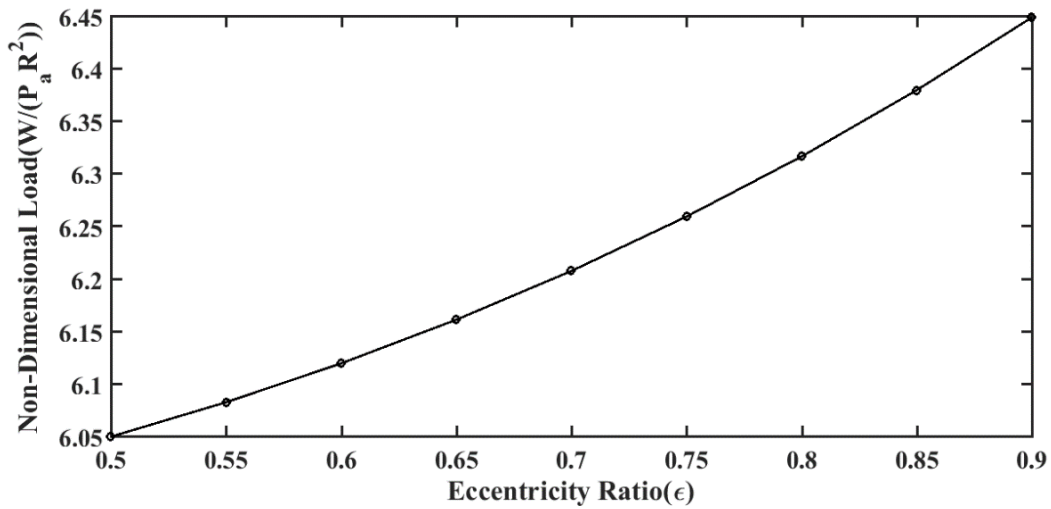


Figure 3.19: Load carrying capacity with designed data.

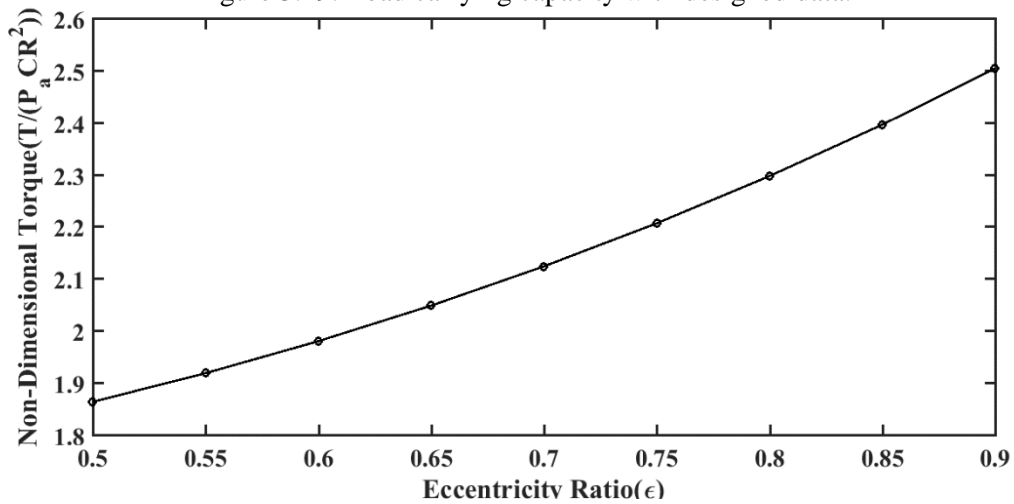


Figure 3.20: Frictional torque with designed data.

3.6 Detail design procedure for gas foil journal bearing

The detailed step by step design procedure for gas foil (bump type) journal bearings based on the relations developed in the earlier section are given below:

Step 1: Input to the bearing designer

- a. The bearing gas, which is mostly the process gas to the turboexpander.
- b. The ambient temperature, pressure and the altitude of operation.
- c. Designed rotational speed of the rotor.
- d. Mean radial clearance of the journal bearings.

Step 2: Solving the static compressible aerodynamic Reynolds equation to find bearing performance parameter based on the radial load.

- a. Materials for the bump foil.
- b. Bump dimensions such as thickness, pitch, length and height of the bump.
- c. Determination of load carrying capacity and starting torque.

Step 3: Perturbation of the load or application of a small displacement of the rotor to the steady state operating condition gives dynamic coefficient such as stiffness and damping coefficients. To save the time of simulation, above two dynamic characteristics can be estimated from results of open literature for the corresponding bearings and compliance number.

Step 4: Determination of the critical speed and unbalanced response using the stiffness, based on formulation described in Chapter 6. The bump material and dimension in step 2 need to be modified if the bending critical speed is found close to the rotational speed.

Step 5: Design of the foils attachment mechanism to the bearing base.

Step 6: Production and assembled drawings of gas foil bearings.

Chapter 4

Bump Type Gas Foil Thrust Bearing

Thrust load in the turbomachines is generated by the pressure differential acting upon the compressor wheel (CW), turbine wheel (TW) and the impulsive force generated due to the axial flow on these wheels. This thrust or axial load is supported by thrust or axial bearing. The gas bearing is preferable for a turboexpander to make it oil-free to avoid contamination with the process gas. The gas bearings used in the high-speed turbomachines can be of rigid or compliant type. Compliant type gas bearings e.g. Gas Foil Bearings (GFB) have many attractive advantages compared to the rigid bearings such as higher load carrying capacity, compensation for misalignment, accommodation of thermal distortion and larger clearance. Gas foil thrust bearings (GFTBs) are designed to take the axial load of the rotor, and they consist of a bearing base, engineered spring structure foil, a smooth top foil and an attachment mechanism between foils and bearing base (Fig. 4.1). Different investigators work on different types of engineered spring structure, and they are tape type, leaf type, bump type and mesh type. The bump type is most popular for its easy fabrication and assembly methodology compared to other types.

A pair of the thrust bearing is preferred in place of single one to accommodate the possibility of accidental thrust reversal. A double thrust bearing has two thrust plates on each side of a shaft collar. Most commonly used rotor bearings configuration schematics is shown in Fig. 4.2. This chapter focuses on the steps to calculate the axial load generated in a vertical cryogenic turboexpander, load carrying capacity of a bump type gas foil thrust bearing and its detail design methodology.

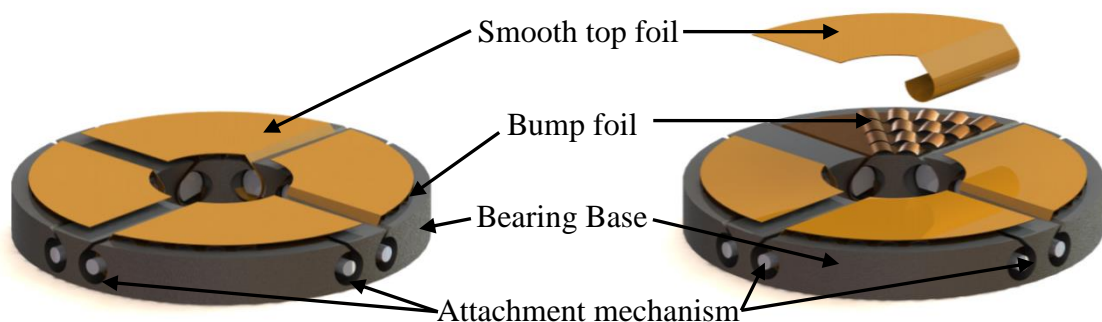


Figure 4.1: Schematic of bump type gas foil thrust bearing.

These bearings are aerodynamic or self-acting bearings. So at start and stop of the rotor, the bearings are subjected to a high rate of wear due to direct contact between

bearing surface and runner. Engineers prefer to use either a coating of solid lubricant on bearing surface or passive magnet to prevent high wear rate. This chapter also discusses the design steps of annular passive magnet to balance the static axial load or dead weight of the vertical rotor.

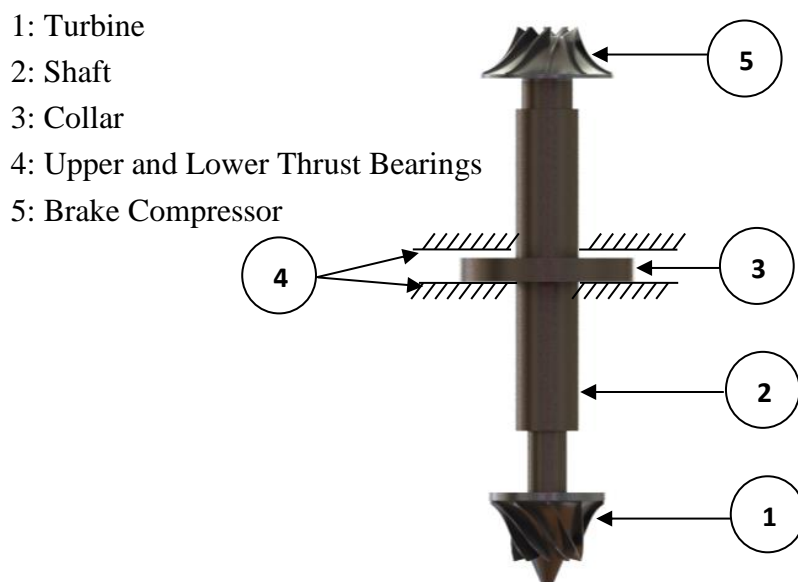


Figure 4.2: Schematic diagram of thrust bearing and the shaft collar.

4.1 Thrust load calculation

The design of thrust bearings starts with determination of thrust load generated by the rotor of the turbomachines. The thrust load is because of following reasons [82]:

- i. Pressure differential at the CW.
- ii. Pressure differential at the TW.
- iii. The impulsive force generated due to the gas flow in the axial direction in both the wheels.
- iv. The weight of the vertically oriented rotor.

There are two ways to calculate the thrust load on the rotor, either using the CFD (Computational Fluid Dynamics) or solving analytical equations based on the Newton's second law. The CFD method gives the precise result but needs huge computational effort at all stages of computation, while using the Newton's second law is quite simple with basic knowledge of thermodynamics and turbomachinery principle. The difference between both the methods is lower than the safety tolerance of the thrust load taken in the

bearing design [82]. Therefore, in the current analysis, Newton's second law is applied to the control volume for the thrust load calculation on the rotor.

Four different forces are acting on both the wheels are shown in Fig. 4.3:

- Pressure force acting on the tip surface (F_1).
- Pressure force at the shroud surface (F_2).
- Impulsive force (F_3).
- Pressure force at the back faces (F_4).

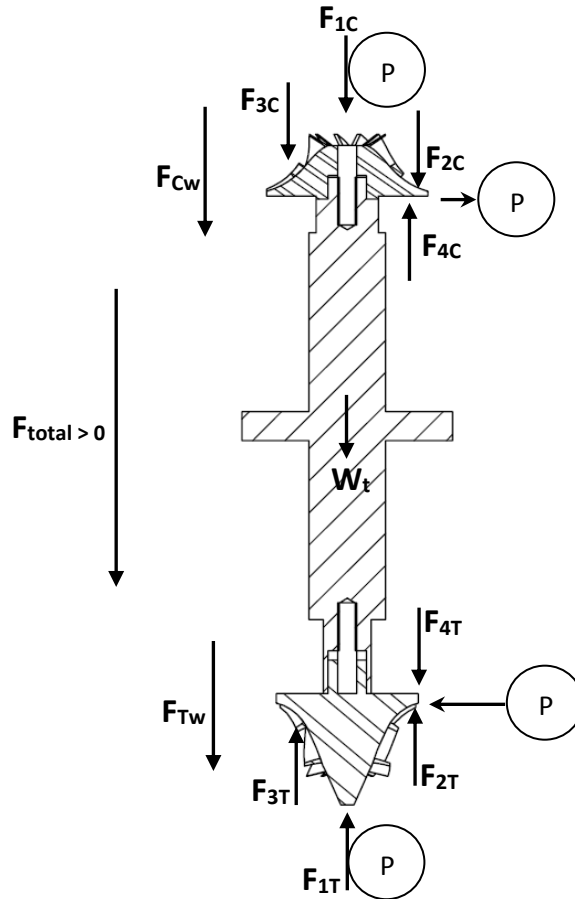


Figure 4.3: Axial forces on the vertical rotor.

Table 4.1: Wheel data for thrust load calculation at 140,000 rpm of rotor [1].

Compressor Wheel		Turbine Wheel	
Inlet mean diameter (D_{IC})	12.00 mm	Inlet diameter (D_{IT})	29.60 mm
Outlet diameter (D_{OC})	33.70 mm	Outlet diameter (D_{OT})	13.32 mm
Shaft Diameter (D_{SC})	16.00 mm	Shaft Diameter (D_{ST})	16.00 mm
Inlet pressure (P_{IC})	3.868 bar	Inlet pressure (P_{IT})	4.319 bar
Outlet pressure (P_{OC})	4.451 bar	Outlet pressure (P_{OT})	1.020 bar
Density of the gas at inlet (ρ_{IC})	4.4235 kg/m ³	Density of gas at the inlet (ρ_{IT})	15.0194 kg/m ³
Mass flow rate (\dot{m}_C)	0.05179 kg/s	Mass flow rate (\dot{m}_T)	0.07646 kg/s
Weight of the rotor (W_t)	2.33 N		

Data necessary to calculate above axial forces in both the wheels are the dimensions of the wheels and thermodynamic states at inlet and outlet of the wheels (Table 4.1). The dimension of wheels and the thermodynamic states are taken from Ph.D. thesis of Balaji [1], which was developed as part of continuous development program of turboexpander at NIT Rourkela. The F_{total} is the resultant of total forces acting on the compressor wheel (F_{CW}), turbine wheel (F_{TW}) and the weight of the rotor (W_t) as indicated in Fig. 4.3.

4.1.1 Axial force at the compressor wheel

The four different axial forces acting on the brake compressor side can be calculated using Eqs. (4.1) to (4.4)[82] and the resulting forces acting on the CW is the algebraic sum of all four forces (Eq. 4.5).

Pressure force acting on the inlet surface,

$$F_{1C} = A_{1C} p_{1C} = \frac{\pi D_{1C}^2}{4} p_{1C} \quad (4.1)$$

Pressure force at the shroud surface,

$$F_{2C} = A_{s,C} p_{M,C} = A_{s,C} \left(\frac{p_{1C} + p_{0C}}{2} \right) \quad (4.2)$$

Where projected shroud area of compressor, $A_{s,C} = \frac{\pi (D_{1C}^2 - D_{0C}^2)}{4}$

The pressure $p_{M,C}$ for current application is considered as mean between inlet and outlet as it is very difficult and time intensive to determine them by means of measurements due to very narrow geometries of the gaps between the wheels and their housings.

Impulsive force acting on the CW based on momentum theorem,

$$F_{3C} = \dot{m}_c \left(\frac{\dot{m}_c}{\rho_{1C} A_{1C}} \right) \quad (4.3)$$

Pressure force at the back face of CW,

$$F_{4,C} = A_{0C} p_{0C} = \frac{\pi}{4} (D_{0C}^2 - D_{sC}^2) p_{0C} \quad (4.4)$$

The pressure p_{0C} is nearly unchanged, when the gap between the bearing housing and the back face of the CW/TW is as large as about 1 mm[82]. For current application, the housing is designed with 3 mm gap for seating of locknut.

The resulting force acting on the CW can be calculated as

$$F_{\text{CW}} = F_{1C} + F_{2C} + F_{3C} - F_{4C} \quad (4.5)$$

4.1.2 Axial force at the turbine wheel

Similar to axial force calculation on the CW, four different axial forces can be calculated on TW using formulas mentioned in Eqs. (4.6) to (4.9). The algebraic sum of all four different forces acting on TW is given in Eq. (4.10).

Pressure force acting on the outlet surface,

$$F_{1T} = A_{OT} P_{OT} = \frac{\pi D_{OT}^2}{4} P_{OT} \quad (4.6)$$

Pressure force at the shroud surface,

$$F_{2T} = A_{ST} P_{MT} = A_{ST} \left(\frac{P_{IT} + P_{OT}}{2} \right) \quad (4.7)$$

$$\text{Where } A_{ST} = \frac{\pi (D_{OT}^2 - D_{IT}^2)}{4}$$

Impulsive force acting on the TW based on momentum theorem,

$$F_{3T} = \dot{m}_T C_{MT} = \dot{m}_T \left(\frac{\dot{m}_T}{\rho_{IT} A_I} \right) \quad (4.8)$$

Pressure force at the back face of TW,

$$F_{4T} = A_{IT} P_{IT} = \frac{\pi}{4} (D_{IT}^2 - D_{ST}^2) P_{IT} \quad (4.9)$$

The resulting force acting on the TW can be calculated as

$$F_{TW} = -F_{1T} - F_{2T} - F_{3T} + F_{4T} \quad (4.10)$$

The resultant forces acting on the rotor is calculated by summing forces acting on CW, TW and weight of the rotor (W_t).

$$F_{Total} = F_{CW} + F_{TW} + W_t \quad (4.11)$$

Table 4.2: Thrust load calculation at 140,000 rpm of the rotor.

Compressor Wheel		Turbine Wheel	
Pressure force at the inlet (F_{1C})	43.75 N	Pressure force at the outlet (F_{1T})	14.21 N
Pressure force over the shroud (F_{2C})	265.66 N	Pressure force over the shroud (F_{2T})	118.66 N
Impulse force (F_{3C})	5.96 N	Impulse force (F_{3T})	0.63 N
Pressure force at the outlet (F_{4C})	307.52 N	Pressure force at the inlet (F_{4T})	210.37 N
Total thrust load at compressor side (F_{CW})	7.85 N	Total thrust load at turbine side (F_{TW})	75.87 N

Axial forces are calculated at the designed rotational speed and mass flow rates to study the thrust load of the rotor. Table 4.2 shows the axial load details on the rotor. The resultant thrust load in the designed rotor is nearly 86 N (in the direction of the turbine) rotating at 140,000 rpm with mass of the rotor being 237.49×10^{-3} kg. This information is essential to design the thrust bearing of desired load carrying capacity of lower thrust bearing. In order to avoid any possible load reversal, in current application upper thrust bearing is also designed. The design of thrust bearing is explained in subsequent sub chapters.

4.2 Working principle and bearings geometry of GFTB

The GFTB is an aerodynamic or self-acting bearing and operates on the principle of aerodynamics. During rotation of the rotor, the rotating member (shaft collar) drags the viscous fluid into the converging wedge. The converging wedge is formed in each sector between leading edge smooth top and the shaft collar by the ramp height (Fig. 4.5). As the shaft collar picks up the speed, a converging gas film is generated between the shaft collar and the top foils, which is responsible for pressure generation over the bearing surface. The compliant bump foil beneath the smooth foil provides stiffness to the thrust bearings. The stiffness of the gas foil thrust bearings is tailored by appropriate bump dimensions and their distribution in each sector.

The parameters, which influence the bearing performance, are shown in Figs. 4.4 and 4.5. The nomenclatures for all the bearing parameters are described below:

R_1 : Inner radius of sector,	s : Bump pitch,
R_2 : Outer radius of sector,	l_b : Half bump length,
β : Angular extent of a bearing pad,	t_b : Thickness of bump foil,
b : Extent of the ramp as a function of β ,	E : Young's modulus,
$P_{(r, \theta)}$: Pressure at coordinate (r, θ) ,	ν : Poisson ratio,
P_a : Ambient pressure,	μ : Absolute viscosity,
h : Film thickness,	t_b : Thickness of Foil,
h_1 : Inlet film thickness,	r : Radial coordinates,
h_2 : Minimum film thickness.	

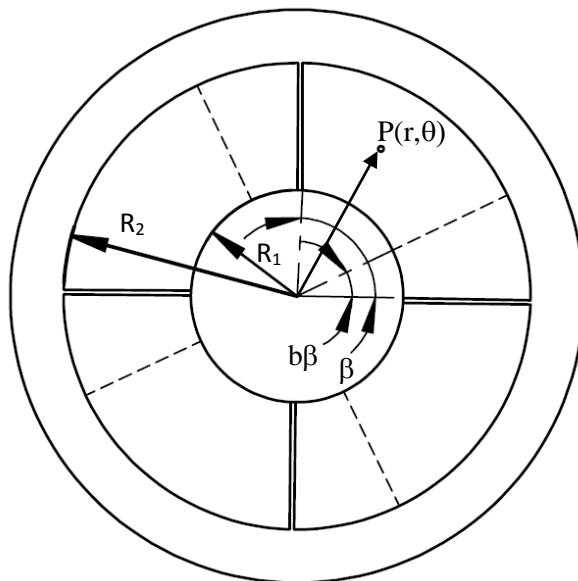


Figure 4.4: Bump and top foil configuration of thrust bearing.

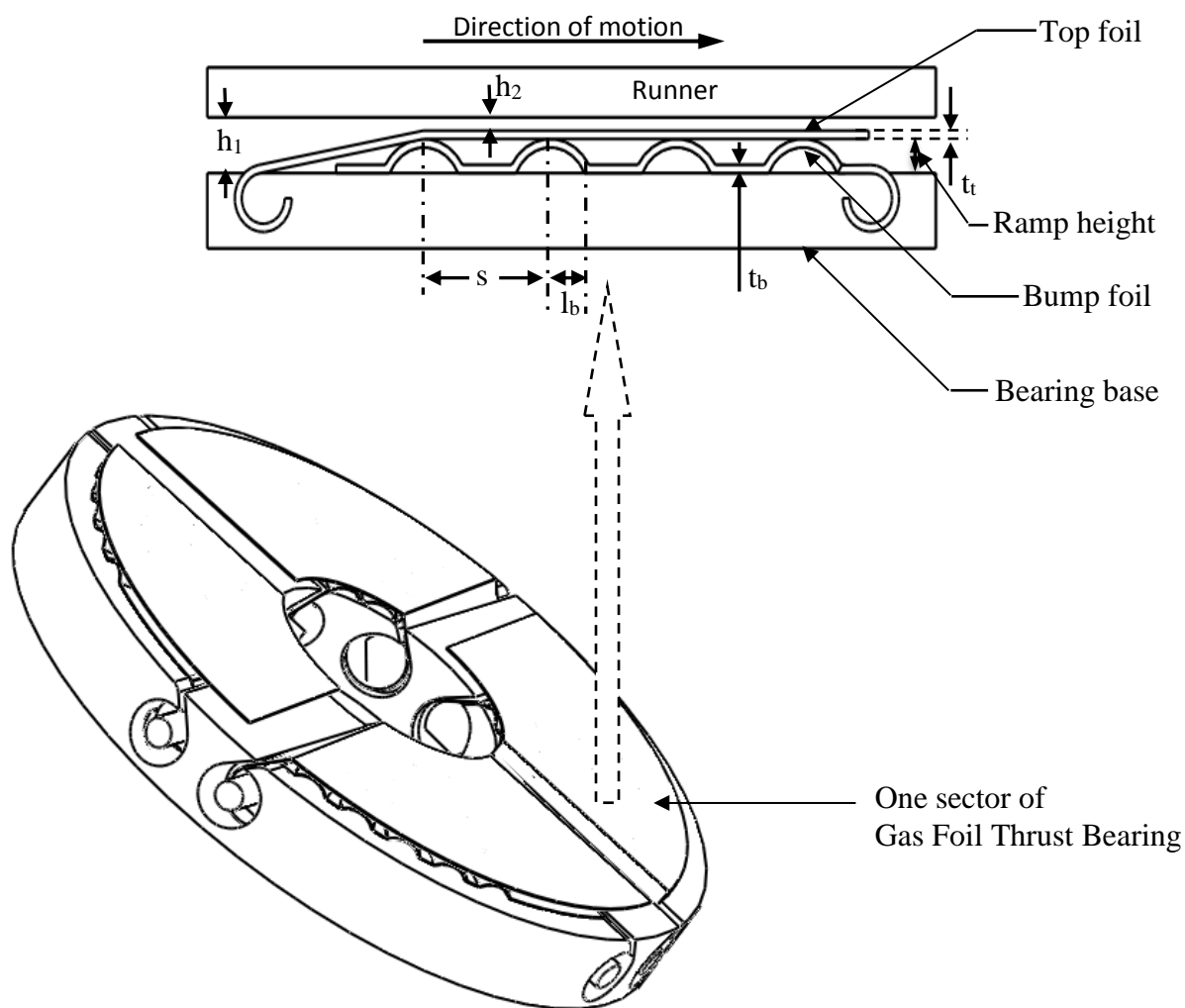


Figure 4.5: Gas foil thrust bearings parameters.

4.3 Performance analysis of gas foil thrust bearing

The performance analysis of GFTB is the next step of the design after determination of thrust load on rotor. The gas foil bearings performance depends on various bearing parameters such as the configuration of bearings, dimension of shaft collar, and dimension of bumps, rotational speed and properties of bearing gas. Many calculation methods are proposed to solve the nonlinear compressible Reynold's equation that governs the pressure distribution on the bearing surface and most of the methods to determine the pressure distribution are complex and need iterative solution[14]. The elasto-hydrodynamic analysis for thrust type foil bearings using Finite Difference Method (FDM) is found to be quite accurate and less complex[14], so the analysis for the current project is done using a similar approach to determine load carrying capacity of the gas foil thrust bearings.

4.3.1 The governing equations

The popular and easy method to analyze gas foil thrust bearings is by solving aerodynamic and structural equation simultaneously. The Reynold's equation for gas foil thrust bearing is also called elasto-hydrodynamic equation, which has been derived based on assumptions given below [14]:

- a. The fluid in the film is isothermal and behaves as a perfect gas.
- b. The stiffness of the bump foil is taken to be uniformly distributed and constant throughout the bearing surface.
- c. The stiffness is constant and is thus independent of the amount of bump deflection.
- d. The top foil is assumed not to deflect about the bumps, but rather to follow the deflection of the bumps themselves.
- e. The deflection of the foils, in their response to the acting forces, is dependent on the local effect only.

The nomenclature for the thrust foil bearings sector and bump foil configuration is shown in Figs. 4.3 and 4.4 respectively. The compressible dimensionless Reynolds equation is expressed in Eq. 4.12[81].

$$\frac{1}{\bar{r}} \frac{\partial}{\partial \bar{r}} \left(\bar{r} \bar{h}^3 \bar{p} \frac{\partial \bar{p}}{\partial \bar{r}} \right) + \frac{1}{\bar{r}^2} \frac{\partial}{\partial \theta} \left(\bar{h}^3 \bar{p} \frac{\partial \bar{p}}{\partial \theta} \right) = \Lambda \frac{\partial (\bar{p} \bar{h})}{\partial \theta} \quad (4.12)$$

The normalization components used in Eq. (4.12) are

$$\bar{r} = \frac{r}{R_2}, \quad \bar{p} = \frac{p}{p_a}, \quad \bar{h} = \frac{h}{h_2} \text{ and } \Lambda = \frac{6\omega\mu_0}{p_a} \left(\frac{R_2}{h_2} \right)^2$$

The gas film thickness (h) represents initial clearance caused by the wedge shape geometry when the elastic foundation is not deformed and subsequent deflection of the elastic foundation (Fig. 4.4). The normalized gas film thickness is a function of bearing geometry, bump configurations, bump materials properties and pressure distribution over bearing surface [14]. The expression for the normalised gas film thickness is given below:

$$\bar{h} = 1 + \bar{g}(\bar{r}, \theta) + \alpha(\bar{p} - 1)$$

where,

$$\begin{aligned} \bar{g} &= (\bar{h}_1 - 1) \left(1 - \frac{\theta}{b\beta} \right), 0 \leq \theta \leq b\beta \\ &= 0, b\beta \leq \theta \leq \beta \\ \bar{h}_1 &= \frac{h_1}{h_2}, \text{ and the compliance number, } \alpha = \frac{2p_a s}{h_2 E} \left(\frac{l_b}{t_b} \right)^3 (1 - \nu^2) \end{aligned}$$

The Eq. (4.12) is further expanded before applying the numerical solution. The expanded equation is given in Eq. (4.13).

$$A + B + C = 0 \quad (4.13)$$

where,

$$\begin{aligned} A &= \frac{\bar{h}^3}{\bar{r}} \bar{p} \frac{\partial \bar{p}}{\partial \bar{r}} + \bar{h}^3 \bar{p} \frac{\partial^2 \bar{p}}{\partial \bar{r}^2} + \bar{h}^3 \left(\frac{\partial \bar{p}}{\partial \bar{r}} \right)^2 \\ B &= 3\bar{h}^2 \frac{\bar{p}}{\bar{r}^2} \left(\frac{\partial \bar{h}}{\partial \theta} \right) \left(\frac{\partial \bar{p}}{\partial \theta} \right) + \frac{\bar{h}^3}{\bar{r}^2} \left(\frac{\partial \bar{p}}{\partial \theta} \right)^2 + \frac{\bar{h}^3}{\bar{r}^2} \bar{p} \left(\frac{\partial^2 \bar{p}}{\partial \theta^2} \right) \\ \text{and } C &= -\Lambda \bar{h} \frac{\partial \bar{p}}{\partial \theta} - \Lambda \bar{p} \frac{\partial \bar{h}}{\partial \theta} \end{aligned}$$

The boundary conditions for solving non-dimensional Reynolds Eqs. (4.13) are given in Eq. (4.14).

$$\left. \begin{aligned} \bar{p} &= 1 \text{ at } \bar{r} = 1 \text{ and } \left(\frac{R_1}{R_2} \right) \\ \bar{p} &= 1 \text{ at } q = 0 \text{ and } b \\ \bar{p} &\geq 1, \text{ over bearing surface} \end{aligned} \right\} \quad (4.14)$$

First boundary condition indicates the pressure at the outer and inner radius of the foil are at ambient pressure. The second indicates ambient pressure at the start and end of the of the sector. Finally, the third condition indicates that the gas foil bearing does not permit generation of sub-ambient pressure.

The pressure is calculated using approximate solution methods, and the resultant pressure is integrated to find the load carrying capacity and torque on bearings as expressed in Eq. (4.15) and (4.16) respectively[14].

$$\bar{W} = \frac{W}{p_a R_2^2} = \int_0^\beta \int_{\frac{R_1}{R_2}}^1 \bar{p} \bar{r} d\bar{r} d\theta \quad (4.15)$$

$$\bar{T} = \frac{T}{p_a h_2 R_2^2} = \int_0^\beta \int_{\frac{R_1}{R_2}}^1 \left(\frac{\bar{h}}{2} \frac{\partial \bar{p}}{\partial \theta} + \frac{\Lambda}{6} \frac{\bar{r}^3}{\bar{h}} \right) \bar{p} \bar{r} d\bar{r} d\theta \quad (4.16)$$

4.3.2 Method of solution

The Reynold's equation, Eq. (4.13) need to be solved to obtain the pressure values over the bearing surface. This can be solved by various numerical methods such as finite element method finite difference method and finite volumetric method. Finite Difference Method (FDM) is widely used and preferable due to the simplicity of the approach. For ease of computation, the whole of the bearing face is divided into four symmetrical sectors (Fig. 4.6). The computational domain covers a single such sector. The solution region is divided into mesh with a uniform grid in θ and r direction and total number of nodes are $M_\theta \times N_r$ (Fig. 4.6).

The Reynold's Eq. (4.13) is discretized and expressed to yield the following algebraic equation(Eq. 4.14):

$$\begin{aligned} & \frac{\bar{p}_{i,j} \bar{h}_{i,j}^3}{\bar{r}_{i,j}^2} \left[\frac{\bar{p}_{i+1,j} - \bar{p}_{i-1,j}}{2\Delta\bar{r}} \right] + \bar{p}_{i,j} \bar{h}_{i,j}^3 \left[\frac{\bar{p}_{i+1,j} - 2\bar{p}_{i,j} + \bar{p}_{i-1,j}}{(\Delta\bar{r})^2} \right] \\ & + \bar{h}_{i,j}^3 \left[\frac{\bar{p}_{i+1,j} - \bar{p}_{i-1,j}}{2\Delta\bar{r}} \right]^2 + \frac{3\bar{p}_{i,j} \bar{h}_{i,j}^3}{\bar{r}_{i,j}^2} \left[\frac{\bar{h}_{i,j+1} - \bar{h}_{i,j-1}}{2\Delta\theta} \right] \left[\frac{\bar{p}_{i,j+1} - \bar{p}_{i,j-1}}{2\Delta\theta} \right] \\ & + \frac{\bar{h}_{i,j}^3}{\bar{r}_{i,j}^2} \left[\frac{\bar{p}_{i,j+1} - \bar{p}_{i,j-1}}{2\Delta\theta} \right]^2 + \frac{\bar{p}_{i,j} \bar{h}_{i,j}^3}{\bar{r}_{i,j}^2} \left[\frac{\bar{p}_{i+1,j} - 2\bar{p}_{i,j} + \bar{p}_{i-1,j}}{(\Delta\bar{\theta})^2} \right] \\ & - \Lambda \bar{h}_{i,j} \left[\frac{\bar{p}_{i,j+1} - \bar{p}_{i,j-1}}{2\Delta\theta} \right] - \Lambda \bar{p}_{i,j} \left[\frac{\bar{h}_{i,j+1} - \bar{h}_{i,j-1}}{2\Delta\theta} \right] = 0 \end{aligned} \quad (4.17)$$

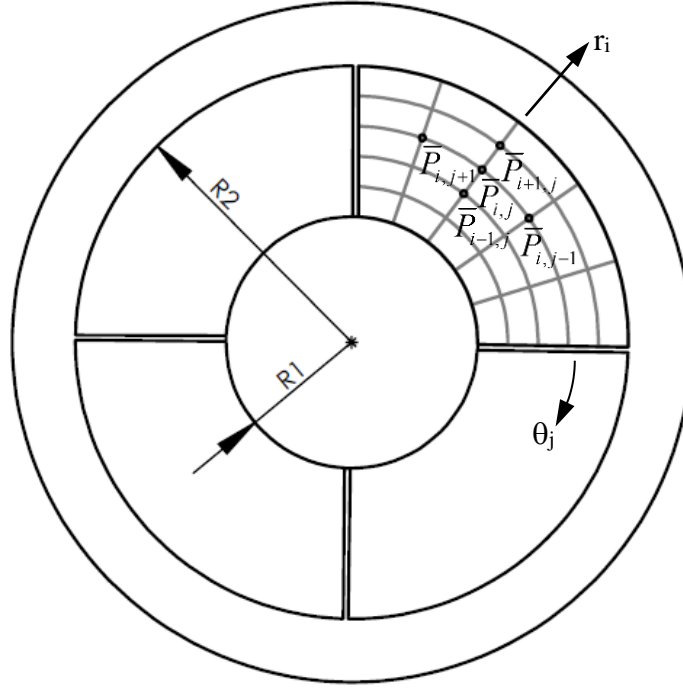


Figure 4.6: Discretization of single sector of thrust bearing surface.

Eq. 4.17 is further simplified to a quadratic form of the equation.

$$D(\bar{p}_{i,j})^2 + E(\bar{p}_{i,j}) + F = 0 \quad (4.18)$$

where,

$$D = -2\bar{h}_{i,j}^3 \left(\frac{1}{(\Delta\bar{r})^2} - \frac{1}{(\Delta\theta)^2 \bar{r}_{i,j}^2} \right)$$

$$E = E_a + E_b + E_c$$

$$E_a = \frac{\bar{h}_{i,j}^3}{\bar{r}_{i,j}^2} \left[\frac{\bar{p}_{i+1,j} - \bar{p}_{i-1,j}}{2\Delta\bar{r}} \right] + \bar{h}_{i,j}^3 \left[\frac{\bar{p}_{i+1,j} + \bar{p}_{i-1,j}}{(\Delta\bar{r})^2} \right]$$

$$E_b = \frac{3\bar{h}_{i,j}^3}{\bar{r}_{i,j}^2} \left[\frac{\bar{h}_{i,j+1} - \bar{h}_{i,j-1}}{2\Delta\theta} \right] \left[\frac{\bar{p}_{i,j+1} - \bar{p}_{i,j-1}}{2\Delta\theta} \right] + \frac{\bar{h}_{i,j}^3}{\bar{r}_{i,j}^2} \left[\frac{\bar{p}_{i+1,j} - 2\bar{p}_{i,j} + \bar{p}_{i-1,j}}{(\Delta\theta)^2} \right]$$

$$E_c = -\Lambda \left[\frac{\bar{h}_{i,j+1} - \bar{h}_{i,j-1}}{2\Delta\theta} \right]$$

$$F = F_a + F_b + F_c$$

$$F_a = \bar{h}_{i,j}^3 \left[\frac{\bar{p}_{i+1,j} - \bar{p}_{i-1,j}}{2\Delta\bar{r}} \right]^2$$

$$F_b = \frac{\bar{h}_{i,j}^3}{\bar{r}_{i,j}^2} \left[\frac{\bar{p}_{i,j+1} - \bar{p}_{i,j-1}}{2\Delta\theta} \right]^2 \text{ and}$$

$$F_c = -\Lambda \bar{h}_{i,j} \left[\frac{\bar{p}_{i,j+1} - \bar{p}_{i,j-1}}{2\Delta\theta} \right]$$

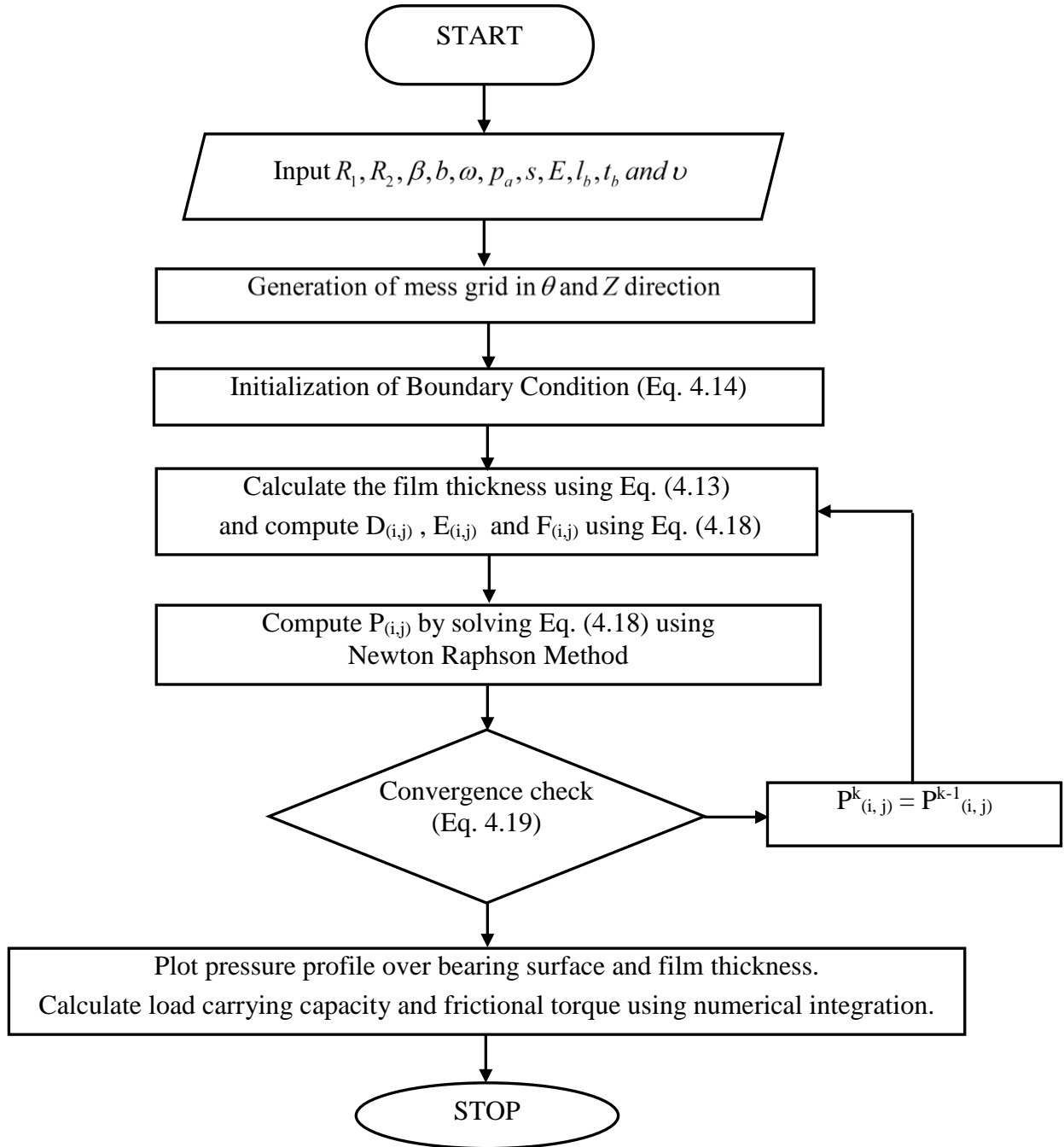


Figure 4.7: Flow chart for computation of thrust bearing performance.

The algorithm for the computer program to determine the load carrying capacity is given in the form of a flow chart in Fig. 4.7.

The solution begins by evaluating the quadratic equation (Eq. 4.18) by an initial guess pressure $\bar{p}_{i,j}$ and film thickness $\bar{h}_{i,j}$. This is done iteratively until a convergence of the pressure is achieved for a film thickness. Convergence is achieved when the relative error between two successive iterations fall below a specified value as given in Eq. (4.19).

$$\frac{|\sum(\bar{p}^{k-1}) - \sum(\bar{p}^k)|}{|\sum(\bar{p}^k)|} \leq 10^{-6} \quad (4.19)$$

4.3.2 Double gas foil thrust bearing

The thrust load will be always unidirectional at designed speed; however, there is some possibility of load reversal or change of load direction because of possible unpredictable flow input to the turbine and brake compressor, Mainly load reversal occur during testing, starting and stopping where inlet fluid conditions are different from the actual operating conditions. Therefore, it is always preferable to use double thrust bearings, and the schematic of the double thrust bearing is shown in Fig. 4.8.

The total bearing clearance is a summation of the clearances of the upper (h_U) and lower (h_L) thrust bearings. When an axial load is developed in the rotor, the clearance in the direction of loading gets reduced, and the build-up pressure or load carrying capacity of the bearing with lesser clearance is increased. The pressure at the other bearing, however, falls due to increased clearance, which leads to decreased resistance to the flow of gas. Finally, the net pressure differential balances the external axial load over the bearing area.

The total bearing film thickness is a summation of the film thickness by upper and lower thrust bearing and their relation in is given in Eq. (4.20)[2].

$$h_U + h_L = h_T \quad (4.20)$$

When the thrust collar is in equilibrium under an external load of W_{ext} , The relation between load carrying capacities of both the bearings is given in load Eq. (4.21)[2].

$$\bar{W}_U + \bar{W}_{Ext} = \bar{W}_L \quad (4.21)$$

where,

The dimensionless load capacity of upper thrust bearing: $\bar{W}_U = \frac{W_U}{p_a R_2^2}$,

Where load capacity of upper thrust bearing is W_U

The dimensionless load capacity of lower thrust bearing: $\bar{W}_L = \frac{W_L}{p_a R_2^2}$,

Where load capacity of lower thrust bearing is W_L

The dimensionless external/thrust load $\bar{W}_{Ext} = \frac{W_{Ext}}{p_a R_2^2}$

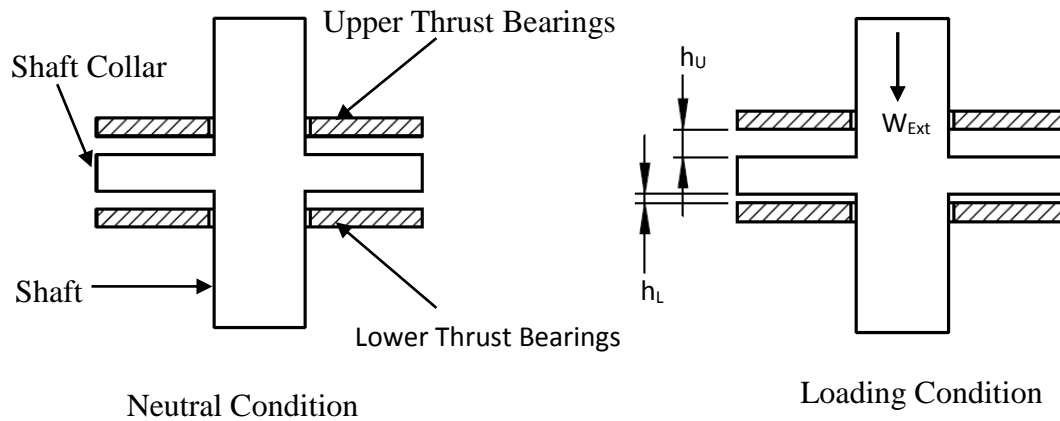


Figure 4.8: Schematic of double thrust bearings.

In the current application, the direction of external load is downward, and it's considered as +ve. However, the sign of the external load in Eq. (4.21) depends on the direction of thrust load as described in section 4.1.

The steps of designing double thrust foil bearings for current application is as follows:

- i. Calculation of external load (W_{Ext}) and its direction as described in section 4.1.
- ii. Selection of bump configurations such as foil thickness, materials, bump pitch, and length for both upper and lower thrust bearings.
- iii. Selection of minimum film thickness for the lower bearing (h_L) and calculation of load carrying capacity of lower thrust bearing (W_L).
- iv. Calculation of load carrying capacity of upper thrust bearing (W_U) for various total clearances (h_T).
- v. Determination of total clearances based on Eq. (4.21) and design of spacer between upper and lower thrust bearing.

4.3.3 Result and discussion

For current application the external or thrust load is nearly 83 N and the selected bump profile is from open literatures[42, 72] as shown in Table 4.3.

Table 4.3: Common journal bearing data for numerical simulation.

Bearing parameters	Dimensions
Inner radius (R_1)	10 mm
Outer radius (R_2)	22 mm
Rotational Speed (N)	140,000 rpm
Angular extent (β)	90°
Ratio of angular extent (b)	0.40
Grid Size	75×75
Viscosity of gas	178.4×10^{-7} N.s/m ²
Bump Foil Young's Modulus (E)	114 GPa
Bump Foil Poisson's Ratio (ν)	0.35
Top Foil Thickness (t_t)	0.1 mm
Bump Foil Thickness (t_b)	0.1 mm
Bump Length ($2l_b$)	2.5 mm
Bump Pitch (s)(maximum)	3.17 mm

A computer programme using MATLAB is developed to determine all essential thrust bearing performance parameters. An elaborate grid refinement study is done for the appropriate grid size to save computational time and to converge within a specified tolerance. Based on the results shown in Fig. 4.9, the variation of load carrying capacity is negligible after grid size of 75×75 along the circumferential and radial directions. Grid sizes higher than this would increase computational time without much variation in the overall results.

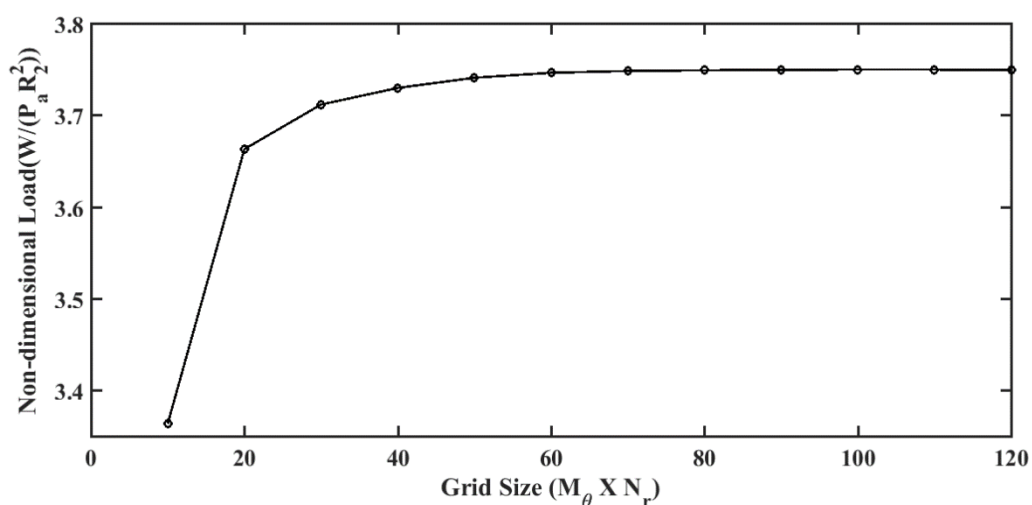


Figure 4.9: Variation of load carrying capacity with grid size.

The load carrying capacity of a pad depends on the angular extent of the pad. The curve in Fig. 4.10 shows that the load carrying capacities increase with the angular extent of a single pad. So the extent of pad angle selected is 90° , and number of pads selected are 4 for the current application. The extent of ramp is chosen based on the parametric study by Heshmat et al.[14]. His extensive studies show the extent of the ramp of $b = 0.5$ gives higher load carrying capacity. For current application the selected value of b is 0.4 to avoid fabrication and assembly issues with smaller radius of thrust bearing. The effect of non-dimensional film thickness on load carrying capacity is shown in Fig. 4.11 and this curve is helpful during the design of double thrust bearings.

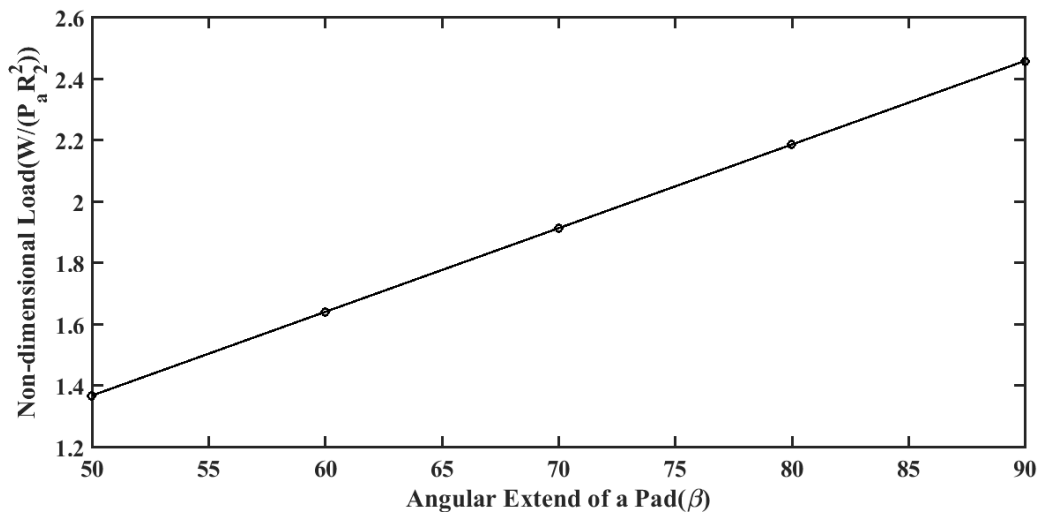


Figure 4.10: Non-dimensional load at various angular extent of a pad.

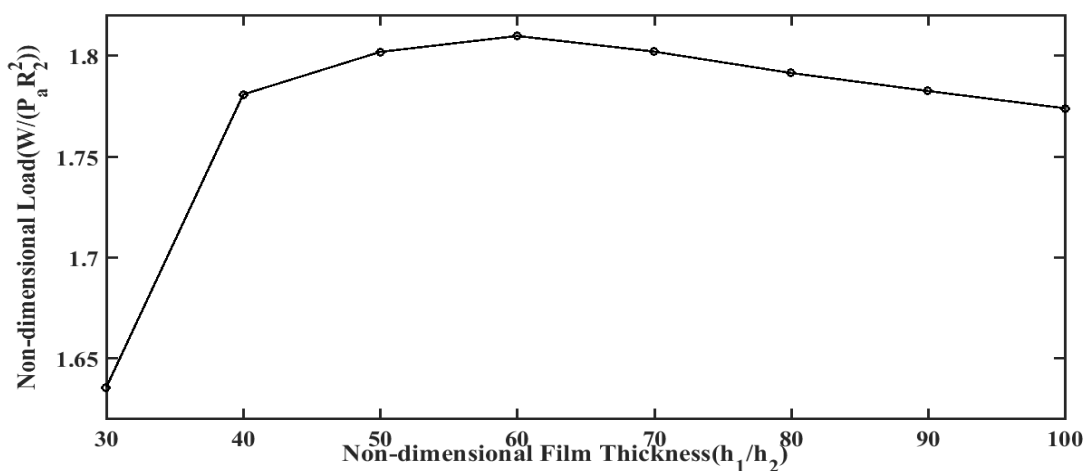


Figure 4.11: Non-dimensional load for different film thickness ratio.

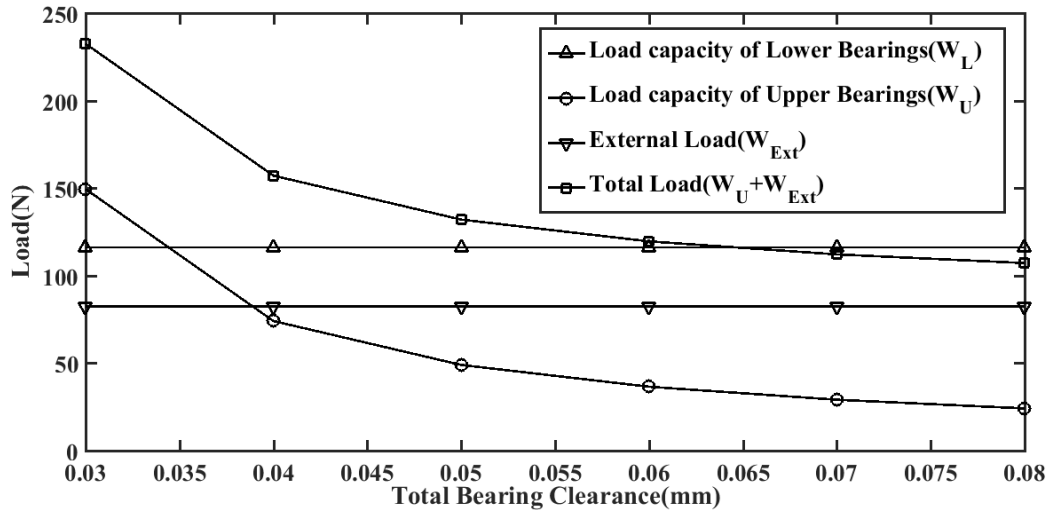


Figure 4.12: Load curves for different total clearance.

Finally, the simulation results for the combined thrust bearing with various clearances are presented in Fig. 4.12. The minimum film thickness for the lower bearing is fixed with 20 μm . The simulation shows the load balancing equation (Eq. 4.21) satisfied for total bearing clearance slightly above 65 μm . So the film thickness for upper bearing at the designed speed of the rotor will be 45 μm . The values of h_1 and h_2 for both the bearings are given in Table 4.4. The dimensions and configuration of the bumps are kept same for both the bearings (Table 4.3) except the value of inlet and minimum film thickness.

Table 4.4: Film thickness data for upper and lower thrust bearings.

Lower Thrust Bearing		Upper Thrust Bearing	
Minimum film thickness (h_2)	0.020 mm	Minimum film thickness (h_2)	0.045 mm
Inlet film thickness (h_1)	0.530 mm	Inlet film thickness (h_1)	0.555 mm

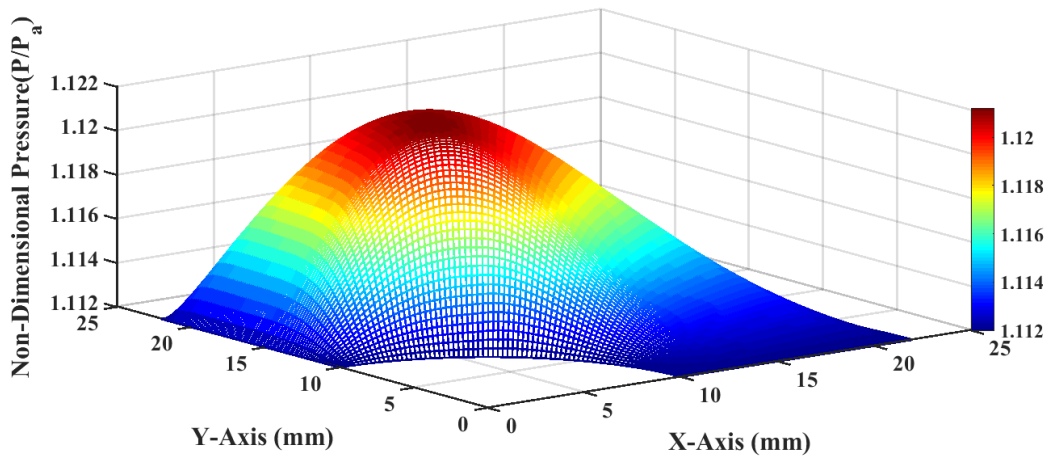


Figure 4.13: Non-dimensional pressure profile over a single sector of the lower thrust bearing surface.

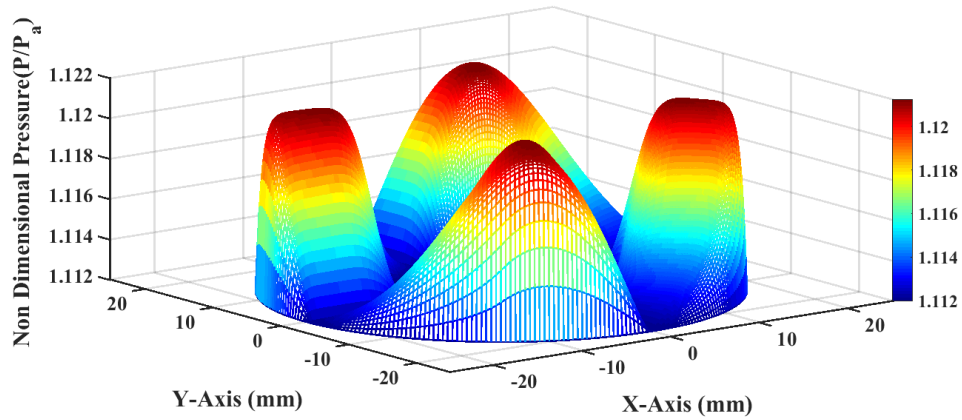


Figure 4.14: Non-dimensional pressure profile over the lower bearing surface.

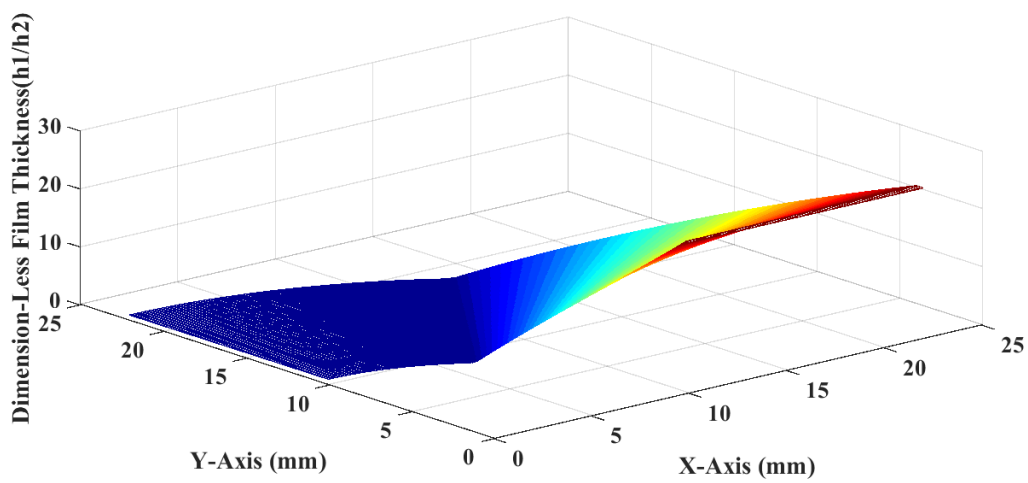


Figure 4.15: Non-dimensional film thickness over a single sector of the lower thrust bearing surface.

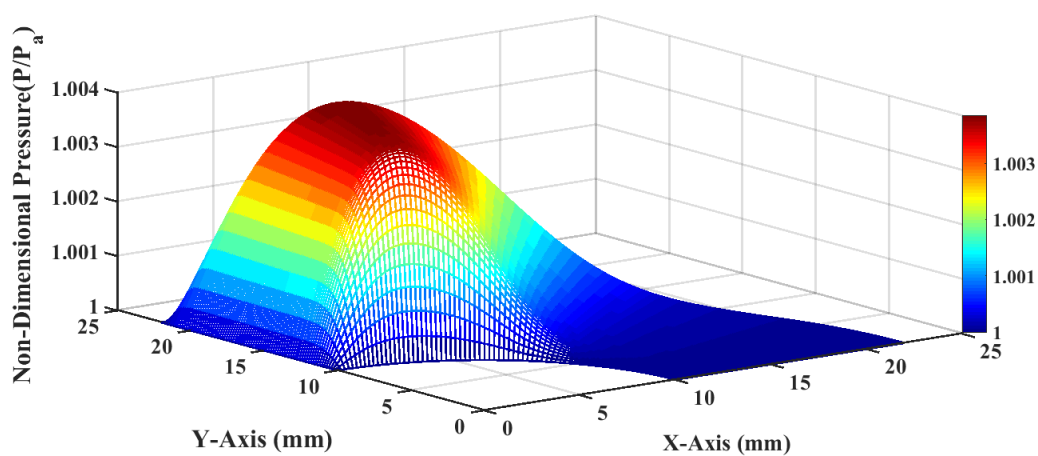


Figure 4.16: Non-dimensional pressure profile over a single sector of the upper thrust bearing surface.

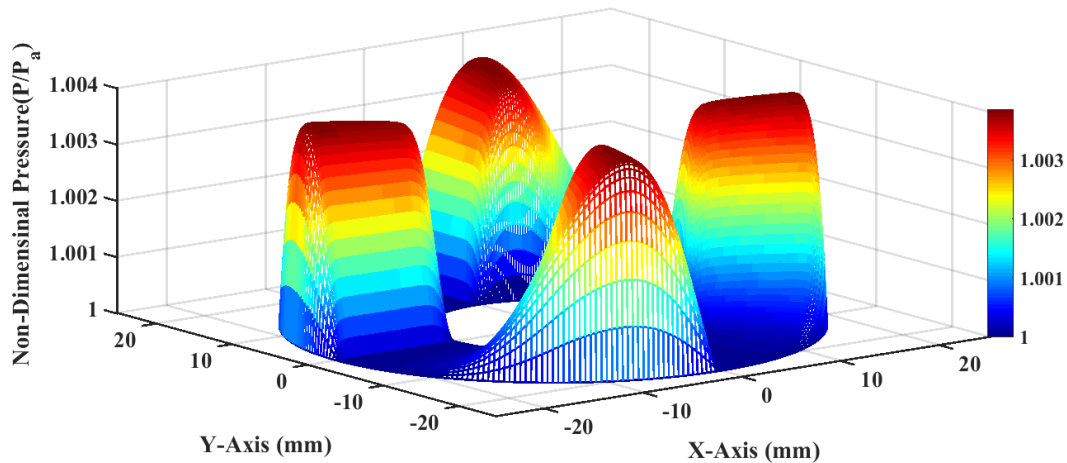


Figure 4.17: Non-dimensional pressure profile over the upper thrust bearing surface.

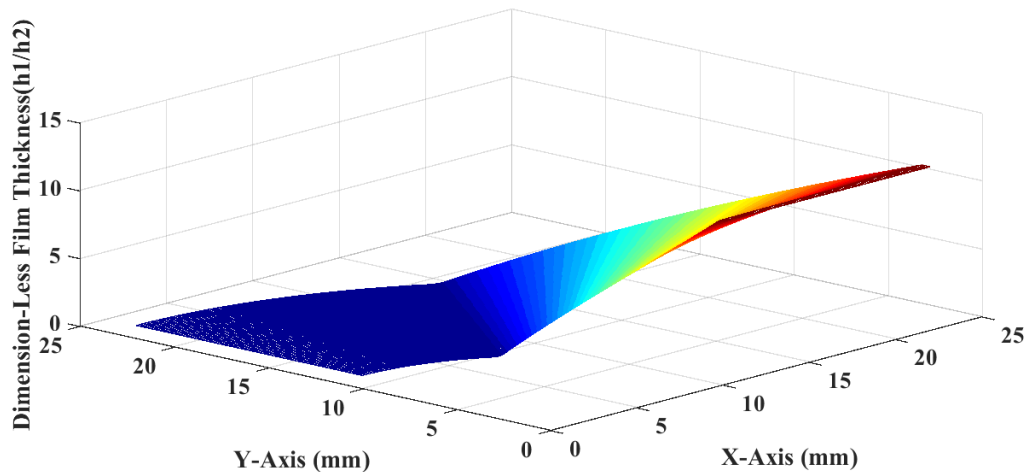


Figure 4.18: Non-dimensional film thickness over a single sector of the upper thrust bearing surface.

The pressure profile and film thickness over the bearing surface for a single sector and pressure profile for complete surface of the bearing is shown in Figs. 4.13 to 4.18.

4.4 Axial passive magnetic bearings

The major issue with the aerodynamic bearings is at start and stop phase of the turbomachine due to direct contact between bearing surface and runner. So an attempt is made to avoid direct contact and minimize the wear rate by designing a passive or permanent magnetic bearing for the vertical rotor of the turboexpander. These bearings do not need any sensors or controller unlike active magnetic bearings. They are found to be compact and quite suitable for the current application.

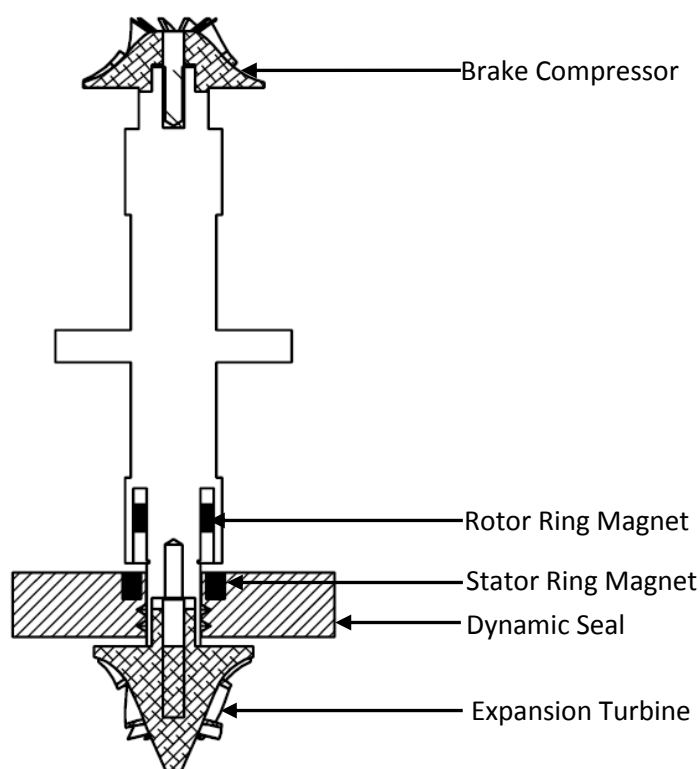


Figure 4.19: Arrangements of ring magnets as axial passive magnetic bearings.

The passive magnet bearing pair is designed for the static conditions to support the dead weight of the rotor during start and stop of the turboexpander. The simplest types of passive magnetic bearings chosen are a pair of ring magnets. One is fixed with the rotor and other with the dynamic seal as shown in Fig. 4.19. Both the rings are axially polarized with opposite direction to create a repulsive force between the rings. The repulsive force between two concentric rings can be determined either by analytical methods or finite element analysis. The analytical method has been found quite promising and faster way to design [83], So the analytical approach is adopted to determine dimensions of magnetic rings with load carrying capacity equivalent to the static load of the rotor.

4.4.1 Mathematical modelling of active magnetic thrust bearings

The basic configuration of the permanent magnet bearings with concentric polarized magnetic rings is shown in Fig. 4.19[83]. Two different methods are used to calculate forces between permanent magnet namely, a dipole method and surface charge density. The dipolar method is quite popular and accurate for the magnetic bearings where the air gap is larger than dimensions of the magnets[83]. The space available in rotor bearing system of current application is suitable for the later method, where magnetic ring dimensions are larger than the air gap. So in current analysis surface charge density

method is adopted, where the surface of the magnets are charged with positive and negative charge according to the direction of polarization. The force of repulsion is calculated between polarized surfaces using Coulomb's law.

The parameters used in the determination of axial forces between surfaces of ring magnets are shown in Fig. 4.20. These parameters are used to calculate magnetic forces between four surfaces A, B, C and D. The elemental magnetic force on discrete surface element 'A1' of the rotor magnet surface 'A' due to the surface element 'B1' on the stator magnet surface 'B' is expressed in Eq. (4.22) [83].

$$\vec{F}_{A1B1} = \frac{J_1 J_2 S_{A1} S_{B1}}{4\pi\mu_0 r_{A1B1}^3} \vec{r}_{A1B1} \quad (4.22)$$

Where,

J_1 : Magnetic polarization of the rotor magnetic ring

J_2 : Magnetic polarization of stator magnetic ring.

S_{A1} : Surface area of element A1 on surface A

S_{B1} : Surface area of element B1 on surface B

μ_0 : Absolute magnetic permeability

$Ru1$: Inner radius of rotor ring magnet

$Ru2$: Outer radius of rotor ring magnet

$Rl1$: Inner radius of stator ring magnet

$Rl2$: Outer radius of stator ring magnet

\vec{r}_{A1B1} : The distance vector between element A1 and B1 in axial direction

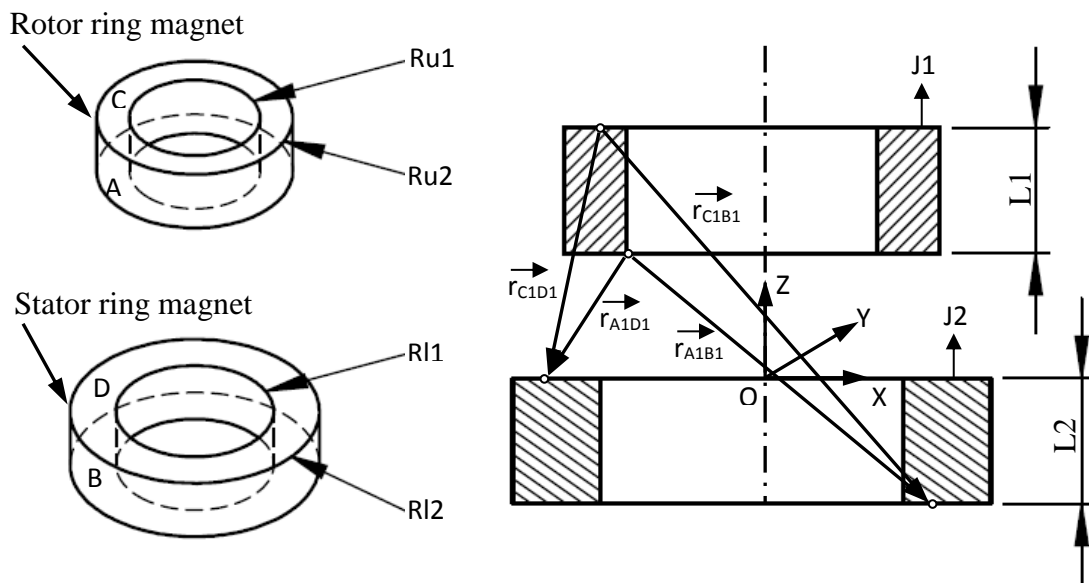


Figure 4.20: Configuration and arrangements of ring magnets.

The elemental forces between elements of surfaces A-D, C-B, and C-D is calculated using similar notation of Eq. (4.22) and those expressions are given from Eqs. (4.23) to (4.25)[83].

$$\vec{F}_{A1D1} = \frac{J_1 J_2 S_A S_D}{4\pi\mu_0 r_{A1D1}^3} \vec{r}_{A1D1} \quad (4.23)$$

$$\vec{F}_{C1B1} = \frac{J_1 J_2 S_{C1} S_{D1}}{4\pi\mu_0 r_{C1B1}^3} \vec{r}_{C1B1} \quad (4.24)$$

$$\vec{F}_{C1D1} = \frac{J_1 J_2 S_{C1} S_{D1}}{4\pi\mu_0 r_{C1D1}^3} \vec{r}_{C1D1} \quad (4.25)$$

Considering 'n' number of discrete surface elements in the rotor magnet and 'm' number of discrete surface elements in the stator magnet, the resultant forces in on the rotor magnet can be expressed as a summation of all the elemental forces which is presented in Eq. (4.26)[83].

$$F_Z = \sum_{p=1, q=1}^{p=n, q=m} F_{A_p B_q} + \sum_{p=1, q=1}^{p=n, q=m} F_{A_p D_q} + \sum_{p=1, q=1}^{p=n, q=m} F_{C_p B_q} + \sum_{p=1, q=1}^{p=n, q=m} F_{C_p D_q} \quad (4.26)$$

4.4.2 Calculation of magnetic forces

The magnetic materials are chosen for rotor and stator magnets based on its availability in the market. Neodymium (NdFeB) alloy magnets of grade N42 is one of the strongest permanent magnet amongst the others and axially magnetized rings are easily available in the market. The dimension of magnets is chosen based on the available space to accommodate rings on the rotor and the stator at the lower end of the rotor. The design data for passive magnetic bearings are given in Table 4.4 for two pairs of ring magnets.

Table 4.5: Design data of the ring magnets.

Magnetic material	NdFeB, Grade N42
J1	1.4 Tesla
J2	1.4 Tesla
μ_0	10^{-6} N/A ²
Pair 1 configuration	Ru1=5 mm, Ru2=7.5 mm , L1=5 mm Rl1=5 mm, Rl2= 7.5 mm , L2=5 mm
Pair 2 configuration	Ru1=5 mm, Ru2=7.5 mm , L1=5 mm Rl1=6.35 mm, Rl2=9.525 mm , L2=3.175 mm

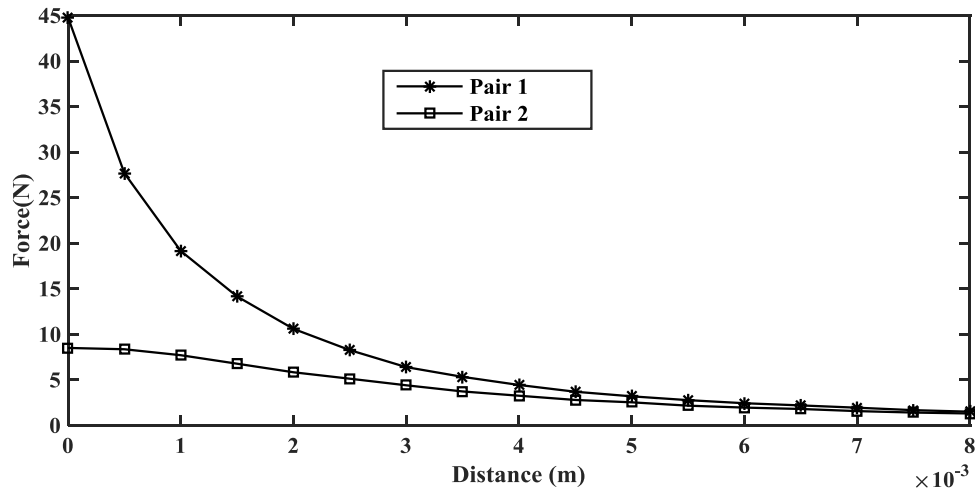


Figure 4.21: Variation of repulsive forces against distance between ring magnets.

The distance to be maintained between the upper and lower ring magnets for both pair of configuration can be determined from Fig. 4.21. Pair 1 configuration shows higher repulsive forces between rotor and stator magnetic rings when the distance between rings is very small but above 8 mm, both the configuration shows similar behavior. The repulsive forces between the ring magnets are just above the dead weight of the rotor (0.998N), when the distance between the rings magnet are maintained at 7 mm.

4.5 Detail design procedure of gas foil thrust bearings

The detailed step by step design procedure for bump type gas foil thrust bearings based on the relations developed in the earlier section are given below:

Step 1: Input to bearing designer

- a. The bearing gas, which is mostly the process gas to the turboexpander.
- b. The dimensions and thermodynamic states of TW and CW.
- c. Dimension and designed rotational speed of the rotor.
- d. Minimum axial clearance of the thrust bearings.

Step 2: Calculation of thrust load because of the pressure differential between turbine wheel and compressor wheel, Impulse forces on both the wheels and the dead weight of the rotor.

Step 3: Solving the static compressible aerodynamic Reynolds equation to determine below bearing performance parameter for double acting gas foil thrust bearing.

- a. The total clearance between upper and lower bearings.

- b. Materials for the bump foil and bump dimensions such as thickness, pitch, length and height of the bump.
- c. Determine the load carrying capacity equal to thrust load of the rotor at designed speed.

Step 4: Reduction of high friction between shaft collar and thrust bearing during start and stop of the application by of one of the method described below:

- a. Use of solid lubricant on either stator or runner surface.
- b. Use of passive magnetic bearings and modification rotor configuration if necessary.

Step 5: Design of the foils attachment mechanism to the thrust bearing base.

Step 6: Production and assembled drawings of gas foil thrust bearings.

Chapter 5

Rotordynamics of the Prototype Rotor

Transverse vibration is one of the major issues encountered in high speed rotating machinery. These issues are difficult to analyze in the preliminary stage and many cases they are realized when a failure occurs. Such failure can lead to the significant penalty to rotating machinery. A prior detection of such failures through vibration analysis or rotordynamics is an essential component of the turbomachinery design process. The rotordynamics helps to find the possible source of the problem and suitable precaution for the same. One of the precautions is to design rotor and bearing system such that the designed speed of the application is far away from bending critical speeds. The rotors with aerodynamic bearings mostly operate below 1st bending critical speed as the low viscosity of bearing gasses results in relatively low damping in aerodynamic bearings and practically it is difficult to cross the rotor speed through 1st bending critical speed [84]. Based on experience, the maximum operating speed of the rotor should not exceed 70% of critical speed.

Apart from critical speed, the mode shapes and unbalanced response are very important for vibration analysis of the rotor. A mode shape is a definite pattern of vibration of the rotor at the critical speed and is determined by the distribution of mass and stiffness along the rotor[84, 85]. The first two modes are the rigid body modes (cylindrical or conical whirl), and the bearing stiffness heavily influences them. From third mode (first bender) onwards the influence of bearings stiffness decrease and the rotor geometry and mass distribution come into the picture. The presence of unbalanced mass causes excessive vibration in the rotating shaft. The unbalanced mass in a rotor is due to material inhomogeneity, manufacturing process, and unsymmetrical slots. Proper rotor balancing procedure can minimize these unbalance mass. However even small unbalance mass in the high-speed rotor can develop an unwanted vibratory response. Thus the unbalance response analysis of the high-speed rotor is very much essential.

Rotordynamics of the high-speed rotor is divided into two accurate approaches. One is finite element method (FEM) and other is a relatively more traditional method, the transfer matrix method (TMM). Traditional TMM has fixed matrix dimensions and easy to solve. In this method, the rotor is modeled as discs and massless elastic elements. The first element is linked to the last element of the rotor by an overall transfer matrix. An overall

transfer matrix is used to determine the critical speed and mode shapes upon applying boundary conditions. Further, this method can be easily modified to compute a response to imbalance with a known unbalance mass. This chapter targets to find multiple critical speeds, mode shapes and unbalance response of the prototype rotor using TMM for the prototype rotor bearing system.

5.1 Transfer matrix method with gyroscopic effect

The transfer matrix method is also called Myklestand and Prohl method, because they developed this method for two different applications independently [84]. In this method, the flexible rotor divided into a finite number of station and each station consists of a lumped inertias (discs) and massless elastic shaft elements (Fig 5.1). The number of stations usually ranges from 8 to 80 [85]. Transfer functions relate the state vectors of the disc and shaft elements by finding point and field matrices. The multiplication of the coefficients of all the matrices gives a resultant matrix, known as the 'overall transfer matrix.' This overall transfer matrix gives expressions for the boundary conditions in the rotor bearing system. The critical speed and mode shapes of the system are determined by computing the overall transfer matrix.

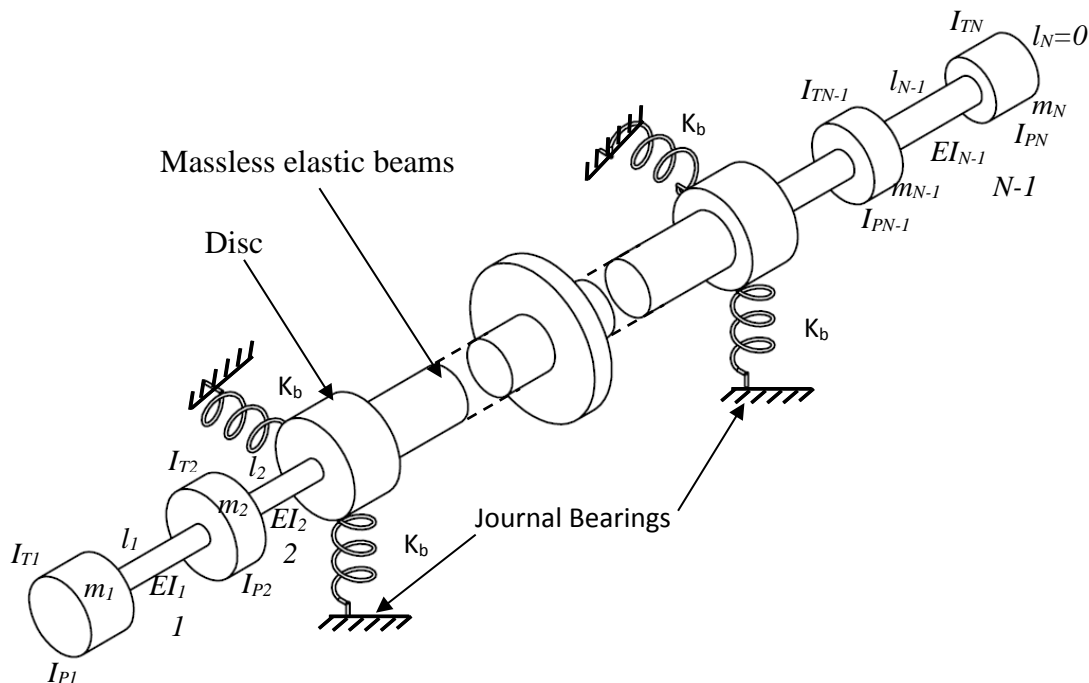


Figure 5.1: Model of a rotor-bearing system with discrete segments.

The disc present in the inertial model contributes to the generation of the gyroscopic couple. This gyroscopic couple changes the bending equations and has a considerable

influence on the dynamic behavior of the high-speed rotors. Therefore gyroscopic couple is crucial to consider in the development of the transfer function. The step by step TMM is explained in section 5.1.1 to determine the critical speed and mode shapes and same method is further extended to determine the response to an imbalance in section 5.1.2.

5.1.1 Critical speed and mode shapes analysis

The steps of computation of critical speeds using TMM can be explained by considering an undamped, symmetric rotor-bearing system with a pair of journal bearings[84]. The prototype rotor is divided into N number of stations, where N denotes the last inertia station of the rotor. Fig. 5.2 shows the free body diagrams of the disc (inertial element) and the elastic elements constituting the n^{th} station. All the discs are lumped with their gyroscopic inertia along with other inertial properties. The transfer equations across the massless elastic beam element and the disc for a synchronous whirl are given in Eqs. (5.1) and (5.3) respectively based on theories of engineering mechanics [84, 85]. The field and point matrixes are computed from these equations.

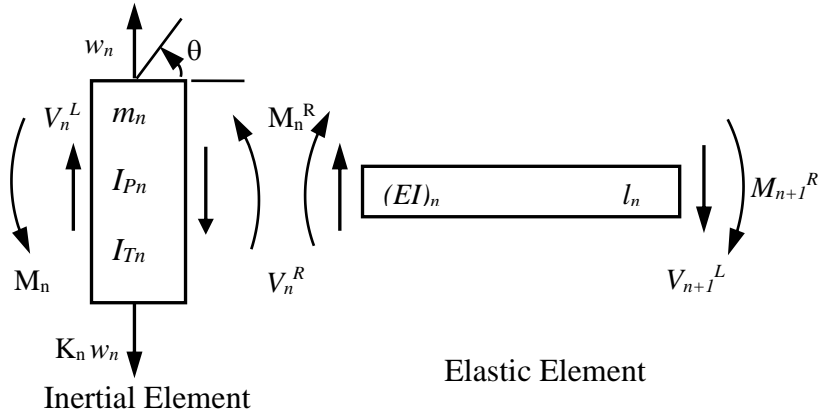


Figure 5.2: Free-body diagrams of the elements in the n^{th} rotor station [85].

The transfer Eq. (5.1) for the massless elastic shaft element is derived using statics and beam deflection theory. The field matrix $[F]_n$ relates the variable of interests (displacement, slope, bending moment and shear force) or the state vectors between right and left of the beam or between the right of the n^{th} disc and left of the $(n+1)^{\text{th}}$ disc[85].

$$\begin{Bmatrix} -w \\ \theta \\ M_y \\ V_z \end{Bmatrix}_{n+1}^L = \begin{bmatrix} 1 & l & l^2/(2EI) & l^3/(6EI) \\ 0 & 1 & l/(EI) & l^2/(2EI) \\ 0 & 0 & 1 & 0 \\ 0 & 0 & l & 1 \end{bmatrix}_n \begin{Bmatrix} -w \\ \theta \\ M_y \\ M_z \end{Bmatrix}_n^R \quad (5.1)$$

Symbolically above equation can be written as:

$$\{Q\}_{n+1}^L = [F]_n \{Q\}_n^R$$

where,

- w : Deflection
- θ : Slope
- $M_{y_n}^L$: Bending moments on the left of the n^{th} disc
- $M_{y_n}^R$: Bending moments on the right of n^{th} the disc
- V_n^L : Shear forces at the left faces of the n^{th} disc
- V_n^R : Shear forces at the right faces of the n^{th} disc
- l_n : Shaft element length
- E_n : Modulus of elasticity
- I_n : Area moment of inertia of the n^{th} station
- $\{Q\}_n$: $\{w, \theta, M, V\}^T$, The state vectors at the n^{th} node.
- $[F]_n$: Field matrix of the n^{th} station

The point matrix of Eq. (5.2) represents the relation between the variable of interests between right and left of the n^{th} disc [84]. The relation is derived from rigid body mechanics, and the transfer equations across the station for synchronous whirl can be expressed as:

$$\begin{Bmatrix} -w \\ \theta \\ M_y \\ V_z \end{Bmatrix}_n^R = \begin{bmatrix} 1 & 0 & 0 & 0 \\ 0 & 1 & 0 & 0 \\ 0 & (m_n \omega^2 - k_n) & 1 & 0 \\ (I_{Tn} - I_{Pn})\omega^2 & 0 & 0 & 1 \end{bmatrix} \begin{Bmatrix} -w \\ \theta \\ M_y \\ V_z \end{Bmatrix}_n^L \quad (5.2)$$

Symbolically above equation can be written as:

$$\{Q\}_n^R = [P]_n \{Q\}_n^L$$

- where, m_n : Mass of the n^{th} element
- I_{Tn} : Transverse mass moment of inertia of the n^{th} element
- I_{Pn} : Polar mass moment of inertia of the n^{th} element
- k_n : Stiffness, (K_b at bearing stations and 0 at all other stations)
- ω : Rotor speed
- $[P]_n$: Point matrix for n^{th} station

The relation between the 1st and the last element of the rotor bearing model can be determined by multiplying all the field and point matrix. The relation can be expressed with an overall transfer matrix $[T_o]$ as:

$$\{Q\}_N^R = [T_o] \{Q\}_1^L \quad (5.3)$$

where, $[T_o] = [P_N][F_{N-1}][P_{N-1}] \dots [F_1][P_1]$

The overall transfer matrix $[T_0]$ is also 4×4 in size as the point matrix $[P]$ and field matrix $[F]$ are all 4×4 matrices. The expanded form of the Eq. (5.3) is written as:

$$\begin{Bmatrix} r_N \\ \theta_N \\ V_N \\ M_N \end{Bmatrix}^R = \begin{bmatrix} d_{11} & d_{12} & d_{13} & d_{14} \\ d_{21} & d_{22} & d_{23} & d_{24} \\ d_{31} & d_{32} & d_{33} & d_{34} \\ d_{41} & d_{42} & d_{43} & d_{44} \end{bmatrix} \begin{Bmatrix} r_1 \\ \theta_1 \\ V_1 \\ M_1 \end{Bmatrix}^L \quad (5.4)$$

In current applications, the turbine and compressor are at the free end of the rotor, so there is no shear force and bending moment of 1st and last element of the rotor. Hence, the boundary condition is written as:

$$\begin{Bmatrix} V_N \\ M_N \end{Bmatrix}^R = \begin{Bmatrix} V_1 \\ M_1 \end{Bmatrix}^L = \begin{Bmatrix} 0 \\ 0 \end{Bmatrix} \quad (5.5)$$

Applying above boundary condition in the Eq. (5.4), the equation is modified as:

$$\begin{Bmatrix} V_N \\ M_N \end{Bmatrix}^R = \begin{bmatrix} d_{31} & d_{32} \\ d_{41} & d_{42} \end{bmatrix} \begin{Bmatrix} r_1 \\ \theta_1 \end{Bmatrix}^L = [D] \begin{Bmatrix} r_1 \\ \theta_1 \end{Bmatrix}^L = \begin{Bmatrix} 0 \\ 0 \end{Bmatrix} \quad (5.6)$$

For Eq. (5.6) to have non-zero solutions determinant of the matrix $[D]$ should be zero, so the critical speeds are the value of ω for which the determinate of the matrix is zero. Once the critical speed is determined, the corresponding mode shapes can be evaluated by assuming unit slope at station 1 and compute the displacements at each station[2].

5.1.2 Unbalance response analysis

The process of computation of unbalance response using TMM is an extension of critical speed analysis explained in section 5.1.1. In the case of unbalance response analysis, the field matrix and point matrix are modified to include bending quantities of the beam and the unbalance mass m_u at an eccentricity e [2, 85].

The discrete rotor element shown in Figs. 5.3 and 5.4 can bend in x-z plane as well as in x-y plane. So state vector and field matrix of Eq. (5.1) for the elastic beam is modified in both plane and re-written in Eq. (5.7)[85].

$$\begin{Bmatrix} \{Q_z\} \\ \{Q_y\} \end{Bmatrix}_{n+1}^L = \begin{bmatrix} [F] & [0] \\ [0] & [F] \end{bmatrix}_n \begin{Bmatrix} \{Q_z\} \\ \{Q_y\} \end{Bmatrix}_n^R \quad (5.7)$$

Where, $\{Q_z\}$ and $\{Q_y\}$ are state vectors in x-y and x-z plane respectively.

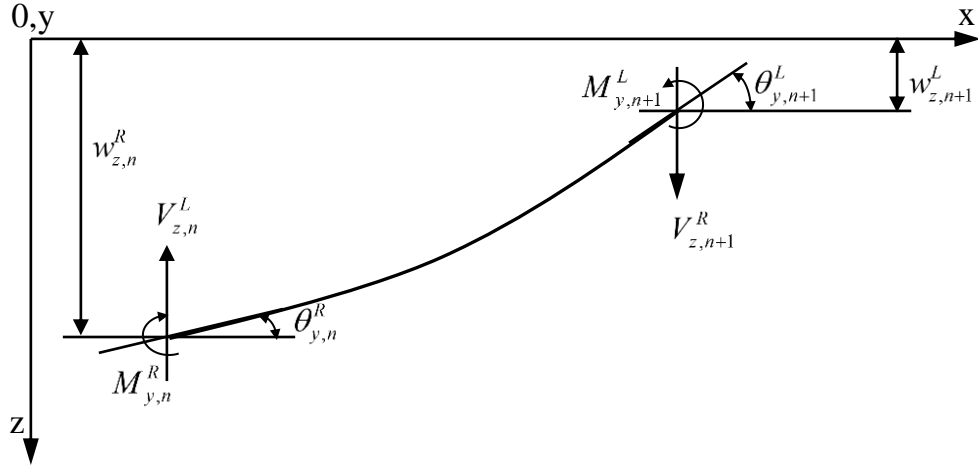


Figure 5.3: Elastic field of n^{th} element in x-z plane.

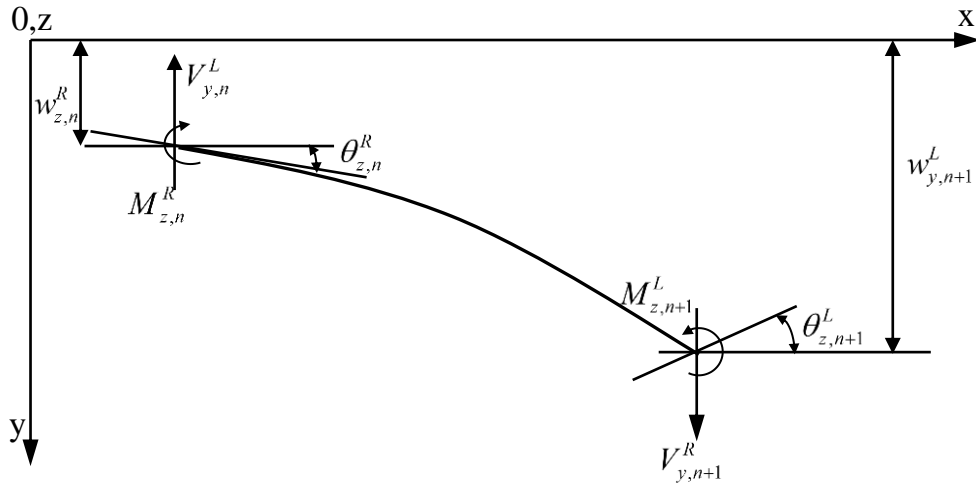


Figure 5.4: Elastic field of n^{th} element in x-y plane.

Further, the responses in y-direction and z-direction are different due to bending of the element. Hence state vectors of Eq. (5.7) are split into sine and cosine terms to get 16 state equations. The modified state vector and field matrix are given in Eq. (5.8) with a unity term ($1 \equiv 1$) appended to the state vectors to maintain the uniformity of matrix multiplication with point matrix of Eq. (5.11). The field matrix for the beam element is shown in Eq. 5.8[85].

$$\begin{Bmatrix} \{Q_{zc}\} \\ \{Q_{zs}\} \\ \{Q_{yc}\} \\ \{Q_{ys}\} \\ 1 \end{Bmatrix}_{n+1}^L = \begin{bmatrix} [F] & [0] & [0] & [0] & \{0\} \\ [0] & [F] & [0] & [0] & \{0\} \\ [0] & [0] & [F] & [0] & \{0\} \\ [0] & [0] & [0] & [F] & \{0\} \\ \{0\}^T & \{0\}^T & \{0\}^T & \{0\}^T & 1 \end{bmatrix}_n \begin{Bmatrix} \{Q_{zc}\} \\ \{Q_{zs}\} \\ \{Q_{yc}\} \\ \{Q_{ys}\} \\ 1 \end{Bmatrix}_n^R \quad (5.8)$$

Symbolically Eq. (5.8) can be written as:

$$\{Q'\}_{n+1}^L = [F']_n \{Q'\}_n^R$$

where,

- $\{Q_{zc}\}$ and $\{Q_{zs}\}$: Cosine and sine of state vectors in x-y plane respectively
 $\{Q_{yc}\}$ and $\{Q_{ys}\}$: Cosine and sine of state vectors in x-z plane respectively
 $[8]_n$: The field matrix of Eq. (5.1)
 $\{Q'\}_n$: Modified state vector for nth station
 $[F']_n$: Modified field matrix of the shaft element

The deflection, slope and moment are continuous and are same in left and right of the disc. So to determine the point matrix for the disc, the transfer equation is modified for the shear force expression. Because of excitation forces which have cosine and sine terms, the shear force will also have cosine and sine response term. The equilibrium relation of the shear forces in left and right is shown in Eq. (5.9) [85].:

$$\left. \begin{aligned} V_{zcn}^R &= V_{zcn}^L - (m_n \omega^2 - k_n) w_{zcn} - c \omega w_{zcn} - \omega^2 u_{zn} \\ V_{zsn}^R &= V_{zsn}^L - (m_n \omega^2 - k_n) w_{zsn} - c \omega w_{zsn} + \omega^2 u_{yn} \\ V_{ycn}^R &= V_{ycn}^L - (m_n \omega^2 - k_n) w_{ycn} - c \omega w_{ycn} - \omega^2 u_{yn} \\ V_{ysn}^R &= V_{ysn}^L - (m_n \omega^2 - k_n) w_{ysn} - c \omega w_{ysn} - \omega^2 u_{zn} \end{aligned} \right\} \quad (5.9)$$

where, unbalances are $u_{yn} = m_n e \omega^2 \cos \beta$ and $u_{zn} = m_n e \omega^2 \sin \beta$ at phase angle of β

The state vector and point matrix of Eq. (5.3) for the disc is modified in both plane and re-written in Eq. (5.10).

$$\left\{ \begin{array}{c} \{Q_{zc}\} \\ \{Q_{zs}\} \\ \{Q_{yc}\} \\ \{Q_{ys}\} \\ 1 \end{array} \right\}_n^R = \left[\begin{array}{cccc|c} [P] & [0] & [0] & [0] & \{m_{zc}\} \\ [0] & [P] & [0] & [0] & \{m_{zs}\} \\ [0] & [0] & [P] & [0] & \{m_{yc}\} \\ [0] & [0] & [0] & [P] & \{m_{ys}\} \\ \{0\}^T & \{0\}^T & \{0\}^T & \{0\}^T & 1 \end{array} \right]_n \left\{ \begin{array}{c} \{Q_{zc}\} \\ \{Q_{zs}\} \\ \{Q_{yc}\} \\ \{Q_{ys}\} \\ 1 \end{array} \right\}_n^L \quad (5.10)$$

Symbolically above equation can be written as:

$$\{Q'\}_n^R = [P']_n \{Q'\}_n^L$$

where,

$[P]_n$: The point matrix of Eq. (5.2)

$[P']_n$: Modified field matrix of the shaft element

$$\{m_{zc}\} = \begin{Bmatrix} 0 \\ 0 \\ 0 \\ -u_z \omega^2 \end{Bmatrix}_n, \{m_{zs}\} = \begin{Bmatrix} 0 \\ 0 \\ 0 \\ u_y \omega^2 \end{Bmatrix}_n, \{m_{yc}\} = \begin{Bmatrix} 0 \\ 0 \\ 0 \\ -u_y \omega^2 \end{Bmatrix}_n \text{ and } \{m_{ys}\} = \begin{Bmatrix} 0 \\ 0 \\ 0 \\ -u_z \omega^2 \end{Bmatrix}_n$$

The relation between the 1st and the last element of the rotor bearing model can be written as:

$$\{Q'\}_N^R = [P'_N][F'_{N-1}][P'_{N-1}] \dots [F'_1][P'_1] = [U_o]\{Q'\}_1^L \quad (5.11)$$

where, $[U_o]$ is the modified overall transfer matrix.

The boundary condition (zero shear forces and bending moments) at the x - z and x - y planes on 1st and last element is:

$$\begin{Bmatrix} V_{zc} \\ M_{zc} \\ V_{zs} \\ M_{zs} \\ V_{yc} \\ M_{yc} \\ V_{ys} \\ M_{ys} \end{Bmatrix}_N^R = \begin{Bmatrix} V_{zc} \\ M_{zc} \\ V_{zs} \\ M_{zs} \\ V_{yc} \\ M_{yc} \\ V_{ys} \\ M_{ys} \end{Bmatrix}_1^L = \{0\} \quad (5.12)$$

Applying above boundary condition in the Eq. (5.11) and removing the last row, the equation is modified as:

$$\begin{bmatrix} d_{3,1} & d_{3,2} & d_{3,5} & d_{3,6} & d_{3,9} & d_{3,10} & d_{3,13} & d_{3,14} \\ d_{4,1} & d_{4,2} & \dots & & & & \dots & d_{4,14} \\ d_{7,1} & & & & & & & \\ d_{8,1} & & & & & & & \\ d_{11,1} & & & & & & & \\ d_{12,1} & & & & & & & \\ d_{15,1} & & & & & & & \\ d_{16,1} & \dots & & & \dots & d_{16,14} & & \end{bmatrix} \begin{Bmatrix} w_{zc} \\ \theta_{zc} \\ w_{zs} \\ \theta_{zs} \\ w_{yc} \\ \theta_{yc} \\ w_{ys} \\ \theta_{ys} \end{Bmatrix}_1^L = - \begin{Bmatrix} u_{3,17} \\ u_{4,17} \\ u_{7,17} \\ u_{8,17} \\ u_{11,17} \\ u_{12,17} \\ u_{15,17} \\ u_{16,17} \end{Bmatrix} \quad (5.13)$$

Symbolically Eq. (5.13) can be written as:

$$[U_o]\{Q'\}_1^L = -\{u'\}$$

Eq. (5.13) is solved with given rotational speed to obtain state vector at the left of 1st station. After determination of state vector of station 1, state vector quantities at any station can be determined using appropriate transfer matrices. The imbalance response is then computed for the specific station by a vector summation of the displacement terms (w_{zc} , w_{zs} , w_{yc} and w_{ys}) in the x - z and the x - y planes. These displacements for a specific station of the rotor are plotted from start to designed speed to study unbalance response.

5.2 The lumped inertia model of the prototype rotor

In the current analysis, the prototype rotor consisting of the turbine wheel, brake compressor and shaft is modeled with 23 stations (Fig. 5.5). The shapes, dimensions and density are different for various parts of the rotor. The choice to divide each part into several elements is based on its shapes, dimensions and materials. The division of the rotor is as follows:

- i. The turbine mounted on a protrusion at the cold end of the shaft (3 elements).
- ii. The stepped shaft region between the turbine and lower journal bearing (3 elements).

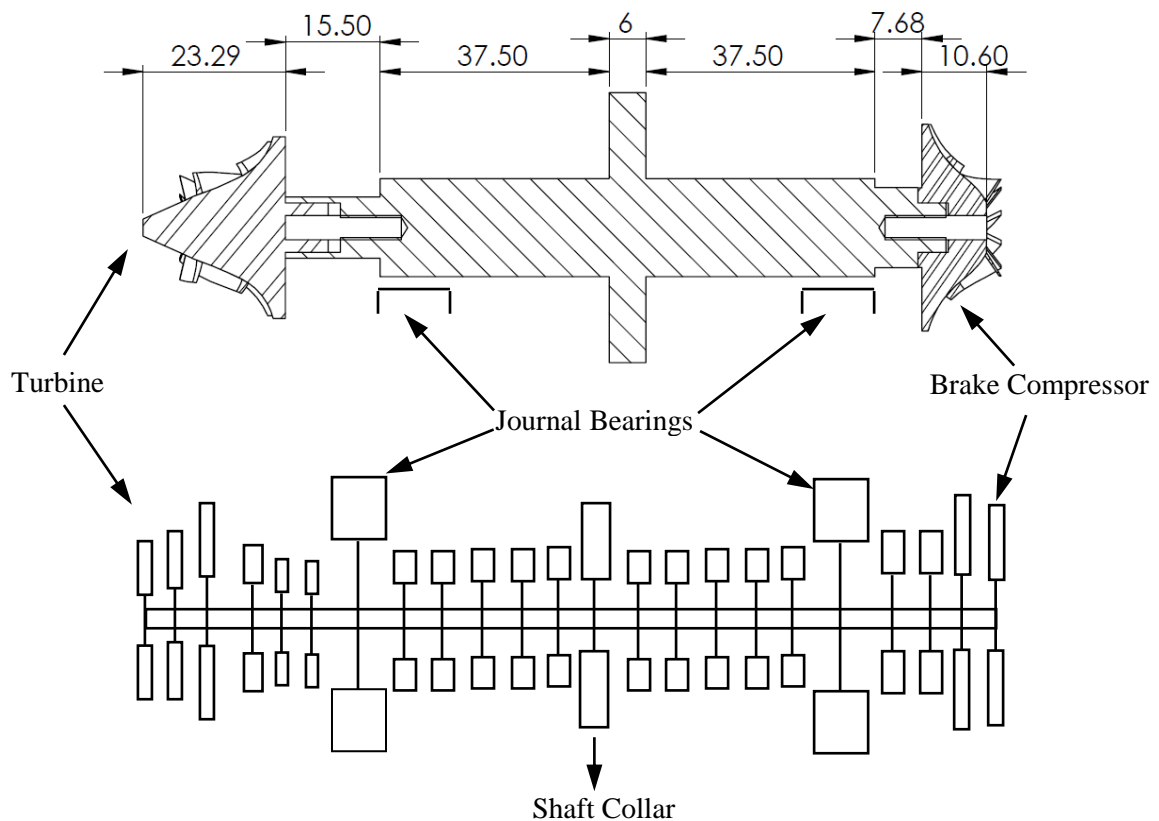


Figure 5.5: Inertial model of the prototype rotor.

- iii. Lower journal bearing (1 element).
- iv. Shaft region between lower journal bearing and collar (5 elements).
- v. The shaft collar (1 element).
- vi. Shaft region between the collar and upper journal bearing (5 elements).
- vii. Upper journal bearing (1 element).
- viii. The stepped shaft region between journal bearing and brake compressor (2 elements).
- ix. The brake compressor mounted on a protrusion at the warm end of the shaft (2 elements).

The inertial properties of all elements are calculated after the division of the rotor for further analysis. The inertial properties of the elements of turbine and compressor are determined from the solid models because of their complex shape. The inertial properties of cylindrical elements are obtained using the formula given in Table 5.1. The rotor data is given in Table 5.2, and they are used to calculate the station data for prototype rotor. Table 5.3 displays the inertia data for all 23 stations. The stiffness and damping of rotor element applicable only at the bearing location i.e. station numbers 7 and 19. The overall stiffness and damping coefficients of the journal bearings are determined from open literature[19] for the calculated bearing and compliane number as described in Chapter 3. The overall stiffness coefficient ($k_7=k_{19}$) at operating speed of 140,000 rpm is $4.12 \text{ E}+5 \text{ N/m}$ and the damping coefficient for similar bump foil is taken from literature ($c_{\omega 7}=c_{\omega 19}$) is $3.84\text{E}+5 \text{ N/m}$.

Table 5.1: Formula for inertial properties of cylindrical element[86].

Rotor inertial parameter	Formula
Mass of the element,	$M_n = \frac{\pi}{4} d_n^2 l_n \rho_n$
Area moment of inertia	$I_n = \frac{\pi}{64} d_n^4$
Transverse mass moment of inertia	$I_{Tn} = \frac{m_n}{12} \left(\frac{3}{4} d_n^2 + l_n^2 \right)$
Polar mass moment of inertia,	$I_{Pn} = \frac{m_n}{8} d_n^2$

where,

- d_n : Diameter of the element
- ρ_n : Density of rotor element
- l_n : Length of the element
- m_n : Mass of the element

Table 5. 2: The rotor data.

Rotor details	Quantity
Density of shaft(K-monel 500), ρ_s	7930 kg/m ³
Density of turbine and compressor (Aluminum 6061-T6), ρ_{Al}	2700 kg/m ³
Mass of turbine	8.0 g
Mass of brake compressor	10.7 g

Table 5.3: Station data of the prototype rotor.

Stn.no:	$M \times 10^{-3}$ (Kg)	l_n (m)	I_n (mm ⁴)	I_{pn} (kgm ²)	I_m (kgm ²)	E_{jn} (N/ m ²)
1	6.70E-04	7.29E-03	6.45E-11	3.04E-09	4.48E-09	6.98E+10
2	3.12E-03	8.00E-03	1.25E-09	6.22E-08	4.77E-08	6.98E+10
3	9.48E-03	8.00E-03	1.32E-08	6.15E-07	3.58E-07	6.98E+10
4	1.08E-02	9.00E-03	9.86E-10	3.42E-07	1.95E-07	1.79E+11
5	2.15E-03	3.25E-03	4.91E-10	2.69E-08	1.54E-08	1.79E+11
6	2.15E-03	3.25E-03	4.91E-10	2.69E-08	1.54E-08	1.79E+11
7	2.72E-02	1.60E-02	3.22E-09	8.69E-07	1.01E-06	1.79E+11
8	7.85E-03	4.63E-03	3.22E-09	2.51E-07	1.4E-07	1.79E+11
9	7.85E-03	4.63E-03	3.22E-09	2.51E-07	1.4E-07	1.79E+11
10	7.85E-03	4.63E-03	3.22E-09	2.51E-07	1.4E-07	1.79E+11
11	7.85E-03	4.63E-03	3.22E-09	2.51E-07	1.4E-07	1.79E+11
12	2.86E-03	3.00E-03	1.02E-09	5.15E-08	2.79E-08	1.79E+11
13	7.70E-02	6.00E-03	1.84E-07	1.86E-05	9.55E-06	1.79E+11
14	2.86E-03	3.00E-03	1.02E-09	5.15E-08	2.79E-08	1.79E+11
15	7.85E-03	4.63E-03	3.22E-09	2.51E-07	1.4E-07	1.79E+11
16	7.85E-03	4.63E-03	3.22E-09	2.51E-07	1.4E-07	1.79E+11
17	7.85E-03	4.63E-03	3.22E-09	2.51E-07	1.4E-07	1.79E+11
18	7.85E-03	4.63E-03	3.22E-09	2.51E-07	1.4E-07	1.79E+11
19	2.72E-02	1.60E-02	3.22E-09	8.69E-07	1.01E-06	1.79E+11
20	3.92E-03	3.84E-03	1.4E-09	8.28E-08	4.54E-08	1.79E+11
21	3.92E-03	3.84E-03	1.4E-09	8.28E-08	4.54E-08	1.79E+11
22	9.76E-03	5.28E-03	2.42E-08	8.57E-07	4.51E-07	6.98E+10
23	3.18E-03	5.28E-03	1.75E-09	7.51E-08	4.49E-08	6.98E+10

5.3 Computation of critical speeds

The critical speeds and mode shapes for the prototype turboexpander rotor have been computed based on theory explained in section 5.1.1. Damping at the bearings has been ignored during computation of critical speeds without introducing any appreciable error[2]. This reduce the size of overall transfer matrix to 4×4 . Also, critical speed is not affected by damping rather damping reduces the spring-mass system. A computer program

is written in Matlab to compute the critical speeds and the corresponding mode shapes of the rotor. The flow chart of the computer program is shown in Fig. 5.6.

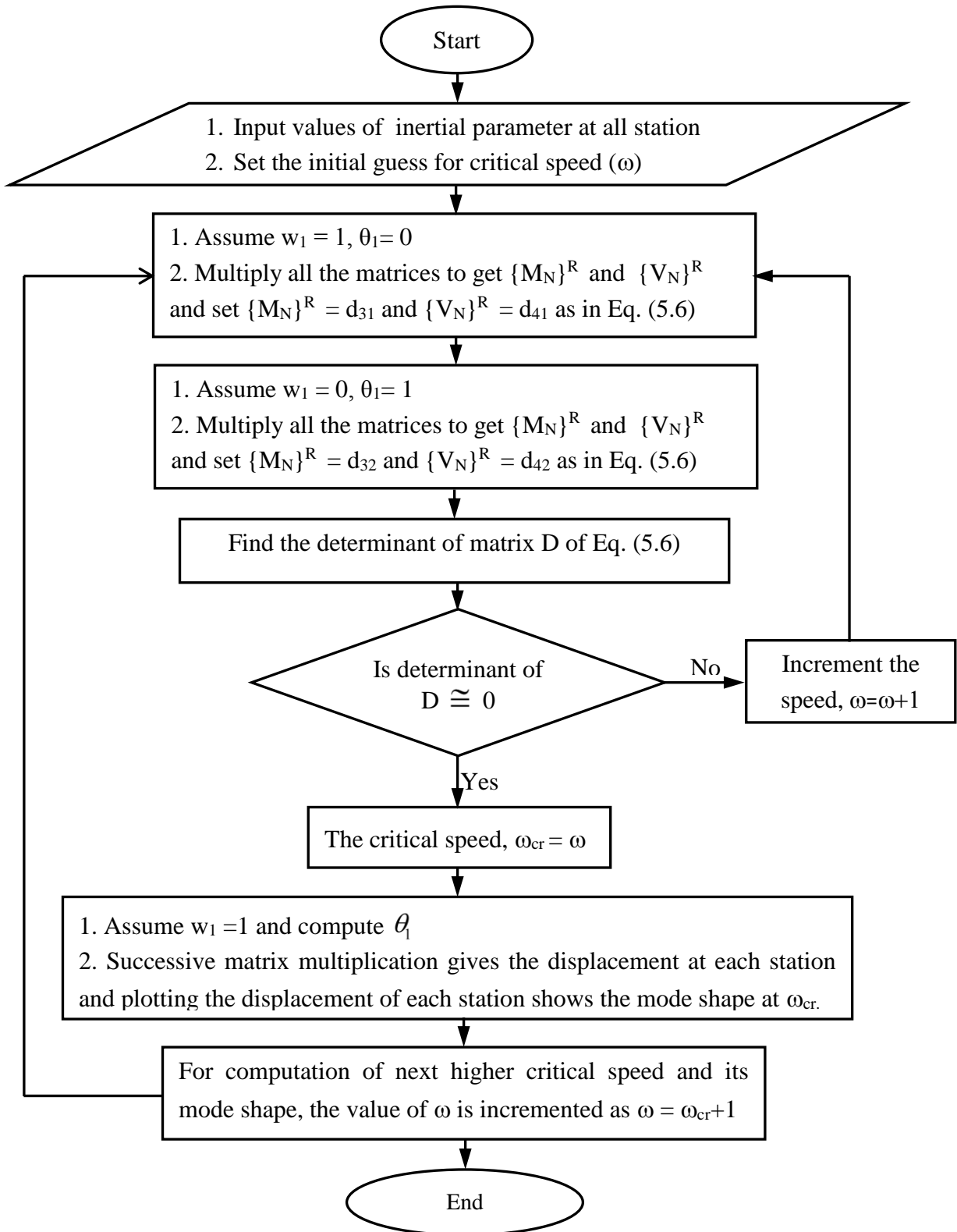


Figure 5.6: Flow chart for critical speed and mode shape calculation.

5.3.1 Simulation results and discussion:

The first four critical speeds for the prototype rotor are shown in Table 5.4. The mode shapes at four critical speeds are computed by normalizing on the first station of the rotor, whose amplitude is taken as unity. The mode shapes for 1st two critical speeds is shown in Figs. 5.7 and 5.8. These two vibration modes are rigid body modes; one is translatory whirl, and the other is conical whirl. These critical speeds are much below the designed rotor speed of 140,000 rpm. These critical speeds have the potential to destroy the journal bearings if rotation speed is close to them. Therefore, a preventive measure such as opening of the compressed air need to be faster to overcome the critical speed during the testing phase of the turboexpander. The mode shape corresponding to the third critical speed has the appearance of a half sine wave (Fig. 5.9). This critical speed is first bending critical speed and this speed is very important for the design of the high-speed rotor. The designed rotor is safe to run for current application because the speed for current application is 140,000 rpm, which is about 66% of 1st bending critical speed. Next higher critical speed is calculated only for the theoretical interest, whose mode shape is a full sine wave (Fig. 5.10).

Table 5.4: Computed critical speed of the rotor.

No.	Critical speed (Hz)	Critical speed (RPM)
1	446	26,752
2	489	29,353
3	3495	209,721
4	7853	471,129

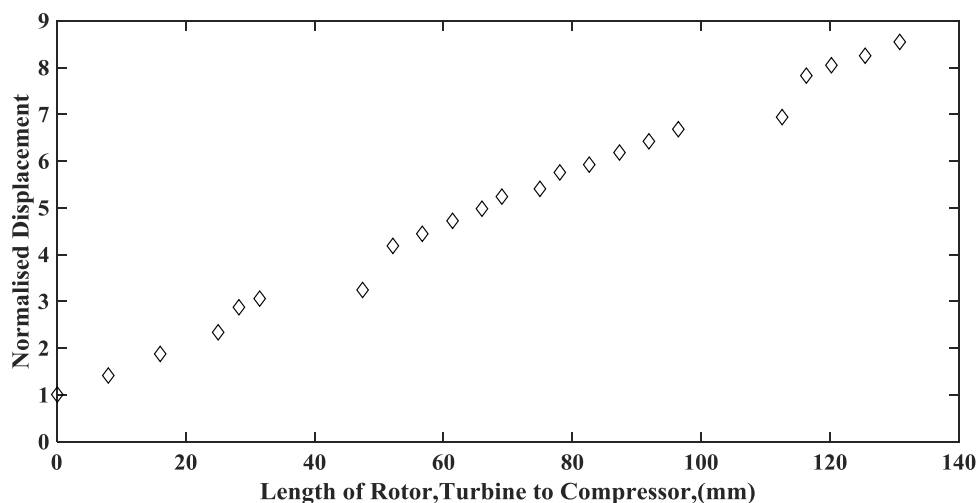


Figure 5.7: Mode shape at 1st natural frequency for the prototype rotor.

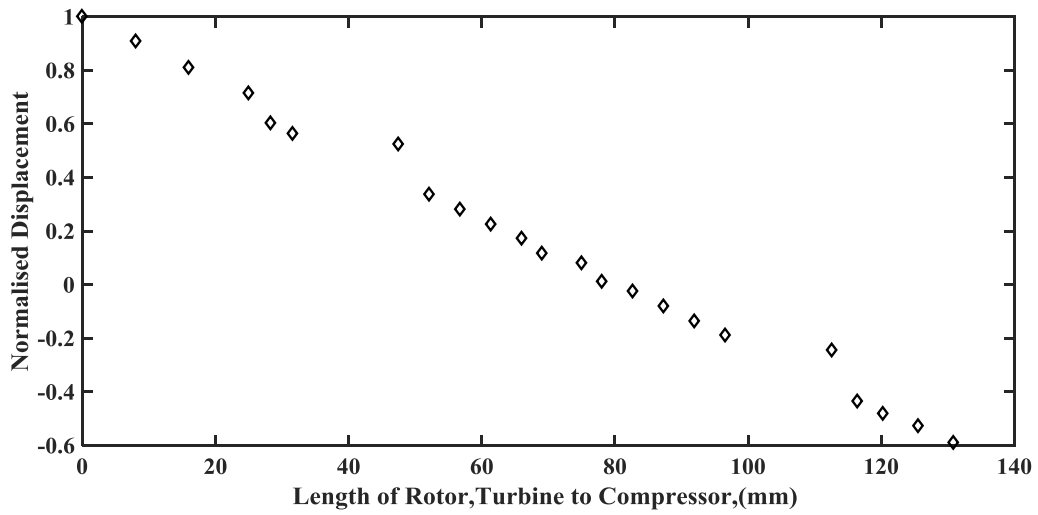


Figure 5.8: Mode shape at 2nd natural frequency for the prototype rotor.

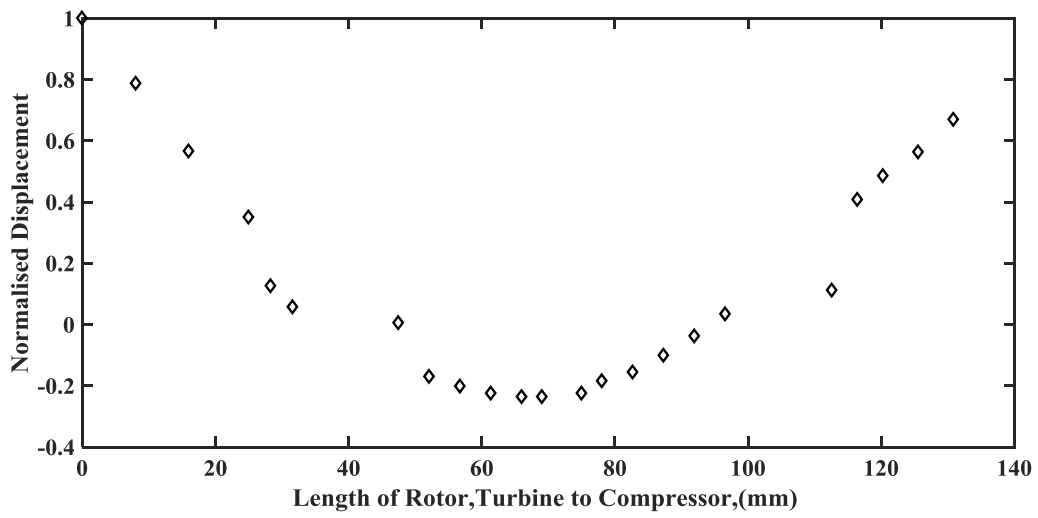


Figure 5.9: Mode shape at 3rd natural frequency for the prototype rotor.

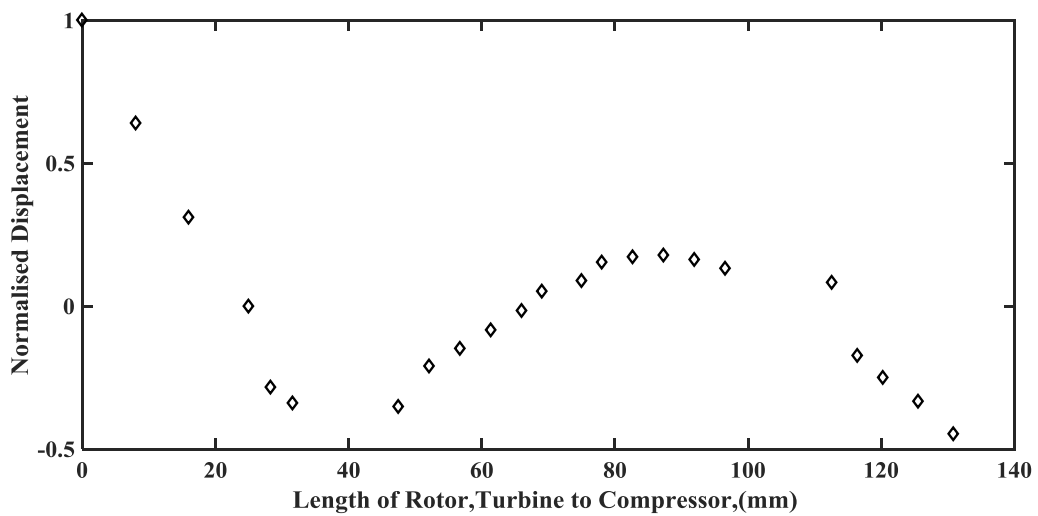


Figure 5.10: Mode shape at 4th natural frequency for the prototype rotor.

5.4 Computation of unbalance response

The unbalance response for the rotor of the prototype turboexpander is simulated using the above-explained theory presented in Section 5.1.2. A computer programme is written in Matlab and its flow chart is shown in Fig. 5.11.

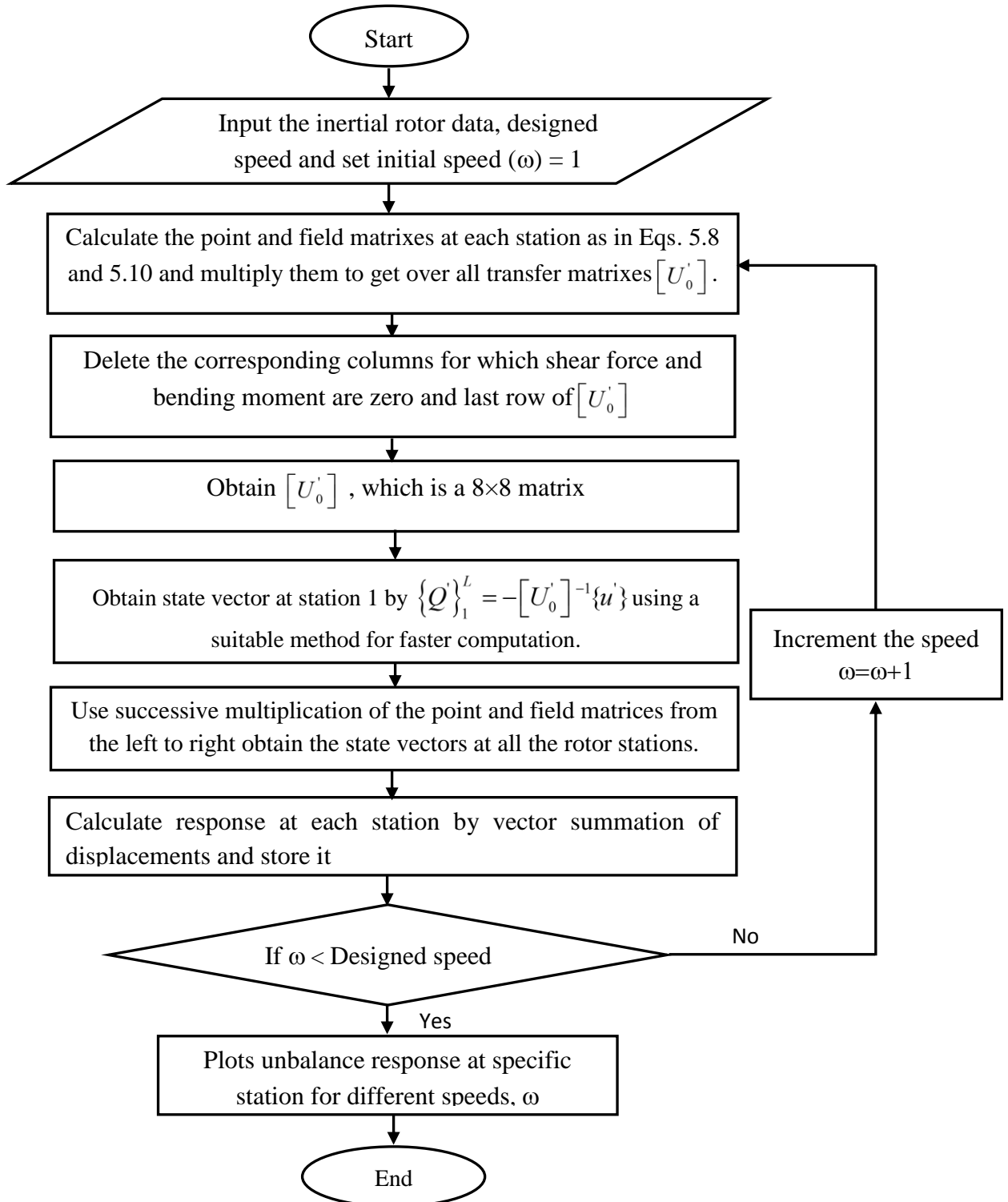


Figure 5.11: Flow chart for determination of unbalance response.

5.4.1 Simulation results and discussion:

The residual unbalance, after balancing, is less than 100 mg.mm measured at the planes of the bearings (as described in Chapter 6). The vibration responses at chosen stations (Table 5.5) are calculated from start to the designed speed (Figs. 5.12 to 5.16). The unbalance of 100 mg.mm at the plane of both journal bearings. High amplitude of vibration at the above chosen stations is likely to prevent the smooth operations of the turboexpander. These stations maintain low clearance during operation, so high response amplitudes increase the possibility of damaging the bearing surface, shroud area of the diffuser and blade of the turbine and compressor.

Table 5.5: Location of shaft for calculation of unbalance response.

No.	Location of the shaft	Station no
1	Journal bearing on turbine side	7
2	Journal bearing on compressor side	19
3	Expansion turbine	3
4	Compressor	22
5	Shaft collar	13

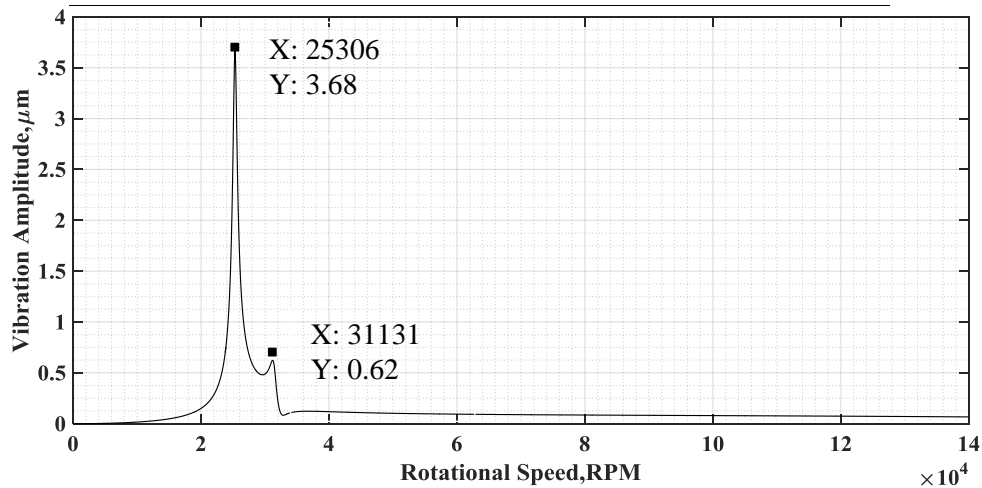


Figure 5.12: Unbalance response near journal bearing on turbine side.

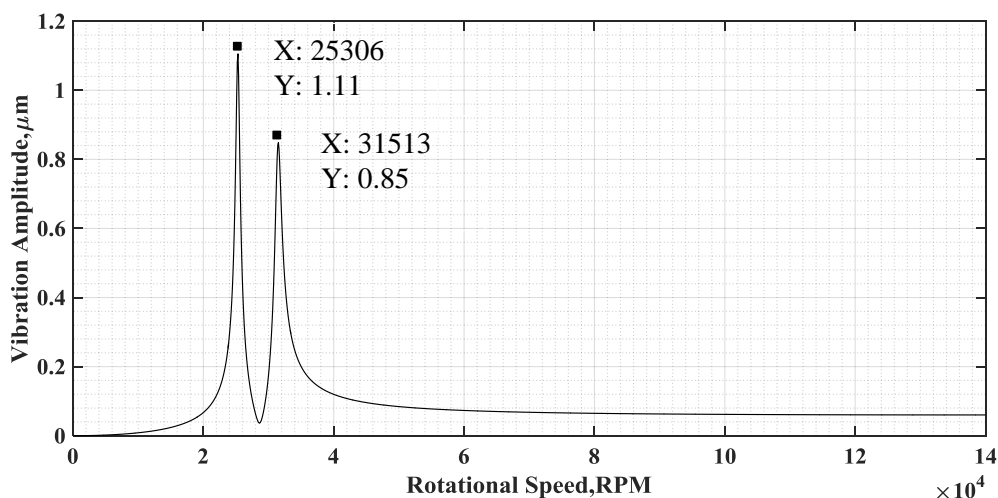


Figure 5.13: Unbalance response near journal bearing on compressor side.

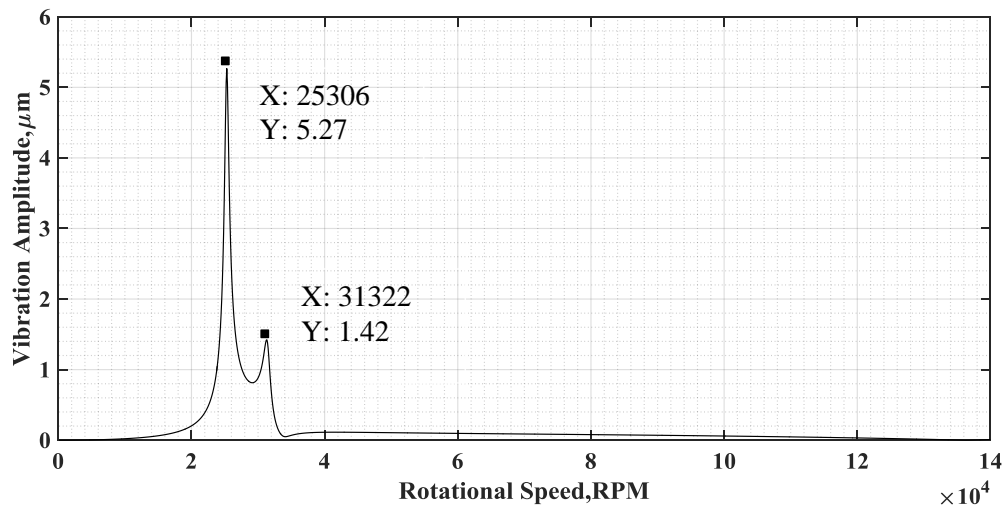


Figure 5.14: Unbalance response near expansion turbine.

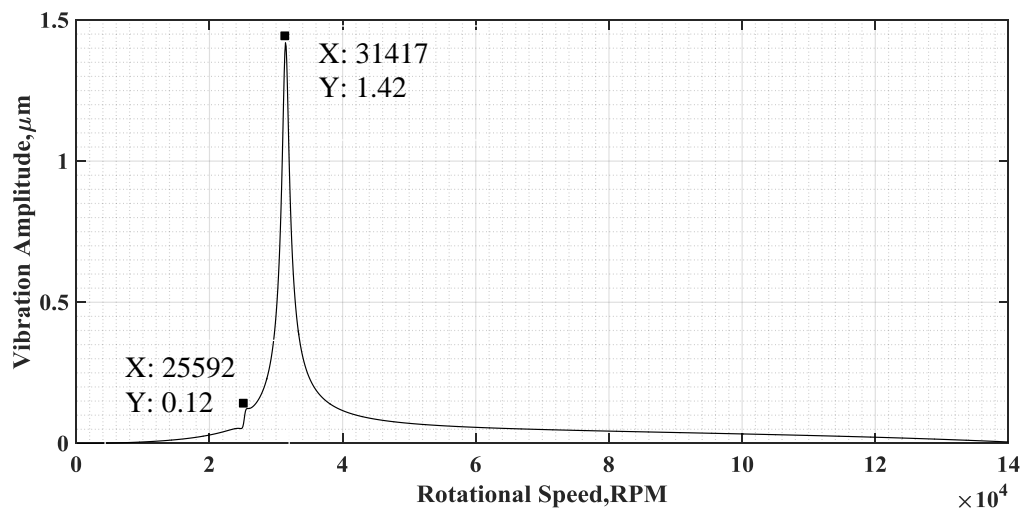


Figure 5.15: Unbalance response near brake compressor

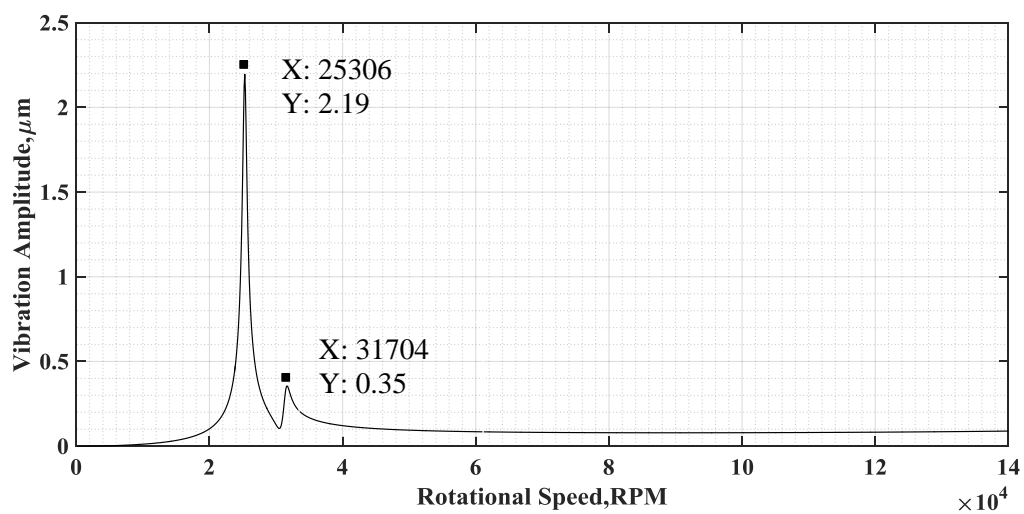


Figure 5.16: Unbalance response near shaft collar.

Results obtained from Matlab computer program shows that the maximum vibration occurs near the turbine (Fig. 5.14) at the speed of 25,306 rpm and this speed is near to the

computed 1st critical speed of the rotor. The maximum amplitude of vibration at this speed is 5.27 μm . Hence the clearance between turbine and shroud must be kept above this value to avoid contact between the turbine and shroud and prevent damage to the blade. This information will be useful in the design of the diffuser of the turboexpander.

The vibration near the journal bearings is found to be high at the speed of 25,306 rpm and the amplitude of vibration is 3.68 μm . This value must be lower than the radial clearing of the bearings. For current application the designed radial clearance is 25 μm . Hence the journal is safe for the designed rotor to run at the designed speed. The analysis of critical speed and unbalance response of the rotor-bearing system for current application is safe to operate at its designed speed of 140,000 rpm.

The rotordynamics has a significant impact on the stiffness of the bearings. A sensitivity analysis is done to establish, how critical speed and unbalance response are effected by bearing stiness. The sensitivity analysis is done with nominal stiffness and stiffness +/- 20%. The variation of critical speed and maximum unbalance response shown in Tables 5.5 and 5.6 respectively. The variation of 1st and 2nd critical speed nearly 2500 rpm, whereas there very small variations in higher critical speed. The variation of maximum unbalance response is nearly 1 μm . The sensitivity analysis provides an idea of stiffness range for correct operation of rotor.

Table 5.6: Sensitivity analysis for critical speed of the rotor.

	Critical speed (RPM) (With -20% nominal stiffness)	Critical speed (RPM) (With nominal stiffness)	Critical speed (RPM) (With +20% nominal stiffness)
1 st	23,935	26,752	29,297
2 nd	26,270	29,353	32,142
3 rd	209,693	209,721	209,750
4 th	4,71,028	471,129	471,415

Table 5.7: Sensitivity analysis for unbalance response.

Nominal Stiffness(k_b)	Maximum Unbalance Response(μm)				
	Lower Journal bearing	Upper Journal bearing	Near expansion turbine.	Near brake compressor	Near shaft collar
-20% of k_b	3.29	0.99	4.69	1.27	1.96
k_b	3.68	1.11	5.27	1.42	2.19
+20% of k_b	4.04	1.21	5.78	1.55	2.41

Chapter 6

Fabrication of Turboexpander with Gas Foil Bearings

A cryogenic turboexpander is considered to be a precision machine as it operates at high speed with very small radial clearances of 10 to 40 μm at its radial bearings and axial play limited to 50 μm . The low clearance demands balanced rotor with less than 100 mg.mm per plane and high surface finish (R_a less than 0.2 μm)[2]. Such low clearance brings challenges in dimensional and geometrical tolerance and demands micron scale manufacturing tolerance on the shaft, impellers, nozzles, diffusers, bearings, dynamic seal and its housings. To meet above challenge special attention has to be paid to the material selection, tolerance analysis, fabrication methodology and assembly of the turboexpander. This chapter explains the fabrication methodology of following important components of turboexpander and its assembly:

- (i) Rotor consists of shaft, expansion turbine, and brake compressor.
- (ii) Gas foils journal bearings and dies for forming journal bump foil.
- (iii) Gas foil thrust bearings and dies for forming thrust bump foil.
- (iv) Housing for bearings and other parts of turboexpander such as spacers, dynamic seals and locknuts.

The detailed fabrication issues of associated components for vertically oriented turboexpander are also addressed. The production drawings of all the components of the assembly are presented in the Appendix. Standard practice is followed for dimensioning and specifying the tolerances[2].

6.1 The rotor

The vertical rotor consists of a shaft with expansion turbine at the lower end and brake compressor at the upper end. The detailed design and fabrication of expansion turbine and the brake compressor using, Hasselgruber approach can be found in the Ph.D. dissertation of Balaji [1]. The materials for turbine and compressor are Aluminium alloy (Al-6160-T6) for its high strength to weight ratio. For current application, the rotor is vertically oriented to facilitates easy installation and maintenance from the top flange of a cold box. Additionally, vertically oriented rotor reduces radial load due to gravity, thus making it

possible to use aerodynamic journal bearings with low load carrying capacity with a low bearing surface area. The dimension of the shaft depend on the position of bearings, deformation, natural frequencies and heat transfer rate. Major features of the shaft, which control dimension of the rotor are described below:

- Bending and torque on the rotor at the designed speed.
- Location of shaft collar.
- Stress at the root of the collar.
- Bending critical speed of the rotor.
- Heat conduction between warm and the cold ends.
- Overall compactness of the system.

The diameter of the rotor is determined by the bending load and torque to be transmitted. For a small cryogenic turboexpander rotor, the torque, as well as the bending load, is small [2]. However, the operating speeds are very high, which demands a consideration of stress distribution, deformation, critical speed and stability, so the diameter is fixed by the stress, deformation and rotodynamic analysis of the rotor. The position of the collar is chosen to be in the middle as it reduces the unbalanced response at the bearings at high rotational speed. Steps at the both the ends of the shaft which provides a seat for the turbine and brake compressor and these steps also serve to locate the brake compressor and the turbine wheel in the radial direction. A step some distance away from the turbine wheel, reduces the cross section of the shaft and, consequently, reduces the heat transfer rate from the lower bearing area to the cold end.

The outer diameter of the collar, which provides as thrust bearings area is fixed from the consideration of centrifugal stress at its root and total deformation at the journal area. The stress and deformations analysis of the rotor is carried out using ANSYS (Figs. 6.1(a) and 6.1(b)). The yield strength (0.2% offset) for age hardened monel K-500 is 790 MPa. The design stress is calculated as 395 MPa with a factor of safety of order 2, accounting cyclic fatigue and other unknown effects. The maximum stress at the root of the collar is 189.6 MPa and this value is under the design stress of the rotor. The shaft material Monel K-500 is a nickel-copper alloy that combines the excellent corrosion resistance characteristic with the added advantage of greater strength and hardness. They maintain excellent mechanical properties at sub-zero temperatures. The radial deformation of the journal area is nearly 20 μm at its designed speed(Fig. 6.1(b)), so the radial clearance for both the journals should be higher than 20 μm . The radial clearance on both

the journal bearings are $25\ \mu\text{m}$ as described in Chapter 3. The major dimensions and the fabricated rotor are shown in Figs. 6.2(a) and 6.2(b). The detailed fabrication drawing of the shaft is shown in Appendix (Drawing. No: TEX-01).

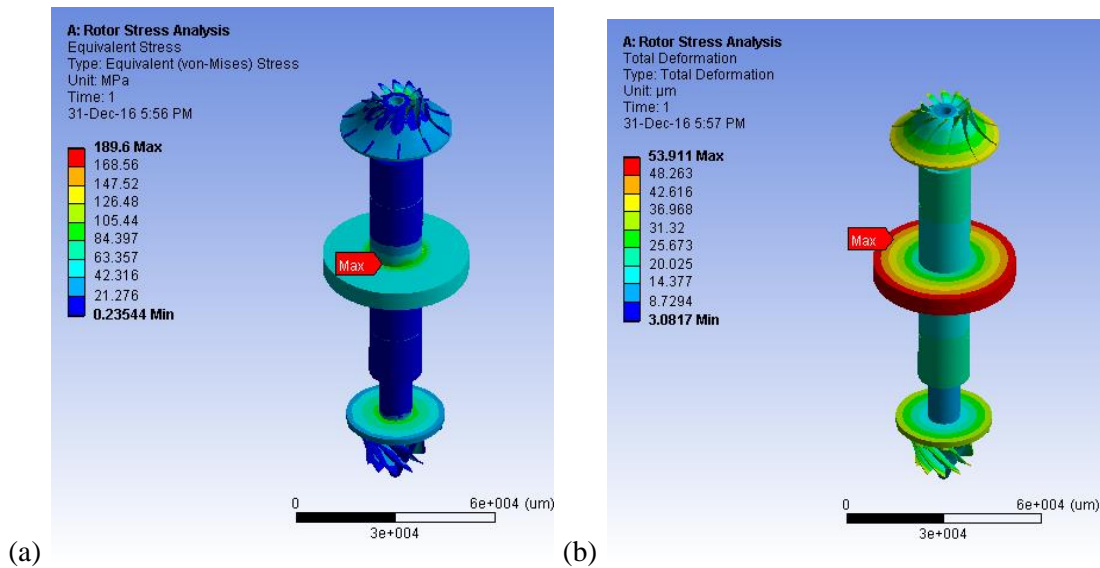


Figure 6.1: FEM analysis of rotor at designed speed: (a) Stress and (b) Deformation.

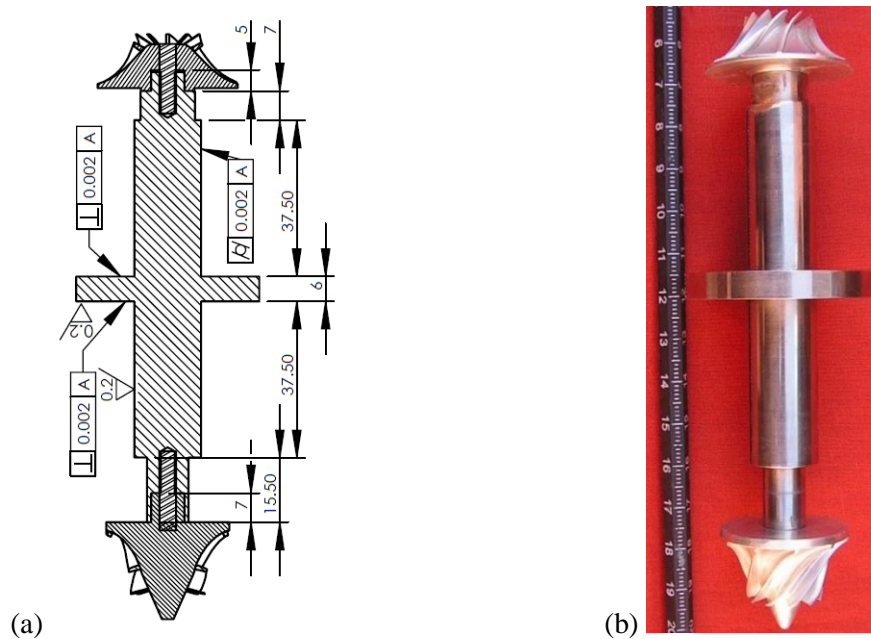


Figure 6.2: The prototype rotor: (a) with dimension (b) Assembled rotor.

6.1.1 Balancing

The most common source of vibration in a turboexpander is rotor imbalance [85]. The imbalance in a rotor arises because the center of mass does not fall on the geometric axis, which is also the axis of rotation. The imbalance occurs from machining inaccuracies and inherent inhomogeneity in the material. An additional imbalance is created, when a

turbine or a compressor is attached to a shaft, due to inherent asymmetry in the mass distribution of the blades. The rotating imbalance forces produce a whirling motion of the rotor known as synchronous whirl [85], which can be reduced only by balancing the rotor. The critical speed and unbalance response study in chapter 5 prevails that, the limit of unbalance at journal bearings of the rotor has to be 100 mg.mm.

Balancing is a method of removing material from different planes in the rotor, such that the mass center and the geometric center coincide. Although in practice real rotors can never be fully balanced owing to errors in measurement, However, the amplitude of vibration can be reduced significantly by dynamic balancing. Since the prototype rotor is designed to run at speed 66% below the first bending critical speed (described in Chapter 5), it would suffice to balance the rotors dynamically using two planes without taking account of shaft flexibility. For the trouble-free operation of cryogenic turboexpanders, a rotor imbalance of 600 mg.mm/kg is considered tolerable [2].

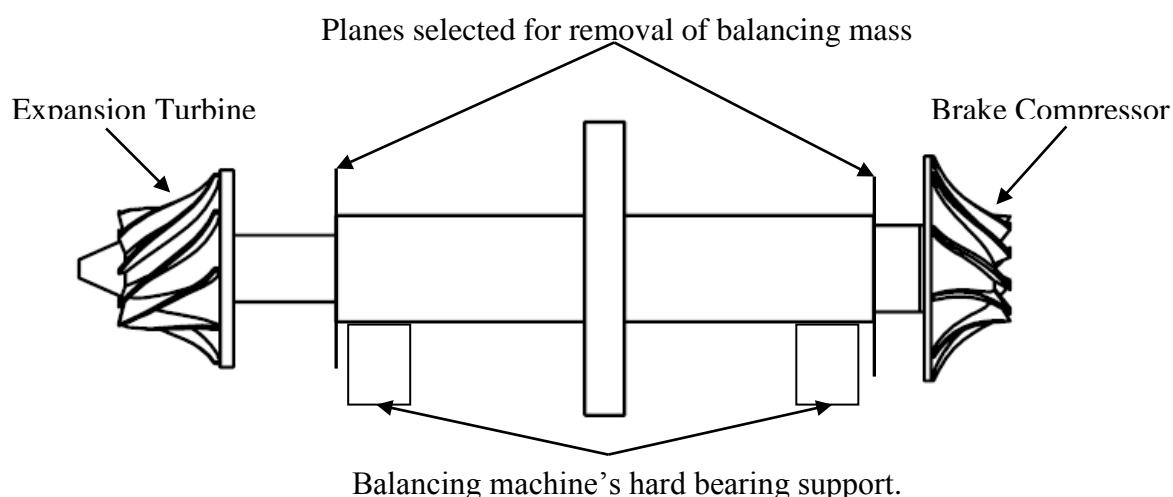


Figure 6.3: Schematic showing the planes and bearing support for balancing the prototype rotor.

The dynamic balancing of the rotor is done using Schenck Ro Tec GmbH make hard bearing type precision balancing machine at BARC, Mumbai. The balancing machine is meant for small rotors and able to balance less than 10 mg per plane. It is a dynamic balancing machine, with the following specifications:

Bearing type: Hard bearing

Make: Schenck, RoTec GmbH D-64273 Darmstadt

Type: HT08

Weight limit: 2 Kg

The entire rotor, consisting of the shaft, the turbine wheel, the brake compressor and the fixing screws at both ends, is taken together for balancing. A pair of rollers, which make

up the hard bearing, supports the journal at the bearing locations. The planes for balancing are shown in Fig. 6.3. A small color tape attached to the shaft acts as a reference or key phasor for phase measurements with a stroboscopic sensor. The rollers directly measure the force transmitted to the hard bearing. The rotor is balanced to within a limit of 100 mg.mm (within 10 mg at 6.5mm radius) of unbalance at both the planes at speed of nearly 2000 rpm. The balancing report for two prototype rotors is mentioned in Table 6.1 and the removed mass is shown in Fig. 6.4. After successful design, fabrication and balancing of rotor, next objective is to fabricate bearings for the rotor as described in subsequent sub-chapters.

Table 6.1: Balancing report of the prototype rotor

Rotor No	Location of balancing plane	Before balancing	After balancing
01	Turbine Side	31.5 mg @ 92 ⁰	6.45 mg @ 141 ⁰
	Brake Compressor side	37.8 mg @ 346 ⁰	7.31 mg @ 229 ⁰
02	Turbine Side	82.6 mg @ 228 ⁰	7.43 mg @ 17 ⁰
	Brake Compressor side	71.8 mg @ 215 ⁰	6.51 mg @ 88 ⁰

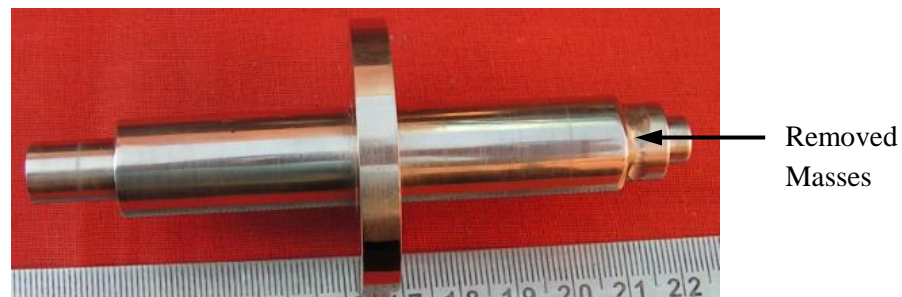


Figure 6.4: Rotor with removed unbalance mass.

6.2 Fabrication of gas foil journal bearings

Four basic elements for manufacturing of bump type journal or radial foil bearings are top foil, bump foil, bearing base and an arrangement to join both foils to the bearing base (Fig. 6.5). The top foil is smooth foil and is placed between the rotor and the bump foil. The relative velocity and a converging wedge between the rotor and the smooth foil are responsible for the generation of aerodynamic pressure, bump foil provides an additional stiffness to the bearings, and the pin and screw are used to assemble the foils and bearing base together. This section discusses details fabrication methodology for gas foil journal bearings.

The fabrication methodology for gas foil journal bearing is shown in Fig. 6.6, where the bearings base, top smooth foil, and bump foils are made separately and

assembled with the help of pin and screw. Spot weld with the bearing base can be replaced with the pin and screw arrangement [53] but welding may distort the thin foils, so the mechanical arrangement is preferred.

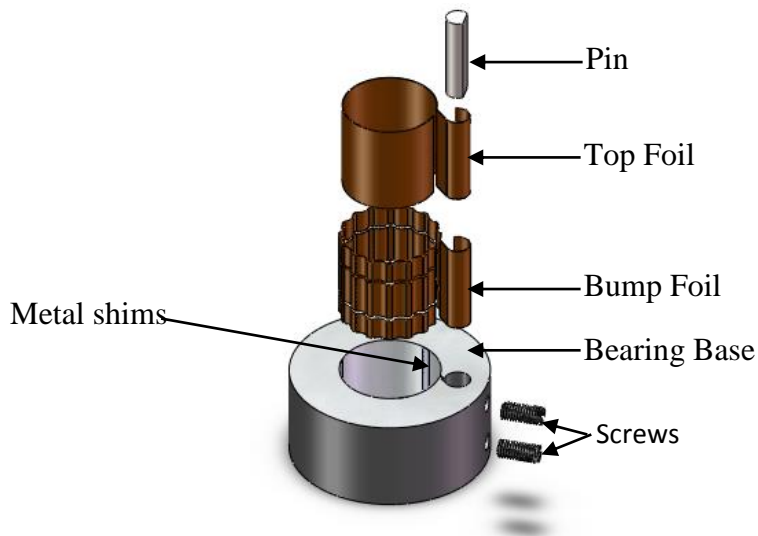


Figure 6.5: Parts of gas foil journal bearings.

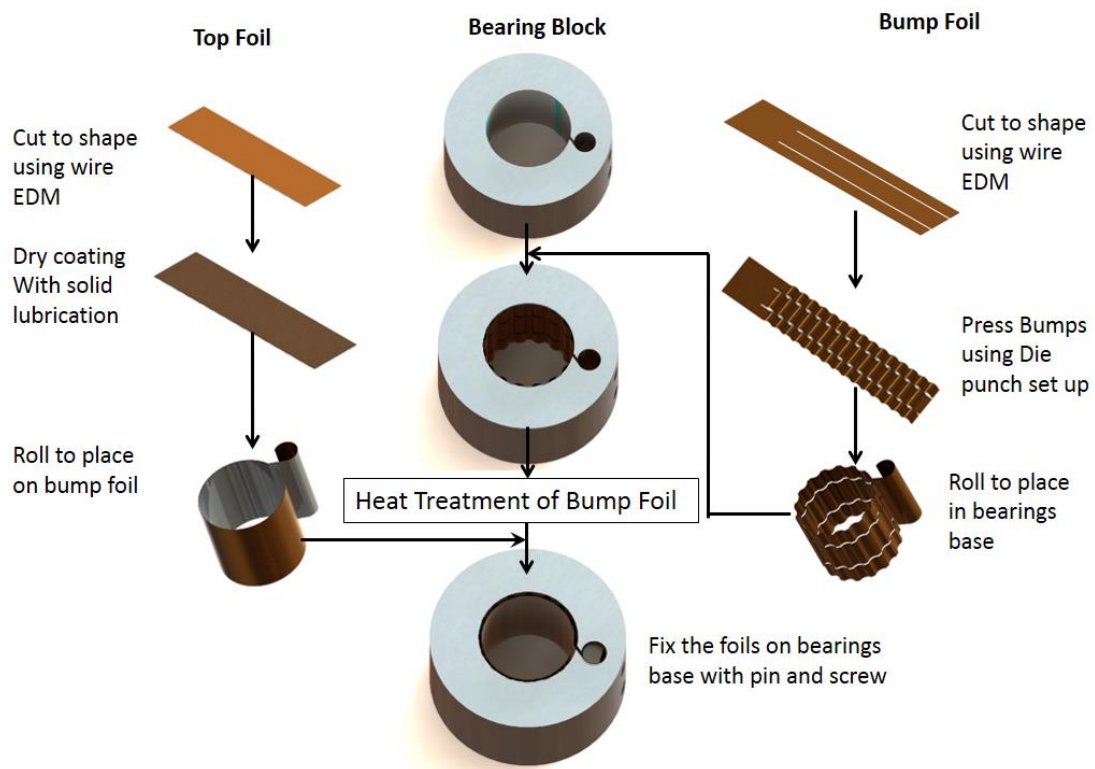


Figure 6.6: Fabrication methodologies of gas foil journal bearings.

6.2.1 Fabrication of bearing base

The aerodynamic pressure between top smooth foil and rotor depends on the convergent wedge for the lubricants. Gravity forms the converging wedge in the horizontal rotor, but for vertically oriented rotors the wedging is developed by placing multiple numbers of

metallic shims in bearing block as shown in Figs. 6.7 and 6.8. The bearing base is fabricated with three equidistance shims of 10 μm heights and width of 4.5 mm. The width of the shims should be greater than the pitch of the bump foil to avoid shims to fall under the bump area. The bearing base is also supplied with an axial hole for pin and screw arrangement to attach the foils on the bearing base as shown in Fig. 6.7. Bearings base with a single axial hole (Fig. 6.7) and two holes (Fig.6.8) are fabricated. The single hole has some difficulties during assembly of the foils with bearing base compared with two axial holes on bearing base. However, the tests are done using both type of bearing base. The detailed fabrication drawing for the bearing base is given in Appendix (TEX-03 and TEX-04).

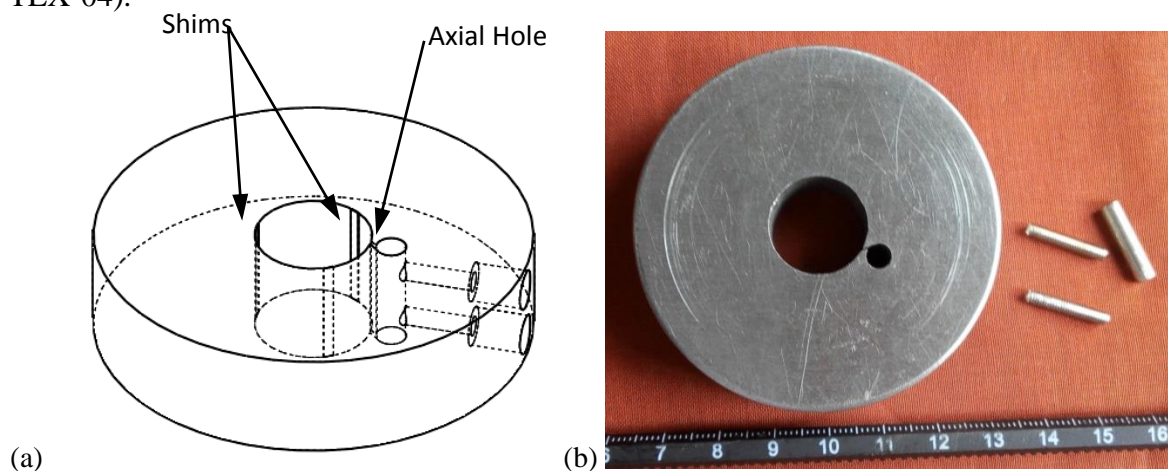


Figure 6.7: Prototype journal bearings base with single axial hole: (a) Isometric view (b) Actual photograph.

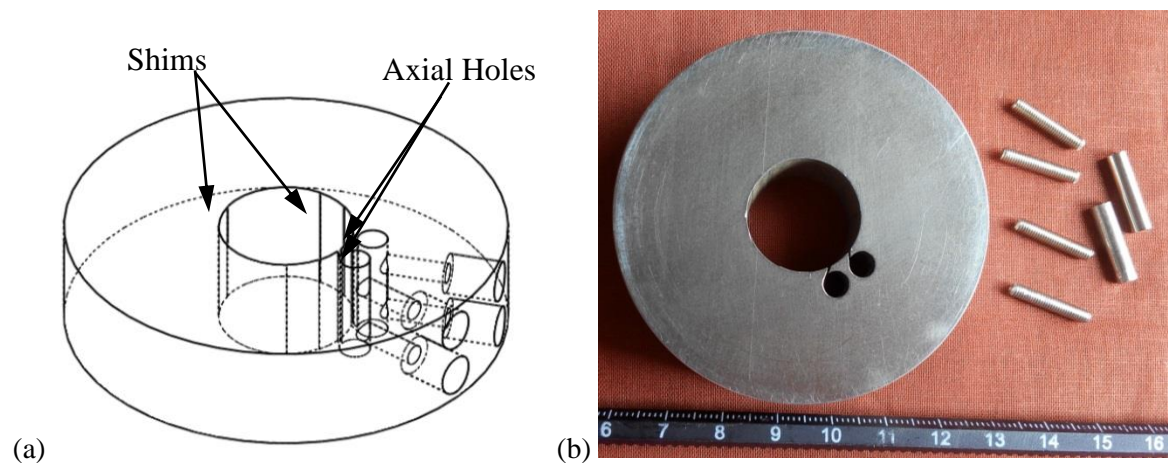


Figure 6.8: Prototype journal bearings base with two axial holes: (a) Isometric view (b) Actual photograph.

6.2.2 Foil Materials

The top and bump foil material significantly affects the bearing performance. So the selection of suitable foil material plays a vital role in designing foil bearings. The bump

foils should be compliant and offer sufficient damping for the rotor bearing system. In the literature for high-temperature application, Inconel is an adequate solution but for application for lower operational temperature stainless steel and copper alloys are cheaper alternatives [54]. The load carrying capacity is compared for various materials of bump foils and phosphor bronze is selected for current application as described in Chapter 3. Coulombs damping characteristics is found to be better for copper alloy such as phosphor bronze compared to stainless steel. So for the current application, the bump and top foils are selected to be phosphor bronze. Table 6.2 shows the chemical composition of foil material obtained from sample study in scanning electron microscope using energy-dispersive X-Ray spectroscopy. Table 6.2 also includes the mechanical properties of the foils.

Table 6.2: Chemical composition and mechanical properties of Phosphor Bronze.

Parameters	Phosphor Bronze
Chemical compositions (Weight %)	Cu 87.83, Sn 3.34, P 0.29, Fe 0.46 , C 1.91, O 5.87 Zn 0.18, Pb 0.042
Elastic Modulus	114 GPa
Density	8800 kg/m ³
Coefficient of Thermal Expansion	18.5 $\mu\text{m}/\text{m}^\circ\text{C}$

Springback is a measure of geometric change made to the workpiece at the end of the forming process when the workpiece is released from the forming load. This springback directly affect the dimensional accuracy of a finished product. The magnitude of a springback depends on the yield strength, Young's modulus, thickness, initial and final bending radius of the workpiece. For foil materials, the experimental springback in bending have been fitted with the relationship expressed in equation 6.1 [87].

$$\frac{R_i}{R_f} = 4 \left(\frac{R_i Y}{E t} \right)^3 - 3 \left(\frac{R_i Y}{E t} \right) + 1 \quad (6.1)$$

Where

- R_i : Initial radius, mm
- R_f : Final radius, mm
- t : Thickness of the foil, mm
- Y : Yield strength, N/mm²
- E : Young's modulus, N/mm²

The springback is calculated for different foils (Table 6.3) to study its behaviour and suitability of the material for gas foil bearings. The springback ratio for Inconel X-750 is found to be high, which indicates there is very small springback during forming and very effective for high-temperature applications, however, the cost of Inconel foil of smaller thickness is very high and unavailable in local markets. The springback ratio for stainless steel is found to be better than phosphor bronze. However, phosphor bronze is preferred for current application, as it is a bearing material and used for spring applications too.

Table 6.3: Spring back ratio of various foil material.

Sl No	Material	Springback Ratio $\left(\frac{R_i}{R_f}\right)$
1	Phosphor bronze	0.862
2	Stainless steel	0.891
3	Beryllium bronze	0.793
4	Inconel X 750	0.923

6.2.3 Fabrication of smooth top foil for journal bearings

The top smooth foils are 0.1 mm thick, and they can be easily cut to shape by shearing mechanism, but there is a possibility of edge distortion [53]. Wire electrode discharge machining (Wire EDM) is chosen to cut the foil to the desired shape to avoid edge distortion. Several layers of 0.1 mm thick annealed phosphor bronze foils are stacked together and pressed under the hydraulic press to make all foils flat and avoid any inaccuracy in the dimension in the process of machining. About 20 layers of foils are stacked together between two aluminum plates of 3 mm thick and cut to the desired size using wire EDM.

These foils will have a surface contact during start and stop of the rotor, so a layer of solid lubricant (MoS_2) is sprayed carefully on one of the faces of the top foil. The thickness of solid lubricant layer was maintained between 4 to 5 μm . The leading end of top foil is rolled before the spray coating is applied (Figs. 6.9 (a) and 6.9 (b)). The production drawing for the top foil is documented in Appendix (FOIL-01).

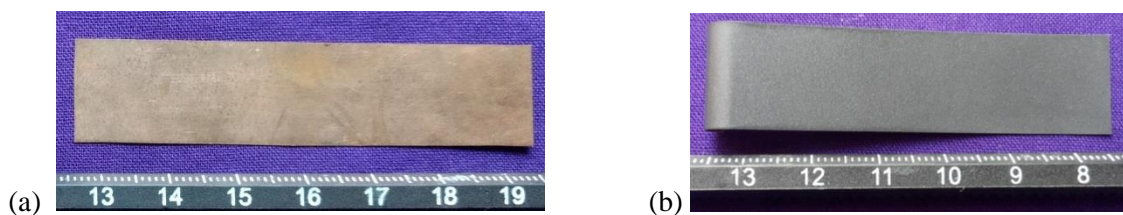


Figure 6.9: Top foil: (a) After wire EDM cut (b) Rolled and coated with MoS_2 .

6.2.4 Fabrication of journal pre-form bump foil

A pre-form bump foil is a smooth foil with multiple numbers of slits. These foils are cut to the shape with two slits before performing forming operation over them to fabricate bumps (Fig. 6.10). The slits are cut to ensure sufficient material flow during pressing operation and to avoid axial misalignment during assembly of foils. The detailed fabrication drawing for the preformed foil is specified in Appendix (FOIL-01). A bunch of thin foils were stacked together and cut to the dimensions using wire EDM, same as the top smooth foil.

Fabrication of bumps over the pre-form foil with desired dimensions and uniformity is necessary for gas foil bearings. The dimensions of the bumps for journal foil bearings are determined in the aerodynamic analysis of journal foil bearings (as described in Chapter 3). Table 6.4 shows all the bump parameters and Fig. 6.11 shows all the parameters for the designed bumps.

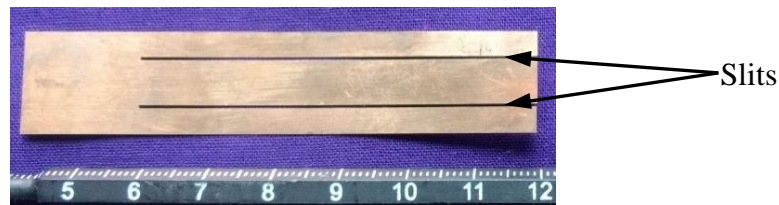


Figure 6.10: Preform foil before forming of journal bumps.

Table 6.4: Dimensions of bumps for journal bearings

Bump Parameters	Values
Thickness(t), mm	0.1
Radius(R), mm	1.57
Height of bumps(H), mm	0.61
Pitch(P), mm	4.2
Width(W), mm	4 and 8

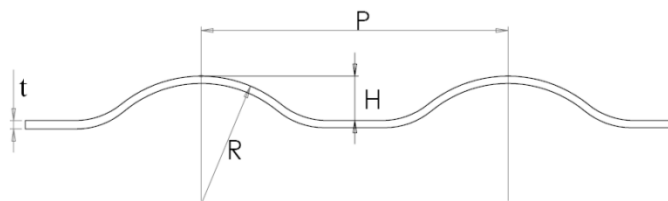


Figure 6.11: Parameters of journal bump foil.

Fabrication of bumps needs a pair of dies and a thin foil. The thin foil is pressed by placing it between the dies. Several publication in open literatures have discussed

fabrication methodology of bump foil using a rigid bottom die and a flexible top die[53, 55]. This chapter discusses the fabrication of bump foil for journal bearings using two different set of dies. The die set designed in 1st phase is with a rigid bottom die and a flexible top die. The issues faced with the die set in the 1st phase such as edge distortion and unequal bump height motivated to redesign of a die set in the 2nd phase with the rigid bottom and top die to get uniform and accurate bump shapes. Both methodologies are discussed in subsequent sub-chapters. The representation of generation I journal bump foil with slits is shown in Fig. 6.12, which needs to be fabricated for current application.

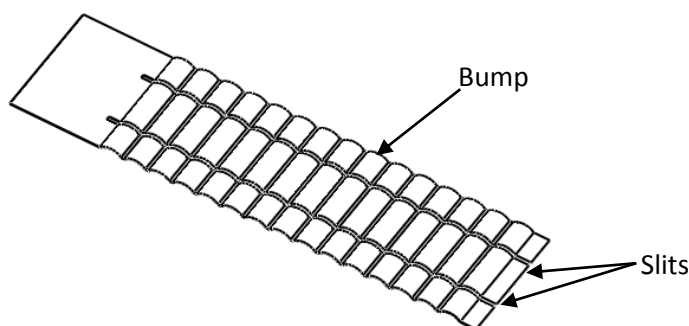


Figure 6.12: Designed generation I bump foil for journal bearings.

6.2.5 Journal bump foil using rigid bottom and flexible top die

The schematic of a cost effective die set with the rigid bottom and flexible top die is shown in Fig. 6.13. The rigid bottom die is a metal die, and the flexible top die is a rubber sheet. The rigid or metal die with corrugated bump shape consisting of multiple die strips is used to make bump foils. The thin foil is placed in between the metal bottom die and rubber sheet. On the top of the rubber sheet, a thick metal plate is placed to ensure uniform pressure to the rubber sheet. During the pressing operation, the flexible rubber sheet applies a hydrostatic pressure on the thin smooth foil and the foil takes the shape of bumps. The extent of forming load to be applied is done experimentally to ensure complete deformation.

The rigid bottom die consists of a set of individual bump die strip, placed inside a tooling frame and locked with the help of locking screw. Fig. 6.14 shows the tooling developed for the fabrication of both generation II bump foil and I. For current application generation I is fabricated and tested. Provision for generation II is designed for future use. The lower die is usually manufactured of a heat resistant alloy to allow the tooling to withstand thermal fatigue [53]. For the present application, the rigid bottom bump die and the top metal plate are fabricated using stainless steel material, SS304 (Figs. 6.15(a) and 6.15(c)). The size of designed die is larger than the current requirement to ensure its use in

future for bearings of larger dimension. The corrugated bumps over the die strip are prepared using wire EDM. The detailed fabrication drawing for the die is presented in Appendix (DIE-01 and DIE-03).

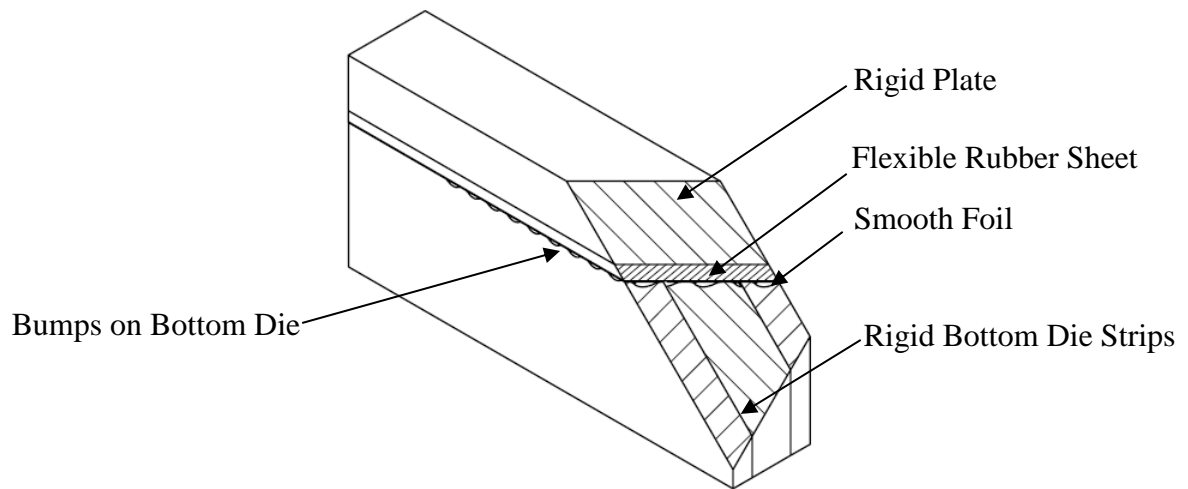


Figure 6.13: Schematic of tooling for fabrication of bump journal foil with top flexible rubber sheet.

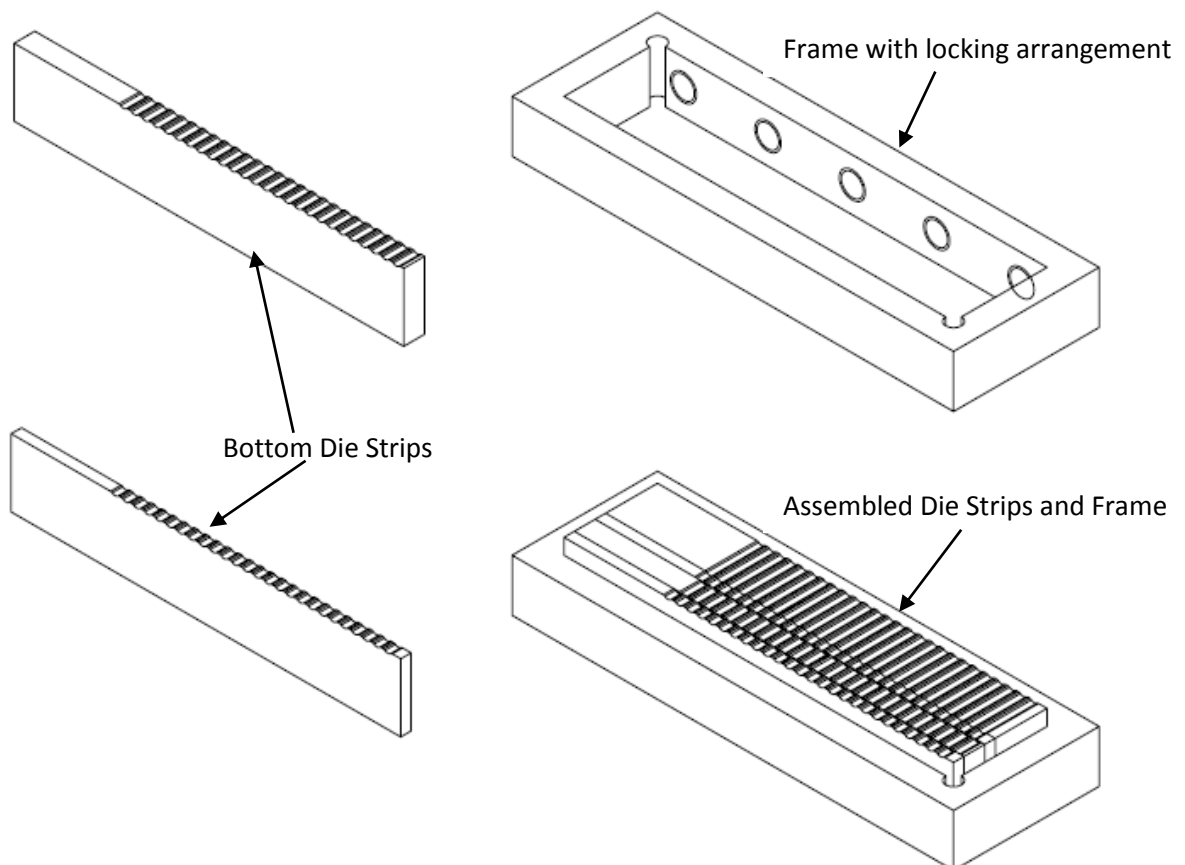


Figure 6.14: Lower rigid die for fabrication of bump journal foil.

The flexible top die for the 1st phase of die set is a rubber sheet. Two different types of rubber sheets are tested for various thickness, and they are PTFE and silicon sheets for the

thickness of 2 mm, 3 mm and 4 mm. The PTFE sheet available in the local market is harder than silicon sheet, and during the forming operation, the bump foil is found to be distorted and inaccurate. The silicon rubber sheet with 2 mm thickness shows uniform bump formation compared to PTFE. So for the current tooling set, the silicon rubber sheet is selected as a flexible punch (Fig. 6.15 (b)).

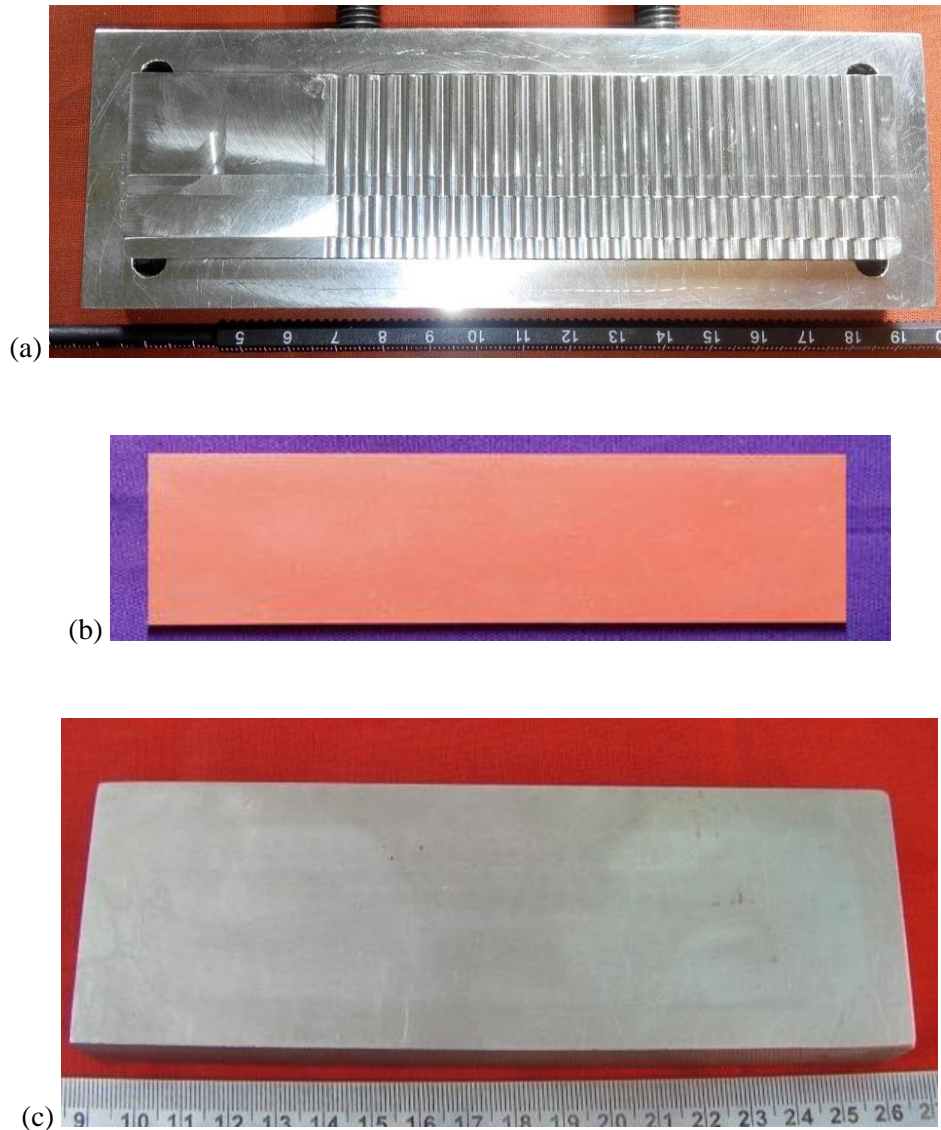


Figure 6.15: Actual photograph die set: (a) Bottom rigid die (b) Rubber sheet (c) Top metal plate.

Fig. 6.16 shows the tooling setup in a hydraulic press forming of the bump foil. The pre-form foil with two slits is fixed on the bottom die with an adhesive tape. Then over the pre-formed foil, the silicon rubber sheet and the top metal plate are placed. During pressing operation, it was found that the foil is sticking with the silicon rubber, so a layer of teflon sheet is placed above the foil. A series of pressing operations are undertaken to determine the actual forming load necessary to achieve satisfactory bump

dimensions. Table 6.5 shows the deformation outcome for a various forming load from 100 to 300 kN.

Table 6.5: Effect of forming load on journal bump formation

Forming load (kN)	Outcome
100	Minor deformation
150	Moderate deformation
200	Moderate deformation
250	Complete deformation
300	Crack on the edges of the bump



Figure 6.16: Photograph of journal bump forming operation.

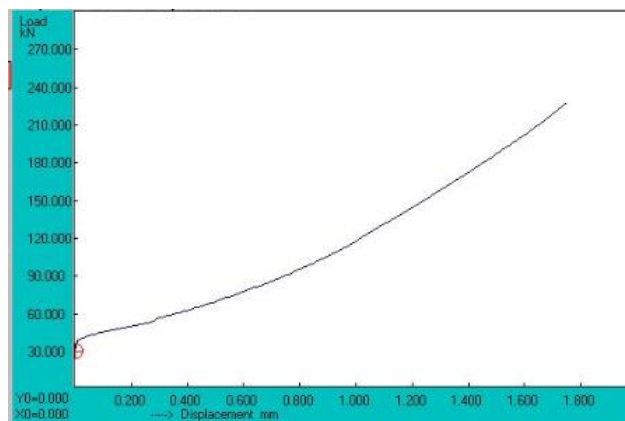


Figure 6.17: Load displacement curve during journal bump formation.

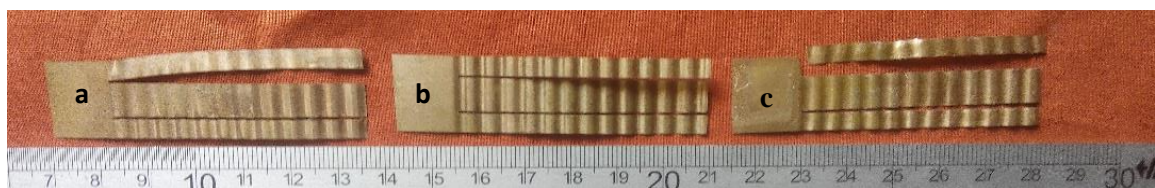


Figure 6.18: Defective fabricated generation I bump foil.

The loads less than 250 kN shows moderate bump formation whereas load above 300 kN damages the rubber layer as well as the bump foil. A few more experiments on forming load between 200 and 250 kN assisted in determining actual forming load. The forming load for current tooling system was found to be 230 kN with a displacement of 1.8 mm (Fig. 6.17). Defective fabricated bump foil for journal bearing is shown in Fig. 6.18.

It is worth mentioning that drawbacks for this fabrication methodology of bump foil using flexible top die are as follows:

- i. The forming load is determined by series of experiment, which is time-consuming, and susceptible to make errors.
- ii. Finite element method (FEM) analysis of bump formation using flexible rubber top die is complicated.
- iii. The spring back formula does not work accurately, and spring back was found to be larger than the theoretical calculation.
- iv. The heights of the bumps across the foil are found to be non-uniform and edges are distorted.

To address the above-discussed issues, both the dies are chosen to be rigid and detail FEM analysis was done to study the behaviour of bump formation, which is documented in the next sub-chapter.

6.2.6 Journal bump foil using rigid top and bottom die

The major issues faced by a flexible top die as described in the previous section can be overcome by use of a rigid top die. With both the dies being the rigid, application of heat during bump forming operation is possible to reduce springback effect and maintain uniformity in the bump height [53]. The decision to go for rigid top die in 2nd phase also makes the die design process relaxed by the use of commercial software such as ANSYS LS-DYNA and DEFORM 3D. These software packages help to predict the forming load needed for bump formation, stress distribution over bump foil and damage to bump foils for various forming parameters. The schematic of the bottom and top die with the workpiece is shown in Fig. 6.19.

The FEM analyses for bump formation is carried using DEFORM 3D. The 3D models for foil, top, and bottom dies are created using SolidWorks (Fig 6.19). The profile of bumps on the bottom die is kept the same as the bump dimension. However, the profile of bumps on the top die is reduced to minimize the springback effect. The detailed profile of the bump for the die is presented in Appendix (DIE-04 and DIE-05). Table 6.6 shows

the input parameters for simulation of bump foil formation and these parameters were used to simulate the load prediction on the top die, deformation, effective stress and damage on the workpiece or bump foil. Fig 6.20 shows the predicted load during forming operation is 14.8 kN for phosphor bronze. The simulated results such as deformation, effective stress and damage of the forming are shown from Figs 6.21 to 6.23 for workpiece material of phosphor bronze. The effective stress is found to be higher than the yield stress of phosphor bronze, and the bumps are formed as per prerequisite with no damage in the bump area.

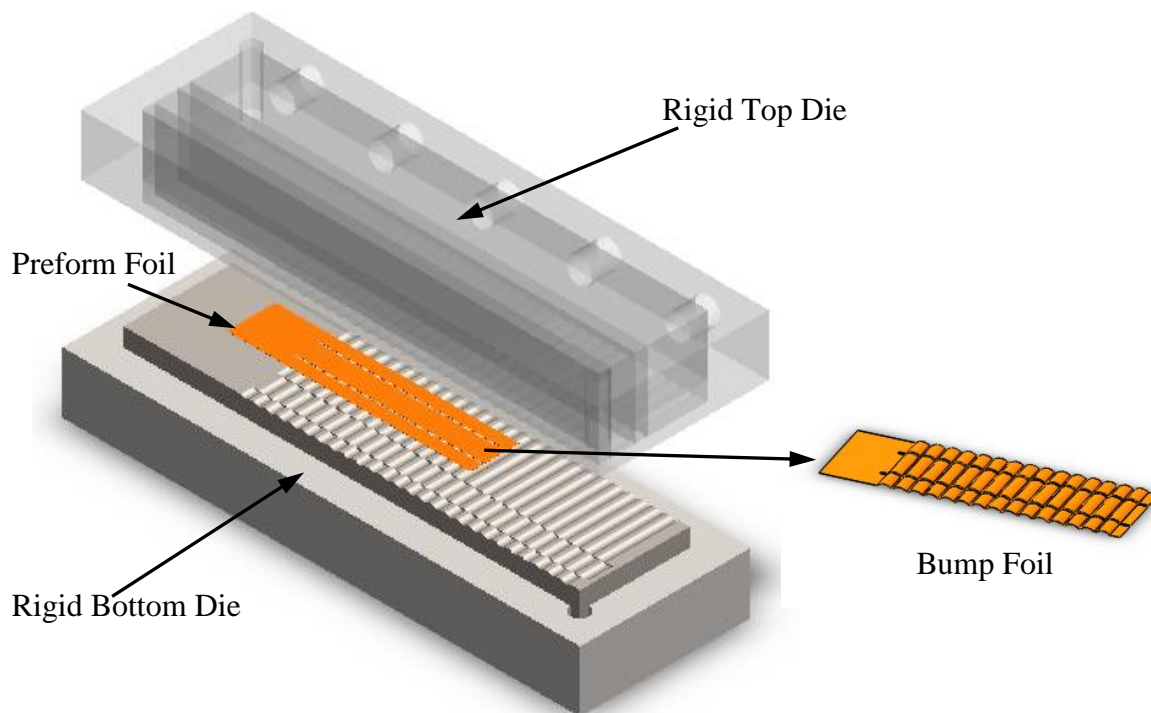


Figure 6.19: Tooling for fabrication of journal bump foil with rigid top and bottom dies.

Table 6.6: Input parameters for forming simulation of journal bump.

Sl No	Input Parameter	Values
1	Workpiece materials	Phosphor bronze
2	Top die/Primary die	Rigid
3	Bottom die	Rigid
4	Movement of the workpiece	Vertically downward
5	Movement of top die	Vertically downward
6	Movement of bottom die	Fixed
7	Stroke speed of the top die	0.1 mm/s
8	No of steps	100
9	Stop conditions	Release the forming load after traveling 0.61 mm

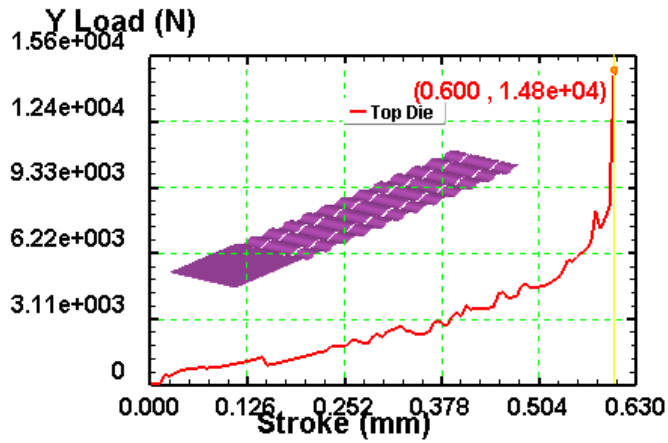


Figure 6.20: Load prediction curves for the top die during bump forming simulation over phosphor bronze.

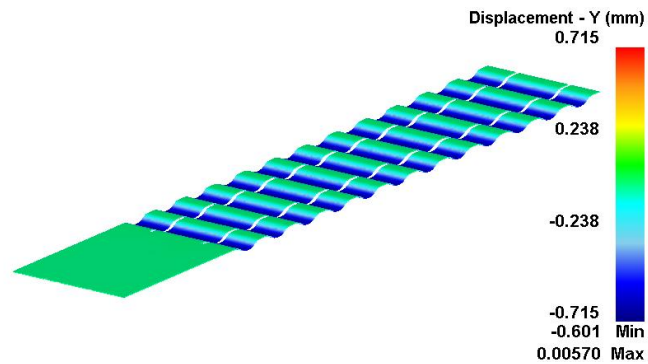


Figure 6.21: Simulated displacement for phosphor bronze journal bump foil.

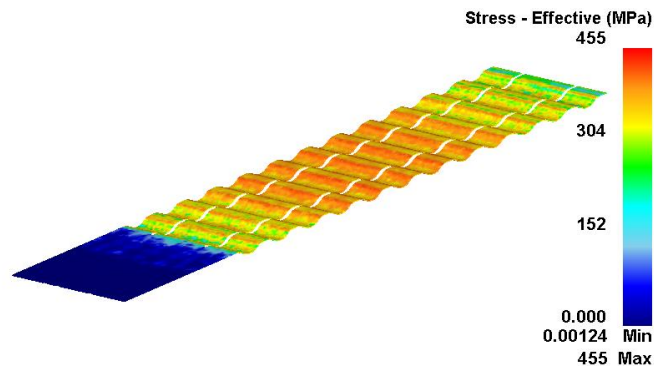


Figure 6.22: Simulated stress distribution for phosphor bronze journal bump foil.

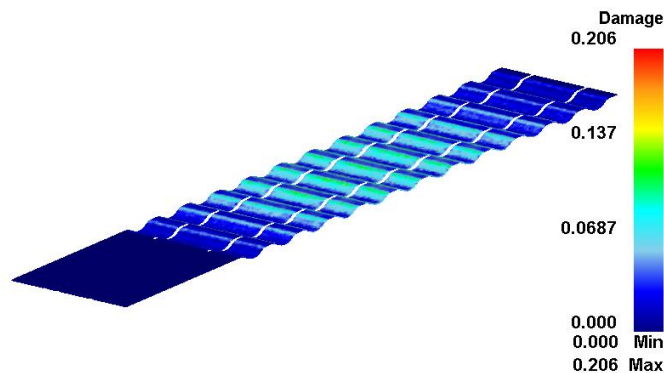


Figure 6.23: Simulated damage for phosphor bronze journal bump foil.

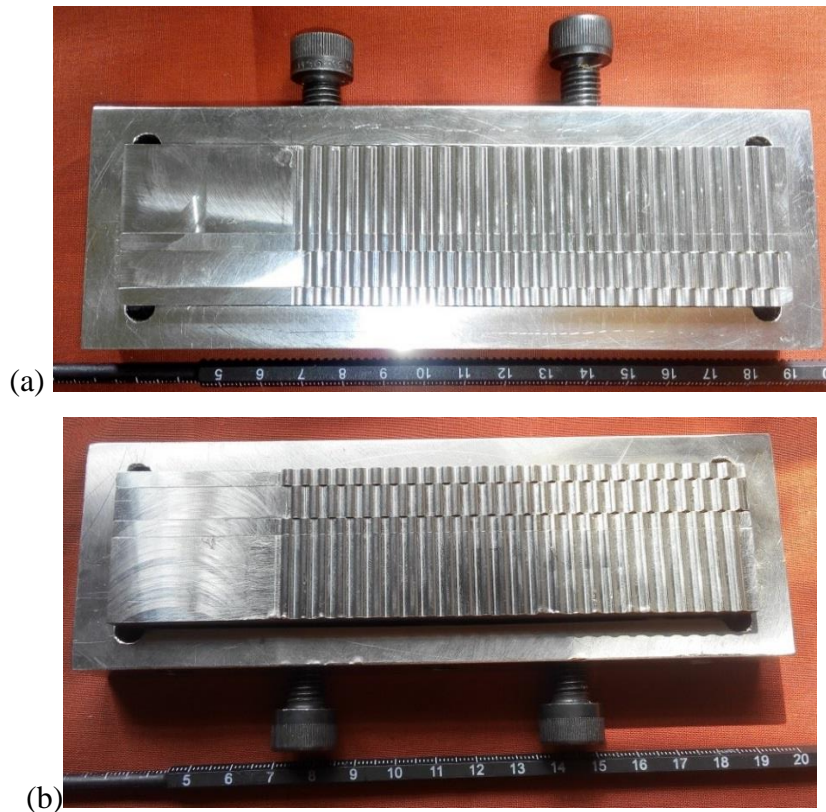


Figure 6.24: Fabricated rigid dies for forming of the bump foil: (a) Top die (b) Bottom die.



Figure 6.25: Fabricated journal bump foil with 2nd die set

The die set is designed for forming both generation I and II bump foils, and the fabricated dies for bump formation are shown in Figs. 6.24(a) and 6.24(b). The fabricated generation I bump foils is shown in Figs 6.25. For the recent application, generation I bump foils with slit is used. However, the die is designed for fabrication of generation II, which is planned for future use as it has higher load carrying capacity compared with generation I [53].

There is two folds increase in the cost of modified die set, but the fabricated bumps confirm uniformity in bump height, which is an essential part of bump forming. Further application of heat during bump formation is possible with rigid bump dies, which increases the flowability of the material and decrease the spring back.

6.2.7 Assembly of gas foil journal bearings

The assembly step comes after fabrication of all parts such as bearings base, top foil, bump foils, pins, and screws. Both top and bump foils on the bearings base can be fixed

either by welding or by using pins and screws. Spot-welding is a procedure frequently used in the manufacture of gas foils bearings. However, welding alters the structure and metallurgy of thin foils and these welds, if not heat treated, can be an initiation site for degradation such as fatigue cracks [53]. So heat treatment is done after the assembly of foils. In current approach pins and screw are used for assembly, where the ends of the bump and smooth foils are rolled to fit into the axial hole ($4\text{ mm}\phi$) on the bearing. In this axial hole, a semi-circular pin is inserted, and two grub screws are fastened in the transverse direction to hold the foils and bearing base together. The assembled journal foil bearing is shown in Fig. 6.26.



Figure 6.26: Assembly of bump and smooth foil on a single axial hole.

During the forming operation of copper alloys by cold working, strength and hardness increase as a result of plastic strain [87]. This is because elastic strain accompanies the plastic strain, and residual stresses remain in the product and can result in stress concentration and cracking of material in service. So, heat treatments for the foils are necessary to relieve the internal stresses. A temperature commonly used for annealing cold-worked copper alloys is 350°C . To prevent oxidation during heat treatment, inert gas or vacuum heat treatment is preferable, but for lightly loaded bearings operating at relatively low temperatures as in current applications are found to be cost effective with air heat treatment [54]. Hence, for current work, air heat treatment is adequate.

The bump stiffness plays a significant role in rotordynamics of gas foil bearing. So it is essential to validate the static bump stiffness of the fabricated gas foil journal bearing with the predicted value. The static stiffness is determined by a compressive test in universal testing machine. The determined bump stiffness is $8.69\text{E}+5\text{ N/m}$ (Fig 6.27). The deviation from the predicated value of $9.59\text{E}+5\text{ N/m}$ is about 9.4%. This deviation may be

because of various assumption taken in the analytical solution and presence of slits in the actual bump foil. A sensitivity analysis is documented in chapter 5, which indicates above deviation can be acceptable in term of critical speed and unbalance response.

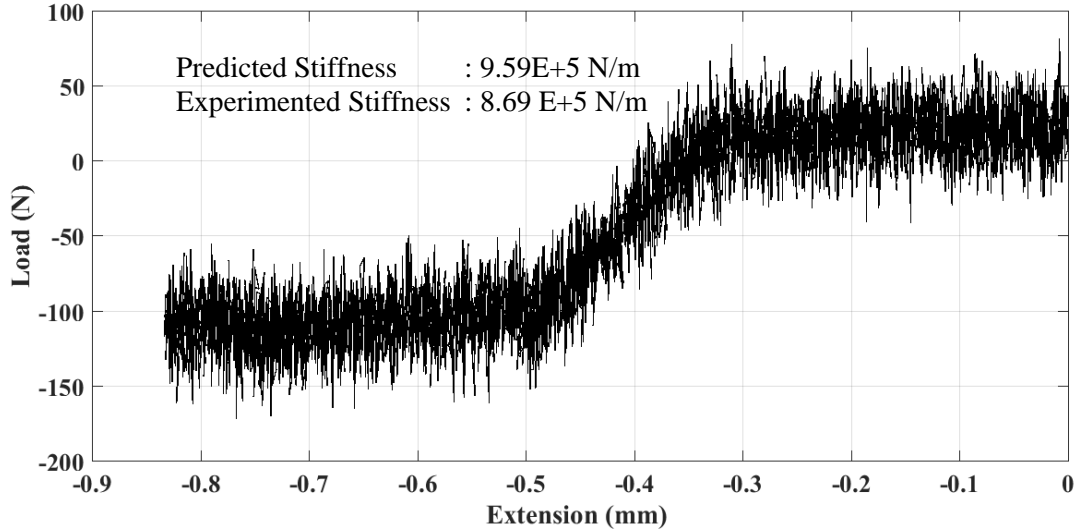


Figure 6.27: Load vs Extension graph to determine bump stiffness.

6.3 Fabrication of gas foil thrust bearings

The axial load due to the difference in pressure between the compressor and the turbine ends is supported by a pair of thrust or axial bearings. The rotor being vertically oriented, its dead weight is also taken by these bearings. To assure protection against accidental thrust reversals, a double thrust bearing is chosen for the prototype turboexpander. A pair of gas foil thrust bearing is designed for the current application, and its detailed designed procedure is prepared in Chapter 4. Computed results for the bearing are given in Table 6.7.

Table 6.7: Designed bearings data for thrust bearing from Chapter 4

Bearing parameters	Dimensions
Inner radius (R_1)	10 mm
Outer radius (R_2)	22 mm
Top Foil Thickness (t_t)	0.1 mm
Bump Foil Thickness (t_b)	0.1 mm
Bump Length ($2l_0$)	2.5 mm
Bump Pitch (s) (maximum)	3.17 mm

Foil thrust bearings designed is divided into a four thrust pads, and each thrust pad is consist of four elements, and they are the top foil, bump foil, bearing base and an arrangement to join both foils to the bearing base. The fabrication methodology for gas

foil thrust bearing is shown in Fig. 6.28, where the bearings block, top smooth foil and bump foils are made separately and assembled with the help of pin and screw. The same procedure is used to fabricate both upper and lower thrust bearings with opposite leading and trailing edge of the gas foil bearings. This section explains about the fabrication of bearing base, top foils, bump forming methodology using two different sets of dies. The FEM analysis is carried for the 2nd die set, where both top and bottom are rigid dies and is similar to the FEM analysis for journal bump foil forming.

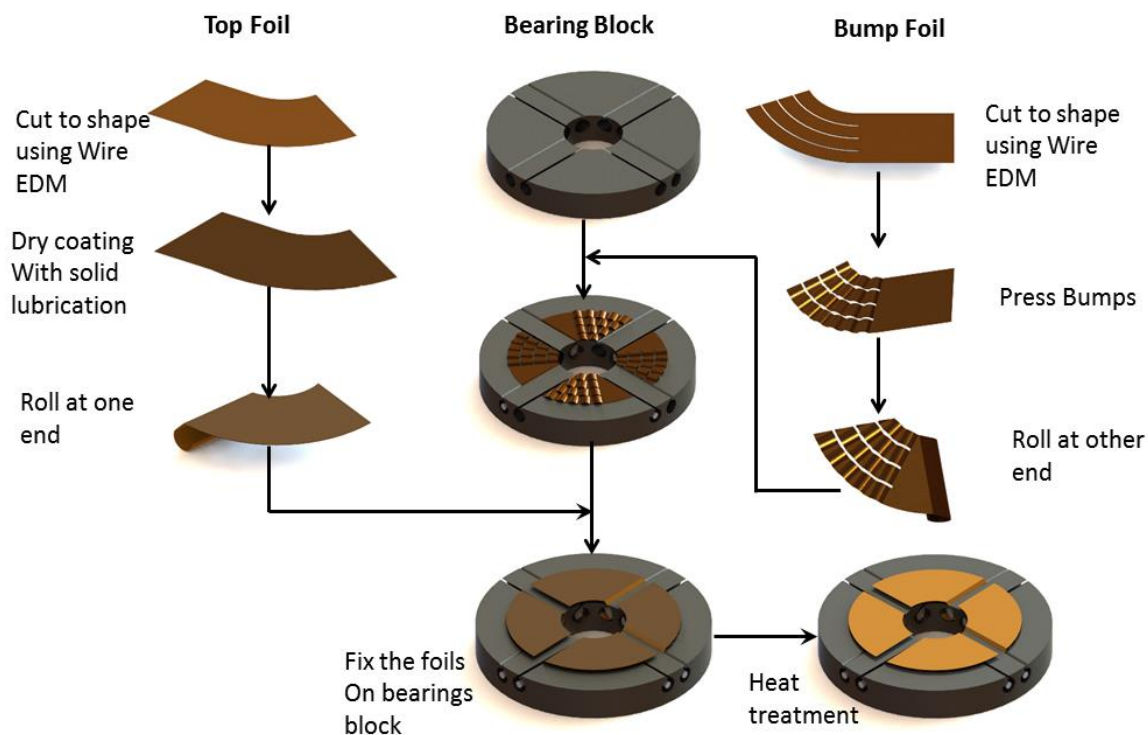


Figure 6.28: Fabrication methodologies of gas foil thrust bearings.

6.3.1 Fabrication of thrust bearing base

The thrust bearing base or bearing backing plate is made from SS304. Although stainless steel is not known as a bearing material, SS304 is selected to keep uniformity with the rest of the components of the turboexpander and to eliminate clearances and stresses due to differential thermal expansion or contraction. The bearing base is first machined and surface ground to produce a parallel and flat surfaces. Wire EDM then machines the slots for the pin, needed to hold the foils, and two threads holes for each pin are made in the rear face of the bearings base (Fig. 6.29). The production drawing for bearings base is presented in Appendix (TEX-05). The bearing block does not permit any serious tolerance on radial direction. The thickness, however, is provided with a dimensional tolerance of 5 μm to maintain interchangeability. The parallelism of the two faces is extremely

important. The prescribed tolerance of $2\ \mu\text{m}$ on the perpendicular distance between the two faces over the entire surface is preferable.

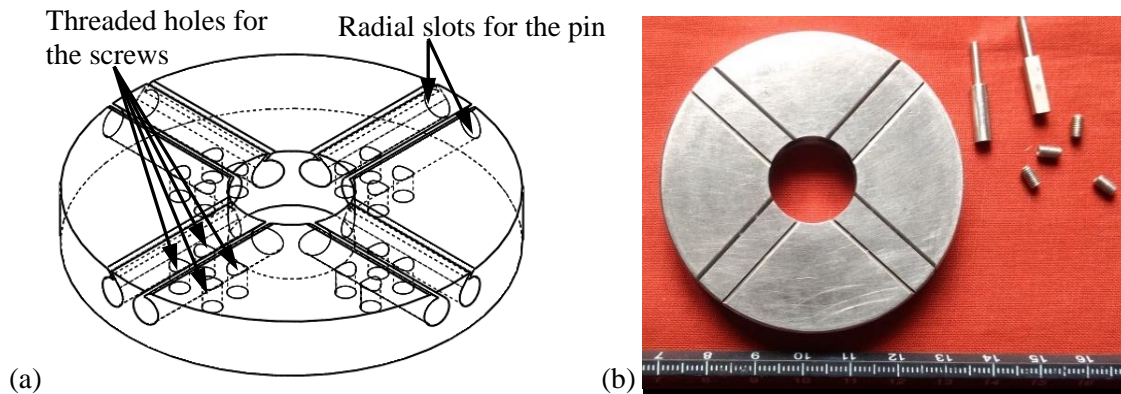


Figure 6.29: Prototype thrust bearings base: (a) Isometric view (b) Fabricated thrust bearing base with pins and screws.

6.3.2 Fabrication of smooth top foil for thrust bearing

Wire electrode discharge machining (Wire EDM) is used to cut the smooth top foil to the desired shape to avoid edge distortion. Similar to the journal top foil, several layers of 0.1 mm thick foils are stacked together and pressed under the hydraulic press to make all foils flat and avoid any inaccuracy in the dimension in the process of machining. About 20 layers of foils are stacked together between two aluminum plates of 2 mm each and then cut to the desired size (Fig. 6.30(a)) using wire EDM. One fabricated smooth foil is shown in Fig. 6.30(b). The production drawing are documented in Appendix (FOIL-02)

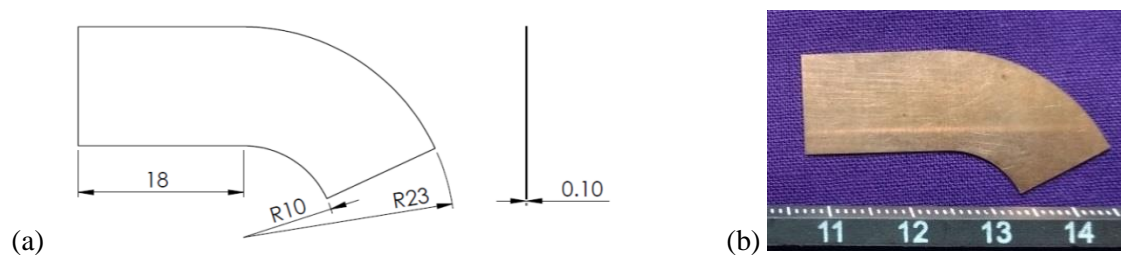


Figure 6.30: Prototype thrust top foil: (a) Dimension and (b) Fabricated.

6.3.3 Fabrication of thrust pre-form bump foil

A bunch of thin foils were stacked together and cut to the dimensions using wire EDM same as the top smooth foil. The foil was cut to the shape with three slits as shown in Figs. 6.31(a) and 6.31(b). The slits are cut to ensure sufficient material flow during pressing operation of the foils. The fabricated drawing are documented in Appendix (FOIL-02)



Figure 6.31: Pre-form thrust bump foil: (a) 2D view (b) Fabricated.

The dimensions of the bumps for thrust foil bearings are determined in the aerodynamic analysis of thrust foil bearings as described in Chapter 4 (Table 6.7). The designed bump foil for the thrust for the bearing is shown in Fig. 6.32.

The tooling for bump foil generation needs a pair of die, which are pressed by placing a smooth foil in between the dies. Two types of die sets are designed to get uniform and accurate bump shapes, and they are:

- a. The rigid bottom die and the flexible top die.
- b. The rigid bottom and top dies.

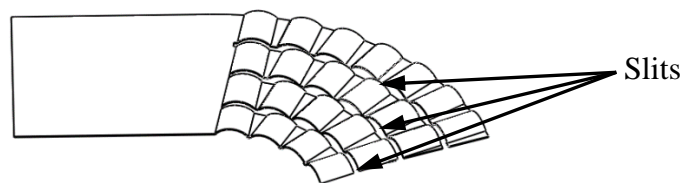


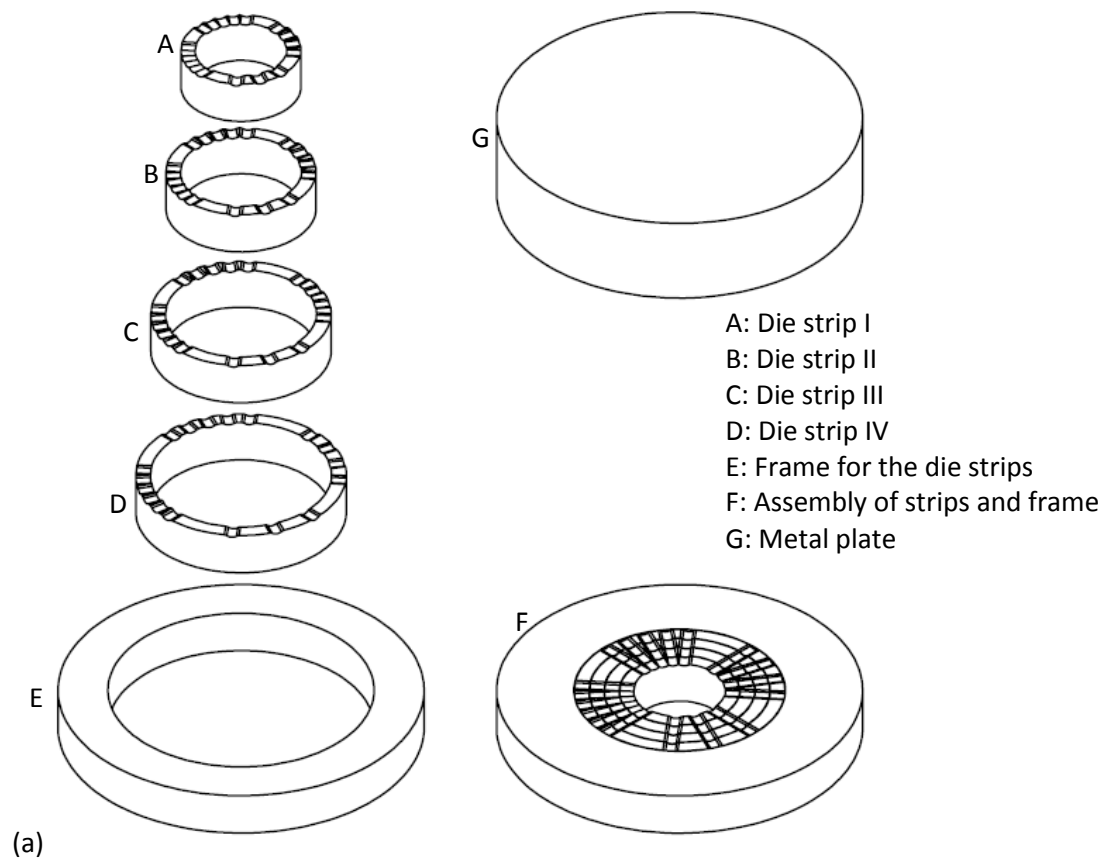
Figure 6.32: Designed bump foil for thrust bearing.

6.3.4 Thrust bump foil using flexible top die

Similar to journal dies, the 1st die set consists of a rigid bottom die, a flexible rubber sheet and a rigid plate. This arrangement reduces the tooling cost, so an attempt is made to fabricate thrust bump foil using flexible rubber sheet as a top die. The rigid die with corrugated bump shape consisting of multiple circular bump strips is also used to fabricate thrust bump foil. The thin foil is placed in between the rigid bottom die and a flexible rubber sheet [72]. On the top of the rubber sheet, a smooth circular metal plate is placed to ensure uniform pressure to the rubber sheet during forming operation. The flexible rubber sheet applies a hydrostatic pressure on thin, smooth foil, and the smooth foil takes the shape of bumps on the rigid bottom die. The amount of forming load to be applied is determined experimentally to ensure the least spring back and equal bump heights.

The bottom die consists of set of circular bump strip, placed inside a tooling frame. The circular bump strips are designed to fabricate bump foil of various pitches. Figs.

6.33(a) and 6.33(b) shows the tooling developed for the fabrication of thrust bump foils. The production drawings are documented in Appendix (DIE-02 and DIE-03). For the current application, the bump die set was fabricated using SS 304. The flexible rubber sheet is a 2 mm thick silicon rubber sheet. Load-displacement curve during forming operation is shown in Fig. 6.34. Experimental studies show forming loads above 120 kN results bump foil with crack and below 110 kN consequences moderate deformation. So all the bump foils are formed with forming load between 110-120 kN for forming bumps of preferred dimensions. The fabricated thrust bump foils with moderate deformation, deformation with crack and complete deformation are shown in Figs. 6.35(a), 6.35(b) and 6.35(c) respectively. Above fabrication methodology for thrust bump foil encounters similar issues as that of journal bump foil, when fabricated with flexible rubber sheet as a top die. These issues are described in sub-section 6.2.5. Therefore, an attempt is made to design and develop a die set with rigid top and bottom dies.



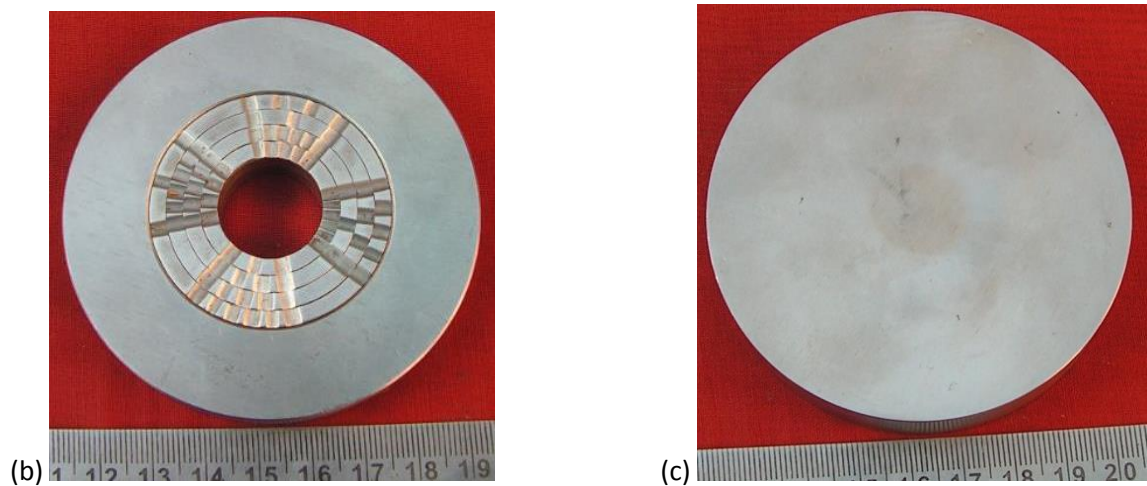


Figure 6.33: Tooling for fabrication of bump thrust foil: (a) Isometrics view
(b) fabricated bottom die and (c) fabricated top plate.

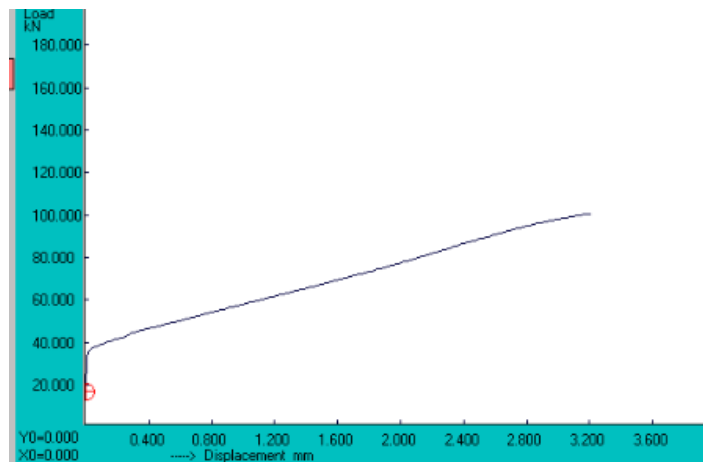


Figure 6.34: Load-displacement curve during journal bump formation.

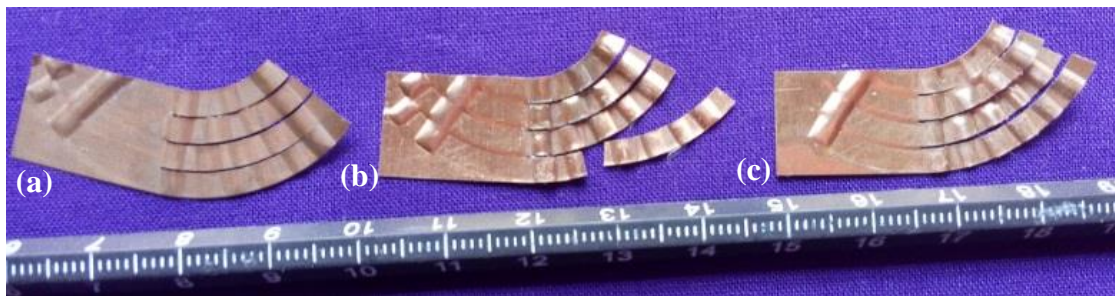


Figure 6.35: Fabricated thrust bump foils: (a) Moderate deformation (b) Deformation with a crack
(c) Complete deformation.

6.3.5 Thrust bump foil using rigid top and bottom dies

A similar approach as described in subsection 6.2.6 is followed to fabricate thrust bump foil with rigid top and bottom dies. The 3D models for all the element of the die set such as a top die, bottom die and pre-form thrust foil is modeled prior to the FEM analysis (Fig.

6.36). The fabrication drawings for above die elements are documented in Appendix (DIE-06 and DIE-07). These models are imported to DEFORM 3D and the forming operation is simulated with known values such as material for the workpiece, the speed of the top dies and other boundary conditions. Table 6.8 shows the parameters for the numerical simulation of the forming process. The above simulation helps the die designer to determine the forming load during bump formation, deflection of the workpiece, stress distribution, and damage over the bump areas. The simulation results before fabrication of the dies save time and cost of forming. Several dies dimensions are modelled and the die set with minimal damage is selected as the final set of die. Figs. 6.37 to 6.40 show the simulation results. The forming load is found to be 130 kN, which indicates the available hydraulic press is sufficient for bump formations (Fig. 6.37). The deflection (Fig. 6.38) shows that the outer edges are deformed higher than the inner edge of bump foil, but the deviation is within limits of bump design. Fig. 6.39 shows the effective stress over the foil is larger than the yield strength of the phosphor bronze, which indicates the complete formation of bumps. There is no damage over the bearing areas as shown in Fig. 6.40. After positive simulations results, the dies are fabricated and Fig. 6.41 shows the fabricated die set and pins for alignment of dies. Finally, the thrust bump foil is fabricated by placing the pre-form foil in between both the dies under a hydraulic press and the fabricated foils are shown in Fig. 6.42.

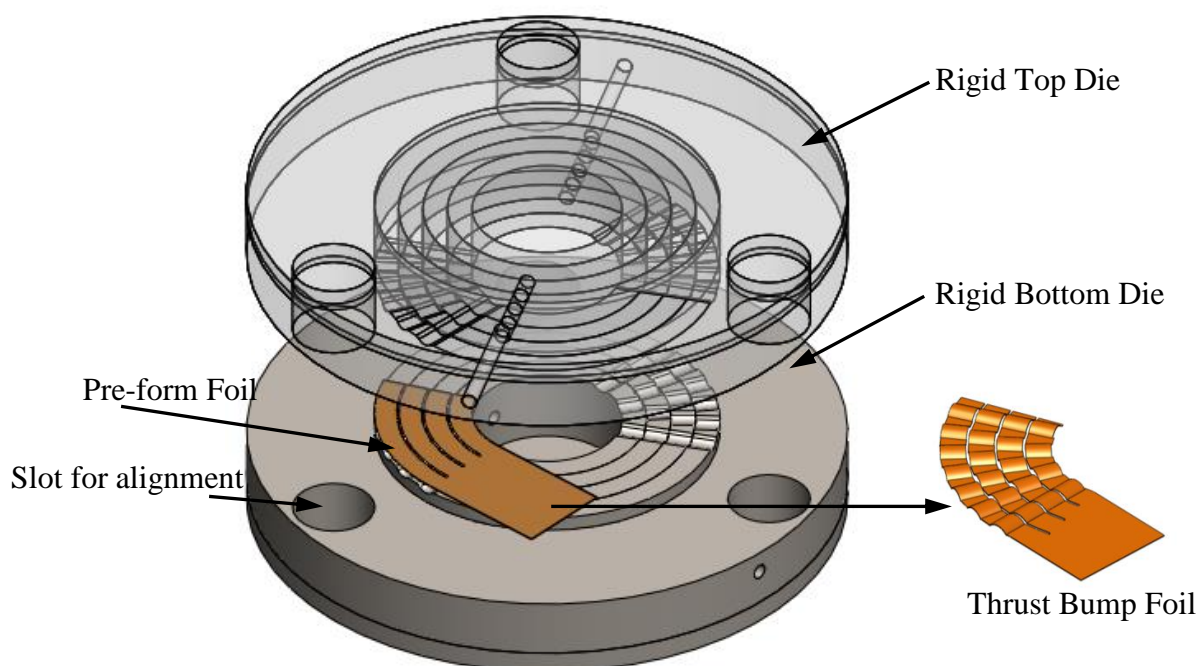


Figure 6.36: Tooling for fabrication of thrust bump foil with rigid top and bottom dies.

Table 6.8: Input parameters for forming simulation of journal bump

Sl No	Input Parameter	Values
1	Workpiece materials	Phosphor bronze
2	Top die/Primary die	Rigid
3	Bottom die	Rigid
4	Movement of the workpiece	Vertically downward
5	Movement of top die	Vertically downward
6	Movement of bottom die	Fixed
7	Stroke speed of the top die	0.1 mm/s
8	No of steps	100
9	Stop conditions	Forming load released after travel of 0.61 mm

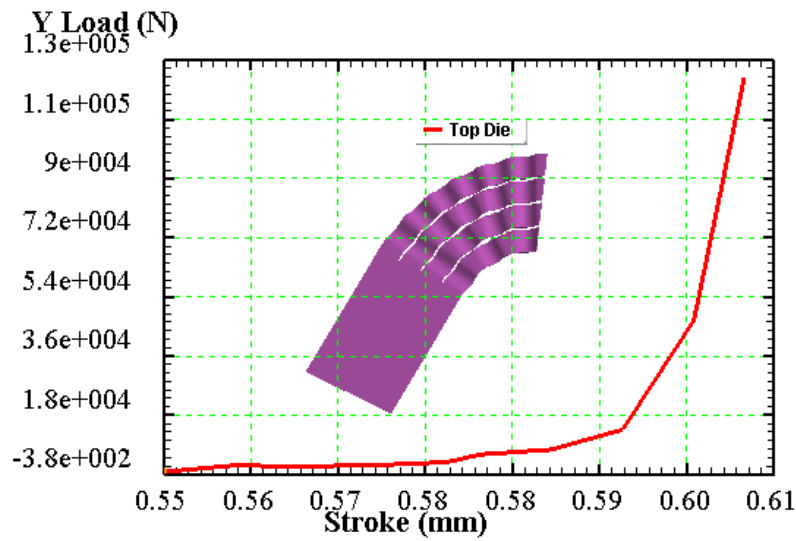


Figure 6.37: Load prediction curves for phosphor bronze thrust bump forming.

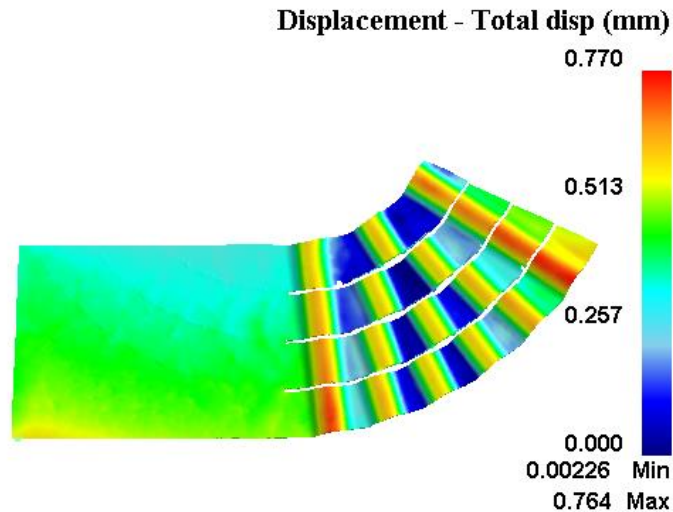


Figure 6.38: Simulated displacement for phosphor bronze thrust bump foil.

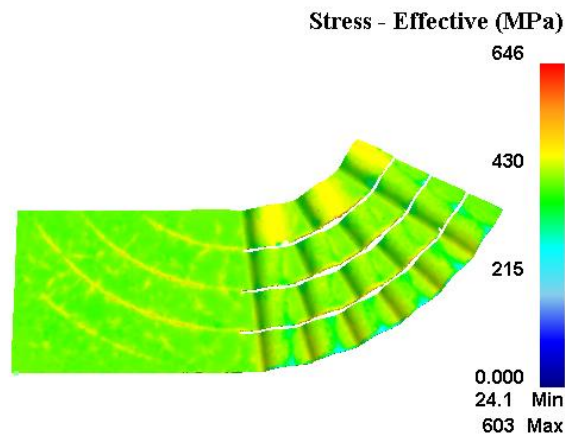


Figure 6.39: Simulated stress distribution for phosphor bronze thrust bump foil.

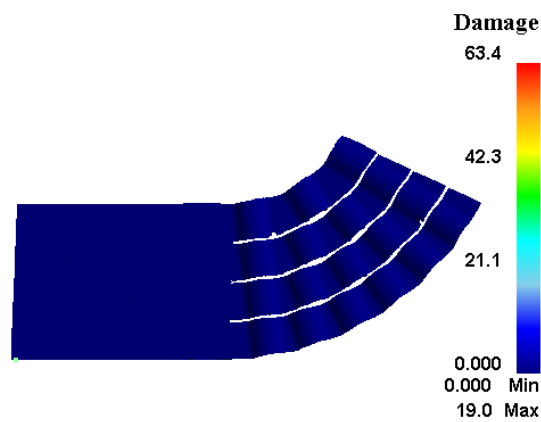


Figure 6.40: Simulated damage for phosphor bronze thrust bump foil.

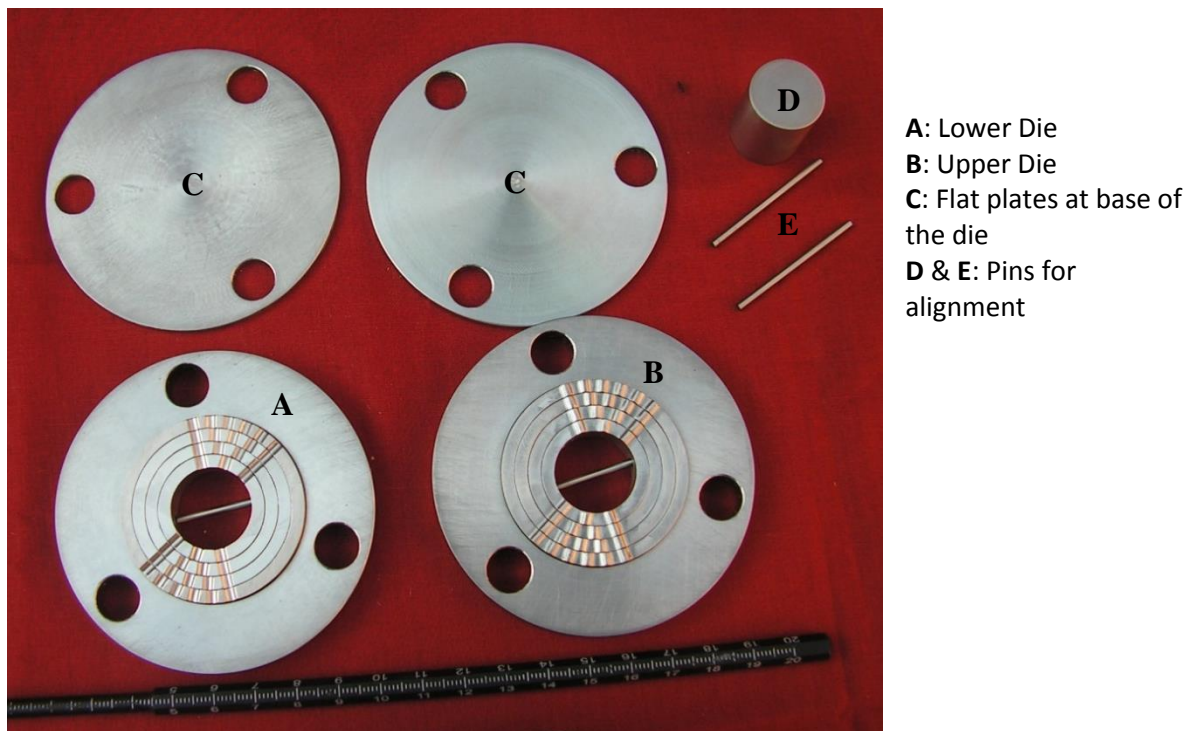


Figure 6.41: Fabricated die for thrust bump forming.



Figure 6.42: Fabricated thrust bump foils using 2nd die set for upper and lower thrust bearing.

6.3.6 Assembly of gas foil thrust bearings

Assembly of gas foil thrust bearing includes the fixing of bump foil and smooth foil on the thrust bearing base. The thrust bearing is divided into four sectors, so the total number of bump foils and top foils are four each. Pins and screws are used for assembly of above foils with the bearing base, and a total number of pins and screws are eight and sixteen respectively.

The leading edge of the bump foil is rolled and placed in the radial holes of the bearing base. In the radial hole, a stepped pin and two grub screws are used to hold the bump foils and bearing base together. Similarly, the smooth foil is rolled and fixed with bearings base after fixing the bump foil. The assembly of top foil should be such that the trailing edge of top foil is towards the leading edge of bump foil. The foils need to be inserted carefully to avoid any distortion of the foils. Fig. 6.43 shows assembled bump foil with the bearing base and Fig 6.44 shows the final assembly of lower and upper gas foil thrust bearings with a thin layer of MoS₂ coating. The coating is provided to minimize the wear of the top foil and collar during start and stop of the rotor.

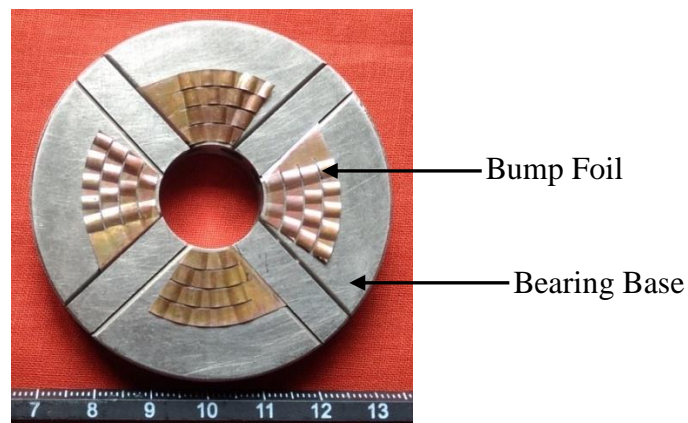


Figure 6.43: Assembled bump foil with the bearing base.



Figure 6.44: Assembled lower and upper gas foil thrust bearing with layer of MoS₂ coating on top foil.

6.4 Fabrication of other parts of turboexpander

The rotor and bearings are the major parts of a turboexpander. There are also other associated components to place the rotor and bearings at its appropriate place, and those components need to be dimensionally accurate for proper function of the turboexpander.

The associated components of bearing unit other than bearings and rotor are:

- (i) Bearing housing
- (ii) Dynamic seal
- (iii) Spacers
- (iv) Locknuts
- (vii) The cold end housing with nozzle and diffuser.
- (viii) The warm end housing with nozzle and diffuser.

The cold end housings and warm end housing are developed in the previous development program and re-used for the current program.

6.4.1 Bearing housings

The bearing housing supports the rotor and a pair of radial and axial bearings. It also houses spacers, dynamic seal, and locknuts. It is one of the most intricate components in the whole assembly as it contains a variety of features. There is a need of careful attention during the design of the bearing housing. A very tight tolerance is essential, and with its variety of features, it can be challenging to the machinist, where resources are limited.

The detailed production drawing of the bearing housing is given in the Appendix (TEX-13). Fig. 6.45 shows a cut model of the bearings housing with various features. The important features are listed below:

- (i) A pair of the flange (A and G) is provided at the top and bottom end of the housing to attach the warm end and cold end housing.
- (ii) A groove (B) is made on the top flange for the O-ring seal. This seal prevents leakage of high-pressure gas from the warm end to the outside.
- (iii) Space for locknuts (C and G) is provided to adjust the position of the turbine and axial play of the rotor.
- (iv) Holes (D) are made for inserting proximity probes for vibration analysis. An arrangement is also made to study machine vibration by using the accelerometer, so a pair of flat faces (E) is made near journal bearings.

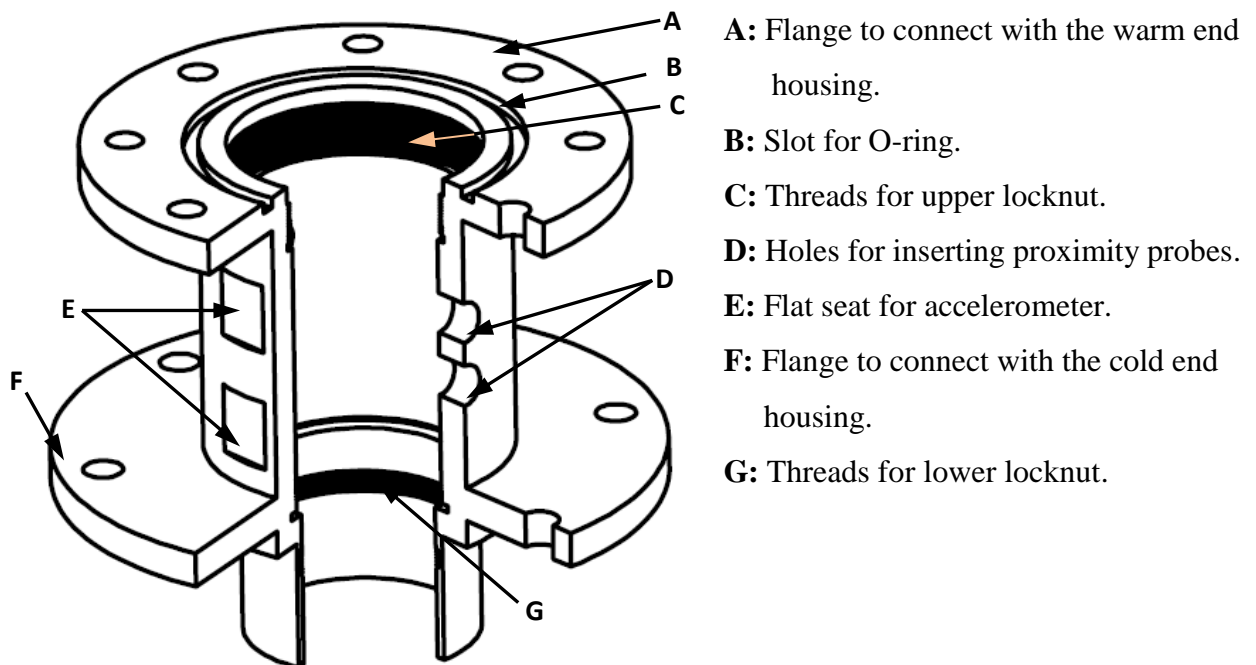


Figure 6.45: Cut view model of the bearing housing.

The bearing housing is the central component of the structural system, accommodating all the precision components. In general, manufacturing tolerance is kept as close as possible for a large component such as the bearing housing. However, for some of the features, a tight tolerance is necessary. The extreme faces of the housing are taken as datum surfaces and should be straight with a flatness specification of $2\ \mu\text{m}$. The inner diameter defines the datum axis. It has been prescribed perpendicularity of $3\ \text{to}\ 5\ \mu\text{m}$, which can be achieved by surface grinding [2]. The fabricated bearing housing is shown in Fig. 6.46.



Figure 6.46: Fabricated bearing housing.

6.4.2 Dynamic seal

Seals are very vital and often critical components in high-speed turbomachines. For current application, a dynamic seal is essential to prevent any leakage of contaminated and warm gasses from bearing area to the turbine side (Fig. 6.47).

A labyrinth seal is a suitable non-contacting dynamic seal as they consume less shaft power, minimal effects on rotordynamics and easy to design and fabricate. The basic principle of a labyrinth seal is based on the arduous path of the labyrinth seals that causes stepwise pressure drop so that the leakage is minimized. The design of labyrinth seal is done to minimize the leakage loss using Elgi leakage formulae [88].

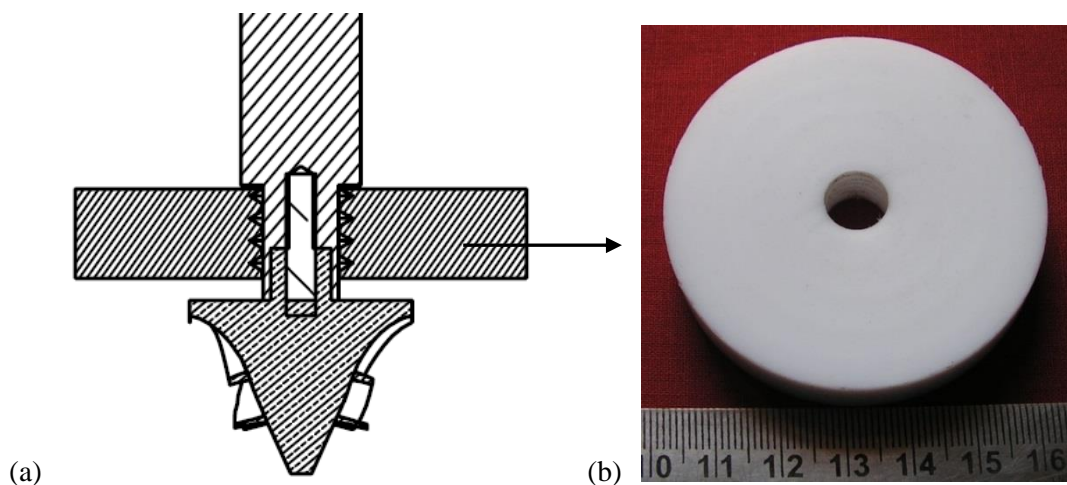


Figure 6.47: Labyrinth seal: (a) The location of the seal (b) Actual photograph.

The material for dynamic seal selected to be teflon as it behaves as a thermal insulator and prevents the heat leak from bearing to cold end side. The Production drawing and the 3D model is presented in Appendix (TEX-11).

6.4.3 Spacers and locknut

Three spacers are designed for the turboexpander, and their location is shown in Fig. 6.48. Spacer I is used for maintaining the required distance between the pair of thrust bearings. The width of the spacer I depend on designed clearance between thrust bearings and with of the shaft collar as described in chapter 4. The width of spacer I being thinner, there is always the possibility of distortion during grinding operation. So sufficient cooling of the job is essential during its fabrication of spacer I.

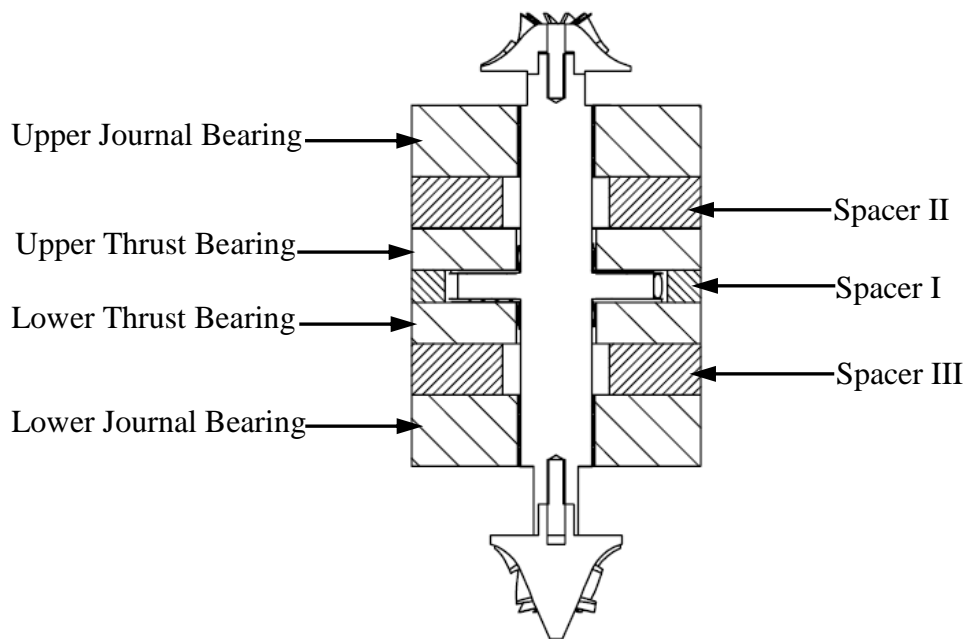


Fig 6.48 Position of spacers in the turboexpander.

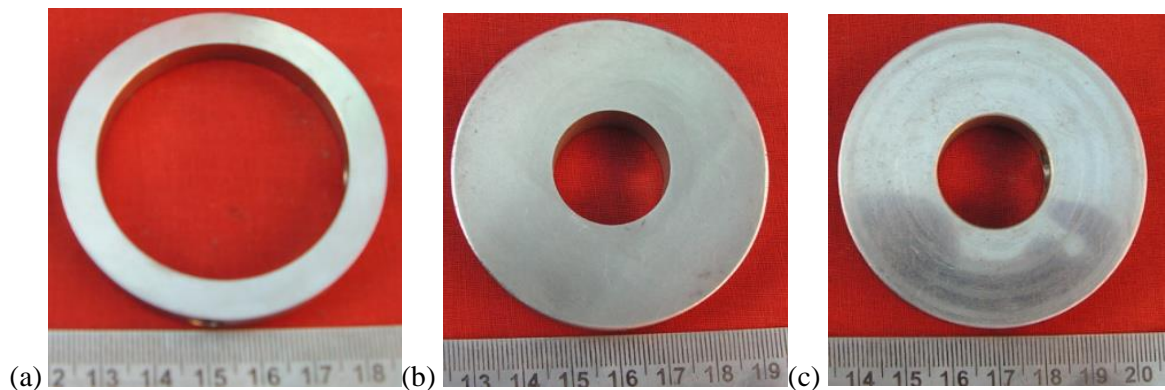


Fig 6.49 Fabricated spacers: (a) Spacer I (b)Spacer II and (c) Spacer III.

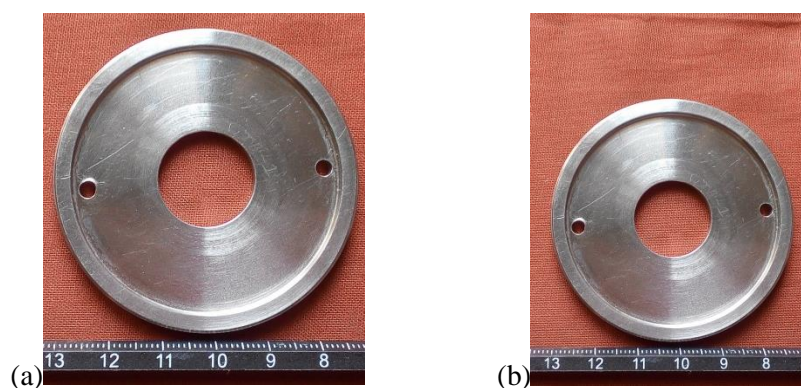


Figure 6.50: Fabricated locknuts: (a) Upper (a) Lower.

The other two spacers (spacer II and III) are used to provide room for inserting proximity probes for vibration analysis one between the lower journal and thrust bearing and other between upper thrust and journal bearings. The fabricated spaces are shown in figure 6.49. The fabrication drawing are are presented in Appendix (TEX-08, TEX-09 and TEX-10)

Two locknuts (Fig. 6.50) are provided to maintain the necessary axial play. One is positioned at the turbine side (lower locknut) and other at the brake compressor side (upper locknut). Threads on their circumference used for fastening with the bearing housing and two holes are used for tightening. These locknuts also help to position the rotor at its accurate place and aligned with the nozzle. The production drawing for the locknuts are given in Appendix (TEX-06 and TEX-07).

6.4.4 Passive magnetic ring bearings

Aerodynamic bearings such as gas foil bearing are subjected to start and stop issue due to contact between rotor and starter. In current applications, two methods were employed to avoid above issue. One is the use of passive magnetic ring bearings as auxiliary bearings and other is the use of solid lubricant coating. In 1st phase of testing, the rotor is tested without any coating or passive ring magnets to study the performance of the rotor. The next phase of the test is with passive magnetic bearings, where one ring magnet is inserted in the rotor and other on the dynamic seal. The configuration of the rings is maintained such that they repel each other. Two configurations based on the size of magnets are shown in Fig.6.51. The rotor, journal bearing base and the dynamic seals are modified to accommodate the ring magnets repelling each other. The distance between the rings is maintained by inserting ring spacers and a circlip. The thickness of each ring spacer is 1mm. The necessary distance to be maintained by the ring magnets as predicted in section 4.4.2. The fabricated parts of ring magnet arrangement are shown in Fig. 5.52. The

production drawing for the modified rotor and dynamic seals are given in Appendix (TEX-02, TEX 12(a), TEX 12(b) and TEX-07)

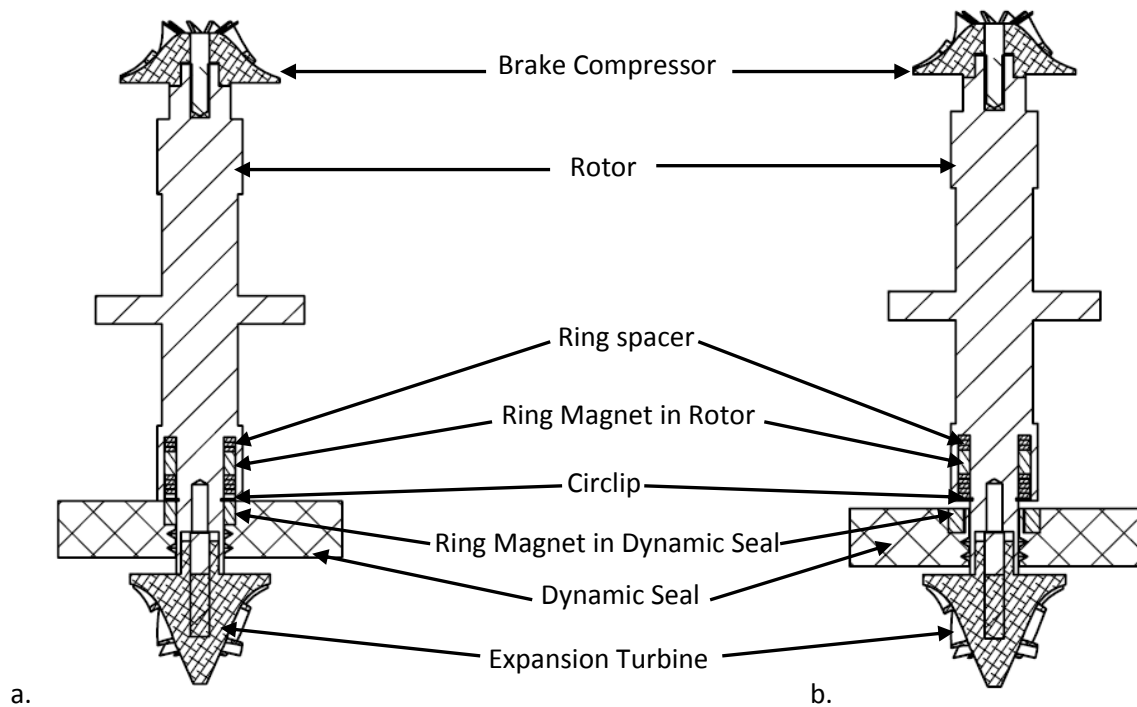


Figure 6.51: Configuration of magnetic ring bearings a. E1 and E2



A: Shaft with circular slot
B: Ring magnet fixed inside the rotor
C: Spacers
D: Circlip
E: Dynamic seal with ring magnets (E1 and E2 are for two different ring pair).

Figure 6.52: Parts of auxiliary passive magnetic bearing.

6.4.5 Coating

A downside of foil bearings is running at low speeds where mechanical contact occurs between the rotor and the top foil. For this reason, the top foils or the journal are usually coated with a dry lubricant to accommodate for the friction between the two elements during startup and shutdown. The traditional solid lubricant includes graphite, MoS₂ and PTFE. However, for high-temperature application Teflon® and, PS304 have been used by various researchers around the world [70]. For current application the temperature being less than 300°C, MoS₂ is used as a solid lubricant. The coating technique employed is the spray technique, where a thin layer of MoS₂ is coated using a pressurized bottled MoS₂ spray. This method of coating needs a careful attention such as distance and time of coating. After a couple of trials, the thickness of the coating was kept between 4 to 5 microns over the top foils. For current application, the coating is done only over the smooth foil instead of over the journal. Some researchers such as DellaCorte et al. coated the journal with a thick layer of PS304 running on foil bearings[89]. The coating over the rotor is attempted with the spray technique but found to be difficult to maintain uniform coating thickness, so coating over the top foil is preferred.

6.5 Assembly of turboexpander components

Assembly of all components together for precision fabrication is challenging and demanding for the proper functioning of the system. One of the major factors that guide the fabrication process of the individual components for successful assembly is the interchangeability. When specific tolerance is applied to all major dimensions, it is called universal interchangeability [2]. Universal interchangeability implies that the factors affecting the interchangeability of a part are specified by tolerance on the product drawings. So a detailed tolerance analysis is necessary before finalizing the production drawing.

The universal interchangeability would give rise to huge production cost. Therefore the method adopted here is the combined features of both interchangeability and machining to outfit. Three components are dimensioned considering interchangeability, and they are the rotor, thrust and journal bearings. These parts are likely to be damage due to rubbing at high speeds, and they require replacements with minimal impact on the system. The rest of the components, especially those controlling the locations of components in the axial directions, are dimensioned in such a way that two spacers

(Spacer II and Spacer III of Fig 6.49) are machined at the end to suit the requirements of the assembly. The critical features of the turboexpander system are:

- a) Axial and radial clearances between the brake compressor and its casing
- b) Total thrust bearing clearance and
- c) Axial and radial clearances between the turbine wheel and the shroud

6.5.1 Analysis of the axial length fit of the prototype assembly

The dimensional relationships for the prototype assembly can be done in a various way. For current application, one dimension loop is identified considering the back face of the brake compressor as a datum. All the components models are assembled in SolidWorks, and the equation for the linkage is framed as:

$$\sum_{i=1}^4 c_i + \sum_{i=1}^{10} l_i - l_{11} - l_{12} + l_{13} = 0 \quad (6.2)$$

where, c_i and l_i are the clearances and dimensions as shown in Fig. 6.53.

Since fabrication strategy adopted incorporates machining to suit for the length fit of the assembly, l_3 (space II of Fig. 6.49) and l_7 (spacer III) are identified as the two dimensions which can be specified at the end by machining. All axial clearances i.e. c_1 , c_2 , c_2 , and c_4 are predefined for proper function of the turboexpander. After fabrication of all components, they are measured and substituted in equation 6.2 to determine the dimension of spacers II and III. These two spacers are machined at the end to fit the bearing unit of turboexpander. The tolerances of individual components are given in the Appendix.

Table 6.9: Instruments used in metrology of fabricated components

Metrology Instruments	Application	Resolution (mm)
Mitutoyo digital Vernier calliper 0-150mm.	Small outside diameters such as a journal bearing base.	0.01
Mitutoyo Vernier Caliper 0-550mm.	Large diameters such as a flange, and the height of bearing housing.	0.01
Mitutoyo outside micrometer 0-25mm.	Shaft, turbine and brake compressor diameters.	0.001
Accurate spectra model, coordinate measuring machine, Range: x= 500, Y=600 and Z=400	Thickness of coating Flatness and squareness of various components	0.0005

A criterion for the analysis of length fit of the turboexpander assembly is precise metrology of the fabricated components. The dimensions of all fabricated components are measured using various instruments, and they are listed in Table 6.9. The coordinate measuring machine is used to check the flatness of bearing bases, spacers, dynamic seal and shaft collar. The standard deviation of the measured coordinates for all components lies within $4\ \mu\text{m}$, which are within the permissible limit.

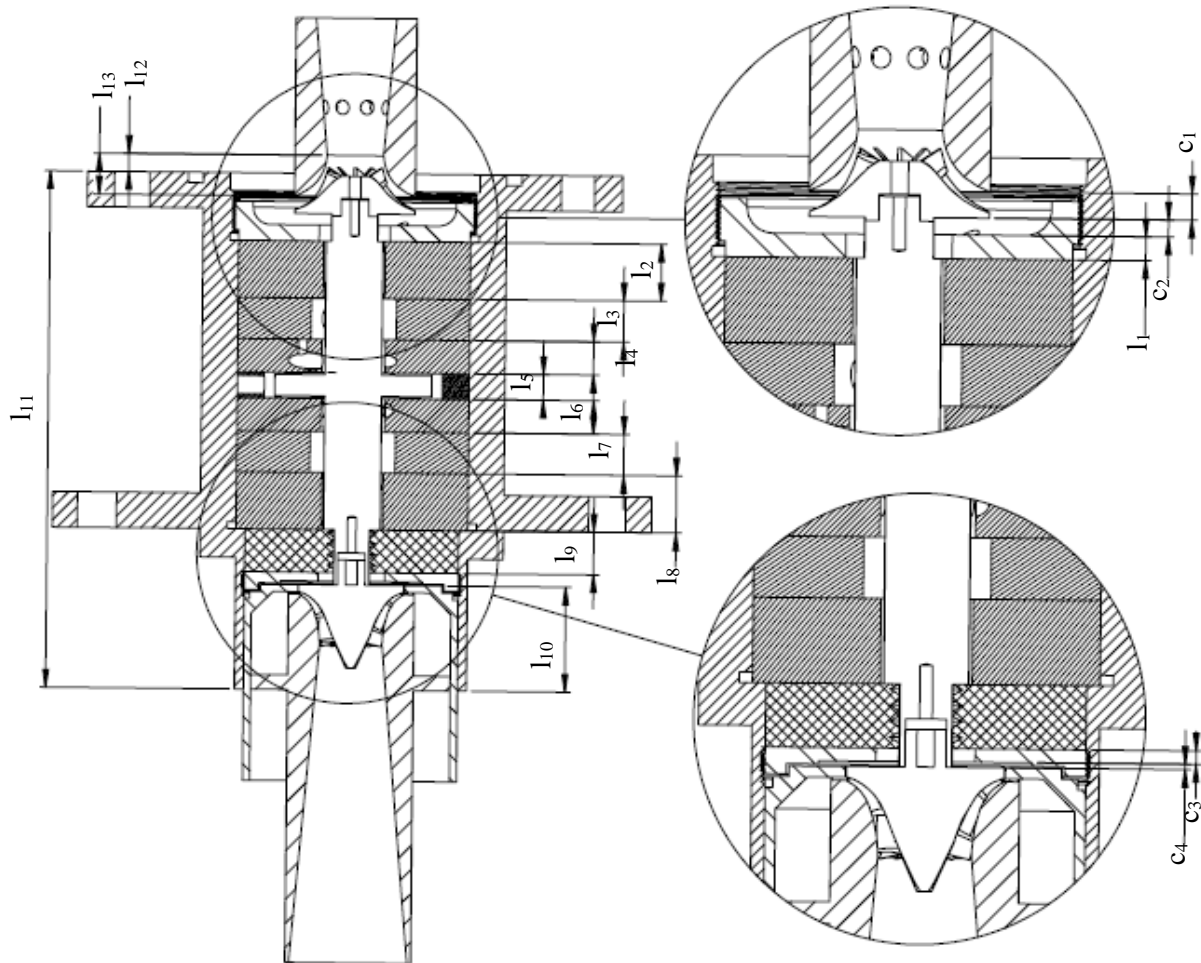


Figure 6.53: Dimensional linkage between bearing housing and other parts.

6.5.2 The assembly sequence

All metallic components are cleaned carefully with acetone to make it dirt free. They are placed in dust free areas with aluminum foil wrappers. The complete assembly of the bearing unit is done in a dust free area. The cold end and warm end unit assembly is described in the Ph.D. dissertation of Balaji [1]. The 2D assembled model is given in Appendix (TEX-14) and assembled bearing unit is shown in Fig 6.54, and the sequence of steps for the assembly of bearing unit is given below:

- i. The bottom locknut of the turboexpander is screwed with the bearing base from the bottom end.
- ii. The labyrinth seal is placed above the lock nut from the top with the help of dwell pin.
- iii. The lower journal foil bearing is placed above the labyrinth seal, the direction of the foils from leading edge to the trailing edge coincides with the rotational direction of the rotor.
- iv. The lower spacer is placed above the journal bearings and below the lower thrust bearing. The rotational direction of the rotor should coincide with the direction of the top foil from fixed to the free end.
- v. The shaft is now fitted so that the lower face of the thrust collar rests on the lower thrust bearing.
- vi. The spacer between the two thrust bearings and the upper thrust bearing are placed over the lower thrust plate. The top foil of the upper thrust bearing from fixed to free end should coincide with the direction of the rotor.
- vii. The upper spacer is placed above the thrust bearings and below the upper journal bearing. Similar to the lower journal bearings, the direction of the top foil from fixed to free end coincides with the rotational direction of the rotor.
- viii. The upper lock nut is screwed with the bearing housing till it touches upper journal bearing face.
- ix. The brake compressor and turbine are mounted on the shaft maintaining the same relative angular positions as that kept during balancing and fixed with a screw.
- x. The nozzle plate placed over the nozzle-diffuser in the cold end housing.
- xi. A radial O-ring is mounted in the corresponding slot in the in the cold end housing that seals the leakage of high-pressure gas to outside and bearing housing is bolted to the cold end housing.
- xii. The brake compressor housing is now attached to the warm end casing with the O-rings in place. The combination is placed on the top flange of the bearing housing with an O-ring in between and fixed by bolts. The O-ring prevents the leakage of brake compressor exhaust gas.
- xiii. The assembly being ready, a pair of the accelerometer is attached to the bearing housing near both the journal bearings. Vibration levels near both the journal

bearings are determined from the output of the accelerometer when the shaft is in the rotation. The rotational speed of the rotor is also determined from this data.

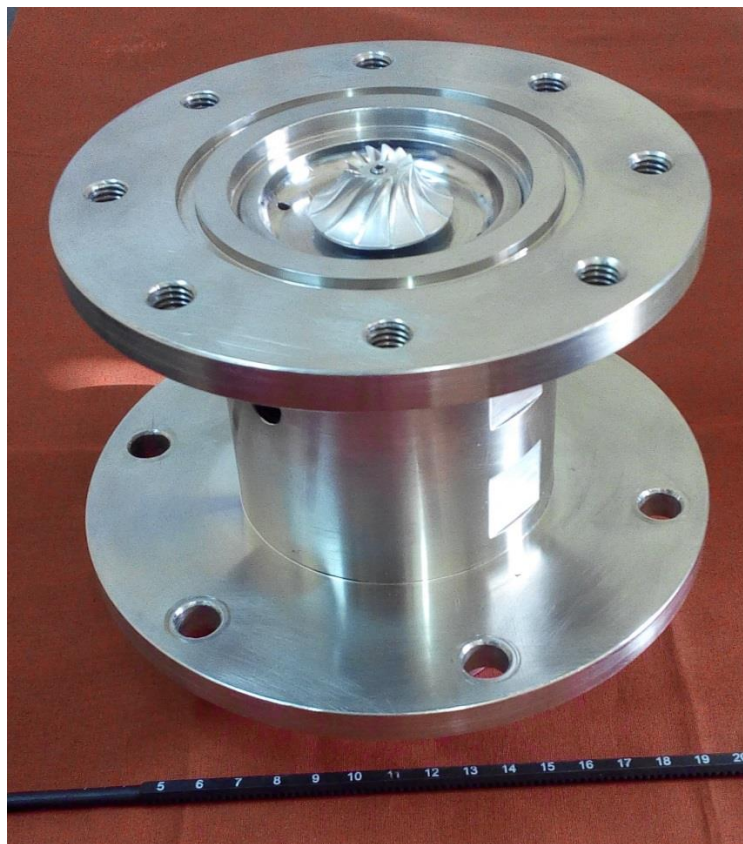


Figure 6.54: Assembled turboexpander bearing housing.

6.5.3 Precautions during fabrication and assembly

The problems faced during assembly raised mostly from fabrication inaccuracies, which is a lack of adequate facilities and resource. Various issues faced during fabrications of the rotor, dies, foil bearings and other parts the turboexpander are described below along with the action taken to overcome the issues:

- i. The 1st set of dies for thrust bump foil is difficult to fabricate due to its complex profile. The initial fabrication methodology adopted is with wire EDM. Facing difficulties with wire EDM, the methodology is changed to EDM process. The fabrication with EDM is time-consuming but found to fabricate accurate bump profile.
- ii. Determination of accurate shape for the foil before forming is difficult, the issue is addressed by cutting foil of larger dimension in wire EDM and shearing cut of excess length before assembly of bump foil.

- iii. The actual forming load with the flexible top die is determined experimentally. However, the issue is resolved by modifying die set with the rigid top die, where the FEM analysis is possible with both the die being rigid.
- iv. The thickness of the coating on journal and thrust bearing need to be experimented before fabrication of bearings to determine the thickness of the coating. The hand spray coating technique is prone to inaccuracy on dimensions. For the current work, the bearing bases are re-fabricated to accommodate appropriate clearance between runner and bearings.
- v. The turbine wheel and compressors are found to be rubbing with the diffusers in the trial runs. So for testing phase, the radial clearances between the turbine wheel and the diffuser and that between the brake compressor and its housing, need to be kept quite large. However large clearances bring down the efficiency of the unit.
- vi. Attachment of journal bump and top foils is found difficult to single axial hole, so two holes are preferable, one for bump foil and other for the top foil.

Chapter 7

Performance of Turboexpander with Gas Foil Bearings

The motive behind the testing of fabricated turboexpander is to study the feasibility of gas foil radial and axial bearings for high-speed cryogenic turboexpander. This chapter aims at documenting the various steps of testing the system which includes description of the test circuit, equipment and instrumentations details. The issues faced during testing phase and steps to overcome above issues are also documented. This chapter also includes the vibration analysis of the turboexpander using accelerometers from initial phases till the stable rotation is achieved. The tests were carried out in room temperature conditions with air as process gas, primarily to study the tribological issues and behavior of the rotor-bearing system.

7.1 Turboexpander test set-up

A detailed description of the test set-up for turboexpander with aerostatic thrust and tilting pad journal bearings is given in the Ph.D. Thesis of Balaji [1]. Removal of gas line to aerostatic gas bearings modifies the existing test rig and make it suitable for aerodynamic gas bearing test rig. The schematic of the current test circuit for measuring gas foil bearing performance is shown in Fig 7.1.

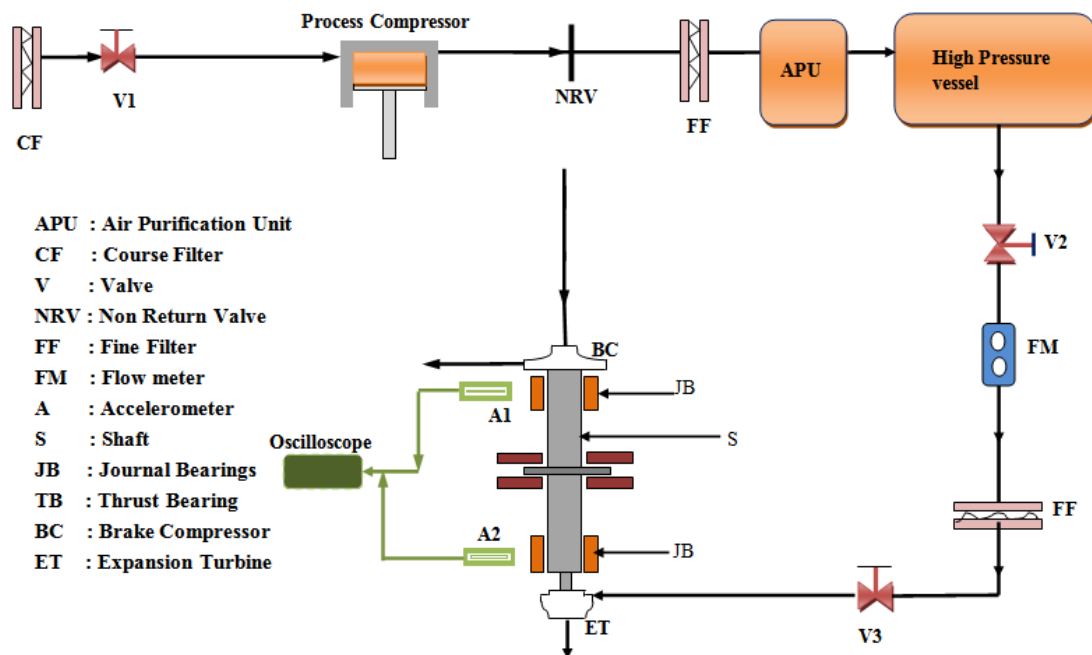


Figure 7.1: Schematic of turboexpander test set up.

The process compressor takes air from the atmosphere through a filter, compresses it and sends to a pressure vessel. The nozzle and expansion turbine are designed for an inlet pressure of 0.7 MPa of inlet pressure to the nozzle. However, due to equipment limitations the test could be performed maximum up to 0.5 MPa. The pressure in the pressure vessel is maintained above the 0.5 MPa to consistently supply of process gas at a pressure of 0.5 MPa for driving the expansion turbine. A high-pressure line connects the vessel to the inlet of the turbine through fine filters and an air purification unit (APU). The exhaust from the turbine can lead to the inlet of the process compressor. But for the current test bed, the testing is done with air as the process gas, so the exhaust air is thrown into the atmosphere. There are pressure gauges to measure the pressure in the vessels, and at the inlet of the turbine.

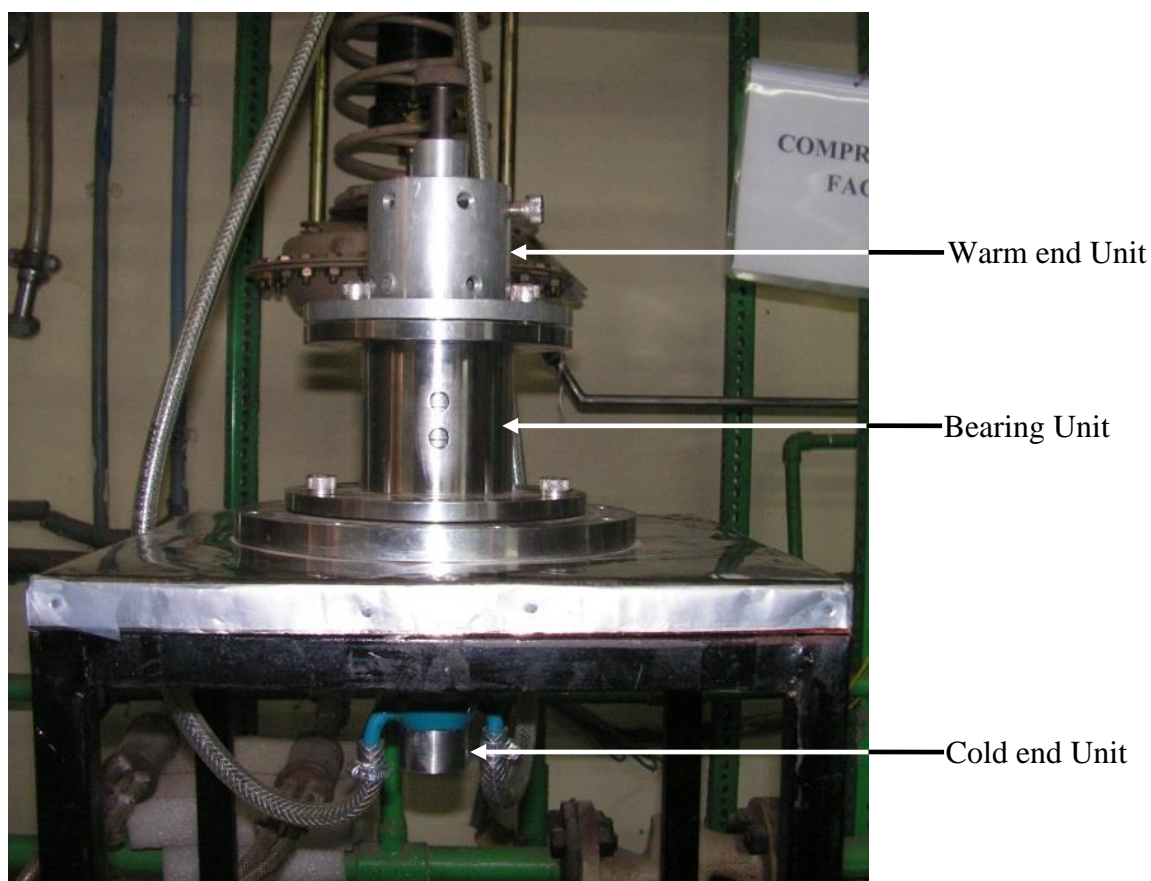


Figure 7.2. Assembled bearing unit with cold end and warm end units.

The assembly of turboexpander with bearing, cold end, and warm end units is shown in Fig. 7.2. One inlet stream divided into two ducts are connected to the cold end unit. The brake compressor takes air from atmosphere and throws the air to atmosphere. Pair of accelerometers and an oscilloscope is connected to the test rig. The accelerometers are mounted on the bearing housing close to the upper and lower journal bearings. The

assembled turboexpander is placed at the test rig with the associated instrumentation (Fig 7.3).

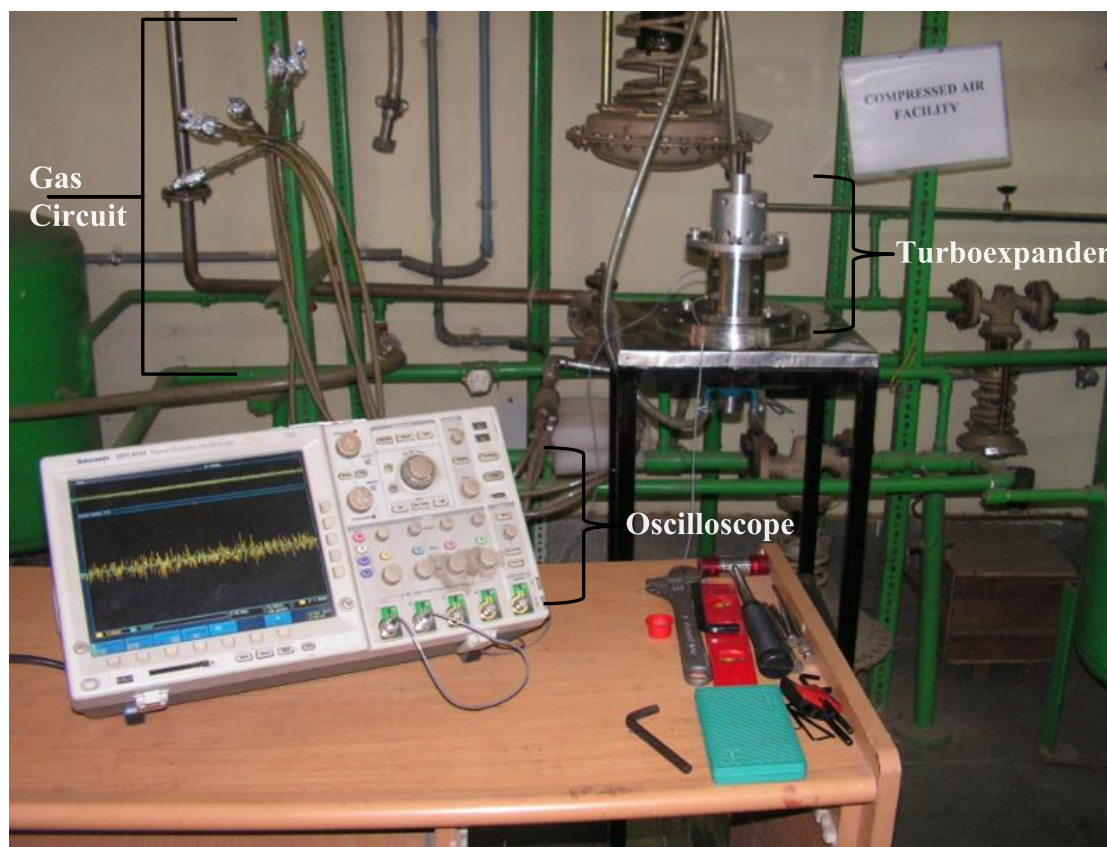


Figure 7.3: The test bed with the turboexpander assembly and instrumentations.

7.2 Speed and vibration measuring equipment

Measurement of speed and vibration can prove the feasibility of gas foil bearings for the current application. The instrumentations used for vibration analysis are two piezoelectric accelerometers and a digital oscilloscope. The piezoelectric accelerometers used are constant current line drive (CCLD) with built-in low-noise pre-amplifiers, and they are suitable for multichannel modal analysis measurements. Two accelerometers are mounted on the bearing housing with the help of white bees wax close to upper and lower journal bearing (Fig 7.4). The accelerometer converts the vibrational displacement or acceleration to an electric signal. The output signal of the accelerometer is captured in an oscilloscope through a cable. A steady pattern of voltage with time is captured on the oscilloscope, over a cycle of rotation. The electric signal is directly proportional to acceleration and acceleration is directly proportional to the vibrational displacement of the housing and ratio between them is also depend on the rotational speed. Therefore, the curve on the oscilloscope shows the vibrational behavior of the bearing housing. From the time period

of the signal, we can deduce the synchronous frequency of excitation, which is the shaft speed.

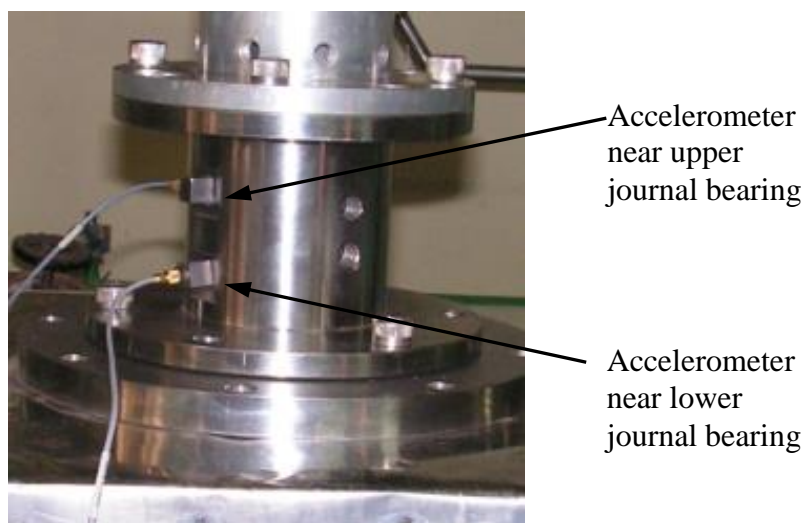


Figure 7.4: Mounting of the accelerometer on the bearing base.

Accelerometers

Two piezoelectric accelerometers with preamplifier are selected for vibration analysis, which are suitable for modal analysis with high sensitivity, low mass, and small physical dimensions. The specification and photographs are shown in Table 7.1 and Figs.7.5(a) and (b) respectively. Accelerometers B&K 4507 and B&K 4508 are mounted near upper and lower journal bearings respectively. The high-frequency range accelerometer (B&K 4508) is mounted near to the turbine as the numerical analysis estimated higher vibration level near the turbine as described in chapter 5.

Table 7-1 Specification of the accelerometer

Make and Model No.	B&K 4507	B&K 4508
Frequency	0.3 - 6000 Hz	0.3 - 8000 Hz
Sensitivity	100 mV/g	100 mV/g
Temperature	-54 - 121 °C	-54 - 100 °C
Residual Noise Level in Spec Freq Range (rms)	± 0.35 mg	± 0.35 mg
Maximum Operational Level (peak)	70 g	70 g
Resonance Frequency	18 kHz	25 kHz

Oscilloscope

The specification for the digital oscilloscope used to display the vibration signals is given in Table 7.2.

Table 7.2 Specification of the oscilloscope

Make	Tektronix
Model No	DPO 4034, 4 channel
Bandwidth	0- 350 MHz
Sample Rates	5 GS/s
Maximum Waveform Capture Rate	3,700 wfms/s

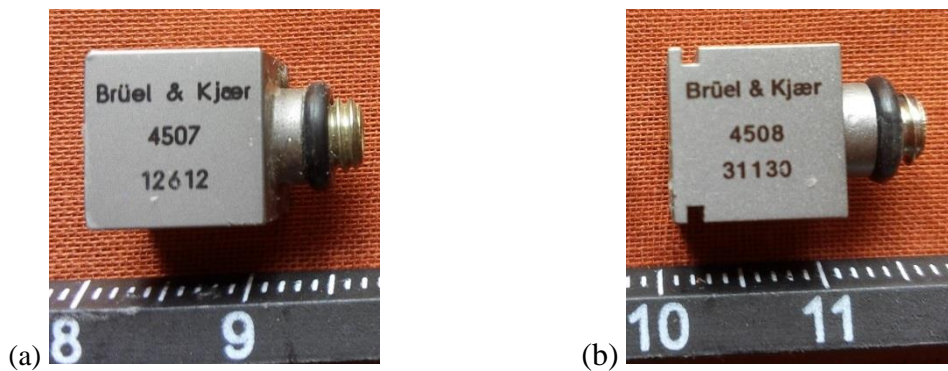


Figure 7.5: Piezoelectric accelerometer: (a) B&K 4507 (b)B&K 4508.

7.3 The experiments

The initial phase of the experiment is carried out without mounting the warm end housing over the bearing housing to sort out the accurate positioning of turbine and nozzle. The locknuts are adjusted to maintain the axial play and proper positioning of the turbine. In the early experiment air supply of 0.2 MPa is provided to run the rotor at low speed. During this phase, many initial problems of alignments are sorted out to run the turbine. Later the air supply is increased slowly up to 0.5 MPa to obtain higher speed. Fig 7.6 shows the photograph of rotor with steady rotation at 0.5 MPa air supply without assembly of warm end unit.

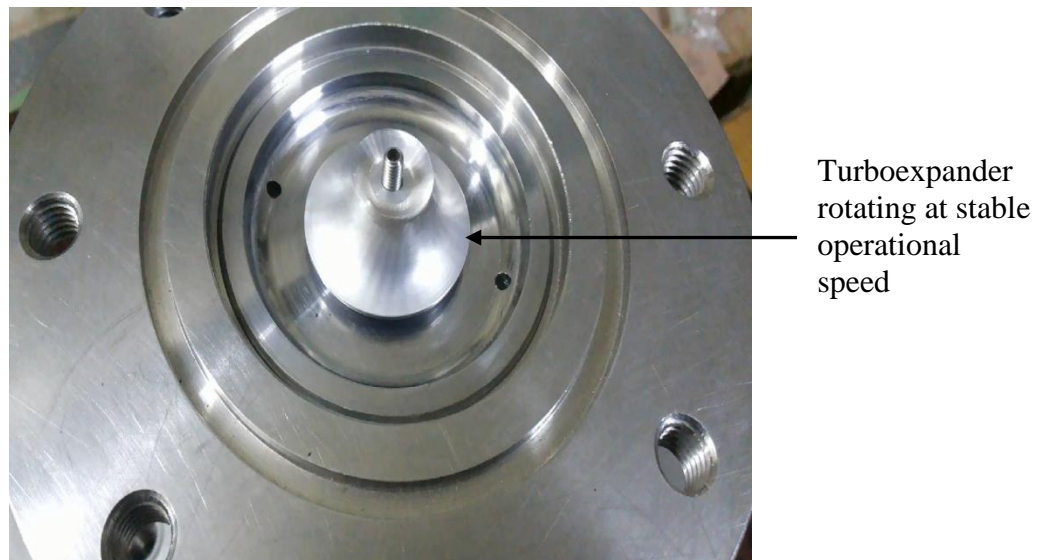


Figure 7.6: The rotor at stable operational speed without warm end unit.

7.3.1 Tribology Issues

The testing is carried out to validate the use of foil bearings for a cryogenic turboexpander. In the test phase, several alternate approaches are adopted for the stable

operation of the cryogenic turboexpander. During start and stop of the machine, the runner comes in contact with the top smooth foil. So, multiple starts and stops wear out the top smooth foil, which increases the nominal clearance between the runner and bearing. The increased clearance decreases the load carrying capacity of the rotor. A layer of solid lubricant coating or uses of active ring magnets are preferred to address the wear issues during start and stop of the rotor. It also reduces starting torque of the rotor. The methodologies adopted for testing the prototype turboexpander are as follows:

- i. Testing without the passive magnetic bearing or solid lubricant coating.
- ii. Testing with the passive magnetic bearing as an auxiliary bearing.
- iii. Testing with a layer of solid lubricant coating on the top smooth foil.

In the early phase of the testing, the test is carried out without active magnets and solid lubricant coating to study the behavior of wear. During this test phase, the starting torque is found to be high as the rotor start rotating only when inlet pressure of the turbine is higher than 0.15 MPa. On increasing air supply, the machine is found to encounter fluctuation of the speed. This is because the runner touches the smooth top foil many times and prevents smooth operation of the turboexpander. The nature of wear of smooth surface and shaft is tested after a single run of the machine. The photographs in Figs 7.7(a) and 7.7(b) shows the uneven wear on the smooth top foils of upper and lower thrust bearings. The wear in the upper thrust bearing is because of load reversal during the testing phase and touches the upper thrust bearing. Above study indicates that there is a need for an arrangement to address the issues encountered during start and stop of the machine. There is no appreciable issue found in gas foil journal bearings for its low load in the vertical oriented rotor. Similarly, no major wear on shaft collar is noticed.

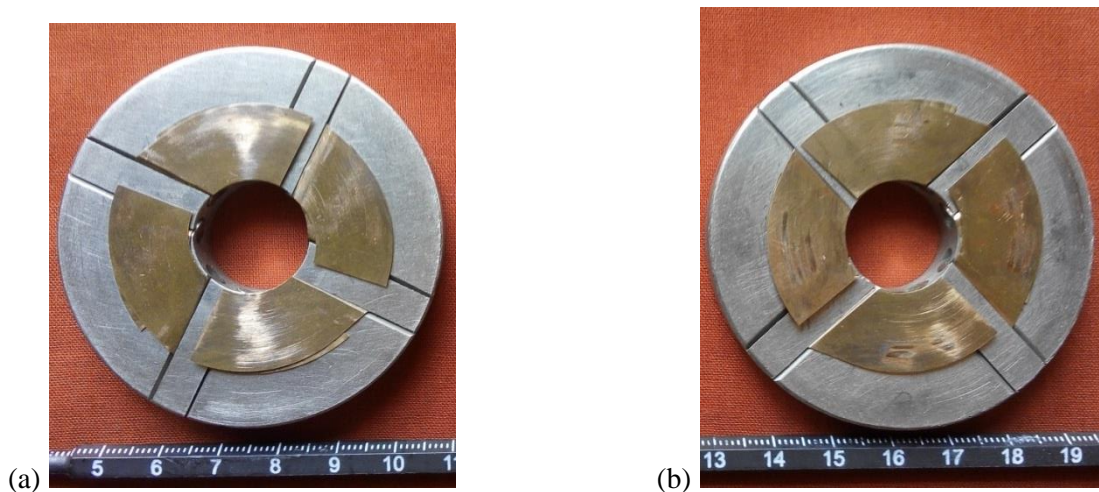


Figure 7.7: Thrust bearings without coating after the test: (a) Upper and (b) Lower.

The next phase of the test is with passive magnetic bearings; one ring magnet is inserted in the rotor and other on the dynamic seal as described in section 6.4.4 (Figs 6.50 and 6.51). Both ring magnet configurations are tested to see the starting and stopping issue. For both configuration the starting torque is found to be less. There is no appreciable difference is found between E1 and E2 configuration during starting of the rotor(Figs 6.50 and 6.51). For both the configuration the turboexpander reaches high speed nearly 40,000 rpm. Any attempt to increase the speed beyond this limit is met with instability manifested in the form of enhanced vibration amplitude. The reason of enhanced vibration can be the use of circlip, which makes the rotor unbalanced, so an accurately balanced rotor is expected to solve the above problem. The state of ring magnet in the rotor is checked after the test, and it is found to be fragmented into small pieces. The high speed of the rotor impact a high centrifugal stress on the ring magnets and magnets being very brittle, it fragmented into pieces. Facing difficulties with passive magnetic bearing, next attempt is to go for solid lubricant coating over the smooth top foil. The proposed magnetic bearing system is viable, if the brittleness of the magnets can be addressed along with proper balancing of the rotor.

In the last phase, a thin layer of solid lubricant coating can be applied either on the journal or over the smooth top foil. For current application, a thin layer of MoS₂ coating is applied over the smooth top foil using hand spray technique. The dimensions of the spacer between thrust bearings are modified to accommodate the coating thickness for maintaining the calculated clearance. The major issue of wear is resolved with this methodology. The rotor could reach to a speed of 81,000 rpm at air supply of 0.5 MPa. The test is conducted for more than 30 starts and stops of the machine, with a total duration exceeding 30 hours. Figs. 7.8 and 7.9 show the negligible wear behavior after multiple starts and stops on the thrust bearings and the shaft collar.

The tribology behavior in journal bearing is examined and it is found to have very minimal wear over the coating. The radial load very small for the vertically oriented rotor, hence the wear is only during the pre-load condition, when the top smooth foil is in contact with the rotor before the lift-off speed. It can be concluded from the above experiment that a thin layer of coating on MoS₂ over the bearing top foil resolve the wear issue during start and stop phase of the rotor for current application. The coating methodology is also found to be cost effective compared to the auxiliary passive magnetic bearing.



Figure 7.8: MoS₂ coated thrust bearing after test a. upper b. lower.



Figure 7.9: Wear on the shaft after the test

7.3.2 Vibrational studies

The oscilloscope shows the vibration level of the housing mounted with two piezoelectric accelerometers close to the upper and lower journal bearings. The signal from the accelerometer is recorded on a storage type oscilloscope during test runs. During the phase of increasing the speed, two critical speeds are noticed where vibration level is suddenly increased. The first is around 25,251 rpm at 0.2 MPa and second is around 29,850 rpm at 0.25 MPa supply of inlet pressure to the turbine. These speeds are close to the calculated rigid critical speeds of the prototype rotor as described in Chapter 5.

The periodic curves are plotted near 1st and 2nd critical speed of the turboexpander are shown in Figs. 7.10 and 7.11. The predicted 1st and 2nd critical speeds are 26,752 rpm and 29,353 rpm respectively. The deviation of 1st and 2nd critical speeds are 5.9% and 1.7% respectively. The above deviation in critical speed may be due to the deviation of stiffness by 9.3 %. There is the possibility of small variation of damping selected for rotordynamic model. Above result indicates the bearing stiffness is acceptable for current rotor-bearing system. Therefore, above observation proves the accuracy of the rotor dynamic model as explained in chapter 5 for the current application. The critical speeds

are noted, and in the successive runs, these speeds are quickly crossed to avoid any excessive vibration of the turboexpander.

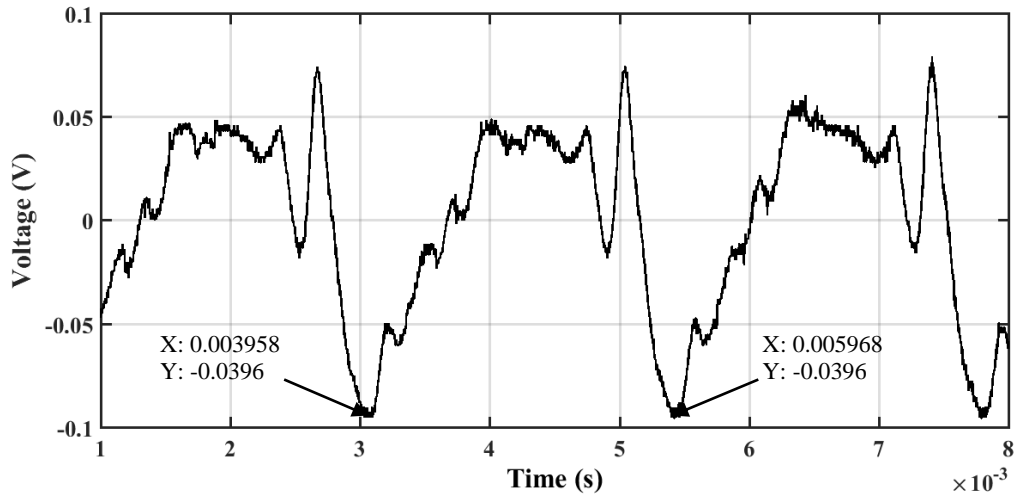


Figure 7.10: Spectrum in time domain at a speed close to 1st critical speed (25,252 rpm) near lower journal bearing.

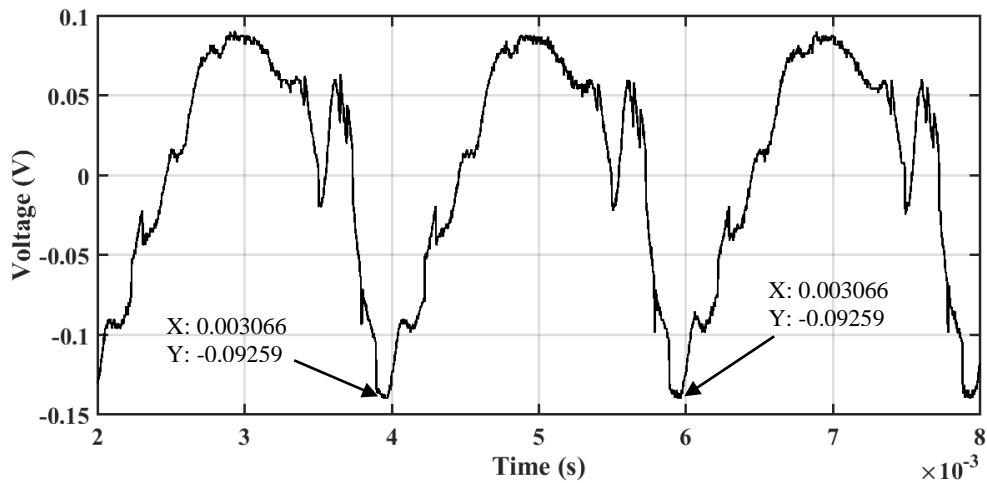


Figure 7.11: Spectrum in time domain at a speed close to 2nd critical speed (29,850 rpm) near lower journal bearing.

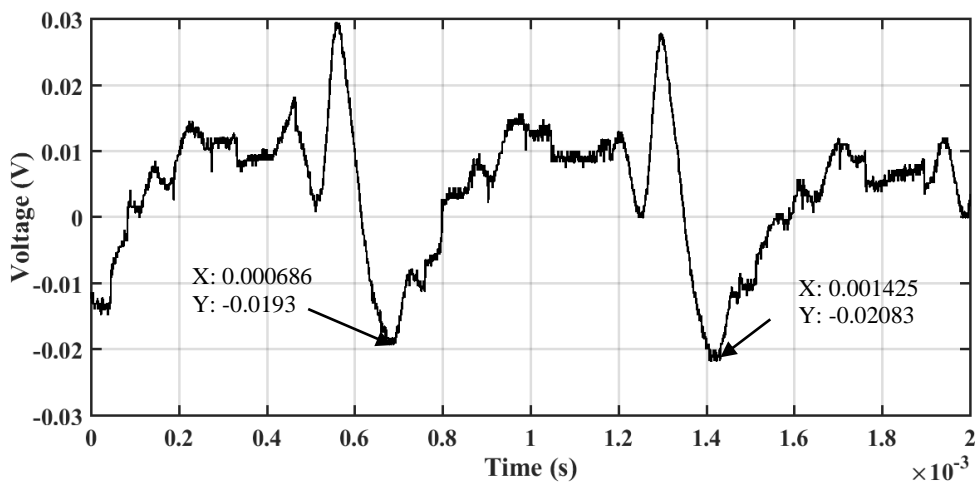


Figure 7.12: Spectrum in time domain at a speed 80,125 rpm speed near lower journal bearing

The stable rotation is achieved at speed close to 80,000 rpm with a synchronous vibration amplitude of 85 mV near the lower journal bearing (Fig. 7.12). The obtained signals are converted to acceleration and FFT of the vibrational spectrum at 80,000 rpm is shown in Figs 7.13 and 7.14 for response at lower and upper journal bearings respectively.

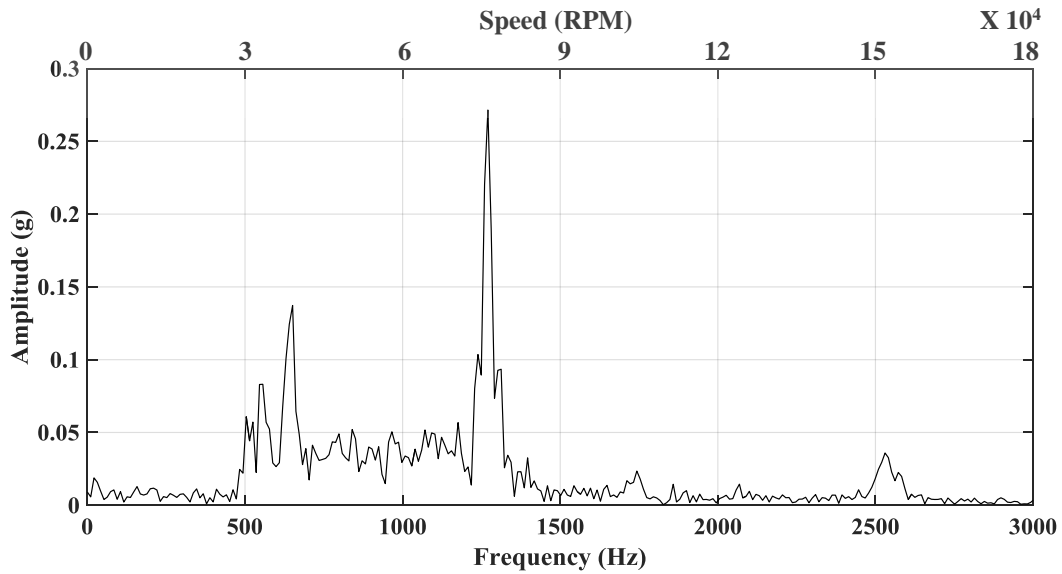


Figure 7.13: FFT Spectrum at a speed of 80000 rpm speed near lower journal bearing

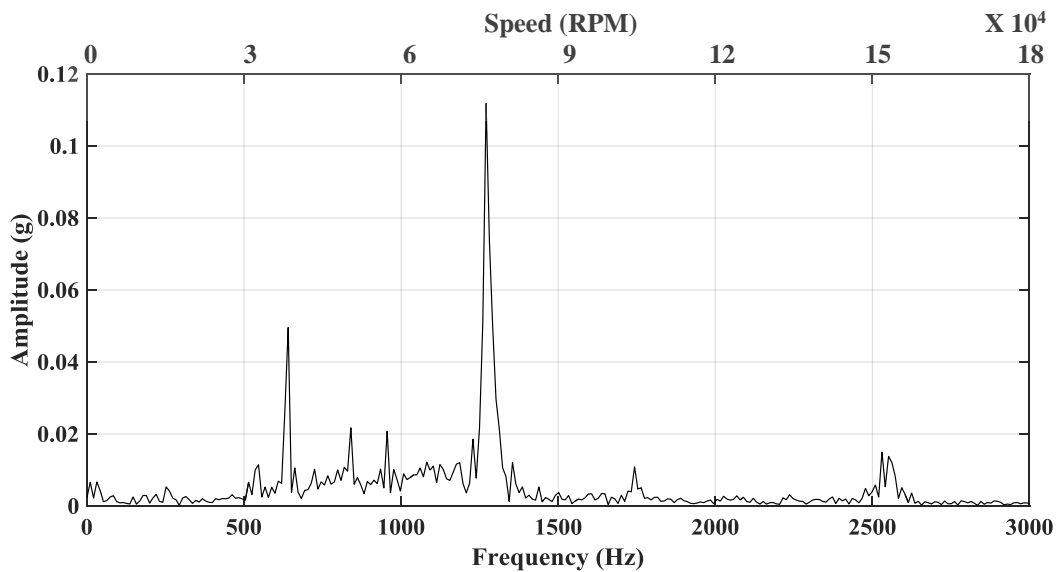


Figure 7.14: FFT Spectrum at a speed of 80000 rpm speed near upper journal bearing

The vibrational spectrum and critical speeds near the upper journal bearing(Fig. 7.14) is compared with the results of vibration analysis using tilting pad and aerostatic bearings of previous development programme [1]. In previous development program, the rotor was rotating at 86,000 rpm with supply pressure of 0.5MPa for the similar rotor and the amplitude of vibration near upper journal bearing was 1.60 g. The 1st and 2nd critical speed for both the cases were close to 22000 and 25000 respectively.

In the current test with modified aerodynamic bearings, the amplitude was found to be decreased by 25% to 1.12 g near upper journal bearing. No comparison could be made with the vibration level near lower journal bearing because of the absence of data in the previous development program. A pick is found near 2X speed, which is possibly due to mechanical looseness and misalignment of bearing unit with cold end and warm end units. A subharmonic frequency is encountered at 0.5X. The subharmonic frequency at ~675 Hz is expected to be because whirling of rotor. Whirling of the rotor is self-excited instability caused by gas whirling in bearing clearance. The vibration spectrum near upper journal bearing shows a minimal level of vibration due to misalignment and rotor whirling. So the fabricated rotor-bearing system is quite acceptable for the current application. The vibration analysis shows enhanced rotor stability; however, to study accurate vibrations of the rotor, accelerometers and oscilloscope need to be replaced with contactless eddy current probes and real-time spectrum analyzer, which is planned for next phase of the development program.

Chapter 8

Conclusions

8.1 Overview

The work presented in this dissertation is a modest attempt to understand the gas foil bearings and its implementation to a high-speed cryogenic turboexpander. The works carried out for this programme consist of design of axial and radial bump type gas foil bearings based on aerodynamic analysis of bearings and rotordynamics of high-speed prototype rotor. Finally, foil bearings and other associated parts of the turboexpander are fabricated with available resources and tested to study the rotor-bearing performance. A challenging attempt is made to progress in the development of gas foil bearings within limited technical and financial resources, and numbers of failures are also encountered before the success of this programme.

The author believes that the documented steps of computational and fabrication methodology will be helpful for the researchers around the world. However, an enormous amount of work is to be done on the aspect of system consistency and standardization before the turboexpander with gas foil bearings can be installed commercially in cryogenic refrigerator or liquefier. With the present work, it can be said that the valuable knowledge is gained with the design and fabrication of the gas foil bearings and associated components. The knowledge gained has resulted in the development of skill that will enable to design more refined systems in the days to come. This knowledge base will serve to fill up the void that presently exists in the field of gas bearing supported cryogenic turboexpanders. The present chapter is dedicated to mention significant points and contributions of the entire work in the form of conclusions. The scope of future work to extend or to modify with new concepts is also suggested in the present chapter.

8.2 Contributions

The following may be realized as a significant contribution to the project:

- i. An extensive literature review is done in the field of the gas bearings for turboexpander and gas foil bearings on its numerical analysis and development. This section can be served as a ready reference for various researchers around the world.

- ii. A detailed design methodology with steps of numerical analysis of radial and axial gas foil bearing is presented based on the pioneering works of Heshmat H. at el. [13, 14]. The detailed steps of analysis may assist as a useful technical source for future programs on gas foil bearings.
- iii. The rotordynamics of the small rotor is carried out to evaluate dynamic behaviour such as critical speed, mode shapes, and unbalanced response. The transfer matrix method is documented with simplified steps, and this can be applied by the researchers to save the time of analysis.
- iv. A detail fabrication methodology of bump forming is explained using two different set of dies. One set with rigid-flexible and other with the rigid-rigid die. The first set with flexible top die minimizes the tooling cost, whereas another die set with rigid top fabricates bumps of uniform dimensions. The FEM analysis of forming process with the 2nd die set using commercial software (DEFORM 3D) is explained, which simplifies the die design process.
- v. A compressive methodology to fabricate the axial and radial gas foil bearings has been presented. The prototype gas bearings have been designed and fabricated using this recipe.
- vi. The design procedure is not only for gas foil bearings but also for the associated components of the turboexpander such as a shaft, spacers, dynamic seal, locknuts and bearing housing. Many dimensions of these parts are computed and others have been selected. The arrangement of above components has been designed keeping in awareness about the geometrical clearances, tolerances and fitting accurately to the existing[1] cold end and warm end units. The bearing unit is designed for easy assembly and dismantling of its components.
- vii. A test rig is modified for studying rotor–bearing performance of turboexpander with gas foil bearings. The prototype turboexpander is tested on this rig, with turbine rotating stably at about 81,000 rpm at room temperature with the limited radial vibration of the rotor. The rotational speed could not be increased to the designed speed of turboexpander (140,000 rpm) due to the limitation of the available air compressor, which could supply the process gas of maximum 0.5 MPa instead of 0.7 MPa. The vibrational spectrum near upper journal bearing is compared with the results of vibration analysis using tilting pad and aerostatic bearings[1] at supply pressure of 0.5 MPa. The comparison succeeds with 25% reduction of the vibration level near upper journal bearing. No comparisons could

be done with vibration level near lower journal bearings due to unavailability of its performance data.

8.3 Future research scope

Development of a precision device product such as a cryogenic turboexpander working with gas foil bearings is a continuous process. This needs re-design, re-fabrication and testing to install the turboexpander in a running cryogenic refrigerator or liquefier. Some further works on the topic, which may be taken up in a greater situation are the following:

- i. Bump forming is one of the bottlenecks of present work, so the bump forming process can be further simplified with low-cost tooling and forming operation. The modified tooling should incorporate with the application of heat treatment during forming operations for uniform bumps with lesser springback.
- ii. A vibration study of the rotor in axial and radial directions is essential to understand the actual behaviour of these high-speed rotors. So the testing procedure needs to be enhanced with contactless eddy current probes and advanced vibration analysis equipment as a replacement for the accelerometer and oscilloscope.
- iii. In the present work, the gas foil bearings are designed with isothermal assumptions at ambient temperature. Due to viscous heat generation, the foil bearing can be subjected to high temperature. Without proper cooling, there is possibility of distortion of thin foils and this leads to failure of the gas foil bearings. To improve the prediction accuracy, a thermo-aerodynamic model needs to be developed with consideration of heat transfer in gas films, thermal resistance by thin foils and heat conduction by the rotor and its housings.

References

- [1] Choudhury B. K., "Design and construction of turboexpander based nitrogen liquefier," Ph. D. dissertation, NIT Rourkela, India, 2013.
- [2] Chakravarty A., "Analytical and experimental studies on gas bearings for cryogenic turboexpanders," Ph. D. dissertation, IIT Kharagpur, India, 2000.
- [3] Davydenkov I., Ravikovich Y. A., Davydov A., Ermilov Y. I., Zakharova N., Adler Y. R., and Shchedukhin S., "Development of cryogenic turboexpanders with gas dynamic foil bearings," *Cryogenics*, vol. 32, pp. 80-83, 1992.
- [4] Bulat M. P. and Bulat P. V., "The history of the gas bearings theory development," *World Applied Sciences Journal*, vol. 27, pp. 893-897, 2013.
- [5] Ghosh P., "Analytical and experimental studies on cryogenic turboexpander," Ph. D. dissertation, IIT Kharagpur, India, 2002.
- [6] Ghosh S. K., "Experimental and computational studies on cryogenic turboexpander," Ph. D. dissertation, NIT Rourkela, India, 2010.
- [7] Agrawal G. L., "Foil air/gas bearing technology—an overview," in *ASME 1997 International Gas Turbine and Aeroengine Congress and Exhibition*, p. V001T04A006, 1997.
- [8] Branagan M., Griffin D., Goyne C., and Untaroiu A., "Compliant gas foil bearings and analysis tools," *Journal of Engineering for Gas Turbines and Power*, vol. 138, pp. 054001-054012, 2016.
- [9] DellaCorte C. and Valco M. J., "Load capacity estimation of foil air journal bearings for oil-free turbomachinery applications," *Tribology Transactions*, vol. 43, pp. 795-801, 2000.
- [10] Nalepa K., Pietkiewicz P., and Zywicka G., "Development of the foil bearing technology," *Tech. Sci*, vol. 12, pp. 229-240, 2009.
- [11] DellaCorte C. and Bruckner R. J., "Remaining technical challenges and future plans for oil-free turbomachinery," *Journal of Engineering for Gas Turbines and Power*, vol. 133, pp. 042502-042507, 2011.
- [12] DellaCorte C., "Oil-Free shaft support system rotordynamics: Past, present and future challenges and opportunities," *Mechanical Systems and Signal Processing*, vol. 29, pp. 67-76, 2012.
- [13] Heshmat H., Walowit J., and Pinkus O., "Analysis of gas-lubricated foil journal bearings," *ASME J. Lubr. Technol*, vol. 105, pp. 647-655, 1983.
- [14] Heshmat H., Walowit J., and Pinkus O., "Analysis of gas lubricated compliant thrust bearings," *ASME J. Lubr. Technol*, vol. 105, pp. 638-646, 1983.
- [15] Jamir T. M., Kakoty S., and Kalita K., "Gas foil bearing analysis and the effect of bump foil thickness on its performance characteristics using a non-linear matrix equation solver," *International Journal of Recent advances in Mechanical Engineering*, vol. 3, pp. 15-31, 2014.
- [16] Radil K., Howard S., and Dykas B., "The role of radial clearance on the performance of foil air bearings," *Tribology Transactions*, vol. 45, pp. 485-490, 2002.

- [17] DellaCorte C., "Stiffness and damping coefficient estimation of compliant surface gas bearings for oil-free turbomachinery," *Tribology Transactions*, vol. 54, pp. 674-684, 2011.
- [18] Lund J., "Review of the concept of dynamic coefficients for fluid film journal bearings," *ASME J. Tribol*, vol. 109, pp. 37-41, 1987.
- [19] Carpino M. and Peng J., "Calculation of stiffness and damping coefficients for elastically supported gas foil bearings," *ASME J. Tribol*, vol. 115, pp. 20-27, 1993.
- [20] Peng Z. and Khonsari M., "Hydrodynamic analysis of compliant foil bearings with compressible air flow," *ASME J. Tribol*, vol. 126, pp. 542-546, 2004.
- [21] Peng Z. and Khonsari M., "On the limiting load-carrying capacity of foil bearings," *ASME J. Tribol*, vol. 126, pp. 817-818, 2004.
- [22] Kim T. H. and San Andrés L., "Limits for high-speed operation of gas foil bearings," *Journal of Tribology*, vol. 128, pp. 670-673, 2006.
- [23] Grau G., Iordanoff I., Bou Said B., and Berthier Y., "An original definition of the profile of compliant foil journal gas bearings: static and dynamic analysis," *Tribology Transactions*, vol. 47, pp. 248-256, 2004.
- [24] Patil M. B., Kalita K., and Kakoty S. K., "Performance analysis of gas foil bearing with different foil pivot configuration," *Advances in Mechanical Engineering*, vol. 2013, pp. 843419-29, 2013.
- [25] Kim T. H. and San Andrés L., "Analysis of gas foil bearings with piecewise linear elastic supports," presented at the World Tribology Congress III, 2005.
- [26] Kai F. and Kaneko S., "Parametric studies on static performance and nonlinear instability of bump-type foil bearings," *Journal of System Design and Dynamics*, vol. 4, pp. 871-883, 2010.
- [27] Feng K. and Kaneko S., "Analytical model of bump-type foil bearings using a link-spring structure and a finite-element shell model," *Journal of Tribology*, vol. 132, p. 021706, 2010.
- [28] Swanson E. E., "Bump foil damping using a simplified model," *Journal of tribology*, vol. 128, pp. 542-550, 2006.
- [29] Lee D.-H., Kim Y.-C., and Kim K.-W., "The effect of Coulomb friction on the static performance of foil journal bearings," *Tribology International*, vol. 43, pp. 1065-1072, 2010.
- [30] Hoffmann R., Munz O., Pronobis T., Barth E., and Liebich R., "A valid method of gas foil bearing parameter estimation: A model anchored on experimental data," *Proceedings of the Institution of Mechanical Engineers, Part C: Journal of Mechanical Engineering Science*, p. 0954406216667966, 2016.
- [31] San Andrés L. and Kim T. H., "Computational analysis of gas foil bearings integrating 1D and 2D finite element models for top foil," Turbomachinery Laboratory, Texas A&M University 2006.
- [32] San Andrés L. and Kim T. H., "Analysis of gas foil bearings integrating FE top foil models," *Tribology International*, vol. 42, pp. 111-120, 2009.
- [33] Carpino M. and Talmage G., "Prediction of rotor dynamic coefficients in gas lubricated foil journal bearings with corrugated sub-foils," *Tribology Transactions*, vol. 49, pp. 400-409, 2006.

- [34] Carpino M. and Talmage G., "Minimum film thickness in a gas foil journal bearing with an unbalanced rotor," *Tribology Transactions*, vol. 53, pp. 433-439, 2010.
- [35] Yu H., Shuangtao C., Rugang C., Qiaoyu Z., and Hongli Z., "Numerical study on foil journal bearings with protuberant foil structure," *Tribology International*, vol. 44, pp. 1061-1070, 2011.
- [36] Kim T. H. and San Andrés L., "Heavily loaded gas foil bearings: a model anchored to test data," *Journal of Engineering for Gas Turbines and Power*, vol. 130, p. 012504, 2008.
- [37] Bhore S. P. and Darpe A. K., "Nonlinear dynamics of flexible rotor supported on the gas foil journal bearings," *Journal of Sound and Vibration*, vol. 332, pp. 5135-5150, 2013.
- [38] Schiffmann J. and Spakovszky Z., "Foil bearing design guidelines for improved stability," *Journal of Tribology*, vol. 135, p. 011103, 2013.
- [39] Iordanoff I., "Analysis of an aerodynamic compliant foil thrust bearing: method for a rapid design," *Journal of Tribology*, vol. 121, pp. 816-822, 1999.
- [40] Heshmat C., Xu D. S., and Heshmat H., "Analysis of gas lubricated foil thrust bearings using coupled finite element and finite difference methods," *Journal of Tribology*, vol. 122, pp. 199-210, 2000.
- [41] Park D.-J., Kim C.-H., Jang G.-H., and Lee Y.-B., "Theoretical considerations of static and dynamic characteristics of air foil thrust bearing with tilt and slip flow," *Tribology International*, vol. 41, pp. 282-295, 2008.
- [42] San Andrés L., Ryu K., and Diemer P., "Prediction of gas thrust foil bearing performance for oil-free automotive turbochargers," *Journal of Engineering for Gas Turbines and Power*, vol. 137, p. 032502, 2015.
- [43] Gad A. M. and Kaneko S., "A new structural stiffness model for bump-type foil bearings: Application to generation II gas lubricated foil thrust bearing," *Journal of Tribology*, vol. 136, p. 041701, 2014.
- [44] Feng K., Liu L.-J., Guo Z.-Y., and Zhao X.-Y., "Parametric study on static and dynamic characteristics of bump-type gas foil thrust bearing for oil-free turbomachinery," *Proceedings of the Institution of Mechanical Engineers, Part J: Journal of Engineering Tribology*, vol. 229, pp. 1247-1263, 2015.
- [45] Conboy T., "Real-gas effects in foil thrust bearings operating in the turbulent regime," *Journal of Tribology*, vol. 135, p. 031703, 2013.
- [46] Bruckner R. J., DellaCorte C., and Prahl J. M., "Analytic modeling of the hydrodynamic, thermal, and structural behavior of foil thrust bearings," vol. NASA/TM—2005-213811, 2005.
- [47] Quan Z., Yu H., Rugang C., Shuangtao C., and Chunzheng C., "Static analysis of viscoelastic supported gas foil thrust bearing with journal inclination," *Journal of Advanced Mechanical Design, Systems, and Manufacturing*, vol. 4, pp. 1210-1220, 2010.
- [48] Somaya K., Yoshimoto S., and Miyatake M., "Load capacity of aerodynamic foil thrust bearings supported by viscoelastic material," *Proceedings of the Institution of Mechanical Engineers, Part J: Journal of Engineering Tribology*, vol. 223, pp. 645-652, 2009.

- [49] Xiong L.-Y., Wu G., Hou Y., Liu L.-Q., Ling M.-F., and Chen C.-Z., "Development of aerodynamic foil journal bearings for a high speed cryogenic turboexpander," *Cryogenics*, vol. 37, pp. 221-230, 1997.
- [50] Hou Y., Xiong L., Wang J., Lin M., and Chen C., "The experimental study of aerodynamic plate-foil journal bearings for high speed cryogenic turboexpander," *Tribology Transactions*, vol. 43, pp. 681-684, 2000.
- [51] Heshmat H., "Advancements in the performance of aerodynamic foil journal bearings: high speed and load capability," *ASME J. Tribol*, vol. 116, pp. 287-295, 1994.
- [52] Heshmat H., "Operation of foil bearings beyond the bending critical mode," *Journal of Tribology*, vol. 122, pp. 192-198, 2000.
- [53] DellaCorte C., Radil K. C., Bruckner R. J., and Howard S. A., "Design, fabrication, and performance of open source generation I and II compliant hydrodynamic gas foil bearings," *Tribology Transactions*, vol. 51, pp. 254-264, 2008.
- [54] Shalash K. and Schiffmann J., "On the manufacturing of compliant foil bearings," *Journal of Manufacturing Processes*, vol. 25, pp. 357-368, 2017.
- [55] Chen H. M., Howarth R., Soyars W. M., Theilacker J. C., and Bernard G., "Application of foil bearings to helium turbocompressor," in *30th Turbomachinery Symposium*, Texas A&M University, pp. 104-113, 2001.
- [56] Sim K., Yong-Bok L., Kim T. H., and Lee J., "Rotordynamic performance of shimmed gas foil bearings for oil-free turbochargers," *Journal of Tribology*, vol. 134, p. 031102, 2012.
- [57] Sim K., Lee Y.-B., and Kim T. H., "Effects of mechanical preload and bearing clearance on rotordynamic performance of lobed gas foil bearings for oil-free turbochargers," *Tribology Transactions*, vol. 56, pp. 224-235, 2013.
- [58] Lee Y.-B., Kwon S. B., Kim T. H., and Sim K., "Feasibility study of an oil-free turbocharger supported on gas foil bearings via on-road tests of a two-liter class diesel vehicle," *Journal of Engineering for Gas Turbines and Power*, vol. 135, p. 052701, 2013.
- [59] Kulkarni S., Naik S. D., Kumar K. S., Radhakrishna M., and Jana S., "Development of foil bearings for small rotors," in *ASME 2013 Gas Turbine India Conference*, p. V001T05A010, 2013.
- [60] Hou Y., Ma B., Yang S., Chen X., Zheng Y., and Chen S., "Experimental study on bump-foil gas bearing with different diametric clearance configurations," *Journal of Mechanical Science and Technology*, vol. 29, pp. 2089-2095, 2015.
- [61] Lee Y., Kim T., Kim C., Lee N., and Choi D., "Unbalance response of a supercritical rotor supported by foil bearings-comparison with test results," *Tribology Transactions*, vol. 47, pp. 54-60, 2004.
- [62] Salehi M., Heshmat H., and Walton J. F., "Advancements in the structural stiffness and damping of a large compliant foil journal bearing: an experimental study," *Journal of Engineering for Gas Turbines and Power*, vol. 129, pp. 154-161, 2007.

- [63] Lee Y.-B., Park D.-J., Kim C.-H., and Ryu K., "Rotordynamic characteristics of a micro turbo generator supported by air foil bearings," *Journal of Micromechanics and Microengineering*, vol. 17, p. 297, 2007.
- [64] Rubio D. and San Andres L., "Structural stiffness, dry friction coefficient, and equivalent viscous damping in a bump-type foil gas bearing," *Journal of engineering for gas turbines and power*, vol. 129, pp. 494-502, 2007.
- [65] Arora V., Van der Hoogt P., Aarts R., and de Boer A., "Identification of dynamic properties of radial air-foil bearings," *International Journal of Mechanics and Materials in Design*, vol. 6, pp. 305-318, 2010.
- [66] Kim D. and Park S., "Hydrostatic air foil bearings: Analytical and experimental investigation," *Tribology International*, vol. 42, pp. 413-425, 2009.
- [67] Kumar M. and Kim D., "Static performance of hydrostatic air bump foil bearing," *Tribology International*, vol. 43, pp. 752-758, 2010.
- [68] Duan W., Sun Y., Ding C., and Yu L., "Structural stiffness of X-750 alloy bump foil strips for compliant foil bearings with different heat treatments," *Journal of Tribology*, vol. 138, p. 031702, 2016.
- [69] Laskowski J. and DellaCorte C., "Friction and wear characteristics of candidate foil bearing materials from 25 C to 800 C," *Lubrication Engineering*, vol. 52, pp. 605-612, 1996.
- [70] DellaCorte C., Zaldana A. R., and Radil K. C., "A systems approach to the solid lubrication of foil air bearings for oil-free turbomachinery," *ASME J. Tribology* vol. 126, pp. 200-207, 2004.
- [71] Jahanmir S., Heshmat H., and Heshmat C., "Assessment of tribological coatings for foil bearing applications," *Tribology Transactions*, vol. 52, pp. 231-242, 2009.
- [72] Dykas B., Bruckner R., DellaCorte C., Edmonds B., and Prahl J., "Design, fabrication, and performance of foil gas thrust bearings for microturbomachinery applications," *Journal of Engineering for Gas Turbines and Power*, vol. 131, p. 012301, 2009.
- [73] Bruckner R. J., "Performance of simple gas foil thrust bearings in air," vol. NASA/TM—2012-217262, 2012.
- [74] Balducchi F., Arghir M., Gauthier R., and Renard E., "Experimental analysis of the start-up torque of a mildly loaded foil thrust bearing," *Journal of Tribology*, vol. 135, p. 031702, 2013.
- [75] Bauman S., "An oil-free thrust foil bearing facility design, calibration, and operation," vol. NASA/TM—2005-213568, 2005.
- [76] Arora V., Van Der Hoogt P., Aarts R., and De Boer A., "Identification of stiffness and damping characteristics of axial air-foil bearings," *International Journal of Mechanics and Materials in Design*, vol. 7, pp. 231-243, 2011.
- [77] Lee Y.-B., Kim T. Y., Kim C. H., and Kim T. H., "Thrust bump air foil bearings with variable axial load: theoretical predictions and experiments," *Tribology Transactions*, vol. 54, pp. 902-910, 2011.
- [78] Fanning C. E. and Blanchet T. A., "High-temperature evaluation of solid lubricant coatings in a foil thrust bearing," *Wear*, vol. 265, pp. 1076-1086, 2008.
- [79] Walowit J. London: Applied Science Publishers Ltd., 1975.

- [80] Rubio D. and San Andrés L., "Bump-type foil bearing structural stiffness: experiments and predictions," *Journal of engineering for gas turbines and power*, vol. 128, pp. 653-660, 2006.
- [81] Huang P., *Numerical calculation of lubrication: methods and programs*: John Wiley & Sons, 2013.
- [82] Nguyen-Schäfer H., *Rotordynamics of automotive turbochargers*: Springer, 2015.
- [83] Bekinal S. I., Tumkur Ramakrishna A. R., and Jana S., "Analysis of radial magnetized permanent magnet bearing characteristics for five degrees of freedom," *Progress In Electromagnetics Research B*, vol. 52, pp. 307-326, 2013.
- [84] Vance J. M., *Rotordynamics of turbomachinery*. Texas: John Wiley & Sons, 1988.
- [85] Rao J., *Rotor Dynamics*. New Delhi: New Age International Publishers, 1983.
- [86] Beer F. P., Johnston Jr E. R., Mazurek D. F., Cornwell P. J., Eisenberg E. R., and Sanghi S., *Vector mechanics for engineers* vol. 1: Tata McGraw-Hill Education, 1972.
- [87] Gale W. F. and Totemeier T. C., *Smithells metals reference book*: Butterworth-Heinemann, 2003.
- [88] Chaudhary G., "Labyrinth seal leakage analysis," M.S. Thesis, Texas A&M University, USA, 2011.
- [89] DellaCorte C., Fellenstein J. A., and Benoy P. A., "Evaluation of advanced solid lubricant coatings for foil air bearings operating at 25 and 500 C," *Tribology Transactions*, vol. 42, pp. 338-342, 1999.

Appendix

Production drawing of fabricated parts

Sl No	Drawing No	Part Name	Material	Quantity
Die for journal and thrust bump foil				
1	DIE-01	Bottom die for journal bumps	SS302	1
2	DIE-02	Bottom die for thrust bumps	SS302	1
3	DIE-03	Blocks for journal and thrust bumps forming	SS302	1+1
4	DIE-04	Modified bottom die for journal bumps	SS303	1
5	DIE-05	Modified top die for journal bumps	SS303	1
6	DIE-06	Modified bottom die for thrust bumps	SS303	1
7	DIE-07	Modified top die for thrust bumps	SS303	1
Bearing Unit parts				
8	TEX-01	Shaft	Monel K-500	1
9	TEX-02	Shaft with ring magnet slot	Monel K-500	1
10	TEX-03	Journal bearing base	SS304	2
11	TEX-04	Journal bearing base for ring magnet	SS304	2
12	TEX-05	Thrust bearing base	SS304	2
13	TEX-06	Lock nut (turbine side)	SS304	1
14	TEX-07	Lock nut (compressor side)	SS304	1
15	TEX-08	Spacer between thrust bearing	SS304	1
16	TEX-09	Lower spacer between journal and thrust bearing	SS304	1
17	TEX-10	Upper spacer between journal and thrust bearing	SS304	1
18	TEX-11	Thermal insulator	Teflon	1
19	TEX-12	Thermal insulator with ring magnet slot	Teflon	1
20	TEX-13	Bearing housing	SS304	1
21	TEX-14	Assembly of bearing unit	-	-
22	FOIL 01	Journal top and bump foil	Phosphor Bronze	2
23	FOIL02	Thrust top foil and bump foil	Phosphor Bronze	8

10 Locking screw holes
M10X1.5 (Five each Side)

Assembly of
Frame and
Bump Dies

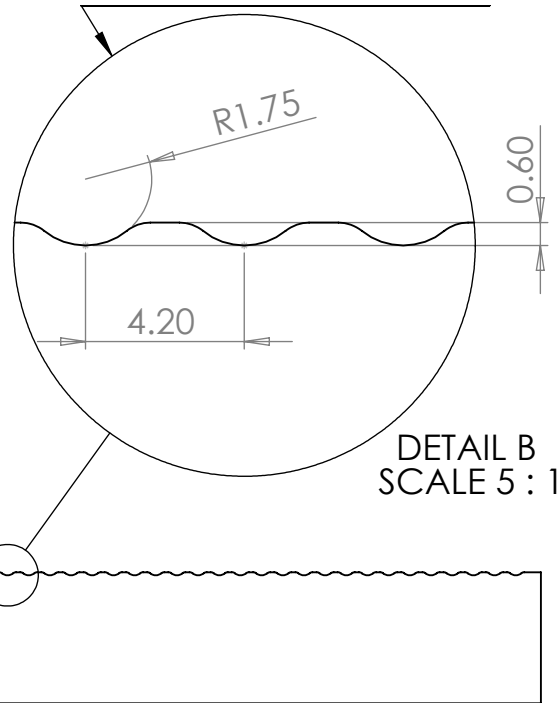
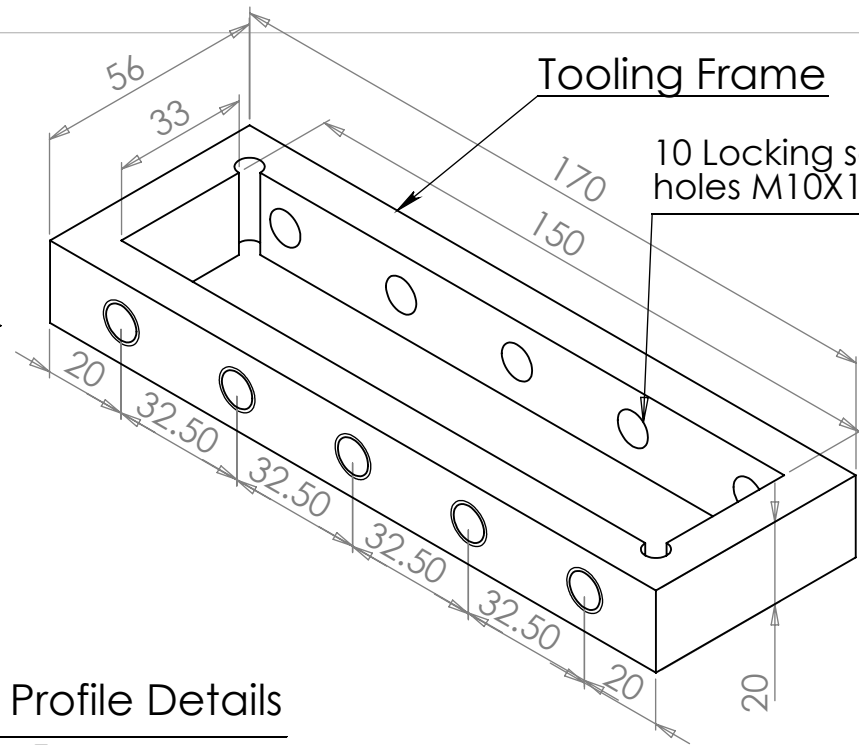
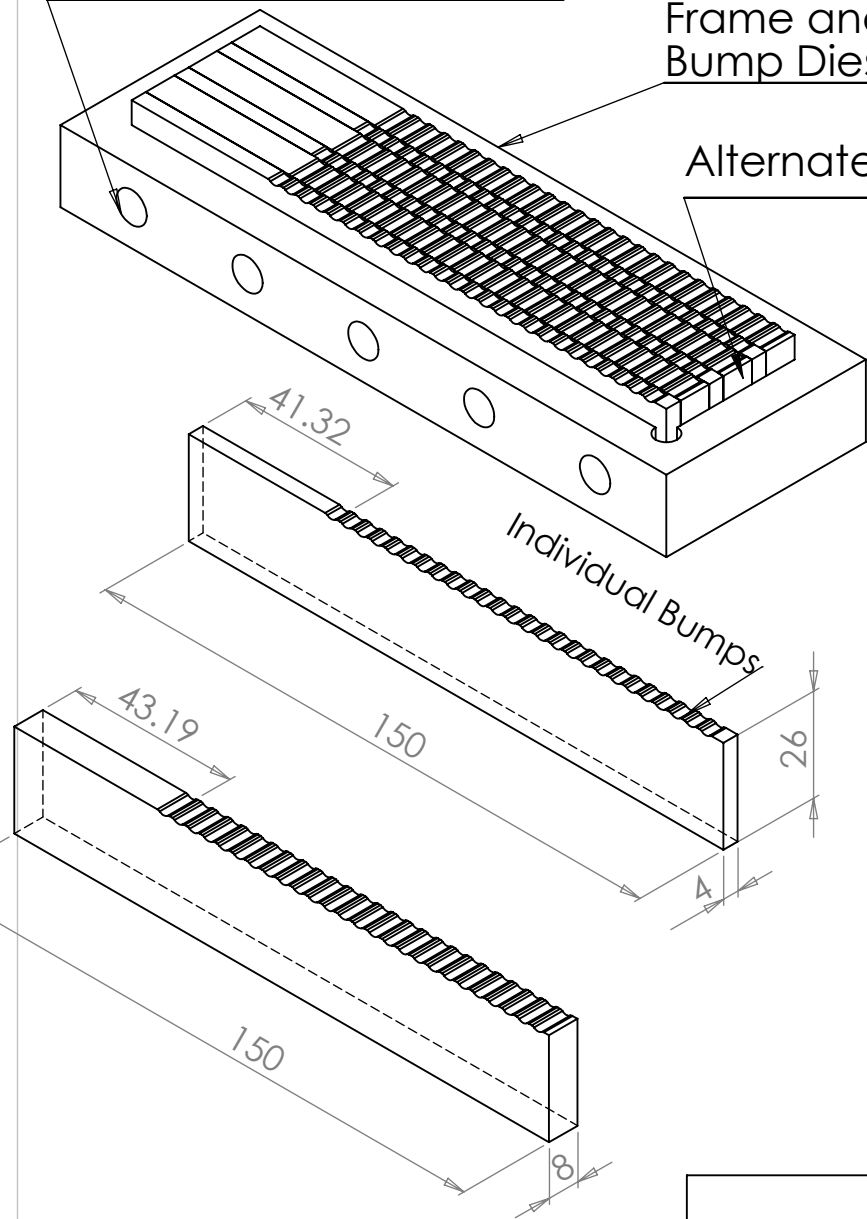
Alternate Bump Dies

Individual Bumps

Bump Profile Details

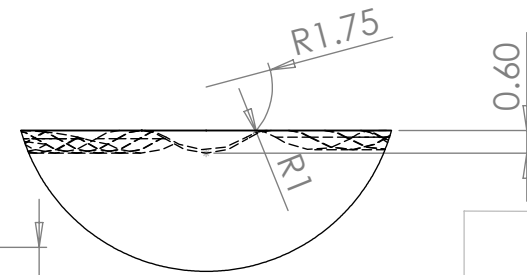
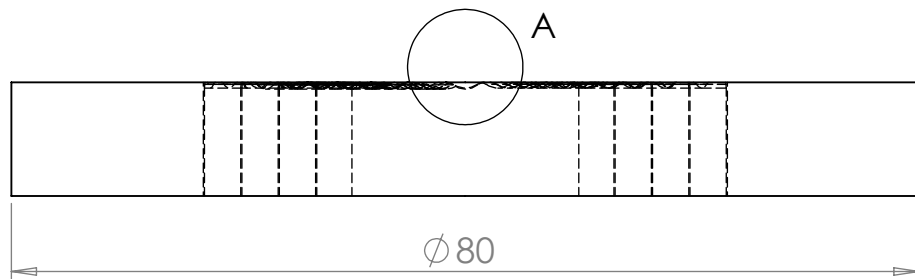
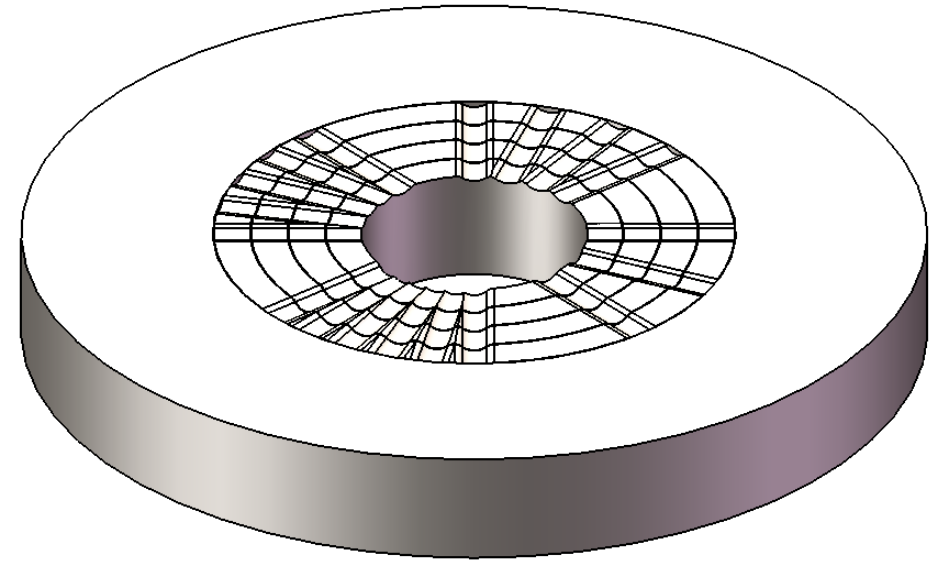
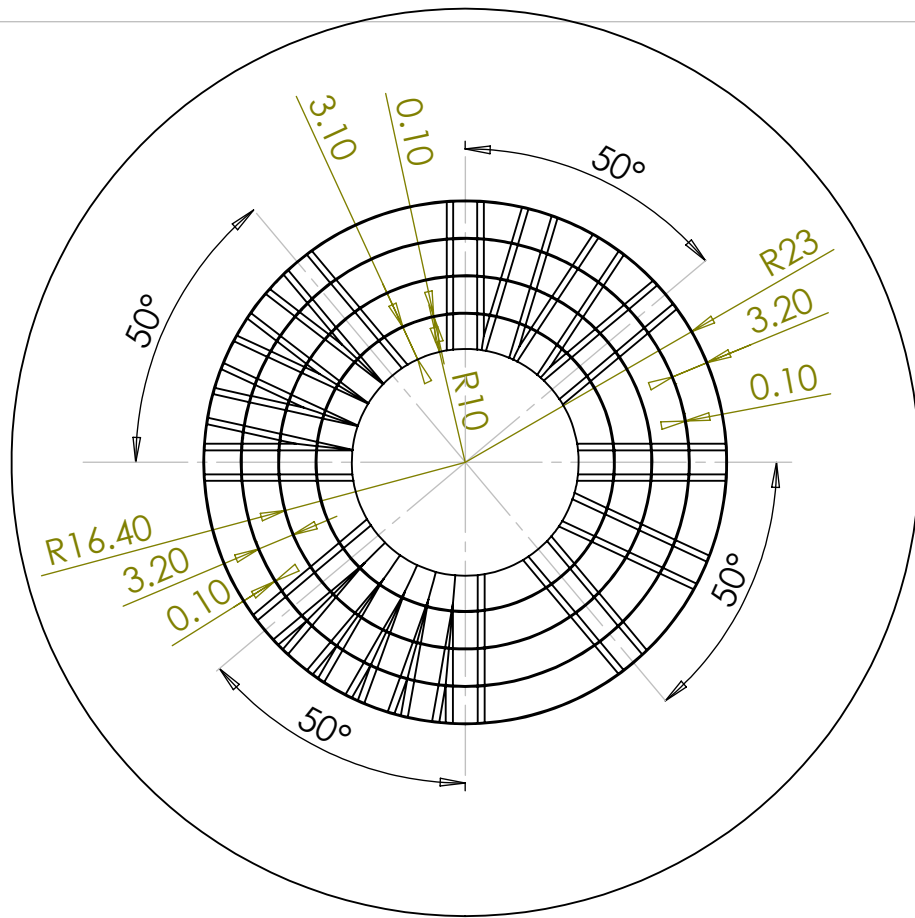
Tooling Frame

10 Locking screw
holes M10X1.5



Note:
All Dimensions are in mm
General tolerance is ± 0.01 mm
Surface Finish $\nabla 1.6$ unless stated otherwise

MECHANICAL ENGINEERING DEPT. NIT Rourkela	
TITLE:	CRYOGENIC TURBOEXPANDER
Bottom Die for journal Bump	
MATERIAL: SS302	DWG NO. DIE-01
SCALE: 1:1.5	DATE: 04/03/2017



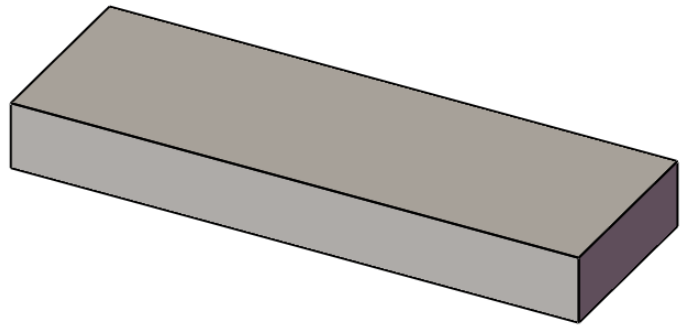
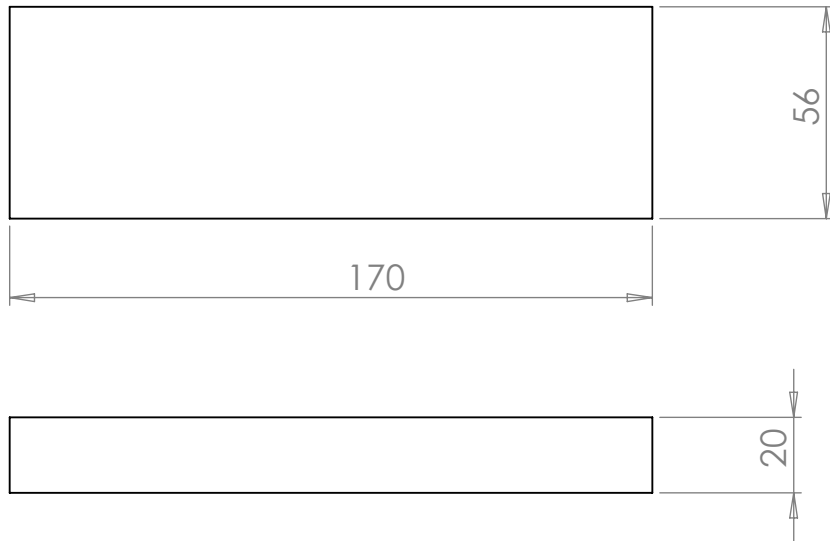
DETAIL A
SCALE 5 : 1

Note:
All dimensions are in mm
General tolerance is +/- 0.01 mm

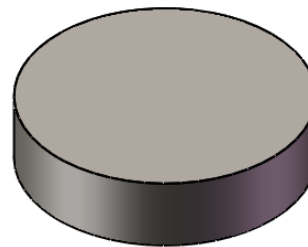
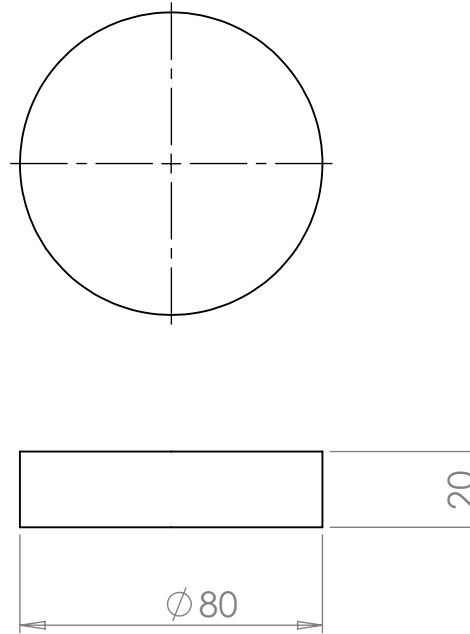
Surface Finish $\sqrt{1.6}$ unless stated otherwise

MECHANICAL ENGINEERING DEPT. NIT Rourkela	
TITLE:	CRYOGENIC TURBOEXPANDER
Bottom Die for Thrust Bumps	
MATERIAL: SS302	DWG NO. DIE-02
SCALE: 1.5:1	DATE: 04/03/2017

Block for Journal Bumps Formation



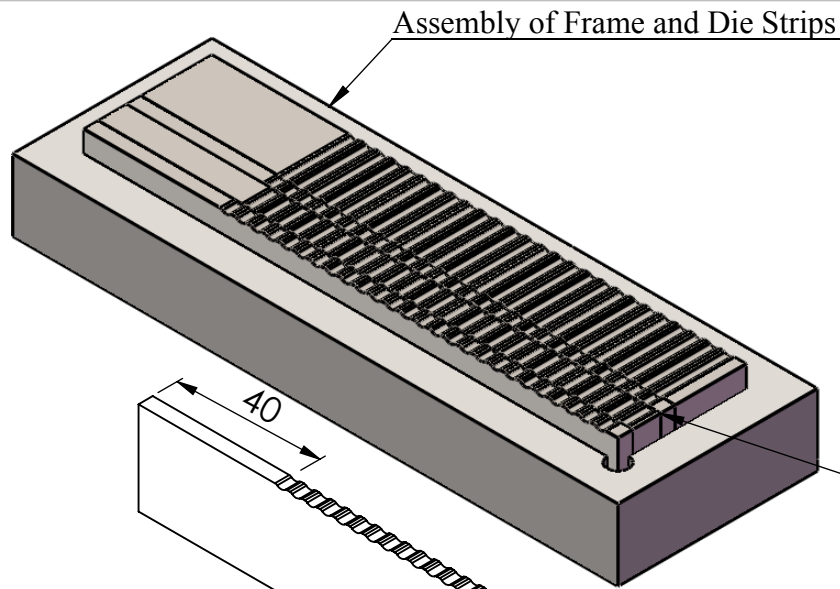
Block for Thrust Bumps Formation



Note:
All dimensions are in mm
General tolerance is +/- 0.01 mm

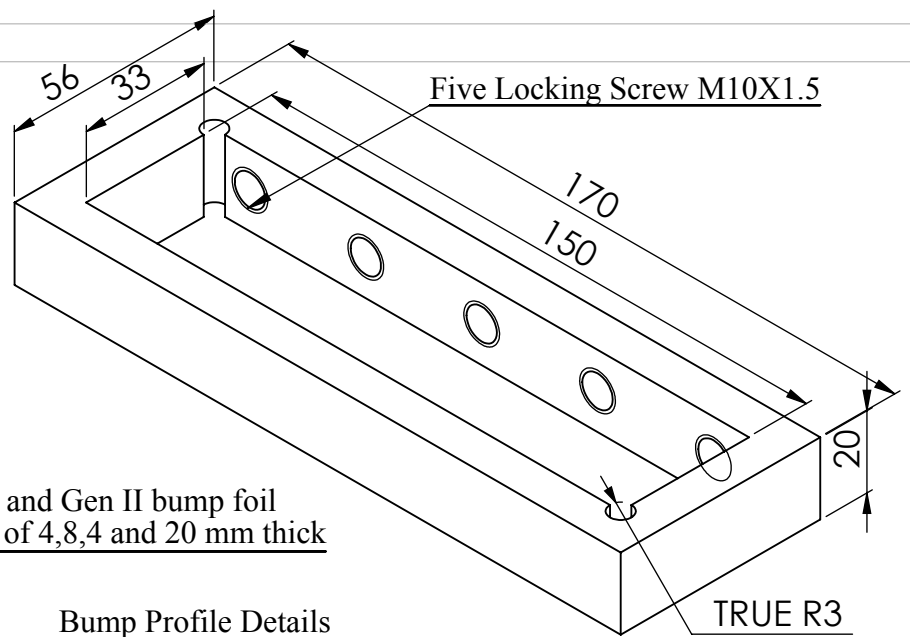
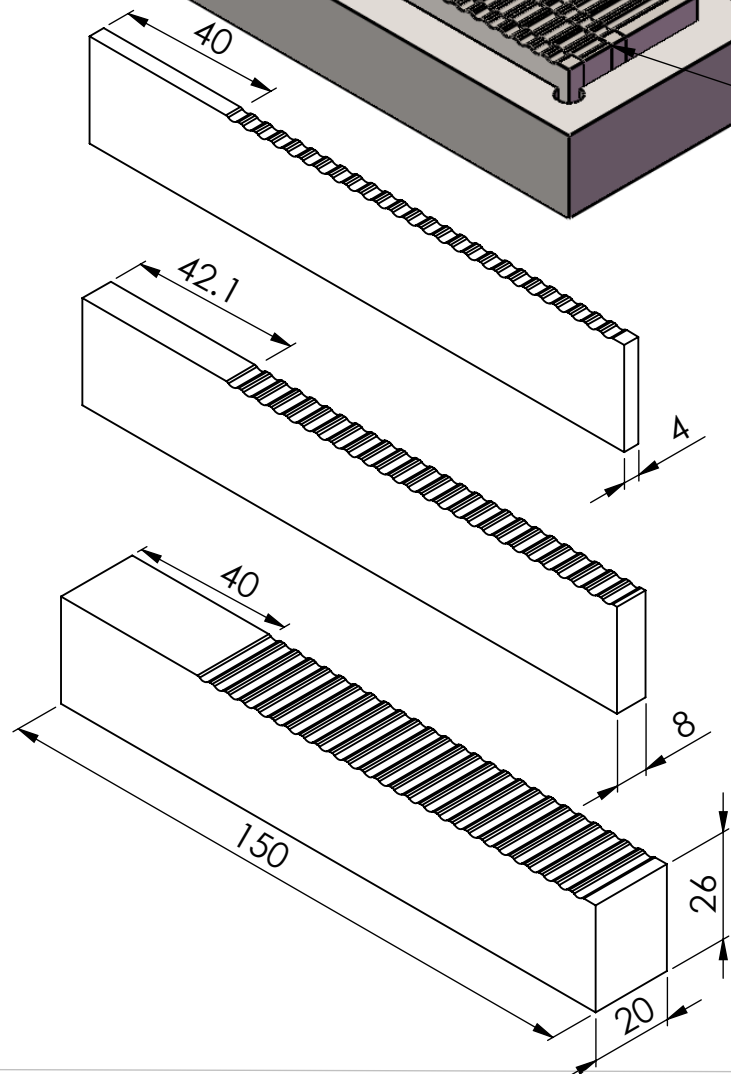
Surface Finish $\sqrt{1.6}$ unless stated otherwise

MECHANICAL ENGINEERING DEPT. NIT Rourkela		
TITLE: CRYOGENIC TURBOEXPANDER		
Blocks for Journal and Thrust Bumps Formation		
MATERIAL: SS302	DWG NO. DIE-03	
	SCALE:1:1	DATE: 04/03/2017



Assembly of Frame and Die Strips

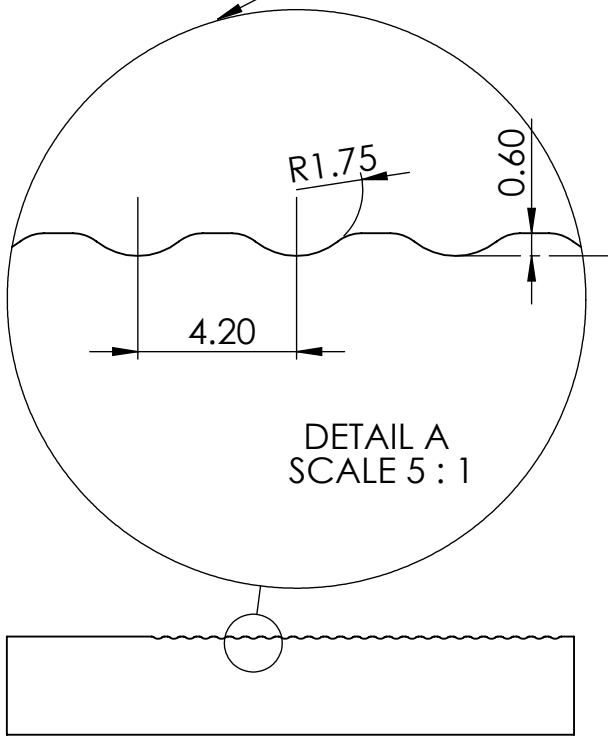
Strips for Gen I and Gen II bump foil in the sequence of 4,8,4 and 20 mm thick



Five Locking Screw M10X1.5

TRUE R3

Bump Profile Details



DETAIL A
SCALE 5 : 1

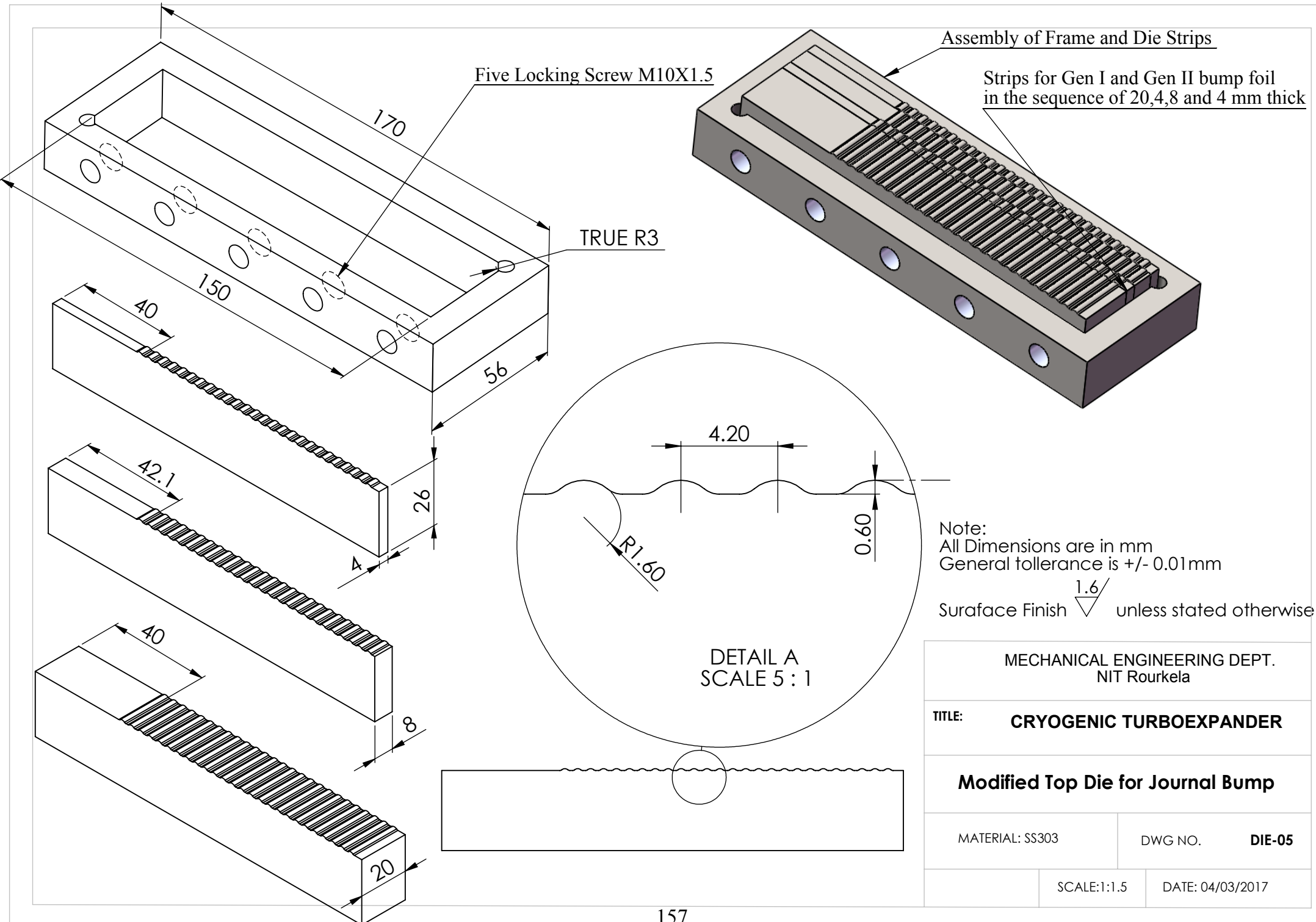
02 Angular Pin of 6X40 and an Angular Cut for Allignment



Note:
All Dimensions are in mm
General tolerance is +/- 0.01mm

Surface Finish $\nabla 1.6$ unless stated otherwise

MECHANICAL ENGINEERING DEPT. NIT Rourkela	
TITLE: CRYOGENIC TURBOEXPANDER	
Modified Bottom Die for Journal bump	
MATERIAL: SS 303	DWG NO. DIE 04
SCALE:1:1.5	DATE: 04/03/2017



Five Locking Screw M10X1.5

Assembly of Frame and Die Strips

Strips for Gen I and Gen II bump foil in the sequence of 20,4,8 and 4 mm thick

TRUE R3

Note:
 All Dimensions are in mm
 General tolerance is +/- 0.01mm
 Surface Finish $\sqrt{1.6}$ unless stated otherwise

DETAIL A
 SCALE 5 : 1

MECHANICAL ENGINEERING DEPT.
 NIT Rourkela

TITLE: **CRYOGENIC TURBOEXPANDER**

Modified Top Die for Journal Bump

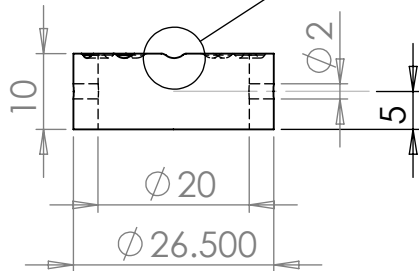
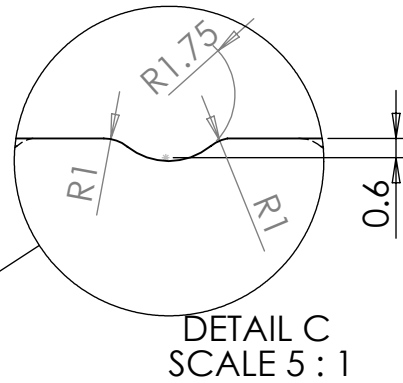
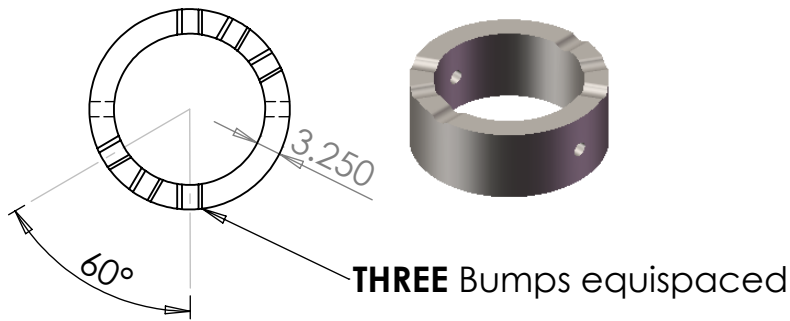
MATERIAL: SS303

DWG NO. **DIE-05**

SCALE:1:1.5

DATE: 04/03/2017

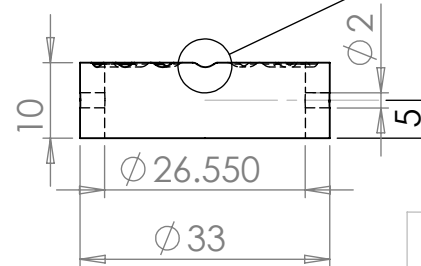
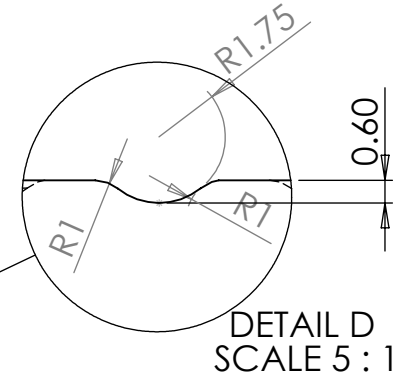
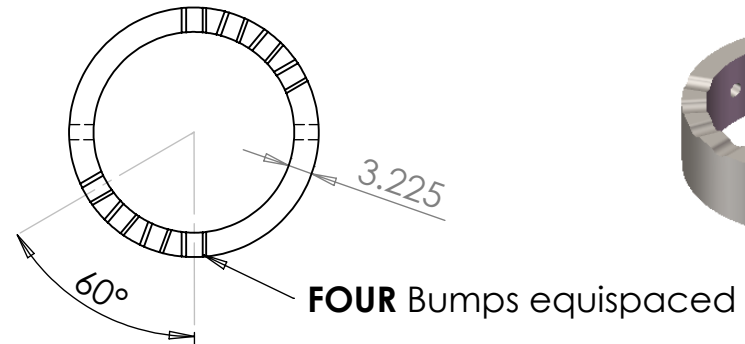
RING 1



Note:
All Dimensions are in mm
General tolerance is +/- 0.01mm

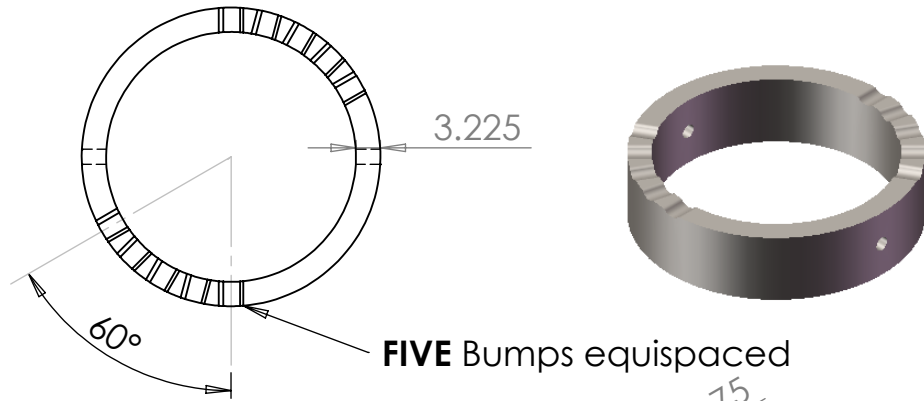
Surface Finish $\sqrt{1.6}$ unless stated otherwise

RING 2

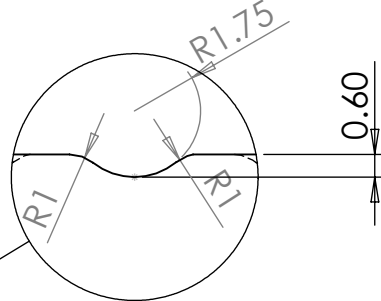


MECHANICAL ENGINEERING DEPT. NIT Rourkela		
TITLE: CRYOGENIC TURBOEXPANDER		
Modified Bottom Die for Thrust Bump: Ring 1 and 2		
MATERIAL: SS303	DWG NO.	DIE 06(a)
SCALE:1:1	DATE:4/3/2017	

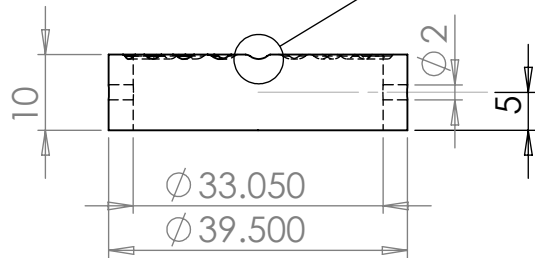
Ring 3



FIVE Bumps equispaced



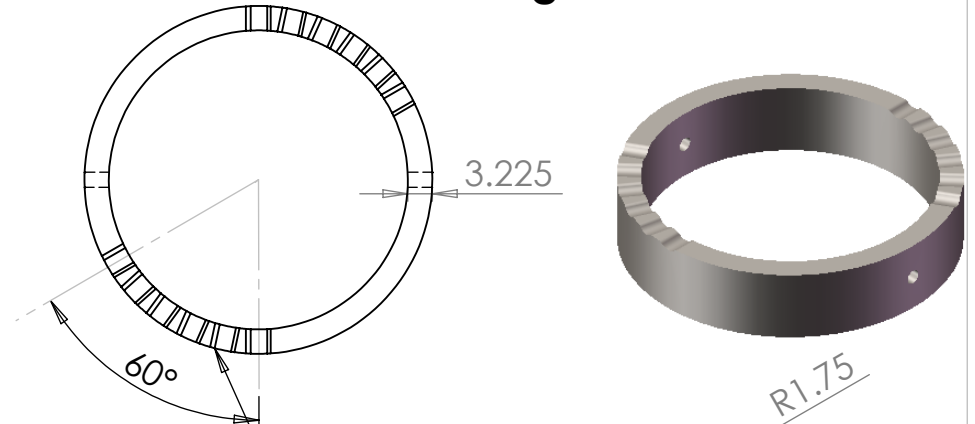
DETAIL E
SCALE 5 : 1



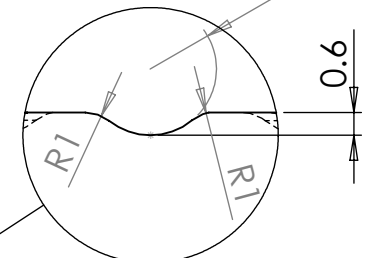
Note:
All Dimensions are in mm
General tolerance is +/- 0.01mm

Surface Finish $\sqrt{1.6}$ unless stated otherwise

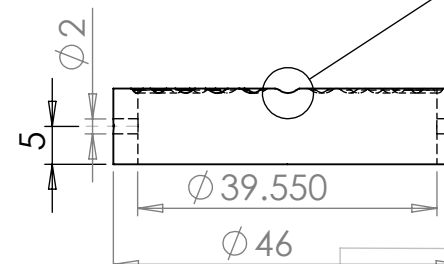
Ring 4



SIX Bumps equispaced



DETAIL F
SCALE 5 : 1



MECHANICAL ENGINEERING DEPT.
NIT Rourkela

TITLE: **CRYOGENIC TURBOEXPANDER**

**Modified Bottom Die for Thrust
Bump: Ring 3 and 4**

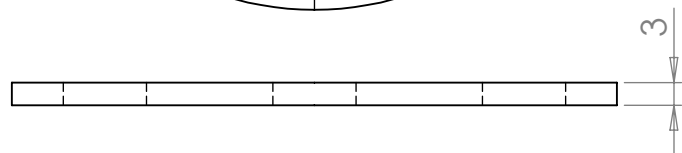
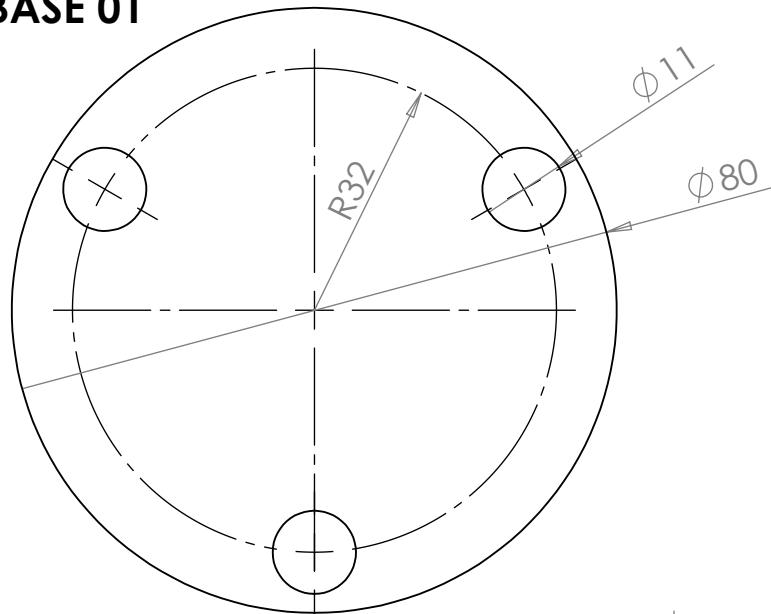
MATERIAL: SS303

DWG NO. **DIE 06(b)**

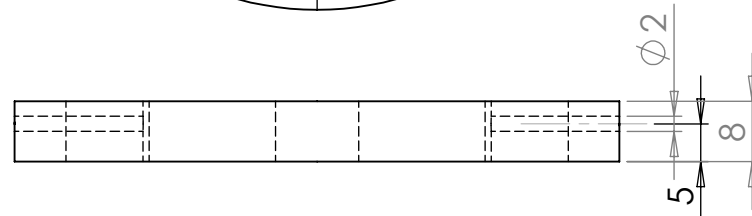
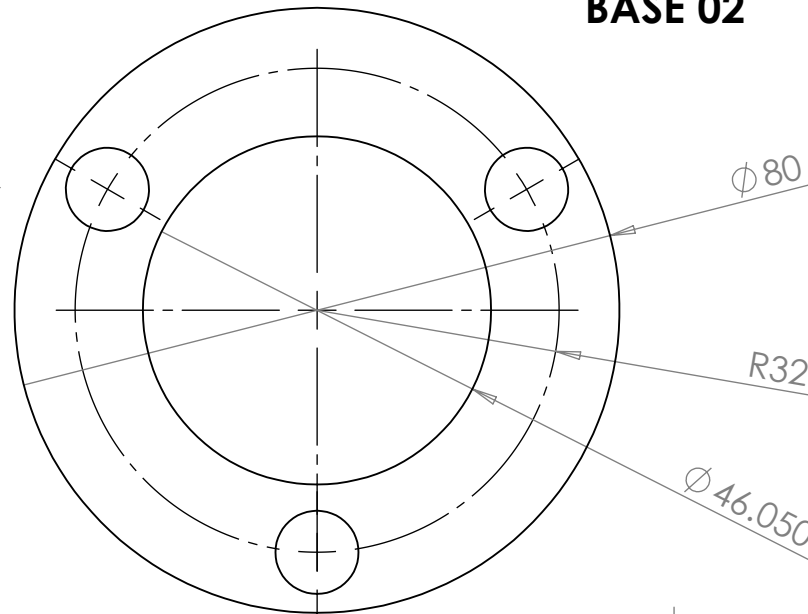
SCALE:1:1.5

DATE:04/03/2017

BASE 01

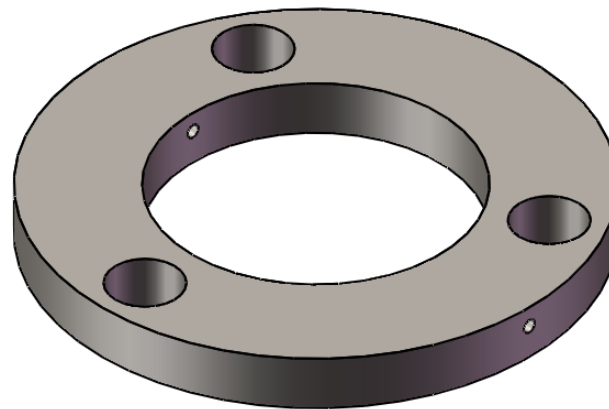
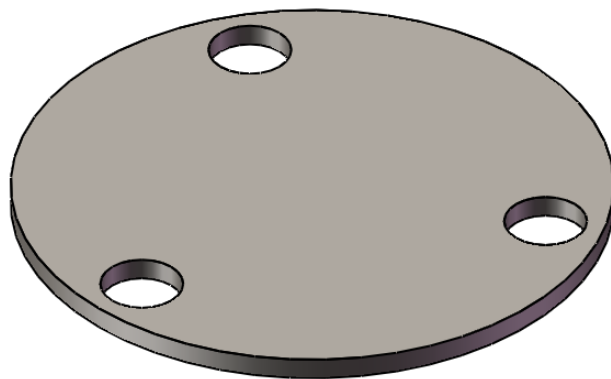


BASE 02



TWO sets of Base01 and Base02 to be fabricated

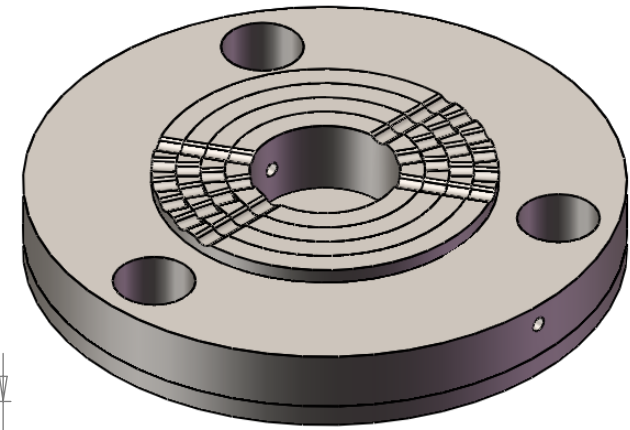
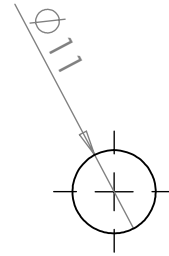
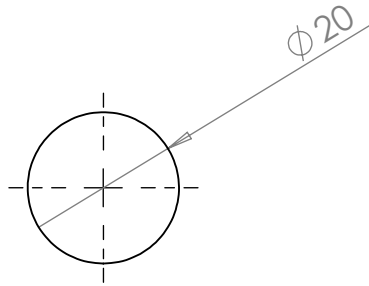
One set for bottomDie and other set for **Top Die**



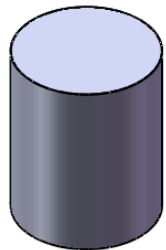
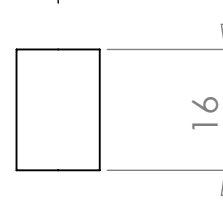
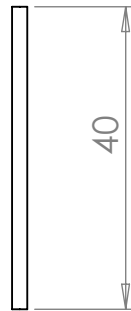
Note:
All Dimensions are in mm
General tolerance is +/- 0.01mm

Surface Finish $\sqrt{1.6}$ unless stated otherwise

MECHANICAL ENGINEERING DEPT. NIT Rourkela	
TITLE: CRYOGENIC TURBOEXPANDER	
Modified Bottom Die for Thrust Bump: Base 01 and Base 02	
MATERIAL: SS303	DWG NO. DIE 06(c)
SCALE:1:1.5	DATE: 03/04/2017



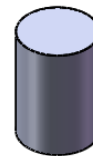
Assembly of Rings and Base



Central Pin(01)



Alignment Pin1(06)



Alignment Pin2(06)

Note:
All Dimensions are in mm
General tolerance is +/- 0.01mm

Surface Finish $\sqrt{1.6}$ unless stated otherwise

MECHANICAL ENGINEERING DEPT.
NIT Rourkela

TITLE: **CRYOGENIC TURBOEXPANDER**

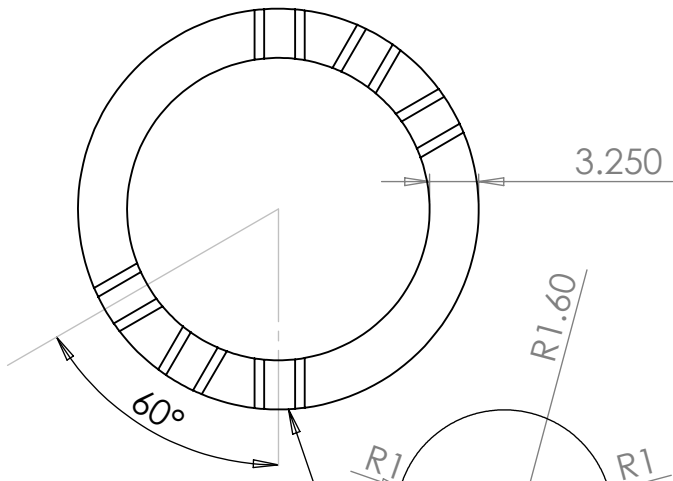
**Modified Bottom Die for Thrust Bump:
Pin and Assembly**

MATERIAL: SS303

DWG NO. **DIE 06(d)**

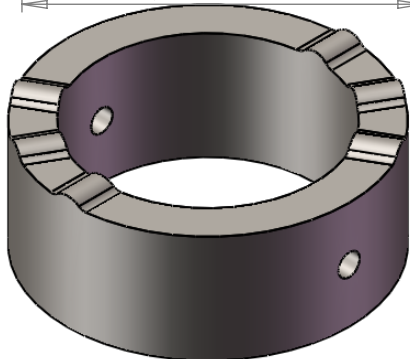
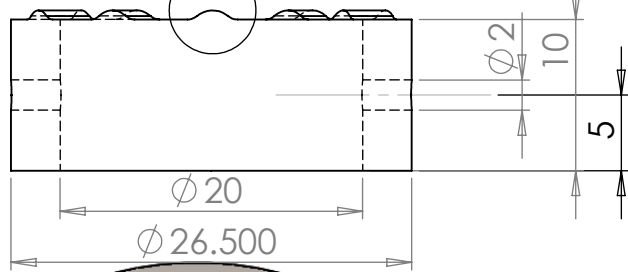
SCALE:1:1

DATE:04/03/2017

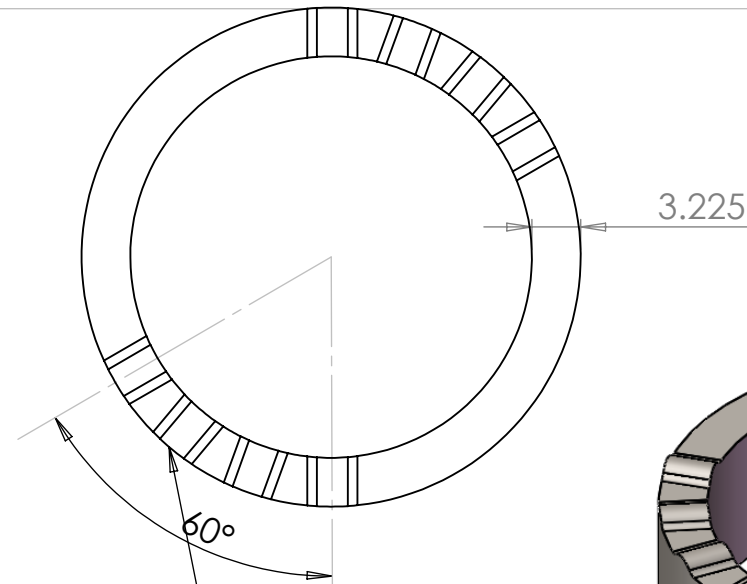


Three Bumps
equispaced

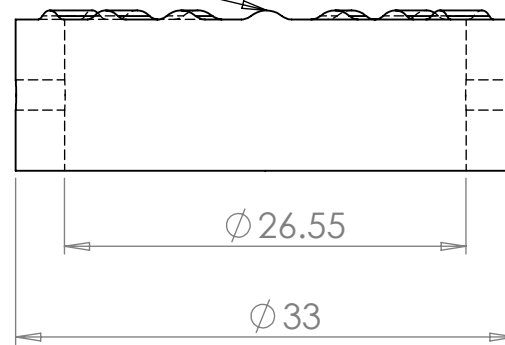
DETAIL C
SCALE 5 : 1



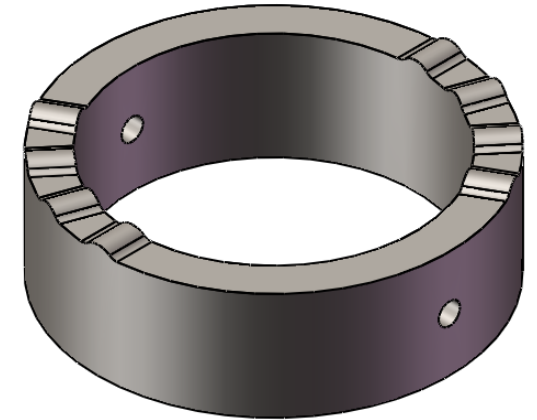
Ring 1



Four Bumps
equispaced



Ring 2



Note:
All Dimensions are in mm
General tolerance is +/- 0.01mm

Surface Finish $\sqrt{1.6}$ unless stated otherwise

MECHANICAL ENGINEERING DEPT.
NIT Rourkela

TITLE: **CRYOGENIC TURBOEXPANDER**

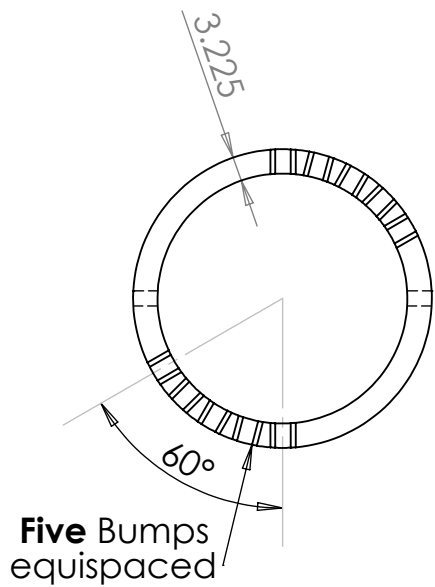
**Modified Top Die for Thrust Bump:
Ring 01 and 02**

MATERIAL: SS303

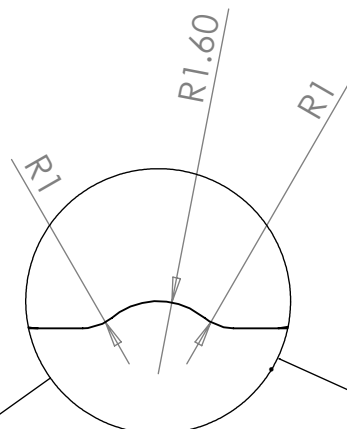
DWG NO. **DIE 07(a)**

SCALE:1:1

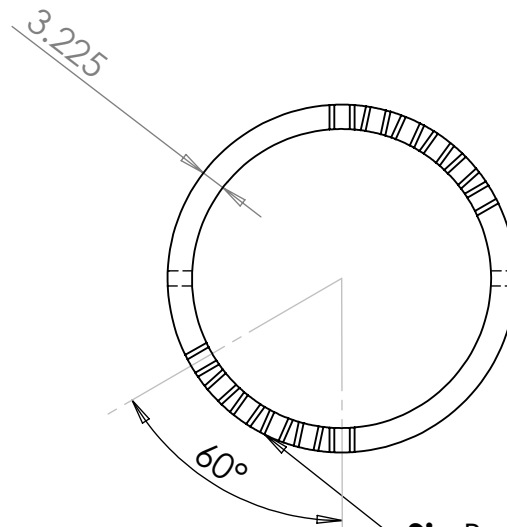
DATE: 04/03/2017



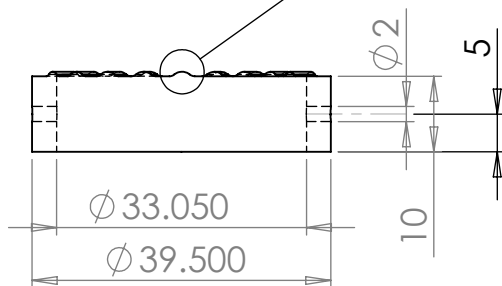
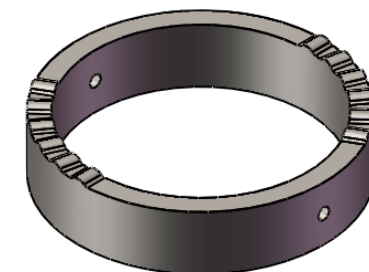
Five Bumps equispaced



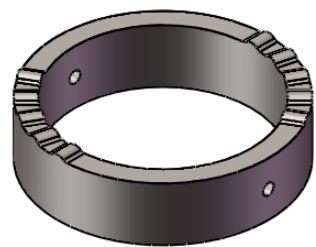
DETAIL D
SCALE 6 : 1



Six Bumps equispaced



Ring 04



Ring 03

Note:
All Dimensions are in mm
General tolerance is +/- 0.01mm

Surface Finish $\sqrt{1.6}$ unless stated otherwise

MECHANICAL ENGINEERING DEPT.
NIT Rourkela

TITLE: **CRYOGENIC TURBOEXPANDER**

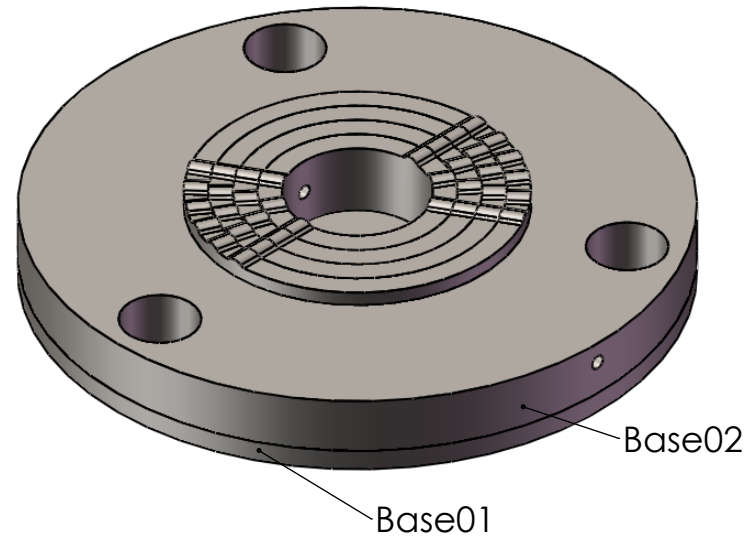
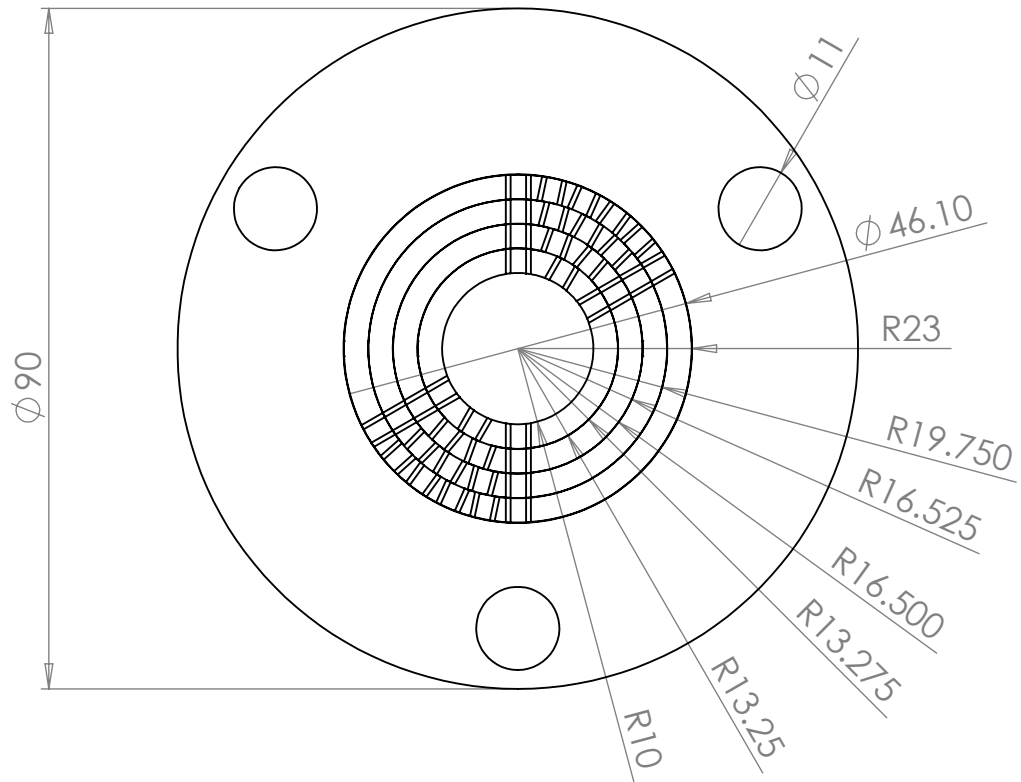
**Modified Top Die for Thrust Bump:
Ring 03 and 04**

MATERIAL: SS303

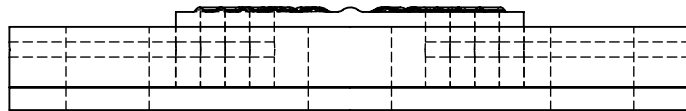
DWG NO. **DIE 07(b)**

SCALE:2:1

DATE: 03/04/2017



Base 01 and Base 02 is same as of bottom thrust die



Note:
All Dimensions are in mm
General tolerance is +/- 0.01mm

Surface Finish $\sqrt{1.6}$ unless stated otherwise

MECHANICAL ENGINEERING DEPT.
NIT Rourkela

TITLE: **CRYOGENIC TURBOEXPANDER**

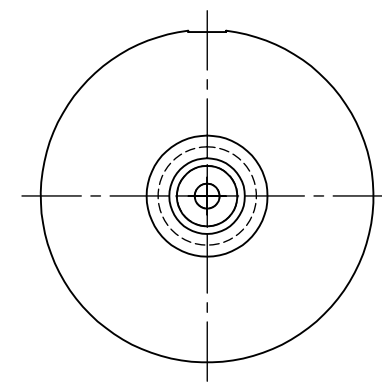
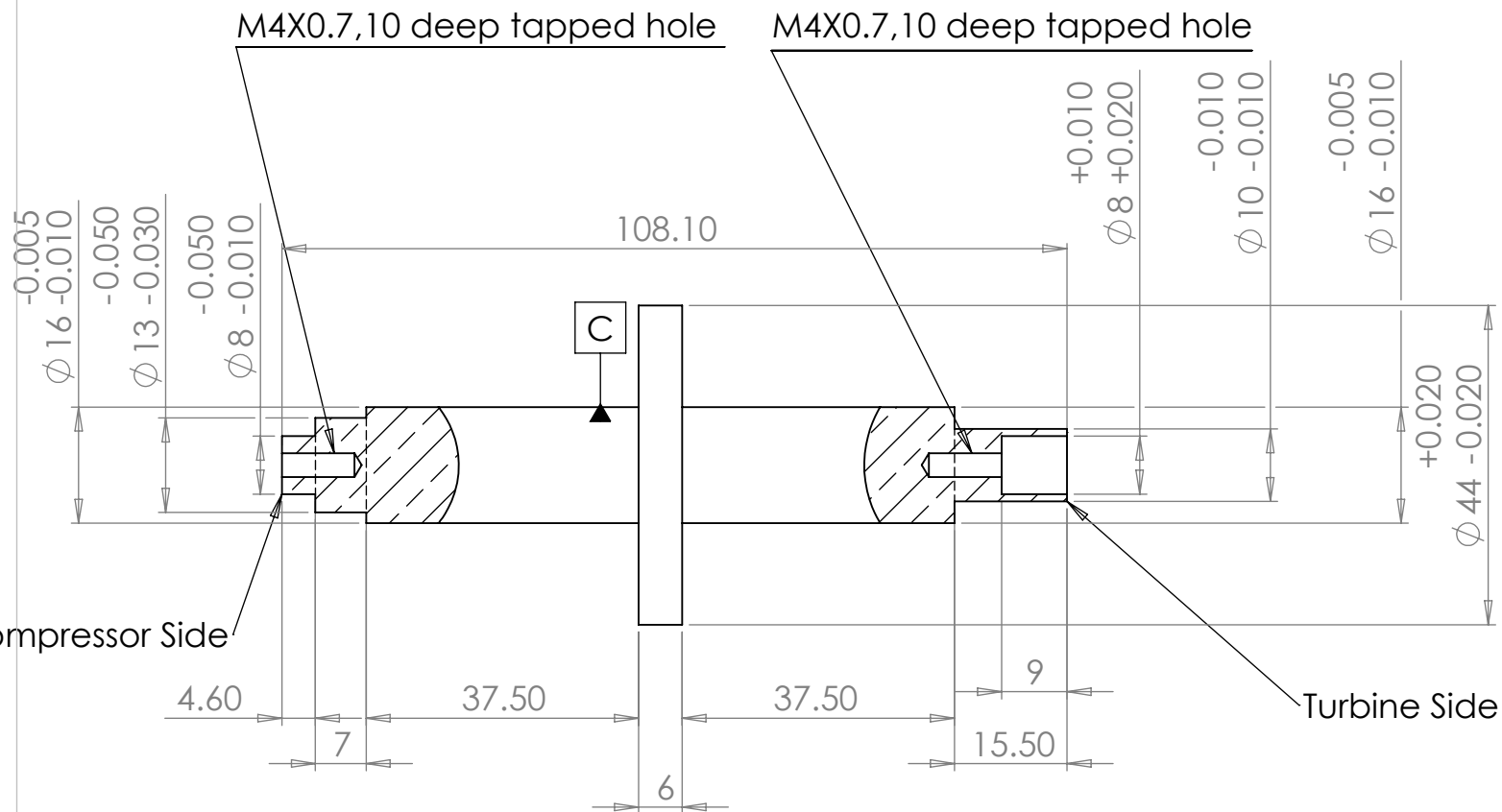
**Modified Top Die for Thrust Bump:
Assembly**

MATERIAL: SS303

DWG NO. **DIE 07(c)**

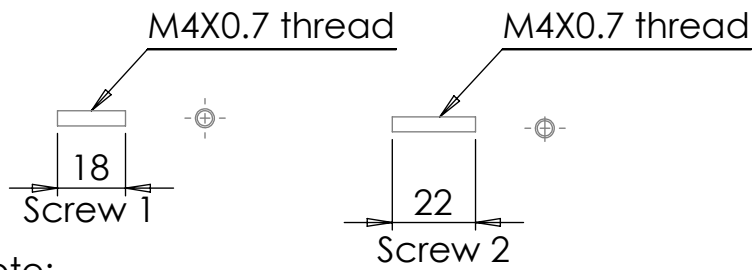
SCALE:2:1

DATE: 04/03/2017



Compressor Side

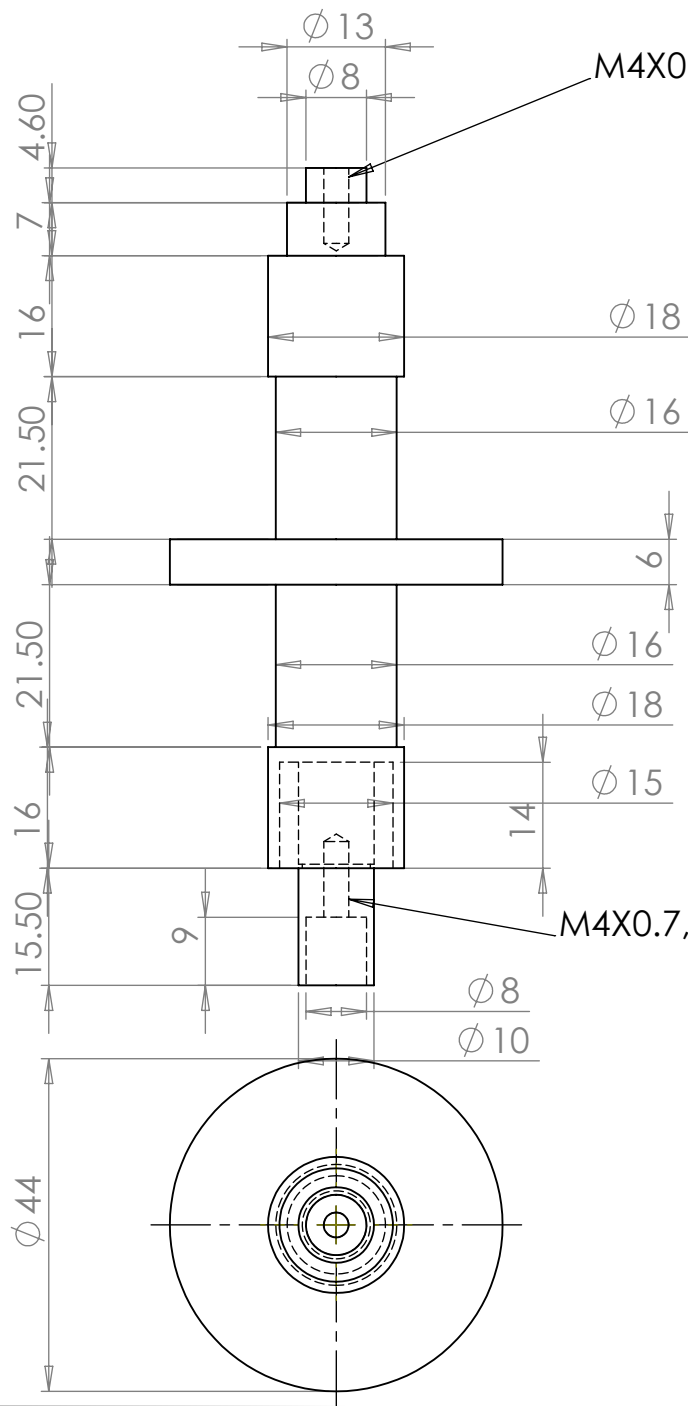
Turbine Side



Note:
 All dimintions to be concentric to datum C with in 0.005 mm
 All dimensions are in mm.
 General tolerance is +/- 01.mm.
 All sharp edges to be rounded to 0.2R.

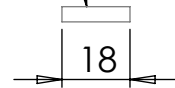
Suraface Finish $\sqrt{1.6}$ unless stated otherwise

MECHANICAL ENGINEERING DEPT. NIT Rourkela	
TITLE:	CRYOGENIC TURBOEXPANDER
Shaft	
MATERIAL: K monel 500	DWG NO. TEX-01
SCALE:1:1	DATE: 04/03/2017

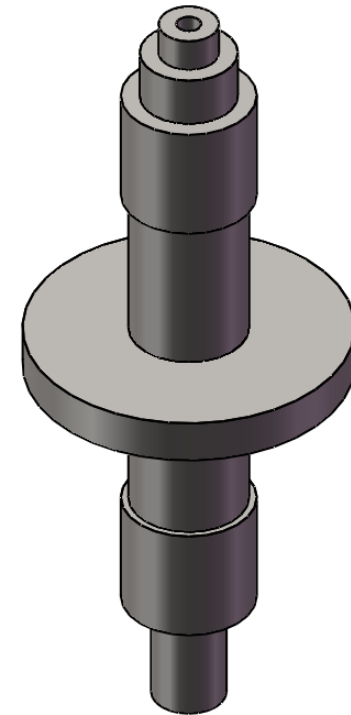


M4X0.7,10 Deep tapped hole

M4X0.7 thread screw



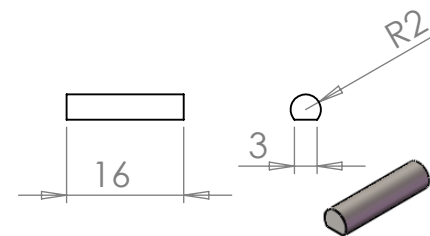
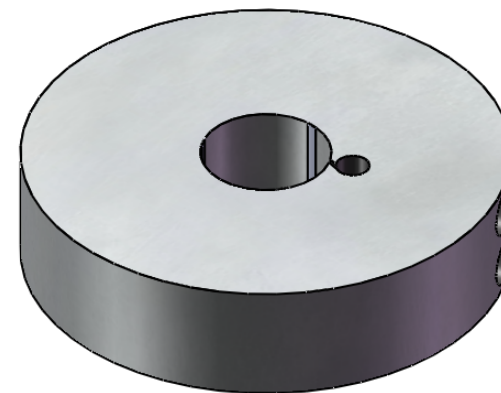
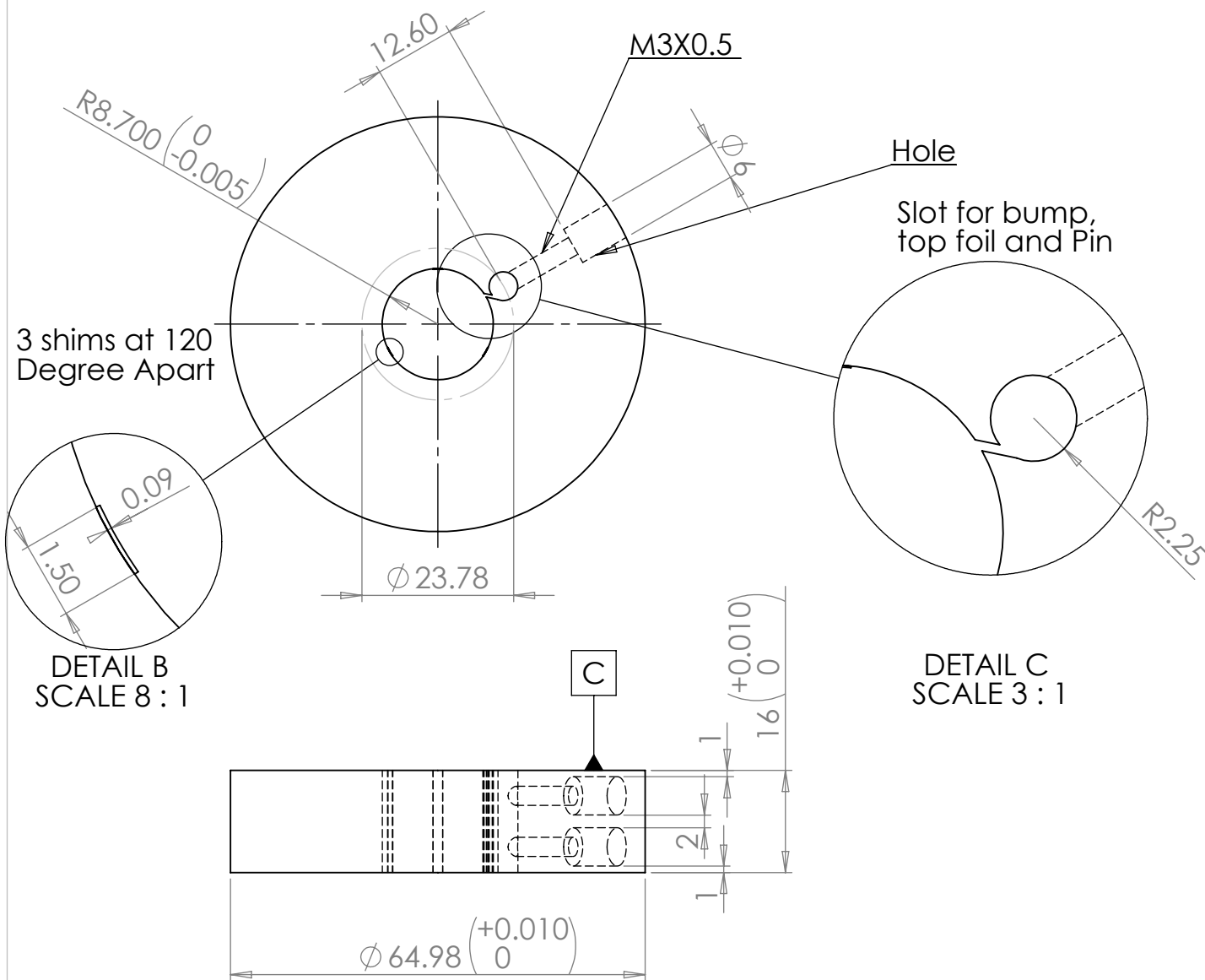
M4X0.7 thread screw



M4X0.7,10 Deep tapped hole

NOTE:
All dimensions are in mm
General tolerance is +/-0.01mm

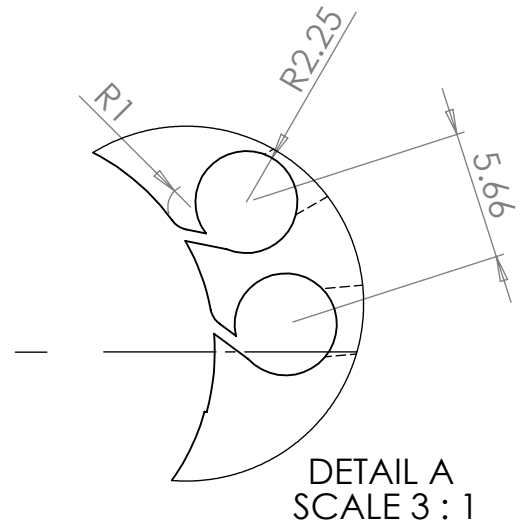
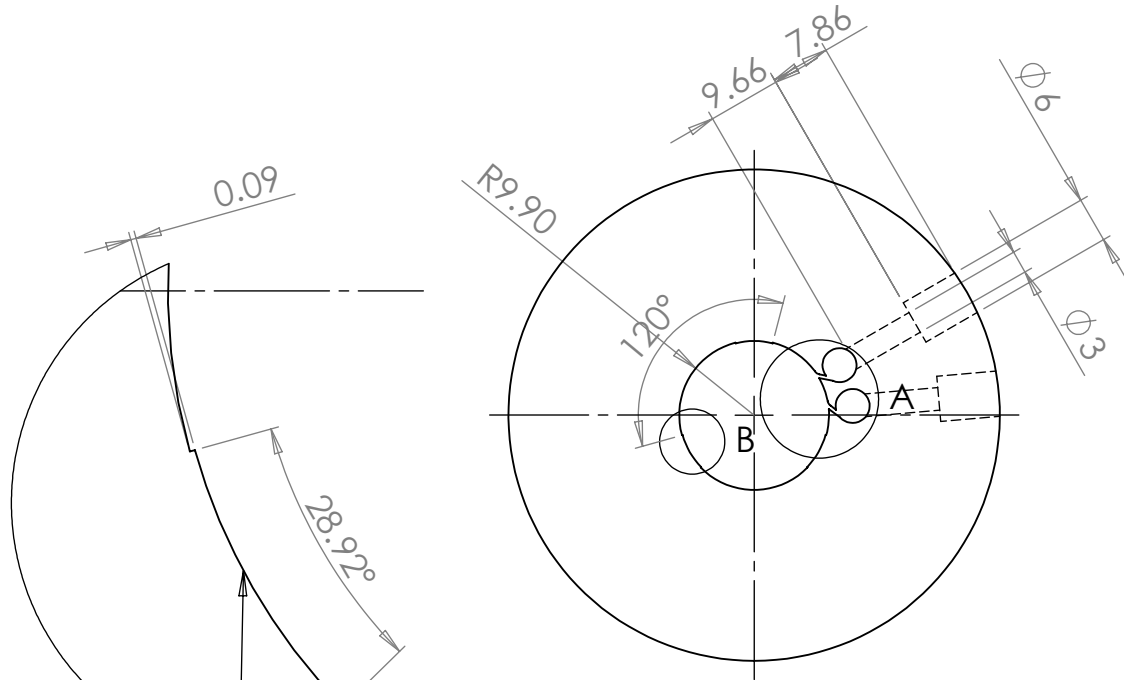
MECHANICAL ENGINEERING DEPT. NIT Rourkela	
TITLE: CRYOGENIC TURBOEXPANDER	
Modified Shaft with Ring Magnet Slot	
MATERIAL: K Monel 500	DWG NO. TEX_02
SCALE: 1:1	DATE: 04/03/2017



One Pin to be inserted in slot

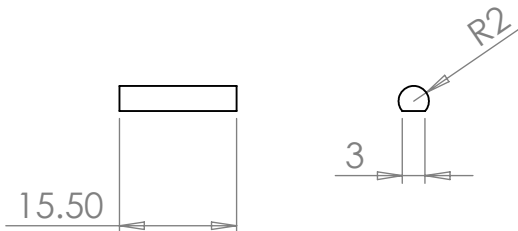
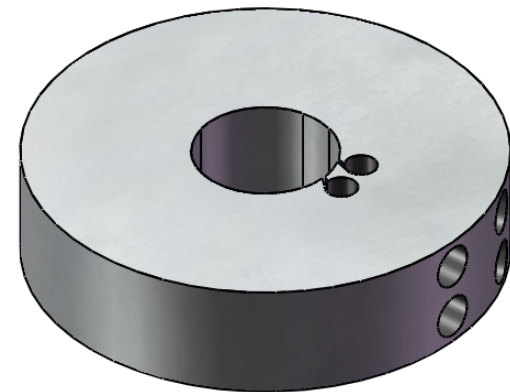
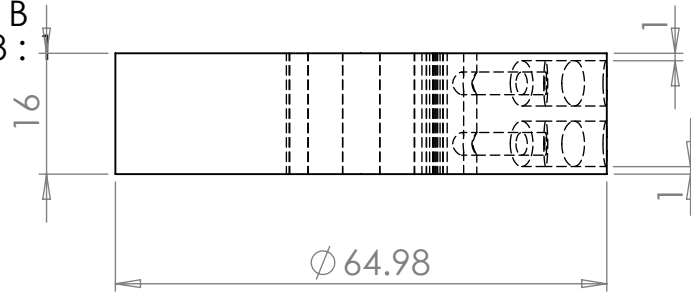
Note:
 All Dimensions to be concentric to datum C withing 0.005 mm.
 All dimensions are in mm.
 General tolerance is +/- 0.1mm.
 All sharp edges to be rounded to 0.2R.
 Material:- SS304

MECHANICAL ENGINEERING DEPT. NIT Rourkela	
TITLE:	CRYOGENIC TURBOEXPANDER
Journal Bearing Base	
MATERIAL: SS304	DWG NO. TEX-03
SCALE 2:1	DATE: 04/03/2017



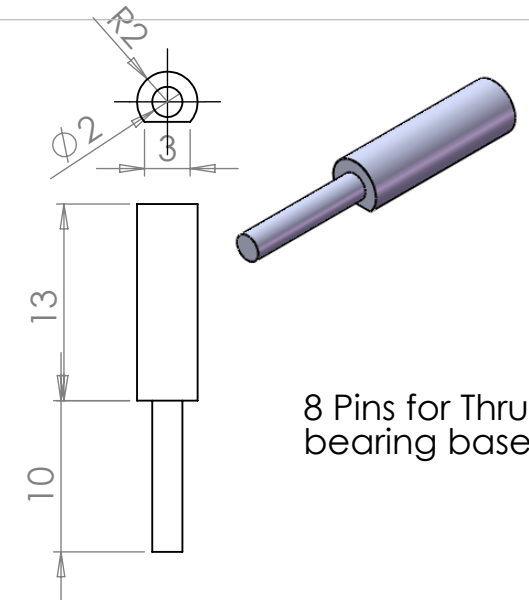
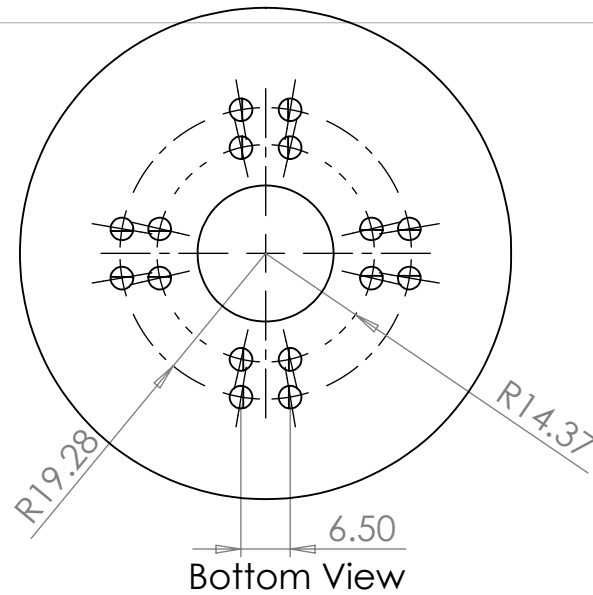
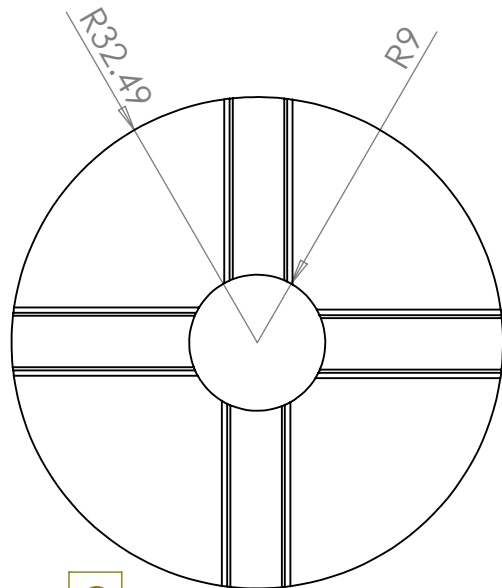
Three projected slot of 0.09 micron at 120 degree apart

DETAIL B
SCALE 8 :

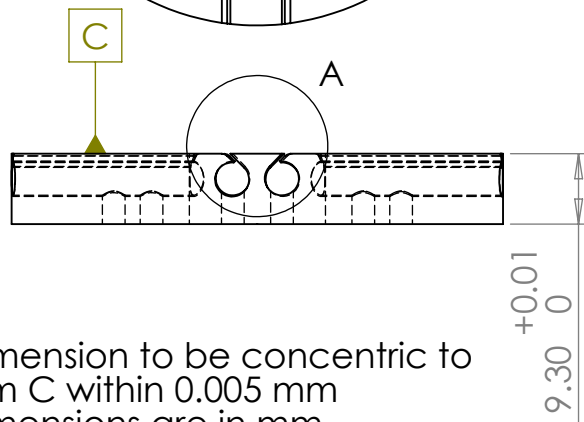


NOTE:
All dimensions are in mm
General tolerance is +/-0.01mm

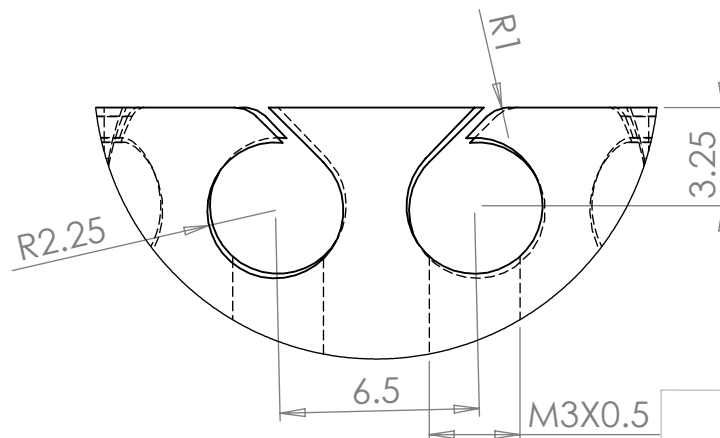
MECHANICAL ENGINEERING DEPT. NIT Rourkela		
TITLE: CRYOGENIC TURBOEXPANDER		
Journal Bearing for Ring Magnet		
MATERIAL: SS304	DWG NO. TEX_04	
	SCALE:1:1	DATE:04/03/2017



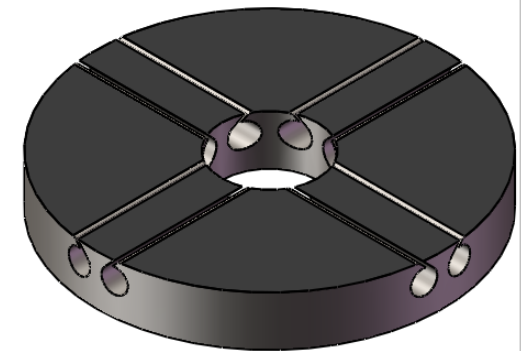
8 Pins for Thrust bearing base



+0.01
9.30 0



DETAIL A
SCALE 4 : 1



Thrust bearing base

Note:
All Dimension to be concentric to datum C within 0.005 mm
All dimensions are in mm.
General tolerance is +/- 0.01mm.

MECHANICAL ENGINEERING DEPT.
NIT Rourkela

TITLE: **CRYOGENIC TURBOEXPANDER**

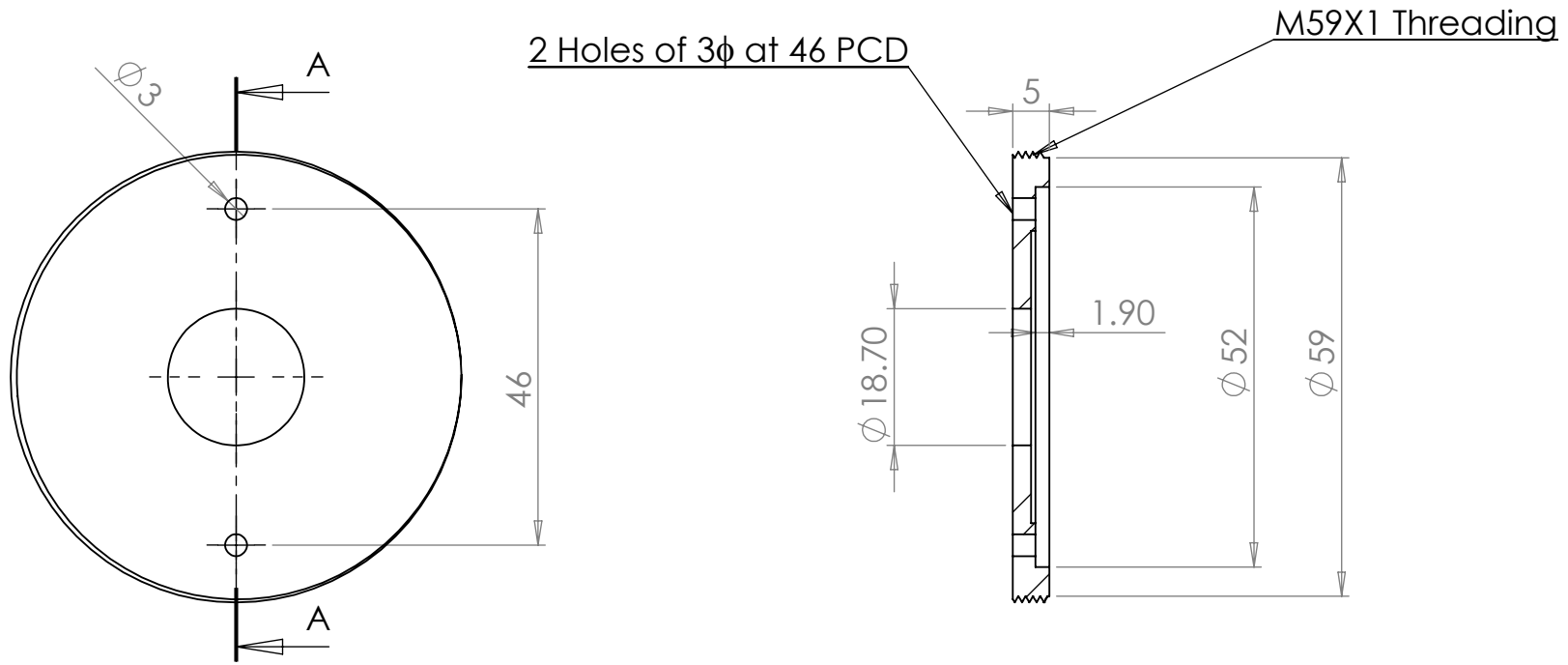
Thrush Bearings Base

MATERIAL: SS304

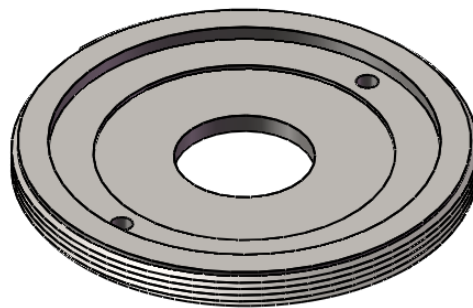
DWG NO. **TEX-05**

SCALE:1:1

DATE: 04/03/2017

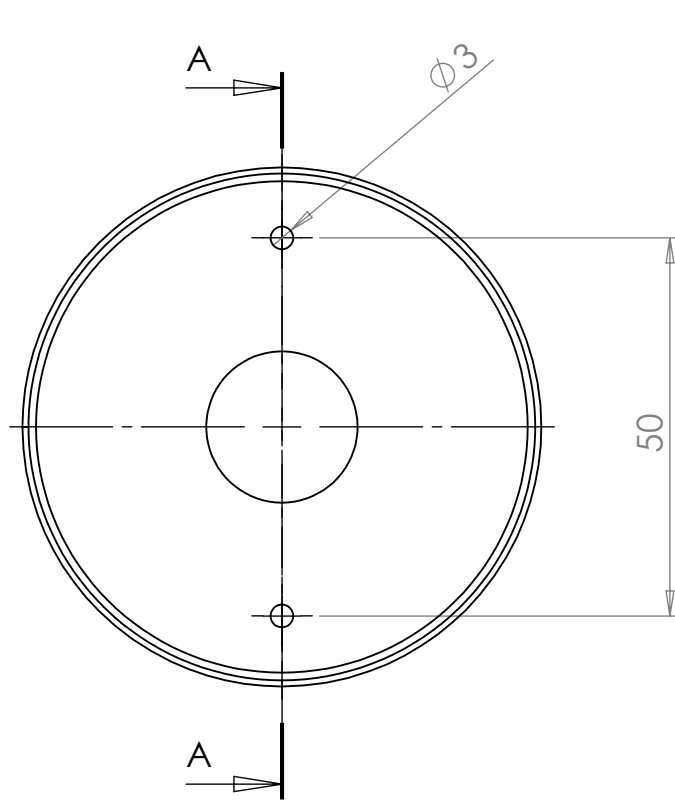


SECTION A-A

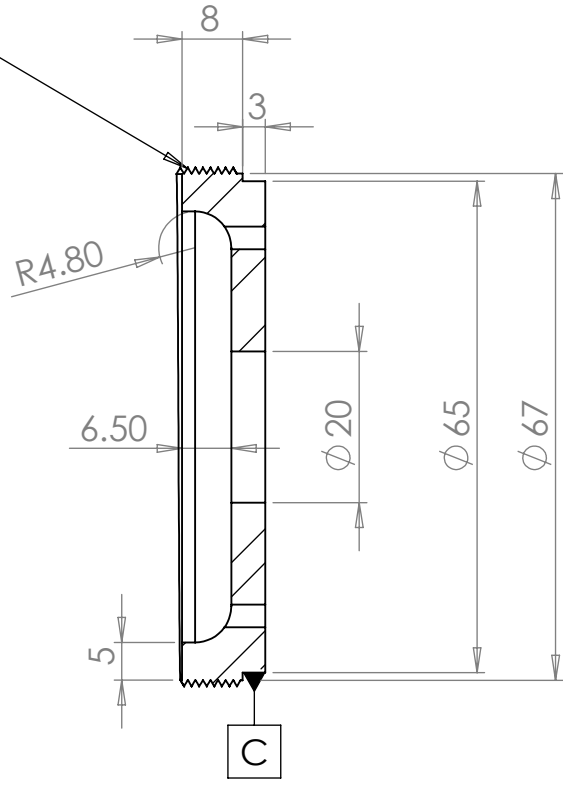


Note:
 All Dimension to be concentric to datum C within 0.005 mm.
 All dimensions are in mm.
 General tolerance is +/- 01.mm.

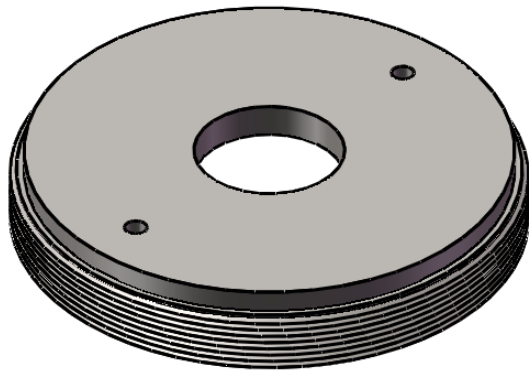
MECHANICAL ENGINEERING DEPT. NIT Rourkela		
TITLE: CRYOGENIC TURBOEXPANDER		
Lock Nut (Turbine Side)		
MATERIAL: SS304	DWG NO. TEX-06	
SCALE:1:1	DATE: 04/03/2017	



M67X1 Threading

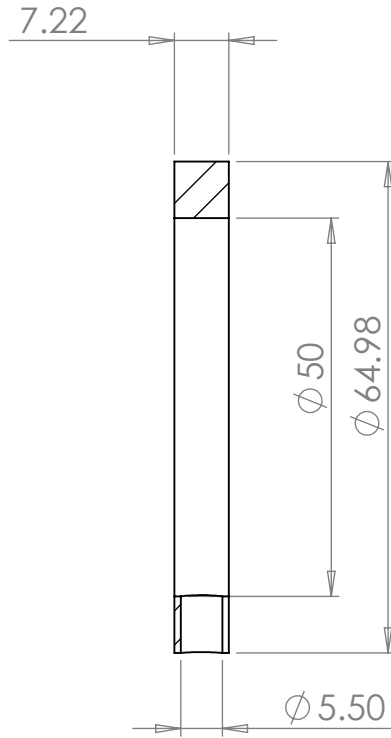
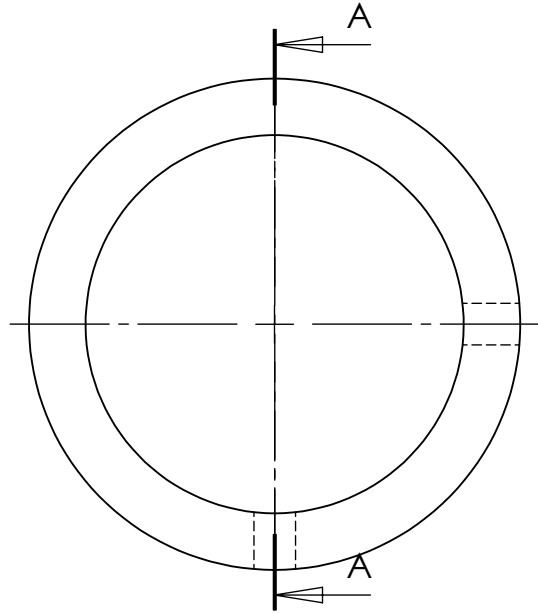


SECTION A-A

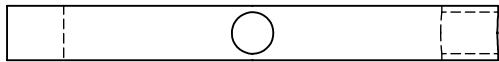


Note:
 All Dimension to be concentric to datum C within 0.005 mm.
 All dimensions are in mm.
 General tolerance is +/- 0.01mm.

MECHANICAL ENGINEERING DEPT. NIT Rourkela	
TITLE:	CRYOGENIC TURBOEXPANDER
Lock Nut (Compressor side)	
MATERIAL: SS304	DWG NO. TEX-07
SCALE: 1:1	DATE: 04/03/2017

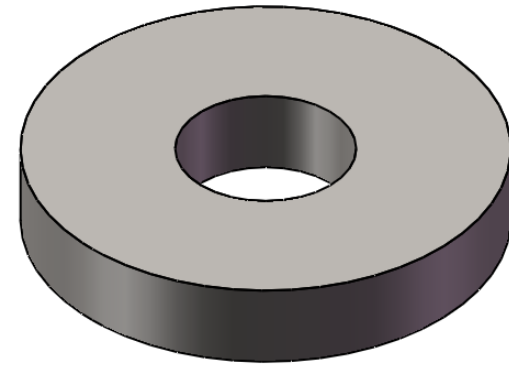
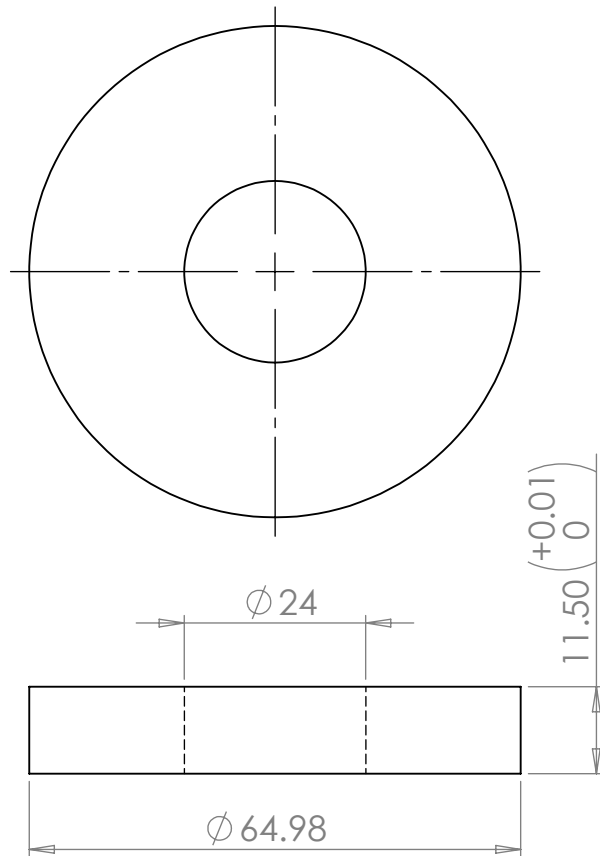


SECTION **A-A**



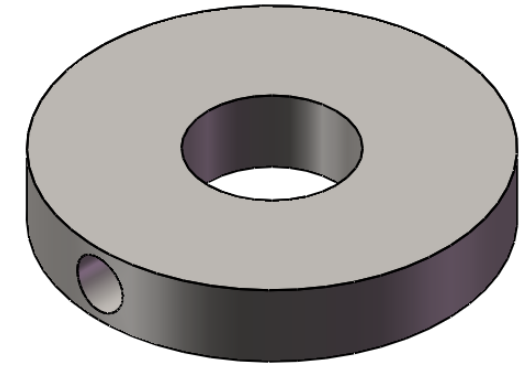
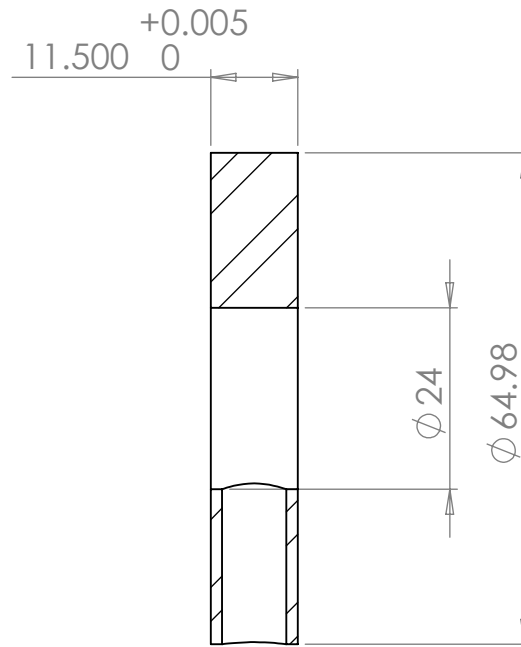
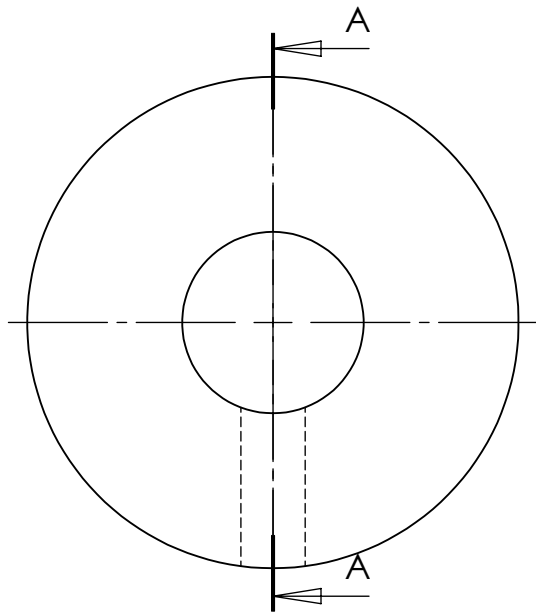
Note:
 All dimensions are in mm.
 General tolerance is +/- 0.01 mm.

MECHANICAL ENGINEERING DEPT. NIT Rourkela	
TITLE:	CRYOGENIC TURBOEXPANDER
Spacer between Thrust Bearings	
MATERIAL: SS304	DWG NO. TEX-08
SCALE: 1:1	DATE: 04/03/2017

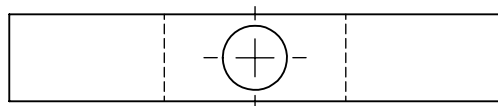


Note:
 All dimensions are in mm.
 General tolerance is +/- 0.01mm.
 Material:- SS304

MECHANICAL ENGINEERING DEPT. NIT Rourkela	
TITLE:	CRYOGENIC TURBOEXPANDER
Lower Spacer betwn Jornal and thrust bearing	
MATERIAL: SS304	DWG NO. TEX-09
SCALE:1:1	DATE: 04/03/2017

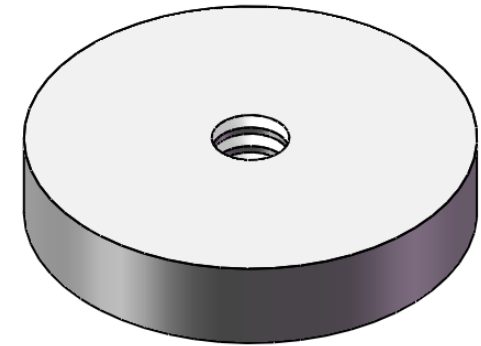
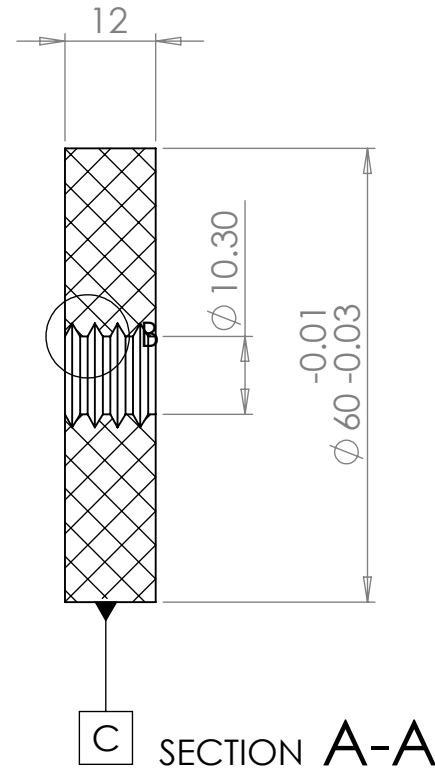
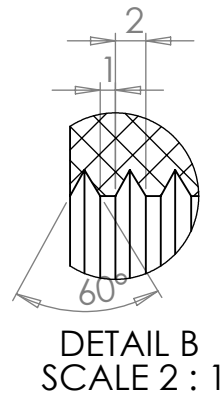
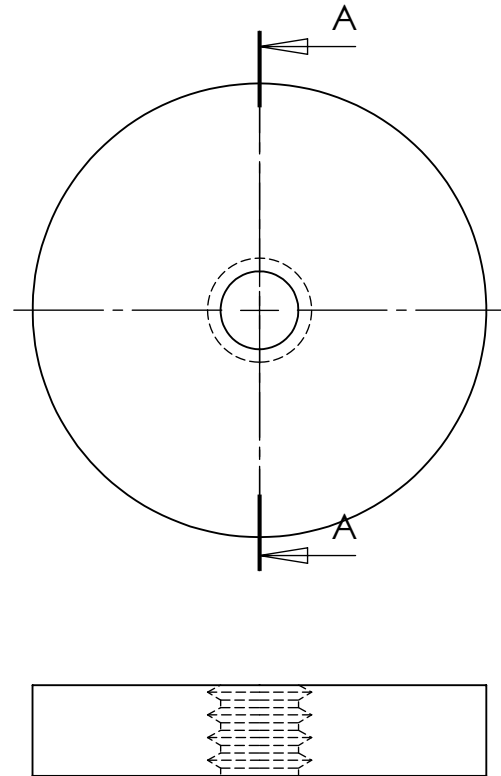


SECTION **A-A**



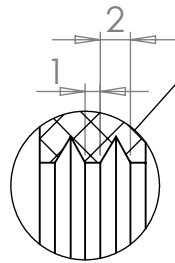
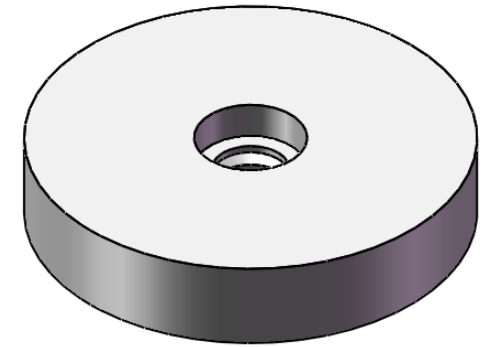
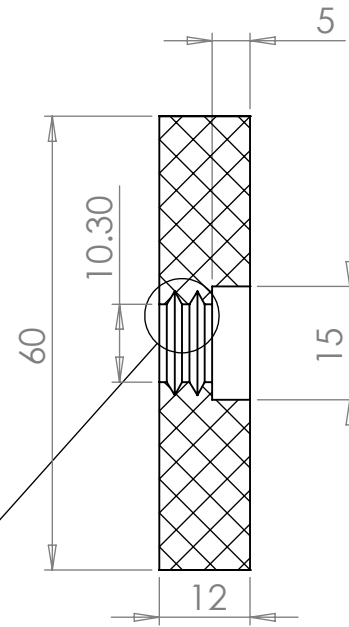
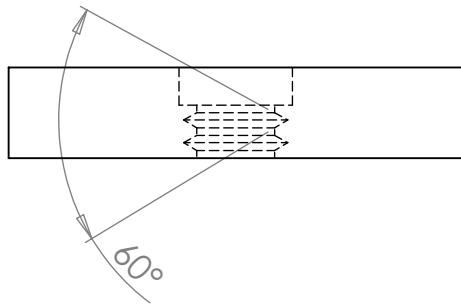
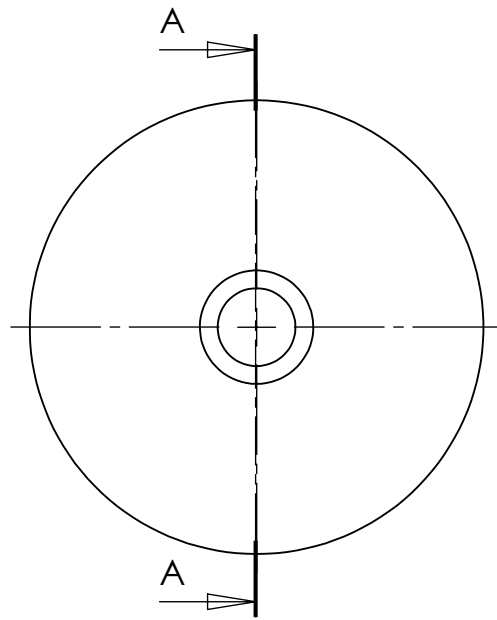
Note:
 All dimensions are in mm.
 General tolerance is +/- 01.mm.

MECHANICAL ENGINEERING DEPT. NIT Rourkela		
TITLE: CRYOGENIC TURBOEXPANDER		
Upper Spacer betwn Thrust and journal bearing		
MATERIAL: SS304	DWG NO. TEX-10	
	SCALE:1:1	DATE: 04/03/2017



Note:
 All Dimension to be concentric to datum C within 0.005 mm
 All dimensions are in mm.
 General tolerance is +/- 0.01mm.

MECHANICAL ENGINEERING DEPT. NIT Rourkela		
TITLE: CRYOGENIC TURBOEXPANDER		
Thermal Insulator		
MATERIAL: TEFLON	DWG NO.	TEX-11
	SCALE:1:1	DATE: 04/03/2017

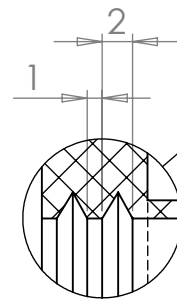
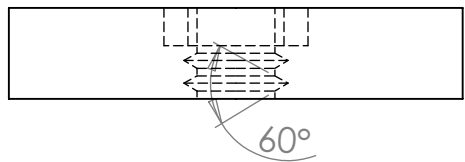
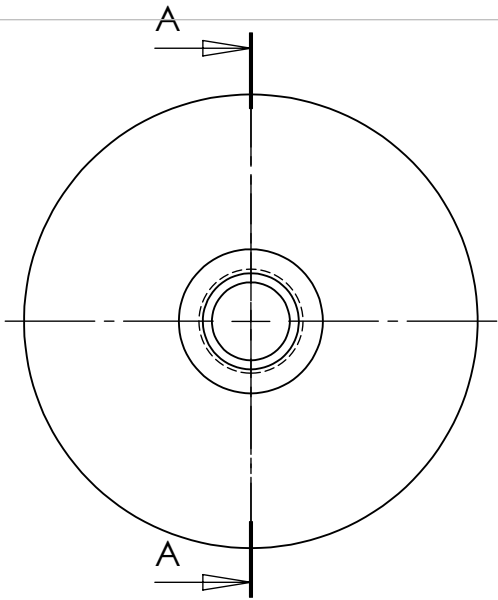


DETAIL B
SCALE 2 : 1

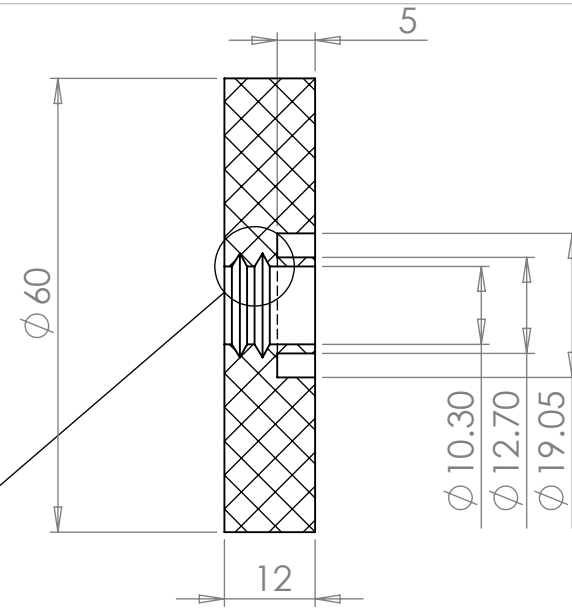
SECTION A-A

NOTE:
All dimensions are in mm
General tolerance is +/-0.01mm

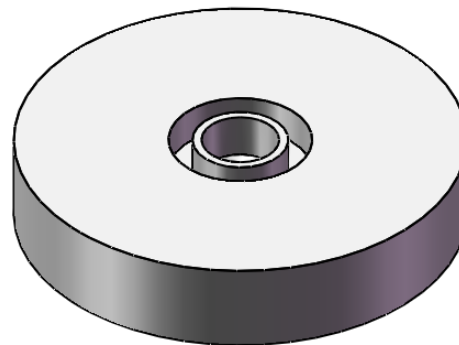
MECHANICAL ENGINEERING DEPT. NIT Rourkela		
TITLE: CRYOGENIC TURBOEXPANDER		
Thermal Insulator With Ring Magnet Slot 1		
MATERIAL: TEFLON	DWG NO. TEX_12(a)	
	SCALE:1:1	DATE: 04/03/2017



DETAIL B
SCALE 2 : 1

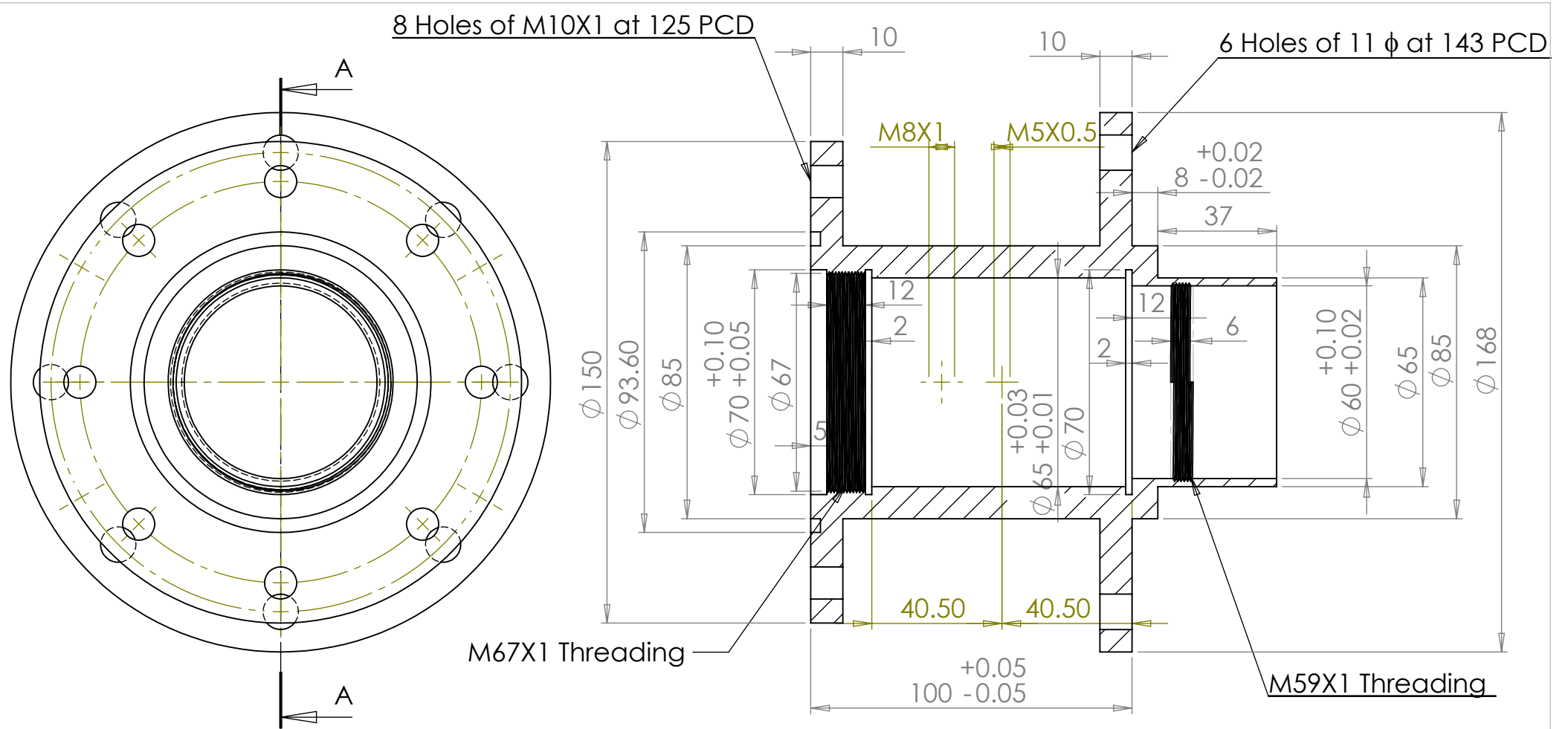


SECTION A-A



NOTE:
All dimensions are in mm
General tolerance is ± 0.01 mm

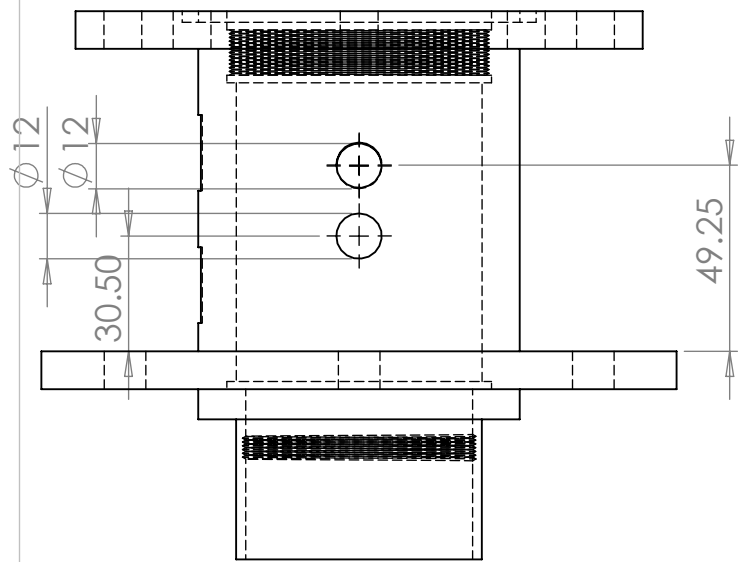
MECHANICAL ENGINEERING DEPT. NIT Rourkela	
TITLE: CRYOGENIC TURBOEXPANDER	
Thermal Insulator with Ring Magnet 2	
MATERIAL: TEFLON	DWG NO. TEX_12(b)
SCALE:1:1	DATE:04/03/2017



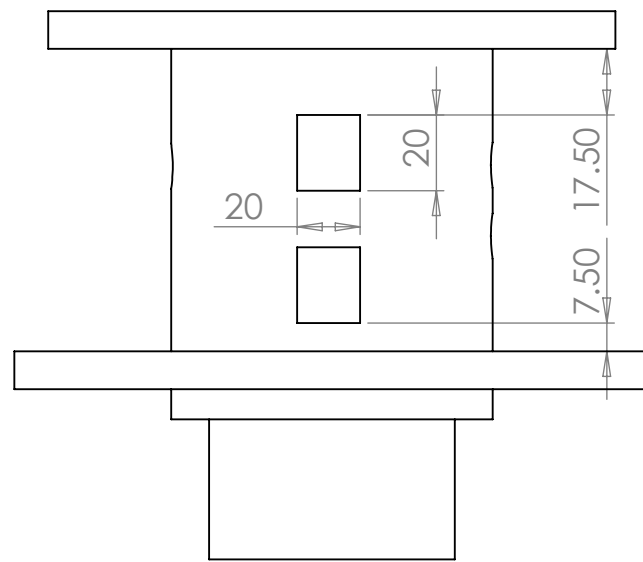
SECTION A-A
SCALE 1 : 1.75

Note:
All dimensions are in mm.
General tolerance is +/- 01.mm.
All sharp edges to be rounded to 0.2R.

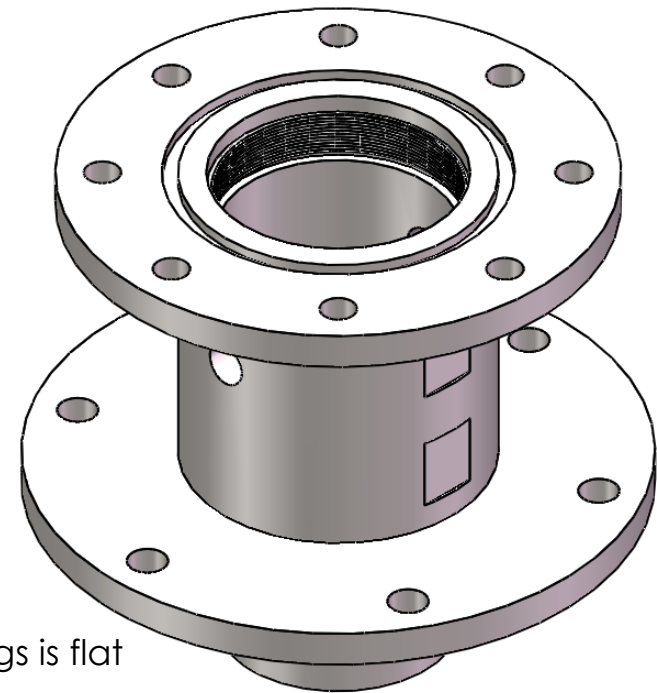
MECHANICAL ENGINEERING DEPT. NIT Rourkela	
TITLE:	CRYOGENIC TURBOEXPANDER
Bearing Housing	
MATERIAL: SS304	DWG NO. TEX-13(a)
SCALE:1:1.75	DATE: 04/03/2017



FOUR holes M12X1



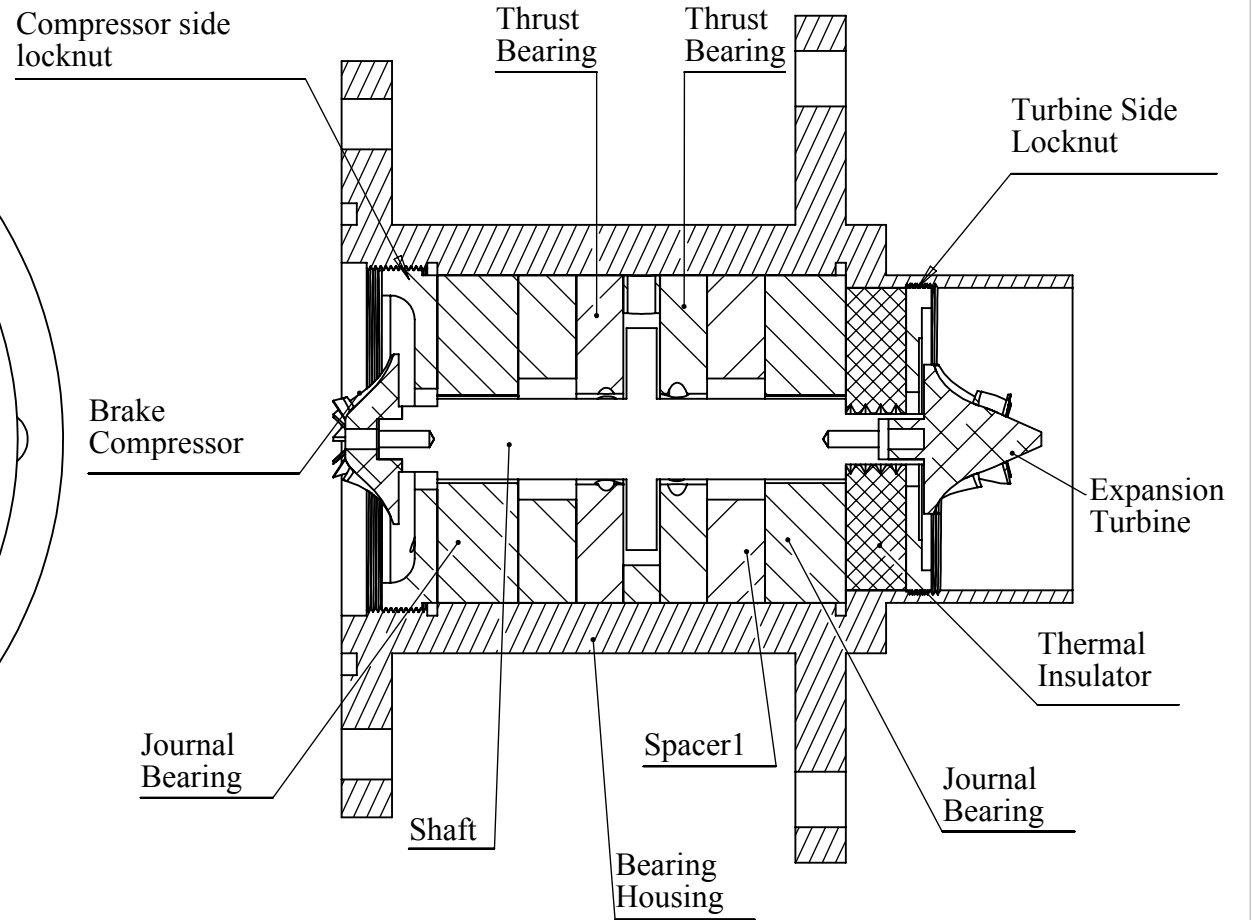
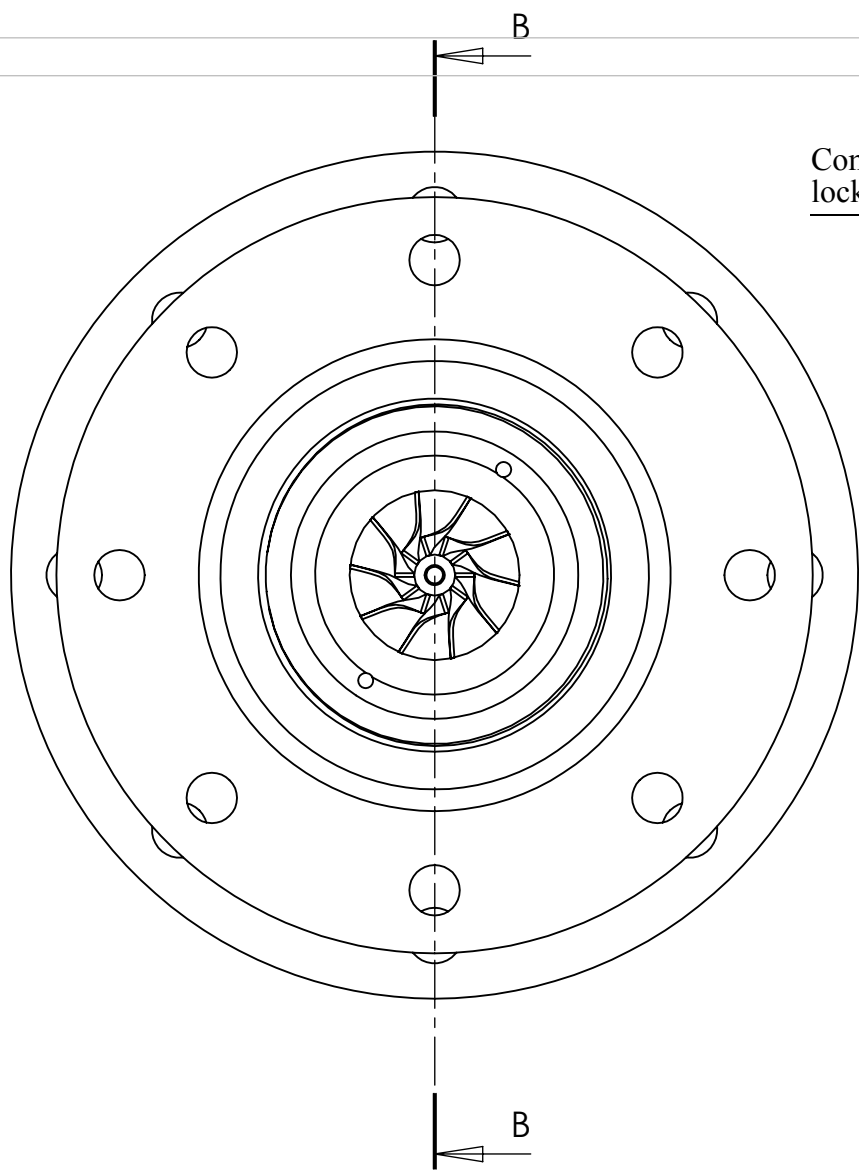
TWO portion near journal bearings is flat 20X20X1 mm



NOTE:

All dimensions are in mm
General tolerance is +/-0.01mm

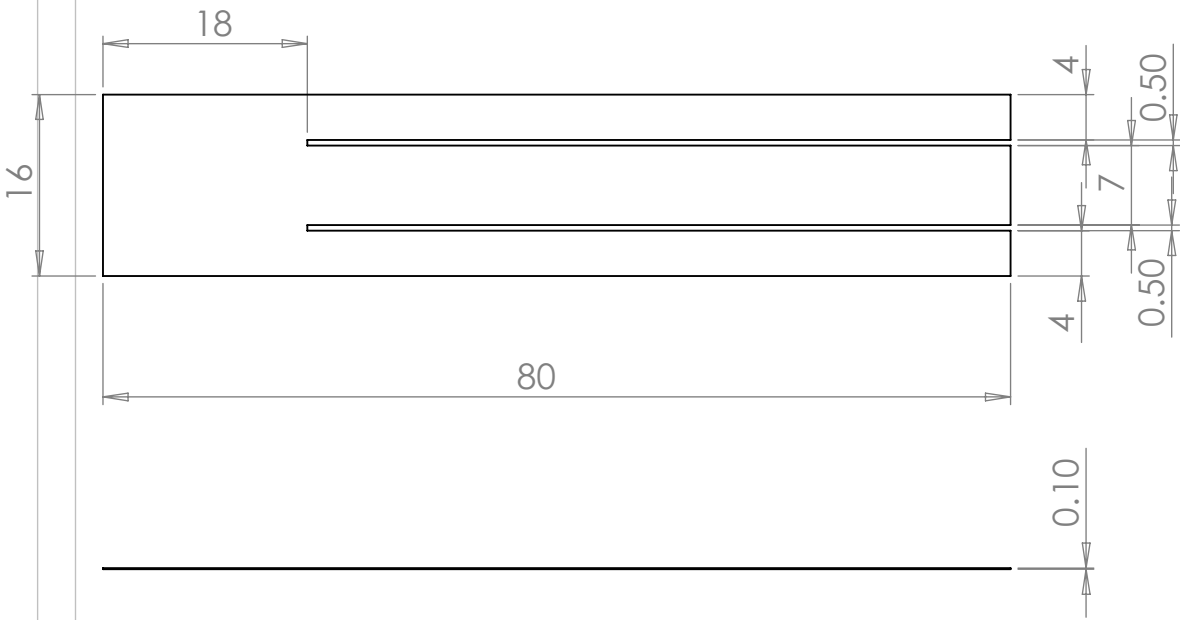
MECHANICAL ENGINEERING DEPT. NIT Rourkela	
TITLE:	CRYOGENIC TURBOEXPANDER
Bearing Housing(b)	
MATERIAL: SS304	DWG NO. TEX_13(b)
SCALE:1:2	DATE: 04/03/2017



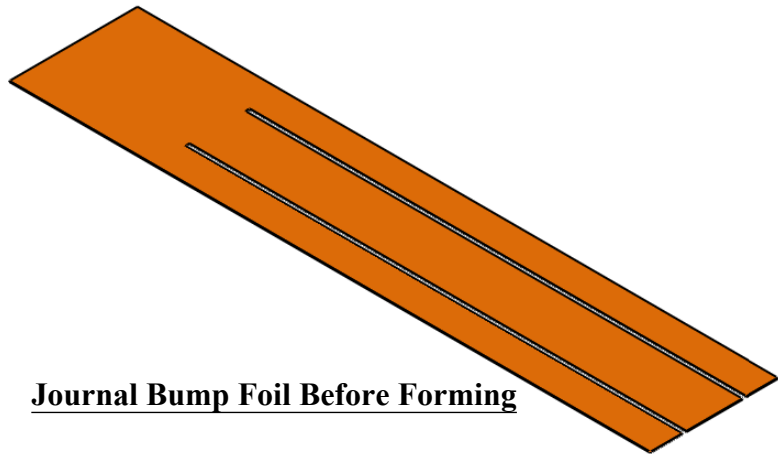
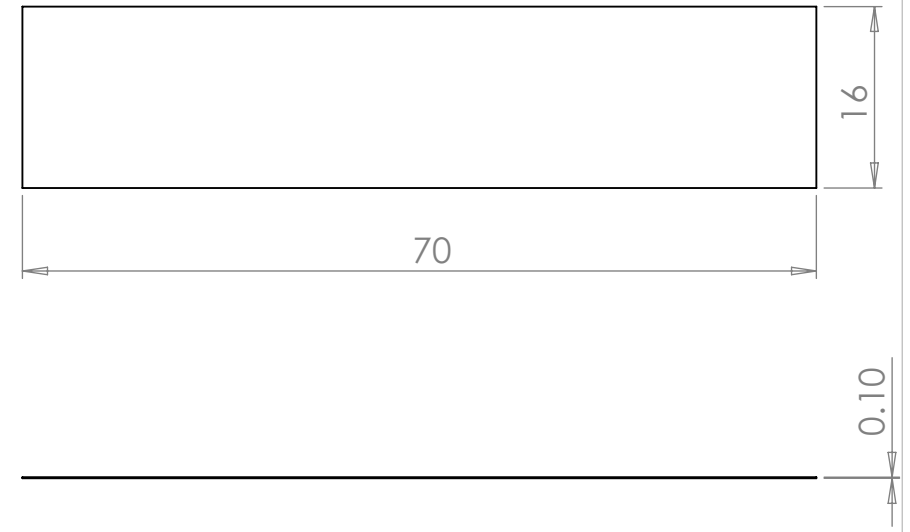
SECTION B-B
SCALE 1 : 1.5

MECHANICAL ENGINEERING DEPT. NIT Rourkela	
TITLE:	CRYOGENIC TURBOEXPANDER
Assembly of Turboexpander (Bearing Unit)	
DWG NO.	TEX-14
SCALE:1:5	DATE:04/03/2017

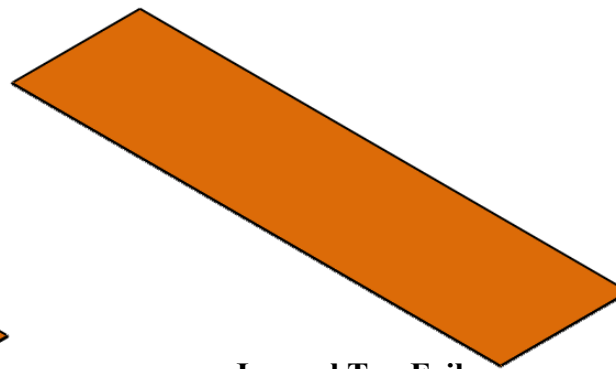
Journal Bump Foil Before Forming



Journal Top Foil



Journal Bump Foil Before Forming

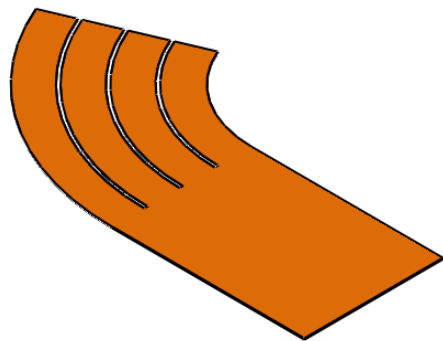
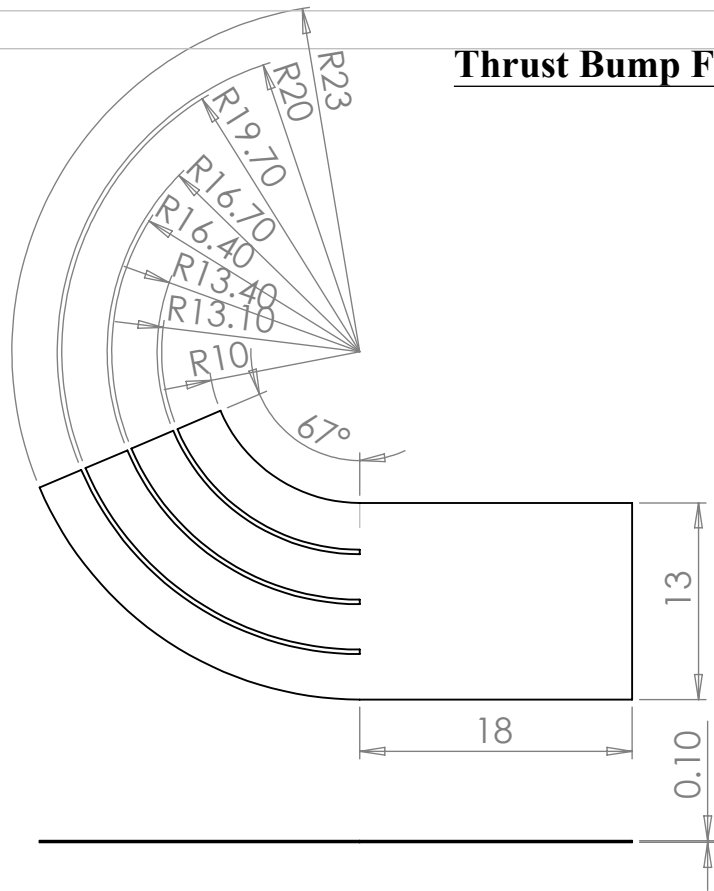


Journal Top Foil

Note:
All dimensions are in mm.
General tolerance is +/- 0.01mm.

MECHANICAL ENGINEERING DEPT. NIT Rourkela	
TITLE:	CRYOGENIC TURBOEXPANDER
Journal Bump and Top Foil	
MATERIAL: Phosphor Bronze	DWG NO. FOIL 01
SCALE:1.5:1	DATE:04/03/2017

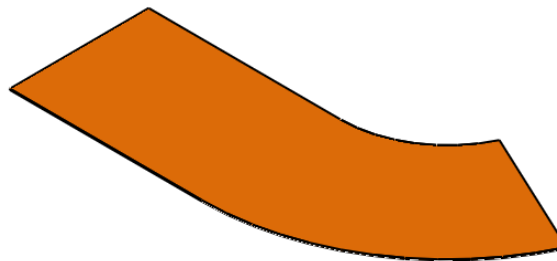
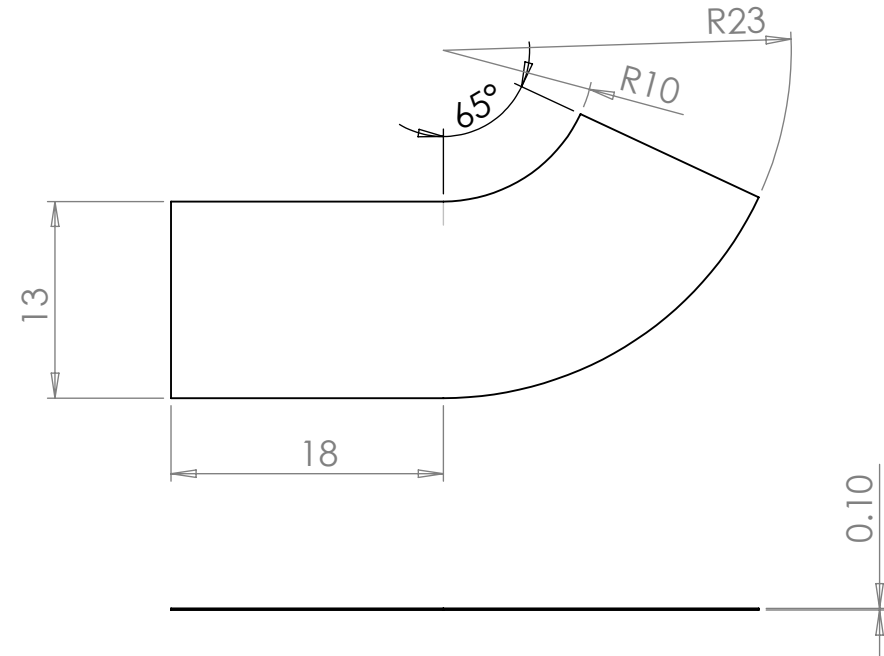
Thrust Bump Foil Before Forming



Thrust Bump Foil Before Forming

Note:
All dimensions are in mm.
General tolerance is +/- 0.01 mm.

Thrust Top Foil



Thrust Top Foil

MECHANICAL ENGINEERING DEPT. NIT Rourkela		
TITLE: CRYOGENIC TURBOEXPANDER		
Thrust Bump and Top Foil		
MATERIAL: Phosphor Bronze	DWG NO.	FOIL 02
SCALE:2:1	DATE: 04/03/2017	

Curriculum Vitae

Name : Suraj Kumar Behera

Email : beherask@nitrkl.ac.in; suraj.behera@gmail.com;

Mailing Address:

Department of Mechanical Engineering

NIT Rourkela, Rourkela -769008

Sundergarh, ODISHA(INDIA)

Phone:+91-661-2462508 , Mobile No: +91-9040893760

Date of Birth & Gender: 12/11/1976, Male

Education

2017 Ph.D. Dissertation submitted, NIT Rourkela

2003 M.Tech, IIT Kanpur

1999 B.E., REC, Rourkela

Employment History

2012 – Till date, Assistant professor , NIT Rourkela

2009-2011, Assistance Professor, C.V.Raman College of Engineering, Bhubaneswar

2007-2009, Group leader, Amdocs, Pune

2006-2007, Team Lead Project, Covansys, Chennai

2003-2006, Assistance System Engineer, Tata consultancy Services, Chennai

1999-2001, Senior Officer, Tata Steel, Dhanbad

Publications:

International Conferences:

1. Behera, S.K., Sarangi, S.K., Sahoo, R.K. and Singh, T.,“ A Methodology for Fabrication of 2nd Generation Gas Foil Thrust and Journal Bearing For Turboexpander Used In Nitrogen Liquefier,” *ICEC 26 - ICMC 2016*, New-Delhi, India, March 2016
2. Behera, S.K., Sarangi, S.K., and Singh, T, “Feasibility Studies on Gas Foil Journal Bearings in Small and High-Speed Oil-Free Cryogenic Turboexpander,” *AsiaTrib-2014*, Agra, India, February 2014.

National Conferences:

3. Behera, S.K., Sarangi, S.K., Sahoo, R.K. and Singh, T “Design of gas foil thrust bearing for vertically operated turboexpander used in cryogenic application” *National Symposium on Cryogenic-26*, Kolkata, India, February 2017.

4. Behera, S.K., Sarangi, S.K., Sahoo, R.K. and Singh, T, “Design and Development of Axial Passive Magnetic Bearings”, *National Symposium on Rotordynamics 2016*, NIT Rourkela, India, January 2016.
5. Behera, S.K., Sarangi, S.K., Sahoo, R.K. and Singh, T, “Design and Fabrication of Gas Foil Journal Bearing for High-Speed Small Turboexpander Used in Cryogenic Application”, *National Symposium on Cryogenic-25*, Hyderabad, India, December 2014.

Published in Referred Journal:

6. Kar, K.K., Sharma, S.D., Behera, S.K. and Kumar, P., 2007. Development of rubber pressure molding technique using silicone rubber to fabricate fiber-reinforced plastic components based on glass fiber and epoxy resin. *Journal of Elastomers and Plastics*, 39(2), pp.117-131
7. Kar, K.K., Sharma, S.D., Behera, S.K. and Kumar, P., 2006. Development of rubber pressure molding technique using butyl rubber to fabricate fiber reinforced plastic components based on glass fiber and epoxy resin. *Journal of applied polymer science*, 101(2), pp.1095-1102
8. Kar, K.K., Sharma, S.D., Behera, S.K. and Kumar, P., 2006. Development of rubber pressure moulding technique using polybutadiene rubber to fabricate fibre reinforced plastic components based on glass fibre and epoxy resin. *Current Science*, 90(11), pp.1492-1499
9. Kar, K.K., Sharma, S.D., Behera, S.K. and Kumar, P., 2006. Development of a rubber pressure moulding technique for fiber reinforced plastics. *Kautschuk Und Gummi Kunststoffe*, 59(4), p.169.